Thermodynamics and correlations of ultracold fermions in a two-dimensional optical lattice

Dissertation
zur
Erlangung des Doktorgrades (Dr. rer. nat.)
der
Mathematisch-Naturwissenschaftlichen Fakultät
der
Rheinischen Friedrich-Wilhelms-Universität Bonn

von
Jan Henning Drewes
aus
Bremerhaven, Deutschland

Bonn, 14.12.2020

Angefertigt mit Genehmigung der Mathematisch-Naturwissenschaftlichen Fakultät der Rheinischen Friedrich-Wilhelms-Universität Bonn.

1. Gutachter:	Prof. Dr. Michael Köhl
2. Gutachter:	Prof. Dr. Martin Weitz
Tag der Promotion:	20.07.2021
Erscheinungsjahr:	2022

Abstract

This thesis reports on experiments with ultracold fermionic ^{40}K atoms in an optical lattice realising a quantum simulation of the two-dimensional Hubbard model. A central aspect of the experiments presented here is the combination of radio frequency spectroscopy techniques and a high resolution imaging setup. Thereby, both the in-situ density and spin distributions can be studied in a spatially resolved way.

In a first experiment, the in-situ density distribution has been investigated. Due to the high resolution of the imaging system, phases coexisting in the inhomogeneous trapping potential have been distinguished. Furthermore, the precise characterisation of the external confinement allows to determine the density equation of state, which fully characterises the thermodynamic properties of the many-body system in the investigated range of temperatures. As a hallmark of the repulsive Hubbard model, the crossover from a metal to a Mott-insulator has been observed.

Furthermore, the precise determination of the equation of states allows us to apply the fluctuation dissipation theorem, in order to infer the suppression of non-local density fluctuations in the repulsive Hubbard model from the compressibility and the on-site occupation.

Finally, a study of the spin degree of freedom is presented. This experiment relies on a novel spin sensitive detection technique, which has been developed during this thesis. Through a correlation analysis of the spatially resolved spin distribution, we have been investigating the influence of doping, interactions and temperature on the uniform spin structure factor. For strongly repulsive interactions and low temperatures, the data show the onset of antiferromagnetic correlations in the Mott-Insulator, which is a key step towards investigating the low temperature phase diagram of the two dimensional Hubbard model.

Kurzfassung

In dieser Arbeit werden Experimente an ultrakalten ^{40}K Fermigasen in optischen Gittern vorgestellt, mit denen eine analoge Quantensimulation des zweidimensionalen Hubbard-Modells realisiert wurde. Ein zentrales Merkmal der vorgestellten Experimente ist die Kombination von Radiofrequenz-Spektroskopiemethoden mit einem hochauflösenden Abbildungssystem. Diese Kombination ermöglicht die räumlich aufgelöste Untersuchung sowohl der Dichte- als auch der Spinverteilung.

In einem ersten Experiment wurde die Dichteverteilung untersucht. Durch die hohe Auflösung des Abbildungssystems können unterschiedliche in der Falle koexistierende Phasen unterschieden werden. Darüber hinaus erlaubt die genaue Charakterisierung des einschließenden Potentials die Bestimmung der Zustandsgleichung, die die thermodynamischen Eigenschaften des Vielteilchensystems im untersuchten Temperaturbereich vollständig beschreibt. Dabei wurde mit dem Übergang von einem Metall zu einem Mott-Isolator eines der Schlüsselmerkmale des repulsiven Hubbard Modells nachgewiesen.

Aufbauend auf der präzisen Bestimmung der Zustandsgleichung wurde in einem weiteren Experiment das Fluktuations-Dissipations Theorems angewandt, um die Unterdrückung von nichtlokalen Dichtefluktuationen im repulsiven Hubbard-Modell abzuleiten.

Abschließend wird eine Untersuchung des Spinfreiheitsgrades vorgestellt. Dieses Experiment beruht auf einer während dieser Arbeit entwickelten spin-sensitiven Detektionsmethode. Mittels einer Korrelationsanalyse der räumlich aufgelösten Spinverteilung wurde der Einfluss von Doping, Wechselwirkung und Temperatur auf den Spinstrukturfaktor untersucht. Für starke repulsive Wechselwirkungen und tiefe Temperaturen zeigen die Messungen die Präsenz von antiferromagnetischen Korrelationen im Mott Isolator und stellen damit einen wichtigen Schritt für zukünftige experimentelle Untersuchungen des Hubbard-Modells bei tiefen Temperaturen dar.

Contents

CHAPTER 1

Introduction

In a many-body system, the interplay of the particles within the ensemble can give rise to intriguing and often unforeseen behaviour that cannot be understood from the properties of the individual constituents of the system alone [1]. In fact, the large number of degrees of freedom in many-body systems is a precondition for the emergence of the laws of thermodynamics and the existence of phase transitions. Beyond that, in solid state materials in particular, several phases are associated with the correlated behaviour of strongly interacting electrons. The most prominent example in this context is high temperature superconductivity (HTS) [2], where the interaction among electrons leads to pairing and lossless conductance. Despite numerous years of both experimental and theoretical research on HTS, the phenomenon has not yet been fully understood and strongly correlated materials remain among the most studied topics in modern physics. Indeed, it is precisely the presence of strong electron-electron interactions in these materials that, together with the large number of particles involved, renders their detailed understanding exceedingly difficult. Therefore, simplified microscopic models have been developed in order to gain insight into the basic physics of strongly correlated materials. However, even simple models describing strongly interacting electrons regularly withhold a complete theoretical analysis. At the same time, these simple models are usually only approximately realised in existing materials so that a direct comparison is often difficult. In order to facilitate this comparison and to test theoretical models in regimes that are not easily accessible by other means, novel platforms have been identified and established as tools to realise interacting many-body systems in well controlled experimental environments [3].

The study of mechanical, thermodynamic and electronic properties of solids has a long history and is deeply connected to technological progress. Nevertheless, the development of quantum mechanics was required to understand the behaviour of conductors, semi-conductors and insulators. This classification applies to crystalline materials, which are formed by the regular arrangement of a large number of atoms in a homogeneous lattice structure. When the most weakly bound electrons and ionic cores of the crystalline solid are only weakly interacting, the thermodynamic and electronic properties of such a material may be approximated by a nearly free electron gas [4]. In this picture, the electron-electron interaction is zero and the periodic Coulomb potential induces only a weak periodic perturbation on the electron motion, which results in the formation of energy bands. While the electronic properties of a material are usually obtained from conduction measurements, the thermodynamics can be accessed through equations of state, which provide a relation between thermodynamic properties of the many-body system. For example, the density equation of state $n(\mu)$ expresses the density n at fixed temperature and kinetic energy as a function of the chemical potential μ. An important thermodynamic quantity that can be derived from the density equation of state is the isothermal compressibility, which acquires a finite value in a conductor but vanishes in insulating phases.

The picture of delocalised electrons fails when interparticle interactions are strong and correlations among the electrons have to be taken into account. Among the first examples of such materials were certain transition metal oxides. In obvious contradiction to the simple band theory, these were observed to be insulating despite an only partially filled band [5]. This phenomenon could later be explained by N. Mott, who proposed that in these materials the coulomb interaction is effectively short ranged and therefore acts only between electrons of opposite spin, which populate the same atomic orbital [6, 7]. In the so-called Mott-insulator each atom, or lattice site, is occupied by a single electron, which corresponds to a half-filled band. In this situation the transport of charges between different sites necessarily requires the creation of doubly occupied sites and therefore conduction is energetically suppressed by the strong repulsive electron-electron interaction. Thermodynamically, the Mott-insulator is characterised by a density plateau and a vanishing compressibility at half filling.

In the 1960s, the Hubbard model was developed to provide a conceptually simple microscopic model of interacting electrons on a lattice [8–10]. It describes electrons in the lowest band of a periodic potential, which tunnel between neighbouring sites and interact only when two electrons of opposite spin occupy an identical site. While especially the latter approximation seems crude in the light of the long-ranged nature of the Coulomb interaction between charged particles, the Hubbard model successfully describes the metal–Mott-Insulator transition and smoothly connects between the two opposing limits of free and completely localised electrons. Another fascinating aspect of the Hubbard model is its link to quantum magnetism: While the interaction in the single-band Hubbard model is restricted to act on-site, the interplay between strongly repulsive interactions and kinetic energy leads to an effective spin-exchange, which couples spins on neighbouring lattice sites and drives the system into an antiferromagnetically ordered ground state at half-filling. In fact, for strong repulsive interactions the Hubbard model corresponds to the antiferromagnetic Heisenberg model of localised spins [11].

The Hubbard model attracted renewed interest in the 1980s due to the surprising observation of superconductivity at unusually high temperatures in the cuprates [12]. The high critical temperatures found could not be explained by the Bardeen-Cooper-Schrieffer theory, which describes the pairing of electrons by phonon mediated interactions occurring in *conventional* superconductors. Therefore, the HTS materials are also termed *unconventional* superconductors. The discovery of HTS fuelled theoretical studies on the two-dimensional (2D) Hubbard model, since it resembles the CuO_2 planes found in the cuprates. Much like the strongly repulsive Hubbard model, the cuprates show antiferromagnetic and insulating behaviour at half-filling and only become conducting upon doping with electrons or holes [13]. The 2D Hubbard model is believed to include the essential microscopic ingredients required for HTS. However, despite its conceptual simplicity, the 2D Hubbard model has not been solved analytically. At the same time, numerical simulations away from half-filling and at low-temperatures have proven to be notoriously involved due to the sign problem [14]. Therefore, the thermodynamic and electronic properties of the 2D Hubbard model at low temperatures remain unclear. In particular, its connection to the microscopic pairing mechanism underlying the phenomenon of high-temperature superconductivity is still under debate [2].

Since the mid 1990s, a new approach to the physics of strongly correlated many-body systems came from the field of atomic physics. While electrons, like every fundamental building block of matter, are fermions with half-integer spin, the quantum statistical properties of constituent particles depend on the number of fundamental fermions of which they are composed. Neutrons and protons are themselves formed by three fundamental fermions and are thus also fermionic. In the case of alkali metals, atoms with an odd (even) number of neutrons in the nucleus can be identified as fermionic (bosonic) and are subject to the corresponding quantum statistics. Experimentally, this was shown in a series of ground breaking experiments realising Bose-Einstein condensates in cold dilute gases of neutral atoms in 1995 [15, 16]. It took nearly ten years until the cooling of fermionic isotopes had reached similar temperatures

and the first degenerate Fermi gas could be created [17]. In parallel to the experimental progress, it was realised that ultracold atoms could provide a well controlled experimental platform for condensed matter physics in the spirit of a quantum simulator [18, 19]. In particular, standing waves of light formed by interfering laser beams were proposed to create the analogue of a crystal lattice in order to simulate the Hubbard model [20]. In these so-called optical lattices, atoms replace the electrons of a real solid state material and the lattice sites are formed by minima of the optical potential instead of positively charged ionic cores. Since the potential depth of the optical lattice is freely tunable through the intensity of the interfering laser beams, the ratio of the kinetic energy and interaction energy can be adjusted to reach the strongly correlated regime. Moreover, magnetic Feshbach resonances are routinely employed to adjust the interaction energy independent of the kinetic energy allowing for more flexible control [21]. First experiments with atoms in the strongly correlated regime of an optical lattice studied the Bose-Hubbard model and demonstrated the transition between a coherent superfluid to an incoherent Mott-insulating state [22] by a study of the matter wave interference in an expanding cloud of atoms. Pioneering experiments on the Hubbard model with fermionic atoms have also focussed on global observables like the total fraction of doubly occupied sites [23] or the response of the cloud size to pressure [24] to observe the metal–Mott-insulator crossover. Beyond that, globally averaged signals from singlet-triplet oscillations [25] and Bragg spectroscopy [26] have been used to study spin correlations in a global fashion. However, in contrast to electrons in solids, atoms in optical lattices naturally experience a spatially varying external trapping potential. This results in a continuous variation of the density from a maximum in the trap centre down to zero in the outer wings of the trap. Thus, in cold atom experiments global measurements are often difficult to interpret since they average over extended regions of the phase diagram and, in particular, over insulating and metallic regions simultaneously. In this situation, high resolution in-situ imaging techniques are advantageous, since they provide local information about the trapped atomic cloud [27]. The power of this approach has been shown in previous experiments, in which in-situ imaging techniques were applied to reveal the formation of Mott-insulating regions in the Bose-Hubbard model [28–30] and to study the equation of state of ultracold Fermi gases [31, 32].

This thesis presents a series of experiments on strongly interacting ultracold atoms in optical lattices. Specifically, we use fermionic Potassium-40 in an optical lattice realising the 2D Hubbard model. A central feature of the experimental setup is the ability to resolve the in-situ density distribution spatially with high-resolution absorption imaging. This techniques allows to determine the equation of state and thereby enables precise studies of the thermodynamics of the 2D Hubbard model. In particular, we observe and characterise the crossover from a metal to a Mott-insulating state as well as its dependence on interaction strength, doping and temperature. Furthermore, the accuracy achieved allowed a study of the behaviour of non-local density fluctuations in the metal–Mott-insulator crossover using the fluctuation dissipation theorem. As cold atom experiments progress towards realising even colder temperatures, novel observables have to be accessed. Therefore, a central part of this thesis is dedicated to the extension of our measurement capabilities to the spin sector, which will allow to characterise the low-temperature phase diagram of the 2D Hubbard model, which is characterised by the emergence of magnetic order. To this end, we developed a spin-sensitive RF-spectroscopy detection scheme. Through an analysis of spin correlations, we obtain the uniform spin structure factor, which signals the appearance of antiferromagnetic correlations at the lowest temperatures achieved in the experiment.

The quantum simulation of solid state physics and especially the Hubbard model using cold atoms remains an active field of research. We note that, in parallel to the work presented here, other groups have reported on the implementation of so-called quantum gas microscopes with site-resolved resolution of fermionic atoms in optical lattices [33–35]. Furthermore, several among these groups also reported on the observation of Mott-insulating states as well as spin and density correlations [36–38]. Most recently, these advances have resulted in the observation of antiferromagnetic long-range order in a small 2D

Hubbard system consisting of approximately 10 by 10 lattice sites [39].

Outline of this thesis

The following list gives an overview over the content of the individual chapters of this thesis:

- **Chapter** 2 serves as an introduction to the physics of interacting fermionic atoms in optical lattices. To this end, we discuss the role of Feshbach resonances to control the interaction strength of atoms with a focus on Potassium-40. Further, the concept of optical trapping by means of far detuned laser beams is introduced. While this technique is also one of enabling technologies for initial cooling and trapping of atoms in our experiments, the central application of optical traps in our experimental setup is to realise periodic potentials that mimic the crystalline structure of solid state materials. Having outlined the ideas behind the main experimental tools, the Hubbard model and its relation to experimentally tunable parameters are briefly presented. The chapter ends with a short overview over thermodynamic properties of the Hubbard model in limiting cases, which aid the understanding of its general features.

- The **Chapters** 3 – 5 provide an overview over the experimental setup, a summary of the preparation of an ultracold gas in an optical lattice as well as a detailed description of the detection part of the sequence combining RF spectroscopy schemes for occupation and spin resolved measurements with high resolution absorption imaging.

- Starting with **Chapter** 6 the experimental results obtained during this thesis are presented. To begin with, we study the in-situ density distribution of the trapped atoms for varying interaction strength and temperature and determine the equation of state of the 2D Hubbard model in the metal–Mott-insulator crossover.

- In **Chapter** 7, we apply the fluctuation–dissipation theorem to study non-local density fluctuations and observe their suppression as the system enters the Mott insulating regime.

- In **Chapter** 8 the focus is shifted to the spin degree of freedom. To this end the detection sequence is adopted to yield spin resolved images, from which the in-situ distribution of the magnetisation can be caulculated with spatial resolution. Through the analysis of spin-spin correlations in these magnetisation maps, we observe the onset of antiferromagnetic correlations around half filling for low temperatures.

- **Chapter** 9 provides a summary of the results presented in this thesis and an outlook on future research topics, which could be studied with our experimental setup.

The experimental work presented in this thesis has been carried out in close collaboration with Eugenio Cocchi, Luke Miller, Jeffrey Chan, Nicola Wurz, Marcell Gall, Ferdinand Brennecke, Daniel Pertot, Marco Koschorrek and Michael Köhl.

Co-authored articles

The following articles have been published in the context of this thesis:

- **Antiferromagnetic correlations in two-dimensional fermionic Mott-Insulating and metallic phases** J. H. Drewes, L. A. Miller, E. Cocchi, C. F. Chan, N. Wurz, M. Gall, D. Pertot, F. Brennecke and M. Köhl. *Phys. Rev. Lett.* **118**, 170401 (2017), DOI: https://doi.org/10.1103/PhysRevLett.118.170401.
- **Thermodynamics versus Local Density Fluctuations in the Metal–Mott-Insulator Crossover** J. H. Drewes, E. Cocchi, L. A. Miller, C. F. Chan, D. Pertot, F. Brennecke and M. Köhl. *Phys. Rev. Lett.* **117**, 135301 (2016), DOI: https://doi.org/10.1103/PhysRevLett.117.135301 .
- **Equation of State of the Two-Dimensional Hubbard Model** E. Cocchi, L. A. Miller, J. H. Drewes, M. Koschorreck, D. Pertot, F. Brennecke and M. Köhl. *Phys. Rev. Lett.* **116**, 175301 (2016), DOI: https://doi.org/10.1103/PhysRevLett.116.175301.

Furthermore, the following articles are related to the work presented here:

- **Measuring Entropy and Short Range Correlations in the Two-Dimensional Hubbard Model** E. Cocchi, L. A. Miller, J. H. Drewes, C. F. Chan, D. Pertot, F. Brennecke and M. Köhl. *Phys. Rev. X* **7**, 031025 (2017), DOI: https://doi.org/10.1103/PhysRevX.7.031025.
- **Coherent Manipulation of Spin Correlations in the Hubbard model** N. Wurz, C. F. Chan, M. Gall, J. H. Drewes, E. Cocchi, L. A. Miller, D. Pertot, F. Brennecke and M. Köhl. *Phys. Rev. A* **97**, 051602 (2018), DOI: https://doi.org/10.1103/PhysRevA.97.051602.

CHAPTER 2

Strongly interacting fermions in optical lattices

This chapter provides a theoretical background on the physics of strongly interacting fermionic atoms in optical lattices and the main experimental tools employed in our experiment. To this end, Section 2.1 introduces basic properties of non-interacting fermionic and bosonic particles. Then, Section 2.2 presents a short review on scattering theory and magnetically tunable Feshbach resonances, which allow to control interactions between atoms in an almost arbitrary manner. Specifically, the Feshbach resonances of Potassium-40 used throughout this work are discussed. Thereafter, Section 2.3 introduces the optical dipole force and the generation of optical lattices by standing waves of light. In Section 2.4 the presented concepts are combined to show how the Hubbard model is implemented in cold atom experiments. The chapter is concluded by a presentation of thermodynamic properties of the Hubbard model in regimes where a simple solution can be obtained and, finally, a conceptual motivation for the existence of antiferromagnetic order in the repulsive Hubbard model is outlined.

2.1 Bosons and fermions

Quantum statistics describes truly indistinguishable particles. These are separable into two classes called *bosons* and *fermions* with integer and half integer spin, respectively. Atoms, which consist of the fermionic constituents protons, neutrons, and electrons, may behave like fermionic or bosonic particles. Fermions and bosons behave fundamentally different under the exchange of two particles at positions i and j. While the wave function of a bosonic many-body state is symmetric and remains unchanged under this permutation, the wave function of a fermionic many-body state is antisymmetric and obtains a minus sign. The consequence of this behaviour is the well known Pauli exclusion principle stating that two identical fermions may not occupy the same quantum state. To understand when theses quantum properties have practical consequences, we follow the wave-particle duality and assign a wavelength to the particles in an ideal gas. This so-called *thermal de Broglie wavelength*

$$\lambda_{\mathrm{dB}} = \frac{h}{\sqrt{2\pi m k_{\mathrm{B}} T}} \tag{2.1}$$

depends on the mass m of the particles as well as the temperature T; h is the Planck constant and k_{B} is the Boltzmann constant. At sufficiently cold temperatures λ_{dB} exceeds the inter particle distance of a gas with N particles in a given volume V. As a consequence, the gas no longer follows the classical Maxwell-Boltzmann statistics of an ideal gas. Instead, the average occupation of a single-particle

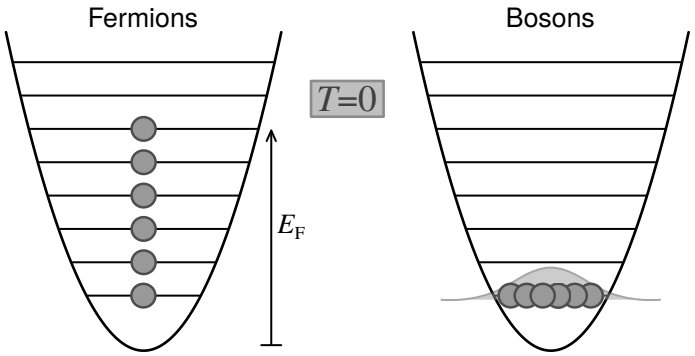

Figure 2.1: Fermions (left) and bosons (right) in a harmonic potential at $T = 0$. While fermionic particles form a degenerate Fermi gas with Energy E_F, bosonic particles accumulate in the ground state to form a Bose-Einstein condensate.

eigenstate with energy $\epsilon_{\mathbf{k}}$ is given by [40]

$$n_{\mathbf{k}} = \begin{cases} \frac{1}{e^{\beta(\epsilon_{\mathbf{k}}-\mu)}+1} & \text{for fermions}\,, \\ \frac{1}{e^{\beta(\epsilon_{\mathbf{k}}-\mu)}-1} & \text{for bosons}\,. \end{cases} \tag{2.2}$$

The different sign for fermionic and bosonic particles has remarkable consequences. The Bose-Einstein distribution allows for an arbitrary large occupation of any state leading to a macroscopic occupation of the ground state below a critical temperature. This coherent state of matter is the *Bose-Einstein condensate*, which was experimentally realised for the first time using dilute gases of alkali atoms in 1995 [15, 16]. Quite differently, for fermionic particles the maximal occupation of a given state is limited to one. Therefore, for fermions Equation 2.2 reduces to a step function at zero temperature

$$n_{\mathbf{k}} = \begin{cases} 1 & \epsilon \leq E_F\,, \\ 0 & \text{else}\,. \end{cases} \tag{2.3}$$

Here, the *Fermi energy* E_F is the energy of the highest occupied state (compare Fig. 2.1). In a three dimensional harmonic trap with trapping frequencies ω_x, ω_y and ω_z, along three orthogonal directions, the Fermi-energy is given by

$$E_F = \hbar(6N)^{1/3}(\omega_x\omega_y\omega_z)^{1/3}\,. \tag{2.4}$$

Typically, the reduced temperature T/T_F is used as an estimate of the degree of degeneracy in cold Fermi gas experiments, where the *Fermi temperature* is defined as $T_F = E_F/k_B$. At finite temperature, the mean occupation of states with an energy larger than the Fermi energy grows and, correspondingly, the Fermi-Dirac distribution becomes smooth. A comparison of the Fermi-Dirac distribution at zero and finite temperature is presented in Figure 2.2. In the limit of high temperatures, both the Fermi-Dirac distribution and the Bose-Einstein distribution approach the Maxwell-Boltzmann distribution of a classical ideal gas.

2.2 Controlling interactions

Non-interacting fermions in a periodic potential already allow to understand conductors, semi-conductors and insulators. However, interactions have to be considered to describe strongly correlated many-body

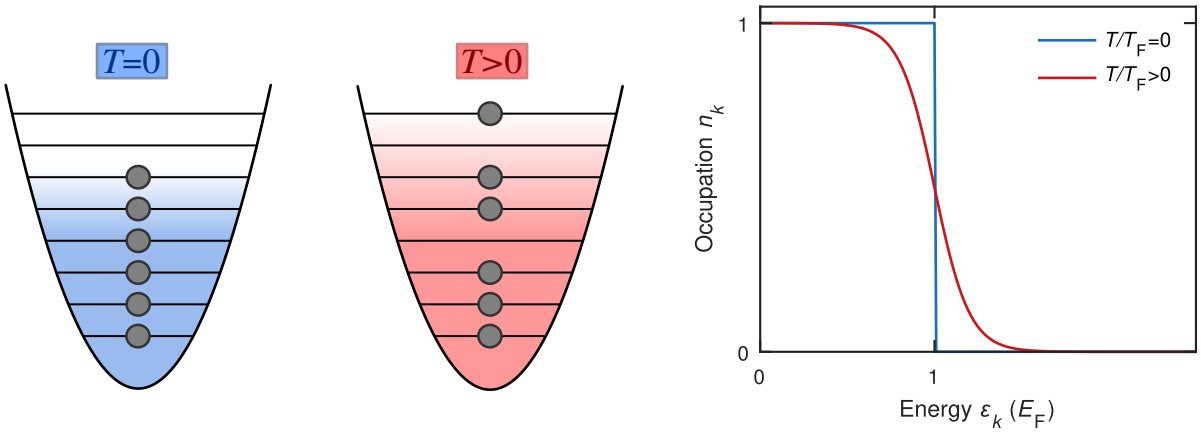

Figure 2.2: Fermi-Dirac distribution. At zero temperature, no states above the Fermi-energy are populated, and the Fermi-Dirac distribution reduces to a step function (blue line). As the temperature increases, states above the Fermi-energy are populated and the Fermi-Dirac distribution becomes smoother (red line).

systems. In an atomic gas, the scattering lengths between atoms are typically short compared to the inter-particle distance. Therefore, a mechanism is required to enhance the scattering length in order to access phenomena occurring in the strongly interacting regime. In atomic physics, magnetically tunable scattering resonances are routinely used for this purpose and allow to tune the interaction almost arbitrarily. A general introduction to the topic of the so-called Feshbach resonances in atomic physics is presented in Refs. [21, 41, 42] and references therein. The following paragraphs highlight the main aspects of Feshbach resonances in cold atom experiments. Section 2.2.1 serves as a short reminder of scattering theory. Section 2.2.2 introduces the basic mechanism behind magnetically tunable scattering lengths and presents the experimentally relevant Feshbach resonances found in spin mixtures of ^{40}K.

2.2.1 Basic scattering theory

This section is restricted to the basic concepts behind the elastic scattering of two neutral particles and focuses on the low-energy sector, since this is the situation typically realised in quantum gas experiments. In depth introductions to scattering theory are found in many quantum mechanics textbooks, for example in the book by Sakkurai [43].

In the limit of large inter particle separation r, the scattering wave function $\psi_{\mathbf{k}}(\mathbf{r})$ of two colliding particles $|a\rangle$ and $|b\rangle$, with relative momentum $\hbar\mathbf{k}$ may be expressed as the sum of an incoming plane wave and a scattered spherical wave with relative momentum $\hbar\mathbf{k}'$ and the scattering amplitude $f(\mathbf{k},\mathbf{k}')$.

$$\psi_{\mathbf{k}}(\mathbf{r}) \propto \left(e^{i\mathbf{kr}} + f(\mathbf{k},\mathbf{k}')\frac{e^{i|\mathbf{k}'||\mathbf{r}|}}{|\mathbf{r}|} \right) |a\rangle\,|b\rangle \ , \tag{2.5}$$

where the conservation of energy implies $|\mathbf{k}'| = |\mathbf{k}|$. The scattering amplitude determines the differential scattering cross section

$$\frac{\mathrm{d}\sigma}{\mathrm{d}\Omega} = \left| f(\mathbf{k},\mathbf{k}') \right|^2 . \tag{2.6}$$

The scattering wave functions are solutions to the Schrödinger equation of the relative motion of the

colliding particles. For a spherically symmetric potential, the Schrödinger equation reduces to

$$\left[-\frac{\hbar^2}{2m}\left(\frac{\mathrm{d}^2}{\mathrm{d}r^2}+\frac{2}{r}\frac{\mathrm{d}}{\mathrm{d}r}\right)+V_{\mathrm{eff}}(r)\right]R_l(r)=ER_l(r)\,, \tag{2.7}$$

where r is the relative distance between the particles, $m=\frac{m_a m_b}{m_a+m_b}$ is the reduced mass, $E=\frac{\hbar^2k^2}{2m}$ is the collision energy and $R_l(r)$ is the radial part of the scattered wave function. The effective potential

$$V_{\mathrm{eff}}=V(r)+\frac{l(l+1)}{r^2} \tag{2.8}$$

includes a centrifugal barrier, which is only relevant for $l>0$ and the inter-atomic potential $V(r)$ whose precise shape depends on the internal states $|a\rangle$ and $|b\rangle$ of the colliding atoms. For particles with low collisional energy the centrifugal barrier prohibits collisions with large angular momentum and only s-wave scattering ($l=0$) remains, which occurs only for distinguishable particles in the case of fermions. The scattering process shifts the phase of the outgoing wave by $\delta_0(k)$, which determines the s-wave scattering amplitude [44]

$$f_{\mathrm{s}}(k)=\frac{1}{k\cot\delta_0(k)-ik}=\frac{1}{-1/a_{\mathrm{s}}+r_e k^2/2-ik}\,. \tag{2.9}$$

Here, $a_{\mathrm{s}}=-\lim\limits_{k\to0}\frac{\tan\delta_0(k)}{k}$ is defined as the *s-wave scattering length* and r_e is the effective range of the potential. For $ka_{\mathrm{s}}\ll1$ the scattering cross section becomes energy independent and is determined by the scattering length alone

$$\sigma_{\mathrm{s}}=4\pi a_{\mathrm{s}}^2\,. \tag{2.10}$$

In the limit introduced above, it is convenient to approximate the actual inter-atomic potential by the regularised pseudopotential [45]

$$V(r)=\frac{4\pi\hbar^2 a_s}{m}\delta(r)\frac{\mathrm{d}}{\mathrm{d}r}r\,. \tag{2.11}$$

For arbitrary k, this potential yields the scattering amplitude

$$f(k)=\frac{1}{-1/a_{\mathrm{s}}-ik}\,, \tag{2.12}$$

which is the zero-range limit of Equation 2.9 and yields the same low energy behaviour. In experiments with ultracold atoms the assumption of a zero-range potential is often justified, since the inter particle distance k_{F}^{-1} is typically much larger than the effective range of the real inter-atomic potentials.

2.2.2 Feshbach resonances in Potassium-40

In order to understand the magnetic tunability of the scattering length a_s between atoms qualitatively, we need to recall the internal atomic level structure. Potassium, like all alkali atoms, possesses a single electron in the outermost shell. The electronic angular momentum $\mathbf{L}$ couples to the electronic spin $\mathbf{S}$ yielding the total electronic angular momentum $\mathbf{J}=\mathbf{L}+\mathbf{S}$. The total electronic angular momentum then couples to the nuclear spin $\mathbf{I}$ yielding the total angular momentum $\mathbf{F}=\mathbf{J}+\mathbf{I}$. The nuclear spin of the fermionic isotope ^{40}K is $I=4$. Thus, in the electronic ground state $4^2S_{1/2}$ the quantum number F takes the values $\frac{9}{2}$ or $\frac{7}{2}$. For zero magnetic field the electronic eigenstates are $|F,m_F\rangle$, where the quantum

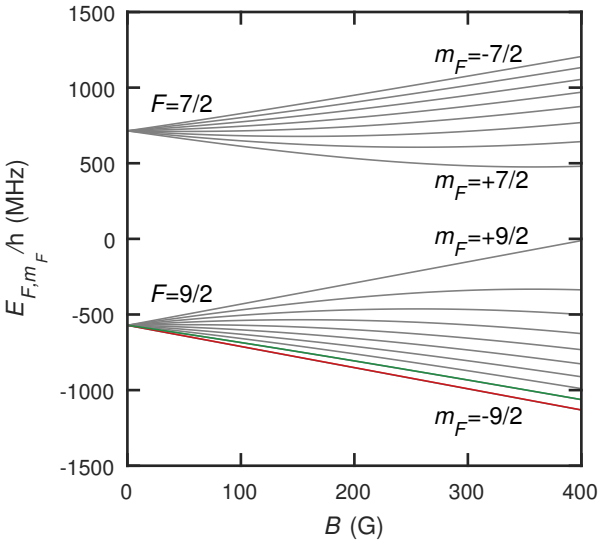

Figure 2.3: Eigenvalues of the hyperfine interaction (Eq. 2.13) as a function of the magnetic field B. In the experiment, the pseudo-spin $\frac{1}{2}$ is formed by $|\downarrow\rangle = |m_F = -9/2\rangle$ (red) and $|\uparrow\rangle = |m_F = -7/2\rangle$ (green) states in the $F = 9/2$ manifold red (green). States up to $m_F = -3/2$ are used as auxiliary states.

number m_F is the projection of $\mathbf{F}$. Although providing a good set of quantum numbers only at low fields, we use this notation throughout this thesis to label the energy levels. At arbitrary magnetic field strength, the interaction between neutral atoms and a magnetic field is described by the Hamiltonian [46]

$$\hat{H}_{\text{int}} = \hat{H}_{\text{hf}} + \hat{H}_{\text{z}} \,. \tag{2.13}$$

The first term on the right hand side describes the field independent hyperfine interaction arising from the coupling of nuclear and electronic angular momenta leading to a splitting of the energy levels in manifolds with different total angular momentum F. In the ground state this interaction is given by

$$\hat{H}_{\text{hf}} = \frac{a_{\text{hf}}}{\hbar^2}\mathbf{I}\cdot\mathbf{J} \,. \tag{2.14}$$

The dot product in Equation 2.14 is given by $\mathbf{I}\cdot\mathbf{J} = \frac{1}{2}(\mathbf{F}^2 - \mathbf{I}^2 - \mathbf{J}^2)$ and $a_{\text{hf}} = -h \times 285.7308(24)\,\text{MHz}$ is the magnetic dipole constant for Potassium-40 in the $4^2\text{S}_{1/2}$ state [47]. The second term of Equation 2.13 is the Zeeman interaction

$$\hat{H}_{\text{z}} = \frac{\mu_{\text{B}}}{\hbar}(g_J\mathbf{J} + g_I\mathbf{I})\mathbf{B} \,, \tag{2.15}$$

which leads to field dependent splitting of the energy levels. In Equation 2.15, g_J is the Landée g-factor of the electron and g_I is the nuclear gyromagnetic factor. Figure 2.3(a) shows the eigenenergies E_{F,m_F} of Equation 2.13 as a function of the magnetic field B.

The basic mechanism behind magnetically tunable Feshbach resonances is illustrated in Figure 2.4(a). Here, we consider the elastic collision of two initially separated atoms prepared in the *open channel* $\alpha = |F_1, m_{F,1}\rangle\,|F_2, m_{F,2}\rangle$ with a channel energy $E_\alpha = E_{F_1,m_{F_1}} + E_{F_2,m_{F_2}}$. A channel $\beta = |F_1', m_{F,1}'\rangle\,|F_2', m_{F,2}'\rangle$ is called *closed* when the channel energy E_β is larger than the threshold energy of the open channel. When two atoms in the open channel approach each other, the spin-spin dipole interaction may induce a coupling to a bound state of a closed channel with $F_1' + F_2' \neq F_1 + F_2$. Therefore, the total magnetic moments of the open and closed channels $\partial E_\alpha/\partial B$ and $\partial E_\beta/\partial B$ may differ. In this case, the offset between the

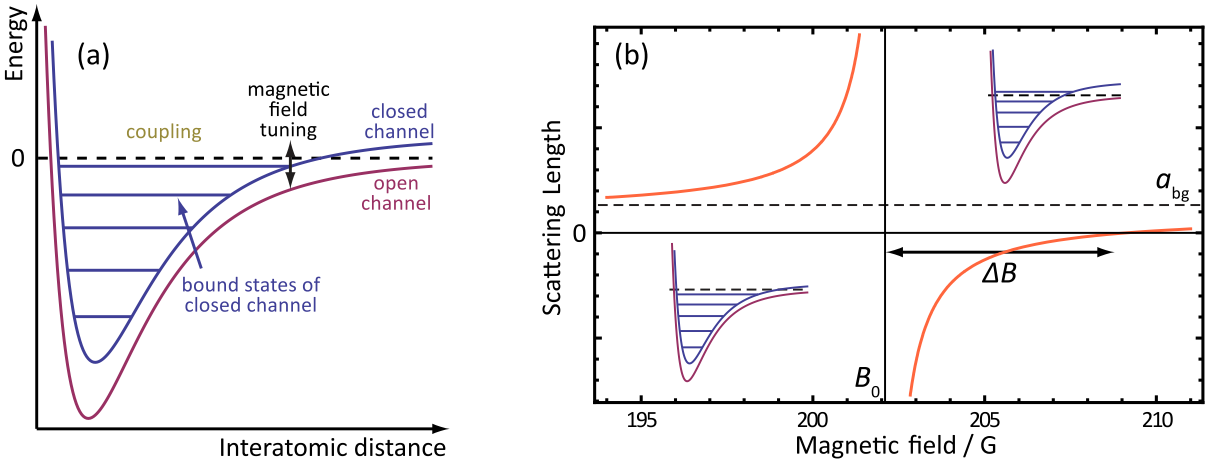

Figure 2.4: (a) Two channel model of a Feshbach resonance. Two particles enter the scattering potential in the open channel with a continuum energy E_C set to zero (dashed line). The magnetically tunable coupling to a bound state in the closed channel determines the phase shift of the outgoing wave and, thus, the scattering length. (b) Exemplary dependence of the scattering length on the magnetic field. Far away from the resonance, the scattering length approaches the background scattering length a_{bg}. The bound state in the closed channel is resonant with the open channel at the Feshbach resonance B_0 where the scattering length (red) diverges. The width of the resonance ΔB is determined by the distance from the resonance to the zero-crossing of the scattering length $B_{non-int} = B_0 + \Delta B$. Figure adopted from [48].

potential curves of the channels is tunable via an external magnetic field B. As the energy difference between the threshold energy of the open channel and a bound state of the closed channel is tuned through resonance, the scattering length diverges, such that all values $-\infty < a_s < \infty$ are accessible upon varying the magnetic field (see Fig. 2.4(b)). In the experiment, we adjust the on-site interaction energy by controlling the scattering length between $|9/2, -9/2\rangle$ and $|9/2, -7/2\rangle$. The only possible closed channel for this mixture is $|9/2, -9/2\rangle\,|7/2, -7/2\rangle$, since the total magnetic quantum number $M = m_{F_1} + m_{F_2}$ is conserved. When only two channels are involved in the scattering process, the magnetically tunable s-wave scattering length a_s is real and given by [21, 49]

$$a_s(B) = a_{bg}\left(1 - \frac{\Delta B}{B - B_0}\right), \tag{2.16}$$

where the background scattering length a_{bg} is typically expressed in units of the Bohr radius a_0, ΔB describes the width of the resonance feature and B_0 is the position of the resonance. The Feshbach resonance between these states has been precisely determined in previous experiments. A combination of the reported results yields $a_{bg} = 174(7)\,a_0$, $B_0 = 202.13(1)\,G$ [50–52] as well as $\Delta B = 7.2(4)\,G$ [52, 53]. In fact, several other Feshbach resonances have been observed in Potassium-40. Figure 2.5 shows a selection of Feshbach resonances which are relevant for our experiment. The corresponding parameters are listed in Table 2.1.

2.3 Optical trapping and optical lattices

In the last section, we have seen how magnetic fields allow to control the interaction in an ultracold gas. In the following sections, the optical dipole force will be introduced, which, on the one hand, allows to trap neutral atoms without applying magnetic fields and, on the other hand, offers control over the

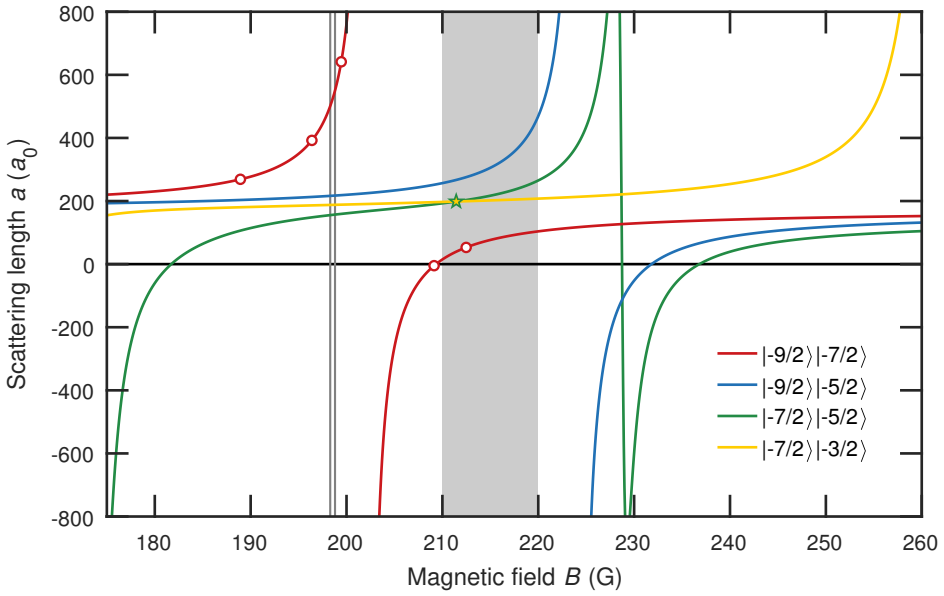

Figure 2.5: Feshbach resonances of ^{40}K between different pairs of hyperfine states. S-wave resonances: $|-9/2\rangle\,|-7/2\rangle$ (red), $|-9/2\rangle\,|-5/2\rangle$ (blue), $|-7/2\rangle\,|-5/2\rangle$ (green) and, $|-7/2\rangle\,|-3/2\rangle$ (yellow). P-wave resonances for $|-7/2\rangle\,|-7/2\rangle$ around $B = 198.30(2)$ G and $B = 198.80(5)$ G [54] as well as $|-9/2\rangle\,|-5/2\rangle$ around $B = 215(5)$ G [53] are indicated in grey. The white points mark the values of the scattering length used to set the on-site interaction U in the experiment.

Open channel	l	a_{bg} (a_0)	B_0 (G)	ΔB (G)	γ_B (mG)	Refs.
$\lvert-9/2\rangle\,\lvert-7/2\rangle$	s	174(7)	202.13(1)	7.2(4)		[50–53]
$\lvert-9/2\rangle\,\lvert-5/2\rangle$	s	167.3	224.21	7.6	0.068	[55]
$\lvert-7/2\rangle\,\lvert-5/2\rangle$	s	183.5 137.6	174.3 228.7	7.9 8.2	0.32 1.1	[55]
$\lvert-7/2\rangle\,\lvert-3/2\rangle$	s	184.8 164.9	169.1 260.5	1 11.2	2 1.2	[55]
$\lvert-9/2\rangle\,\lvert-5/2\rangle$	p		215(10)			[53]
$\lvert-7/2\rangle\,\lvert-7/2\rangle$	p		198.3			[54]
$\lvert-7/2\rangle\,\lvert-7/2\rangle$	p		198.8			[54]

Table 2.1: Parameters of the experimentally relevant s- and p-wave resonances of ^{40}K shown in Figure 2.5.

dimensionality [56, 57], geometry [58] and kinetic energy using standing waves of light, so-called *optical lattices*. Most importantly, atoms in optical lattices provide an emulator for crystalline materials and allow to study solid state physics in a fully tunable experimental environment.

Section 2.3.1 serves as a short introduction to the interaction between light and matter, which gives rise to the optical dipole force and radiation pressure. Second, Section 2.3.2 explains how optical lattices are formed by the interference of laser beams. Section 2.3.3 introduces the band structure and eigenstates of atoms in optical lattices. Finally, the contribution of the optical lattice to the spatially varying confinement is discussed in Section 3.5.4.

2.3.1 Optical dipole potentials

A didactic presentation of the mechanisms employed for optical trapping of neutral atoms has been presented in Ref. [59]. Incident light, possessing an electric field $\mathbf{E}(\mathbf{r}, t)$ with the driving frequency ω induces an oscillating atomic dipole moment $\mathbf{d} = \alpha(\omega)\mathbf{E}(\mathbf{r}, t)$, which in turn couples to the electric field. This atom-light interaction can be split into a dispersive and a dissipative part. The dispersive part induces an energy shift of the atomic ground state $V_{\mathrm{dip}} \propto -\langle \mathbf{dE} \rangle \propto -Re[\alpha(\omega)]I(\mathbf{r})$, leading to a conservative dipole force. At the same time, the atom absorbs photons from the driving field with a scattering rate $\Gamma_{\mathrm{sc}} \propto \langle \dot{\mathbf{d}}\mathbf{E} \rangle \propto Im[\alpha(\omega)]I(\mathbf{r})$, which induces a scattering force. Note, that both V_{dip} and Γ_{sc} are proportional to the intensity $I(\mathbf{r}) = \frac{c\epsilon_0}{2}|\mathbf{E}|^2$ at position $\mathbf{r}$. While the dissipative scattering force is regularly applied to cool atoms, e.g. in magneto-optical traps, it is also a source of heating in optical dipole traps [60]. Thus, it has to be avoided as much as possible in this situation.

To begin with, we approximate the atom as a harmonic oscillator and describe the displacement of the outer electron in the presence of a driving electric field. A solution of the equation of motion yields the *complex polarisability*

$$\alpha(\omega) = 6\pi\epsilon_0 c^3 \frac{\Gamma/\omega_0^2}{\omega_0^2 - \omega^2 - i(\omega^3/\omega_0^2)\Gamma} \tag{2.17}$$

with the atomic resonance frequency ω_0. Using this expression and applying the rotating wave approximation, we find

$$V_{\mathrm{dip}} = \frac{3\pi c^2}{2\omega_0^3}\frac{\Gamma}{\Delta} I(\mathbf{r}), \tag{2.18}$$

$$\Gamma_{\mathrm{sc}} = \frac{3\pi c^2}{2\omega_0^3}\left(\frac{\Gamma}{\Delta}\right)^2 I(\mathbf{r}), \tag{2.19}$$

for the dipole potential and the scattering rate, respectively. In Equations 2.18 and 2.19 the detuning is defined as $\Delta = \omega - \omega_0$, such that a driving field with $\Delta < 0$ ($\Delta > 0$) is red (blue) detuned with respect to the atomic resonance. This convention will be used throughout this thesis. A comparison of the scaling of the dipole potential and the scattering rate with detuning and intensity indicates that it is advantageous to use far detuned light with a high intensity in order to minimize heating due to spontaneous scattering of light from the trapping beams. In addition, the sign of the detuning plays an important role for optical trapping. While red detuned beams attract atoms to regions of high intensity, atoms are repelled from regions of high intensity for blue detuned light.

While the classical treatment yields the correct dependence on the detuning, a quantum mechanical treatment is necessary to find a more accurate expression for the decay rate Γ. To this end, we approximate the electronic level structure by a two level system consisting of a ground state $|g\rangle$ with energy E_{g} and an excited state $|e\rangle$ with energy E_{e}. The energy difference between the two states yields the atomic resonance

frequency $\omega_0 = (E_e - E_g)/\hbar$. Then, the correct expression for the decay rate depends on the dipole matrix element of the two states

$$\Gamma = \frac{\omega_0^3}{3\pi\epsilon_0\hbar c^3}|\langle e|\,\mathbf{d}\,|g\rangle|^2\,. \tag{2.20}$$

In the case of alkali atoms, such as Potassium, the multi-level structure of the electronic transition further modifies the expression for the polarisability. In general, we have to sum over all possible excited states to find the atomic polarisability [61]

$$\alpha = \sum_f |\langle f|\,\mathbf{d}\,|i\rangle|^2 \left(\frac{1}{E_f - E_i - \hbar\omega} + \frac{1}{E_f - E_i + \hbar\omega}\right)\,. \tag{2.21}$$

Therefore, the calculation of the polarisability for a multi-level atom requires the knowledge of the dipole matrix elements $\mu_{if} = \langle f|\,\mathbf{d}\,|i\rangle$ between the initial state $|i\rangle$ and final states $|f\rangle$. With the Clebsch-Gordon coefficients c_{ij} the transition matrix element can be calculated from $\mu_{if} = c_{ij}\|\mu\|$, where $\|\mu\|$ is the reduced dipole matrix element [62]. Often, it is sufficient to restrict the summation to the D1 ($4^2S_{1/2} \rightarrow 4^2P_{1/2}$) and D2 ($4^2S_{1/2} \rightarrow 4^2P_{3/2}$) transitions for alkali atoms. Moreover, in optical dipole traps the, hyperfine splitting in the excited states is usually not resolved ($\Delta > E_{\mathrm{hfs}}$). In this case, a good approximation for the dipole potential is given by [59]

$$\begin{aligned} V_{\mathrm{dip}}(\mathbf{r}) = \frac{\pi c^2\Gamma}{2\omega_0^3}\Bigg(&\left(2 + qg_F m_F\right)\left(\frac{1}{\omega - \omega_{\mathrm{D2}}} + \frac{1}{\omega + \omega_{\mathrm{D2}}}\right) \\ &+ \left(1 - qg_F m_F\right)\left(\frac{1}{\omega - \omega_{\mathrm{D1}}} + \frac{1}{\omega + \omega_{\mathrm{D1}}}\right)\Bigg) I(\mathbf{r}) \end{aligned}\,, \tag{2.22}$$

where $q = \pm 1, 0$ indicates the polarisation of the light field, g_F is the Landé factor and m_F denotes the magnetic hyperfine state. As evident from Equation 2.22, the application of linear polarised light ($q = 0$) allows to generate state independent trapping potentials.

Until now, we have neglected the explicit spatial dependence of the intensity distribution $I(\mathbf{r})$. However, optical trapping clearly requires a gradient in the potential in order to work. Typically, simple Gaussian laser beams (TEM_{00} mode) are used to trap cold atoms. The intensity distribution is thus given by

$$I(\mathbf{r}) = \frac{2P_0}{\pi w_x(z) w_y(z)} \exp\left(-\frac{2x^2}{w_x^2(z)} - \frac{2y^2}{w_y^2(z)}\right) \tag{2.23}$$

Here, P_0 is the power in the centre of the beam; $w_\nu(z) = w_{0,\nu}(1 + z^2/z_{\mathrm{R}}^2)^{1/2}$ denote the beam radii in the direction perpendicular to the direction of propagation z where the intensity has dropped to $1/e^2$ of the maximal value; the smallest beam radius $w_{0,\nu} = w_\nu(z = 0)$ is called beam waist; together the beam waist and the laser wavelength λ determine the Rayleigh length $z_{\mathrm{R}} = \pi w_{0,\nu}^2/\lambda$, which describes the divergence of the beam after the focus. Due to the spatially varying intensity, already a single red detuned laser beam with appropriate beam parameters is sufficient to create an, usually strongly anisotropic, optical trap for a pre-cooled cloud of neutral atoms. In the example above, different beam waists along x and y account for a possible ellipticity of the beam.

2.3.2 Optical lattices

In the last section, we have seen how an electric field induces a dipole potential for neutral atoms. Employing the interference between two counter propagating laser beams, also periodic potentials, so called optical lattices, can be created. In close analogy to solid state physics the periodic potential leads to a band structure for the trapped atoms, with allowed energy bands separated by band gaps. Thereby, optical lattices allow to realise 'artificial crystals' in which atoms replace the electrons and potential minima form the analogue of ionic cores found in real crystals.

One-dimensional optical lattice

For simplicity, we will first limit the following discussion to the one-dimensional lin-lin lattice configuration of two beams with identical wavelength λ propagating along the x and $-x$ direction and parallel linear polarisation. This configuration is most easily realised by reflecting a focussed Gaussian laser beam in itself. With equal power in both beams, the optical lattice potential is given by

$$V_{1D}(\mathbf{r}) = V_x e^{-2\frac{y^2+z^2}{w_x^2}} \cos^2(kx) \,, \tag{2.24}$$

where the periodicity of the potential is determined by the wave number $k = 2\pi/\lambda$. Usually, the lattice depth $V_x = s_x E_r$ is expressed in units of the recoil energy $E_r = \hbar^2 k^2/2m$ with the atomic mass m. According to the description above, the laser detuning defines the sign of V_x (cf. Section 2.3.1). The exponential factor in Equation 2.24 shows the transverse variation of the lattice depth due to the Gaussian shape of the interfering beams and w_x denotes the beam waist. Note that the axial confinement is neglected in Equation 2.24. This is justified, since the Rayleigh length is typically much larger than the beam waist. Therefore, the lattice depth is approximately constant over the axial extent of the cloud in the x-direction.

Three-dimensional optical lattice

In our experiment, we realise a three-dimensional optical lattice. It is straight forward to construct such higher dimensional lattices from the superposition of orthogonal one-dimensional standing waves, provided the potentials are separable. This is achieved by using mutually orthogonal linearly polarised beams to prevent cross interferences between the different optical lattices. In addition, we employ beams with different frequencies forming the standing waves. Thereby, any remaining cross interference is time averaged. The resulting combined potential is given by the sum of the individual 1D lattice potentials

$$V_{3D}(\mathbf{r}) = V_z e^{-2\frac{y^2+z^2}{w_x^2}} \cos^2(k_x x) + V_y e^{-2\frac{x^2+z^2}{w_y^2}} \cos^2\left(k_y y\right) + V_z e^{-2\frac{x^2+y^2}{w_z^2}} \cos^2(k_z z) \,, \tag{2.25}$$

where w_ν denotes the beam waist of the beams forming a lattice along the ν-axis and V_ν is the corresponding lattice depth. While for an isotropic 3D-lattice $k_x = k_y = k_z$ we realise $k_x = k_y \approx k_z/2$ to implement an anisotropic lattice.

In a deep optical lattice, the confinement at individual lattice sites may be approximated by a harmonic potential with the on-site trapping frequency

$$\omega_{\text{on-site},\nu}^2 = \frac{2k^2}{m}|V_\nu| \tag{2.26}$$

along each axis $\nu \in \{x, y, z\}$. Note that the on-site trapping frequency depends only on the lattice depth and is identical for red ($V_\nu < 0$) and blue detuned lattices ($V_\nu > 0$). In the harmonic approximation, the ground state energy of the local quantum harmonic oscillator (the so-called zero-point energy) is given by

$$E_0 = \frac{\hbar}{2} \sum_\nu \omega_{\text{on-site},\nu} \,. \tag{2.27}$$

As we will shortly see, the zero-point motion has important consequences for the overall shape of the optical potential.

External confinement

Close to the centre of the trap the combined potential can be approximated by the sum of homogeneous one-dimensional lattice potentials and an additional harmonic confinement along each direction

$$V_{3\text{D}}(\mathbf{r}) \approx V_z \cos^2(kx) + V_y \cos^2(ky) + V_z \cos^2(kz) + \frac{m}{2}\left(\omega_x x^2 + \omega_y y^2 + \omega_z z^2\right) , \tag{2.28}$$

where the external harmonic confinement is characterised by the effective trapping frequencies ω_x, ω_y and ω_z. Three major contributions to the external potential can be identified:

1. The decrease of the lattice depth of each lattice along the corresponding transverse directions results in a decrease of the on-site trap frequency as the distance from the centre of the beam increases. Along the x-direction, the on-site trap frequency decays as

   $$\omega_{on-site}(\mathbf{r}) = \omega_{on-site}(0) \exp\left\{-y^2/w_x^2 - z^2/w_x^2\right\}. \tag{2.29}$$

   Irrespective of the laser detuning, this effect creates an anti-confining potential for the trapped atoms. In the harmonic approximation, this contribution to external confinement can be expressed as

   $$\omega_x^2 = -\frac{2}{m}\left(\frac{E_{\text{r},y}\sqrt{|s_y|}}{w_y^2} + \frac{E_{\text{r},z}\sqrt{|s_z|}}{w_z^2}\right). \tag{2.30}$$

2. In a red-detuned lattice, the atoms are trapped in local maxima of the intensity distribution (where $\cos^2(kx) = 1$). This creates a negative energy offset, which decreases with the intensity and results in a confining potential. In the blue-detuned case, this effect is absent since the atoms are trapped in local minima of the intensity (where $\cos^2(kx) = 0$).

3. Finally, imperfect interference of the beams forming the lattice leads to a running wave component that acts as a dipole trap following the Gaussian envelope of the optical lattice. Imperfect interference may arise from a power imbalance γ_ν of the counter propagating beams or non-matching polarisation. The running wave component creates an attractive (repulsive) dipole potential for red (blue) detuned light.

For a 1D optical lattice along the x-axis, the last two contributions can be summarised to give the following potential

$$V_{1\text{D}} = V_x e^{-2\frac{y^2+z^2}{w_x^2}}\left(\frac{\left(1-\sqrt{\gamma_x}\right)^2}{4\sqrt{\gamma_x}} + \cos^2(kx)\right) \tag{2.31}$$

Again, the atoms are trapped in local maxima (minima) of the intensity for red (blue) detuned light yielding $\cos^2(kx) = 1$ ($\cos^2(kx) = 0$). Therefore, the contribution to the external confinement along the x- direction of the 3D optical lattice becomes

$$\omega_x^2 = -\frac{4}{m}\left(V_y \frac{\left(1 \pm \sqrt{\gamma_y}\right)^2}{4\sqrt{\gamma_y}} \Big/ w_y^2 + V_z \frac{\left(1 \pm \sqrt{\gamma_z}\right)^2}{4\sqrt{\gamma_z}} \Big/ w_z^2\right) \tag{2.32}$$

and the upper (lower) sign is valid for a red (blue) detuned lattice. The overall external confinement is given by the sum of Equations 2.30 and 2.32. The experimental calibration of the external confinement is a crucial input to our data analysis and will be presented in Chapter 3.5.4. In the next section, we concentrate on the periodic part of the potential to find the eigenstates and eigenenergies of non-interacting neutral atoms in an optical lattice.

2.3.3 Single-particle eigenstates in an optical lattice

In a separable potential, the dynamics separate along the coordinate axes and the eigenstates of the 3D optical lattice are formed by the product of the eigenstates of the independent 1D lattices. Therefore, this section is restricted to the description of single-particle eigenstates in a homogeneous 1D optical lattice. First, delocalised Bloch states and the band structure resulting from a periodic potential will be introduced. For the discussion of the physics of tight binding models, like the Hubbard model, it is convenient to consider localised states with a well defined position rather than delocalised states with well defined momentum. To this end, the Bloch functions are employed to construct a basis of localised Wannier functions. With this localised basis, the kinetic and potential energy of atoms in the optical lattice may be related to the single-band Hubbard model, which will be introduced in Section 2.4.

Bloch waves

The eigenstates in a homogeneous 1D optical lattice potential $V(x)$ are found by solving the Schrödinger equation

$$\hat{H}\phi_{n,q}(x) = \epsilon_n(q)\phi_{n,q}(x) \qquad \text{with} \qquad \hat{H} = -\frac{\hbar^2}{2m}\frac{\partial^2}{\partial x^2} + V(x)\,. \tag{2.33}$$

The Bloch theorem states that the eigenstates of a particle in a periodic potential are given by the product of a plane wave and a periodic function $u_{n,q}(x) = u_{n,q}(x + a)$ with the same periodicity $a = \pi/k$ as the lattice potential [4, 63]

$$\Phi_{n,q}(x) = e^{iqx} u_{n,q}(x)\,. \tag{2.34}$$

For each quasi-momentum q infinitely many solutions with different eigenenergies exist. This is reflected by the band index n. Since each solution of the Hamiltonian possesses a well defined momentum these so-called Bloch waves are delocalised.

Both the periodic potential and $u_{n,q}(x)$ can be expanded in plane waves with wavevectors $l\,2\pi/a = l\,2k$ according to

$$V(x) = V_x \cos^2(kx) = \frac{V_x}{2}\left(e^{2ikx} + e^{-2ikx} + 2\right) \quad \text{and} \quad u_{n,q}(x) = \sum_l c_l^{n,q} e^{2ilkx} \quad \text{with} \quad l \in \mathbb{Z}. \tag{2.35}$$

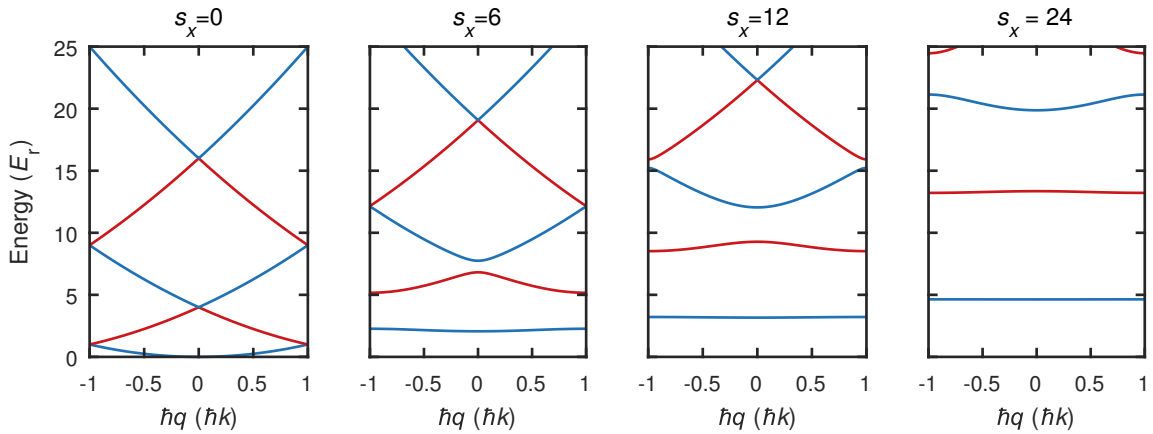

Figure 2.6: Band structure of a 1D optical lattice. (a) For $V_0 = 0\,E_\mathrm{r}$ the bands correspond to the quadratic dispersion relation of a free particle folded into the first Brillouin zone. (b) At finite lattice depth, gaps between bands open at the edge of the Brillouin zone. (c,d) When the lattice depth is increased further, the band gaps increase and the bands approach flat, equidistant harmonic oscillator energy levels. Bands with even (odd) band index n are shown in red (blue).

Using Equation 2.35 the Hamiltonian $\hat{H}$ may be expressed in matrix form

$$H_{l,l'} = \begin{cases} (2l + q/k)^2 E_\mathrm{r} + V_x/2 & |l - l'| = 0 \\ V_x/4 & |l - l'| = 1 \\ 0 & |l - l'| > 1. \end{cases} \tag{2.36}$$

A diagonalisation of $H_{l,l'}$ yields the eigenstates and eigenenergies of the homogeneous periodic potential. For typical experimental lattice depths it is sufficient to restrict the matrix to $-6 \leq l \leq 6$ to obtain accurate results for the lowest bands. The resulting band structure $\epsilon_n(q)$ is presented in Figure 2.6 in a reduced zone scheme showing only the first Brillouin zone $]-\hbar k, \hbar k]$ for different lattice depths. For $V_0 = 0\,E_\mathrm{r}$ the band structure corresponds to the harmonic dispersion relation of a free particle (Figure 2.6(a)). However, for a finite lattice depth the individual bands become separated by band gaps whose width increases with the lattice depth (Figure 2.6(b,c)). For deep lattices, the bands approach the equidistant energy levels of a harmonic oscillator.

Wannier functions

The Bloch functions describe delocalised particles with a well defined quasi-momentum. However, in order to calculate the terms of the Hubbard Hamiltonian, the particles are usually described in an orthonormal Wannier basis [64]. The Wannier functions are localised at the lattice sites, which makes them a convenient choice for tight-binding models. The Wannier function of an atom in the nth band of a 1D optical lattice may be expressed by a Fourier composition of Bloch functions

$$w_n(x - x_i) = \frac{1}{\sqrt{L}} \sum_q e^{iqx_i} \phi_q^n(x)\,, \tag{2.37}$$

where L is the number of lattice sites and x_i denotes the positions of the potential minima. Figure 2.7 shows the probability density of Wannier functions of the lowest band in a one dimensional optical lattice. With increasing lattices depth, the Wannier functions become increasingly localised and approach the

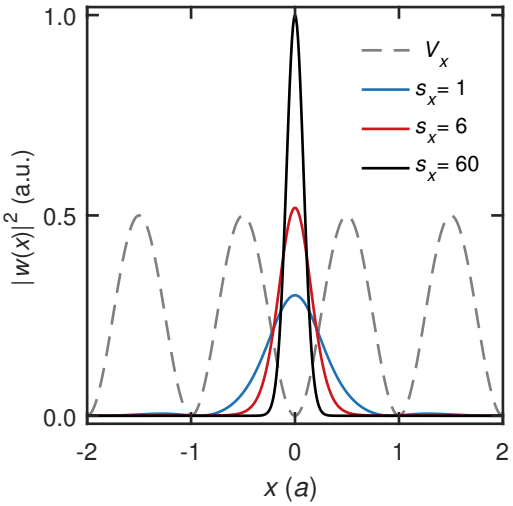

Figure 2.7: Wannier functions. Probability density $|w(x)|^2$ for varying lattice depth as a function of position. As the lattice depth is increased, the wave functions become increasingly localised. The lattice potential for a fixed arbitrary depth is indicated in grey to highlight the lattice sites.

Gaussian eigenfunctions of the harmonic oscillator.

2.4 The Hubbard model

The Hubbard Hamiltonian was formulated as a minimal model to describe strongly interacting electrons in periodic potentials. Due to its broad applicability and especially the hope that it provides insight into the problem of high temperature superconductivity it has been studied intensively in the context of condensed matter both experimentally and theoretically. A new experimental approach to the model was unveiled when D. Jaksch et al. [65] suggested to use cold atoms in optical lattices to study the (Bose)-Hubbard model in an analogue quantum simulation.

In second quantisation, atoms in an optical lattice $V(\mathbf{r})$ are subject to the following Hamiltonian

$$\begin{aligned}\hat{H} = &\sum_{\sigma} \int \mathrm{d}^3 r\, \hat{\Psi}^{\dagger}_{\sigma}(\mathbf{r}) \left[-\frac{\hbar^2}{2m}\nabla^2 + V_0(\mathbf{r}) + V_{\mathrm{T}}(\mathbf{r}) \right] \hat{\Psi}_{\sigma}(\mathbf{r}) \\ &+ \frac{1}{2}\frac{4\pi a_s \hbar^2}{m} \sum_{\sigma,\sigma'} \int \mathrm{d}^3 r\, \hat{\Psi}^{\dagger}_{\sigma'}(\mathbf{r}) \hat{\Psi}^{\dagger}_{\sigma}(\mathbf{r}) \hat{\Psi}_{\sigma}(\mathbf{r}) \hat{\Psi}_{\sigma'}(\mathbf{r}) \,.\end{aligned} \tag{2.38}$$

Here, we specifically consider fermionic field operators $\hat{\Psi}_{\sigma}(\mathbf{r})$ with spin $\sigma = \{\uparrow, \downarrow\}$. The first term in Equation 2.38 includes both the kinetic energy and the slowly varying external trapping potential $V_{\mathrm{T}}(\mathbf{r})$ that arises from the intensity distribution of the employed optical fields (cf. Section 2.3.2). In the second term, we have already accounted for the short range nature of interactions, which are parametrised by the s-wave scattering length a_s(cf. Section 2.2.1). In a single band approximation, the field operators can be

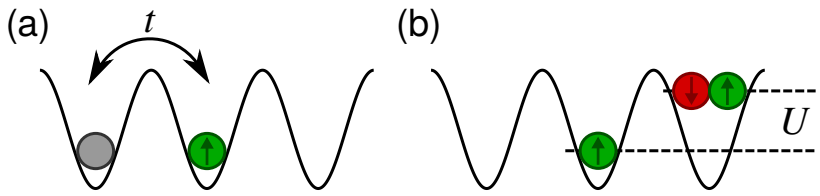

Figure 2.8: The first two terms of the Hubbard model describe (a) the tunnelling of a particle to a neighbouring site with a *tunnelling rate* t and (b) an energy shift U due to the interaction between particles of opposite spin occupying the same lattice site.

expanded in a Wannier basis. This yields

$$\hat{\Psi}^{\dagger}_{\sigma}(\mathbf{r}) = \sum_i \hat{c}^{\dagger}_{i,\sigma} w^{*}_{0}(\mathbf{r} - \mathbf{r}_i) \text{ and} \tag{2.39}$$

$$\hat{\Psi}_{\sigma}(\mathbf{r}) = \sum_i \hat{c}_{i,\sigma} w_0(\mathbf{r} - \mathbf{r}_i)\,, \tag{2.40}$$

where the operator $\hat{c}^{\dagger}_{i,\sigma}$ ($\hat{c}_{i,\sigma}$) creates (destroys) a fermion with spin σ on lattice site i. Applying this expansion to Equation 2.38 results in the one-band Hubbard Hamiltonian

$$\hat{H} = -t \sum_{\langle i,j\rangle,\sigma} \left(\hat{c}^{\dagger}_{i,\sigma}\hat{c}_{j,\sigma} + h.c.\right) + U \sum_i \hat{n}_{i,\uparrow}\hat{n}_{i,\downarrow} - \sum_{i,\sigma} \mu_i \hat{n}_{i,\sigma}\,, \tag{2.41}$$

where we have restricted the interactions to act on-site and tunnelling to occur between neighbouring sites only. In Equation 2.41 the particle number operator $\hat{n}_{i,\sigma} = \hat{c}^{\dagger}_{i,\sigma}\hat{c}_{i,\sigma}$ counts the number of particles per spin on a lattice site. The total number of particles on a lattice site is thus $\hat{n}_i = \sum_\sigma \hat{n}_{i,\sigma}$. Comparing the remaining terms in Equations 2.38 and 2.41, we relate the tunnelling amplitude $t \equiv t_{ij}$ between two neighbouring sites i and j to the Wannier functions $w_0(\mathbf{r} - \mathbf{r}_i)$

$$t_{ij} = \int \mathrm{d}^3 r\, w^{*}_{0}(\mathbf{r} - \mathbf{r}_i) \left[-\frac{\hbar^2}{2m}\nabla^2 + V_0(\mathbf{r})\right] w_0(\mathbf{r} - \mathbf{r}_j)\,. \tag{2.42}$$

Analogously, the on-site interaction parameter for particles with opposite spin on the same lattice site is identified as

$$U = \frac{4\pi\hbar^2 a_\mathrm{s}}{m} \int \mathrm{d}^3 r \left|w_0(\mathbf{r} - \mathbf{r}_i)\right|^4\,. \tag{2.43}$$

Finally, the last term in the Hubbard Hamiltonian 2.41 accounts for the spatially varying energy offset induced by the external trapping potential $V_T(\mathbf{r})$. The corresponding energy offset at a lattice site i is given by

$$\epsilon_i = \int \mathrm{d}\mathbf{r}\, V_\mathrm{T}(\mathbf{r}) \left|w_0(\mathbf{r} - \mathbf{r}_i)\right|^2 \approx V_\mathrm{T}(\mathbf{r_i})\,. \tag{2.44}$$

Together with the global chemical potential μ_0 this expression defines the local chemical potential $\mu_i = \mu_0 - V_T(\mathbf{r_i})$ in Equation 2.41. Throughout this work, we rely on the *local density approximation* (LDA) [66]. Within the LDA, i.e. as long as the external trapping potential varies slowly, e.g. with respect to the correlation length, the inhomogeneous system is treated as locally homogeneous. With the precise calibration of the trap $V_\mathrm{T}(\mathbf{r})$ (see Sec. 3.5.4) the potential is divided into spatial segments in which the potential is approximately constant. Then, the properties of the gas are defined by the local chemical

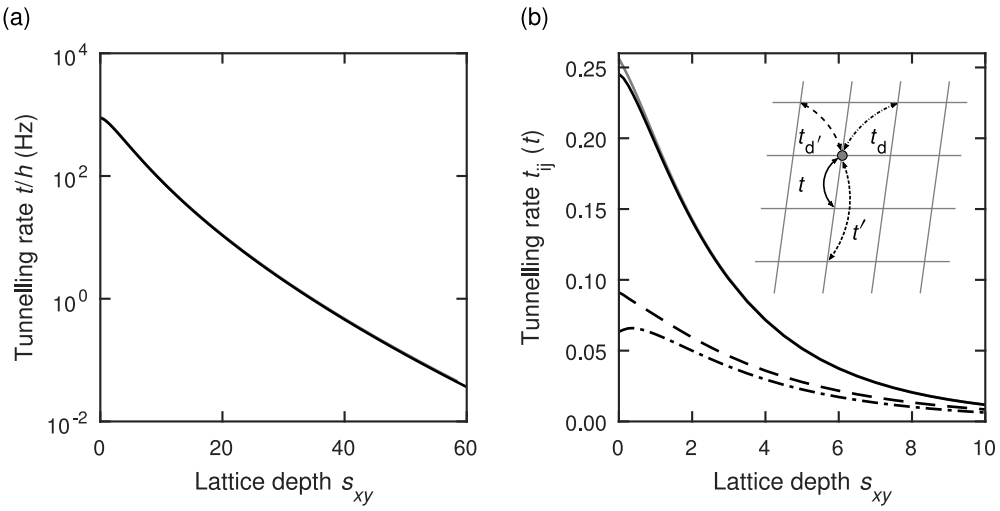

Figure 2.9: Tunnelling rates versus lattice depth. (a) Shows the nearest neighbour tunnelling t for the oblique lattice with an angle of 85.67°. In (b) the contribution from further-neighbour tunnelling (b) is presented in units of t. Both for the square lattice (solid grey) as well as for the oblique lattice (solid black) the dominating contribution stems from tunnelling along a straight line t'. In the non-separable case, the tunnelling amplitudes t_d and $t_{d'}$ along the short (dashed) and the long diagonals (dash-dotted), respectively, are non-zero. The oblique lattice and the tunnelling matrix elements are schematically shown in the inset of (b).

potential μ_i. This relationship allows to convert the measured spatial density distribution $n(\mathbf{r})$ into the equation of state $n(\mu)$, which may then be compared to numerical simulations of homogeneous systems.

Tunnelling matrix elements in the 2D optical lattice

Above, we have only discussed the case of a 1D optical lattice. We noted that the extension to 2D and 3D optical lattices is straight forward as long as the periodic potentials remain separable. Experimentally, cross interference between the individual standing waves have to be avoided (cf. Section 3.5.2) and the lattices have to be mutually orthogonal. Due to technical limitations in our setup the latter could not be realised for the two standing waves forming the horizontal lattices. Instead, the angle between the two standing waves is fixed to the maximally achievable value of 85.67 °. To estimate the impact of the non-orthogonal lattice angle on experimental parameters, Figure 2.9 shows a comparison of the tunnelling elements obtained using the actual oblique lattice potential and the ideal separable square lattice potential. While the nearest-neighbour tunnelling rates t are almost indistinguishable in Figure 2.9(a) [67][1] the next-nearest neighbour tunnelling matrix elements shown in Figure 2.9(b) are notably different. In a separable lattice, tunnelling along the diagonal is strictly zero, since the Wannier functions are orthogonal. In contrast, the non-separable oblique lattice leads to finite tunnelling rates t_d ($t_{\mathrm{d}'}$) along the short (long) diagonal to t. For our lattice angle and a typical lattice depth of $6\,E_\mathrm{r}$, we find $t'/t \approx 4\,\%$ and $t_\mathrm{d}/t \approx t_{\mathrm{d}'}/t \approx 2\,\%$. In a recent study of the attractive Hubbard model, Mitra et al. [69] use DQMC simulations to estimate corrections for a range of observables in the Hubbard model arising from the presence of next-nearest neighbour tunnelling matrix elements with similar amplitudes as in our experiments and find that their contributions to experimental observables are negligible. In conclusion, we neglect all but the nearest-neighbour tunnelling term for the lattice depths realised in the experiments

[1] All calculations have been carried out using a script provided by the group of D. Jaksch. The code and a detailed documentation thereof can be found online [68].

presented in this thesis ($V_0 > 5\,E_r$). In this limit, the dispersion relation of non-interacting atoms in a two-dimensional optical lattice is given by

$$\epsilon(\mathbf{q}) = -2t\left[\cos\left(q_x a\right) + \cos\left(q_y a\right)\right] , \tag{2.45}$$

where $a = \pi/k_{\mathrm{lat}}$ is the lattice constant.

On-site interaction

According to Equation 2.43, the on-site interaction U depends on the scattering length a_s as well as on the precise shape of the Wannier-functions. We obtain the scattering length using carefully calibrated values of the Feshbach field and the parametrisation of the scattering resonance according to Equation 2.16. For deep lattices the localised wave functions are usually well approximated by the eigenstates of a harmonic oscillator potential. In this limit, the exact energy of two particles interacting via a short range potential can be found [70]. This description can also be used to include the anisotropy of our three-dimensional lattice potential [71, 72]. However, for shallower lattices the harmonic approximation fails and we have to use a correction to obtain reliable results [73]. To confirm the calculated values, we initially left U as a free parameter when we fitted our data to numerical simulations of the 2D Hubbard model using numerical linked cluster expansion (NLCE) [74] and generally found good agreement with the calculated on-site interaction energy. An exception are weakly interacting systems where the calculated value $U/t = 1.6$ significantly deviates from the fitted value of $U/t = 2.5$. This behaviour can be attributed to a failure of the NLCE method at low interactions, where the delocalisation of the lattice gas limits the convergence of the expansion to higher temperatures as compared to more strongly interacting systems [75, 76].

2.4.1 Non-interacting Hubbard model

Without interactions, i.e. $U = 0$, Equation 2.41 reduces to

$$\hat{H}_0 = -t \sum_{\langle i,j\rangle,\sigma} \left(\hat{c}^\dagger_{i,\sigma}\hat{c}_{j,\sigma} + h.c.\right) - \mu \sum_i \hat{n}_i \, . \tag{2.46}$$

This is the non-interacting Hubbard model. Already this very simple case contains the existence of metallic and band insulating phases of electrons in periodic potentials. A convenient approach to find the eigenstates of this Hamiltonian 2.46 is to transfer the problem to momentum space [77]. To this end, we express creation and annihilation operators in a plane wave expansion

$$\begin{aligned} \hat{c}^\dagger_{\mathbf{l},\sigma} &= \frac{1}{\sqrt{L}} \sum_{\mathbf{k}} e^{-i\mathbf{k}\mathbf{l}} \hat{c}^\dagger_{\mathbf{k},\sigma} \, , \\ \hat{c}_{\mathbf{l},\sigma} &= \frac{1}{\sqrt{L}} \sum_{\mathbf{k}} e^{i\mathbf{k}\mathbf{l}} \hat{c}_{\mathbf{k},\sigma} \, , \end{aligned} \tag{2.47}$$

where L is the number of lattice sites and $\mathbf{k} = (k_x, k_y) = \frac{2\pi}{L}(n_x, n_y)$ is the discretised wave vector. The creation and annihilation operators respect the fermionic anticommutation relations

$$\{\hat{c}_{\mathbf{k},\sigma}\hat{c}^\dagger_{\mathbf{k}',\sigma'}\} = \delta_{\mathbf{k},\mathbf{k}'}\delta_{\sigma,\sigma'} \, , \{\hat{c}^\dagger_{\mathbf{k},\sigma}\hat{c}^\dagger_{\mathbf{k}',\sigma'}\} = 0 \, , \{\hat{c}_{\mathbf{k},\sigma}\hat{c}_{\mathbf{k}',\sigma'}\} = 0 \, . \tag{2.48}$$

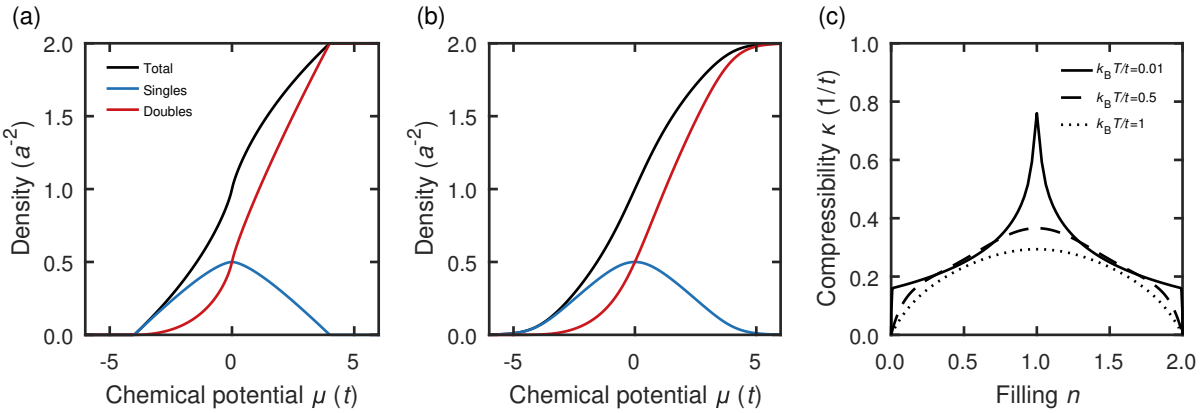

Figure 2.10: Equation of state of the non-interacting Hubbard model. We show the total density (black), singly occupied sites (blue) and doubly occupied sites (red) as a function of chemical potential μ, of the non-interacting Hubbard model for temperatures $k_B T/t = 0.01$ (a) and $k_B T/t = 0.5$ (b). (c) shows the thermal compressibility as a function of filling for three different temperatures.

A replacement of the operators in Equation 2.46 with expression 2.48 yields the diagonal Hamiltonian

$$\hat{H}_0 = \sum_{\mathbf{k},\sigma} (\epsilon_{\mathbf{k}} - \mu) \hat{c}^{\dagger}_{\mathbf{k},\sigma} \hat{c}_{\mathbf{k},\sigma} = \sum_{\mathbf{k},\sigma} (\epsilon_{\mathbf{k}} - \mu) \hat{n}_{\mathbf{k},\sigma} \ . \tag{2.49}$$

In the tight binding limit $\epsilon_{\mathbf{k}} = -2t \sum_x \cos a k_x$. Within the grand canonical ensemble the density matrix is given by

$$\hat{\rho} = \frac{e^{-\beta \hat{H}}}{Z} \ , \tag{2.50}$$

with the partition function

$$Z = \mathrm{Tr}\left[e^{-\beta \hat{H}} \right] . \tag{2.51}$$

The thermal average $\langle \ldots \rangle$ of an hermitian operator $\hat{O}$ is given by

$$\langle \hat{O} \rangle = \mathrm{Tr}\left[\hat{\rho} \hat{O} \right] . \tag{2.52}$$

With these expressions, the average total number of particles becomes

$$\langle \hat{n} \rangle = \frac{1}{Z} \mathrm{Tr}\left[\sum_{\mathbf{k}} \hat{n}_{\mathbf{k}} e^{-\beta \hat{H}} \right] = \sum_{\mathbf{k}} \left[1 + e^{\beta(\epsilon_{\mathbf{k}} - \mu)} \right]^{-1} \ . \tag{2.53}$$

The last expression reminds us of the Fermi-Dirac distribution. The thermodynamic behaviour of the non-interacting Hubbard model is thus completely determined by the Fermi-Dirac statistics and the filling. Figures 2.10 (a) and (b) show Equation 2.53 as a function of the chemical potential for a temperature of $k_B T/t = 0.01$ and $k_B T/t = 0.5$, respectively. In addition, we show the expectation values of singly and doubly-occupied sites $\langle \hat{d} \rangle$ and $\langle \hat{s} \rangle$, which are easily derived from the density using the fact that, without interactions, spin-up and spin-down particles are entirely uncorrelated

$$\langle \hat{d} \rangle = \langle \hat{n}_{\uparrow} \hat{n}_{\downarrow} \rangle = \langle \hat{n}_{\uparrow} \rangle \langle \hat{n}_{\downarrow} \rangle \ \text{and} \tag{2.54}$$

$$\langle \hat{s} \rangle = \langle \hat{n} \rangle - 2 \langle \hat{n}_{\uparrow} \hat{n}_{\downarrow} \rangle \ . \tag{2.55}$$

Compressibility

In ultracold atom experiments it is difficult to directly quantify the conductivity of a many-body system as this would require transport measurements. However, an experimentally more accessible quantity that allows to distinguish between metallic and insulating phases is the isothermal compressibility

$$\kappa = \frac{1}{V}\frac{\partial \langle \hat{n}(\mu)\rangle}{\partial \mu} \,. \tag{2.56}$$

The isothermal compressibility describes the reaction of a many-body state to a change in the chemical potential. A system with finite compressibility is metallic, since a change in density upon compression implies that empty states were available which permit the redistribution of density and thus particle transport. On the contrary, when the system is gapped against charge excitation there are no energetically accessible empty states and the compressibility vanishes. At the same time, the system is insulating since there is no particle transport. In Figure 2.10(c) we show the compressibility κ for different temperatures and as a function of filling. For all temperatures, the compressibility vanishes for the empty as well as for the completely filled band, while a maximal compressibility is found at half filling. This indicates the crossover from an insulating vacuum (a band insulator of holes) to a metallic state (with a partially filled band) and to a band insulator, when the band is completely filled. The divergence of the compressibility at half filling as the temperature approaches $T = 0$ is reminiscent of the van-Hove singularity [78] in the density of states[2] for a uniform square lattice.

In Chapter 6, we study the effect of interactions introduced into the Hubbard model. In the limit of weakly interacting systems, we will compare the equation of state and compressibility to the non-interacting Hubbard model presented here.

2.4.2 Atomic limit

The opposite limit to the non-interacting Hubbard model is the atomic limit with $t = 0$. In this case each lattice site is independent. Thus, to find the equation of state in this limit, we consider all the possible micro-states of an isolated lattice site, $|0\rangle$, $|\downarrow\rangle$, $|\uparrow\rangle$ and $|\downarrow\uparrow\rangle$. These states are eigenstates of the interaction Hamiltonian $H = U\hat{n}_\uparrow\hat{n}_\downarrow - \mu\hat{n}$ with eigenvalues $U/4$, $-U/4-\mu$, $-U/4-\mu$ and $-U/4-2\mu$, respectively. We easily find the partition function for a single site

$$Z^0 = \mathrm{Tr}\left[e^{\beta\hat{H}}\right] = e^{-\beta U/4} + 2e^{-\beta(-U/4-\mu)} + e^{-\beta(-U/4-2\mu)} \tag{2.57}$$

and the average number of particles per site

$$\langle\hat{n}\rangle = \langle\hat{n}_\uparrow + \hat{n}_\downarrow\rangle = Z^{-1}\,\mathrm{Tr}\left[(\hat{n}_\uparrow + \hat{n}_\downarrow)e^{\beta\hat{H}}\right] = Z^{-1}\left(2e^{-\beta(-U/4-\mu)} + 2e^{-\beta(-U/4-2\mu)}\right) \,. \tag{2.58}$$

Figure 2.11 presents the occupation as a function of the chemical potential. In contrast to the non-interacting case, where we had a metallic region around half filling smoothly connecting the vacuum and the band-insulating region, we now observe a plateau around half filling, where the density does not change and the compressibility vanishes (Figure 2.11(b)). The formation of this insulating many-body state can be understood as a splitting of the band into a lower and an upper band, which are separated by the interaction energy. When the lower band is full, each site is occupied with a single electron. Now, any

[2] The analytical result for the density of states for non-interacting fermions on the square lattice is $g(\epsilon) = \frac{1}{2\pi^2 t}\mathrm{K}\left[1-\left(\frac{\epsilon}{4t}\right)^2\right]$, where $\mathrm{K}[x]$ is the elliptical integral of the first kind [77].

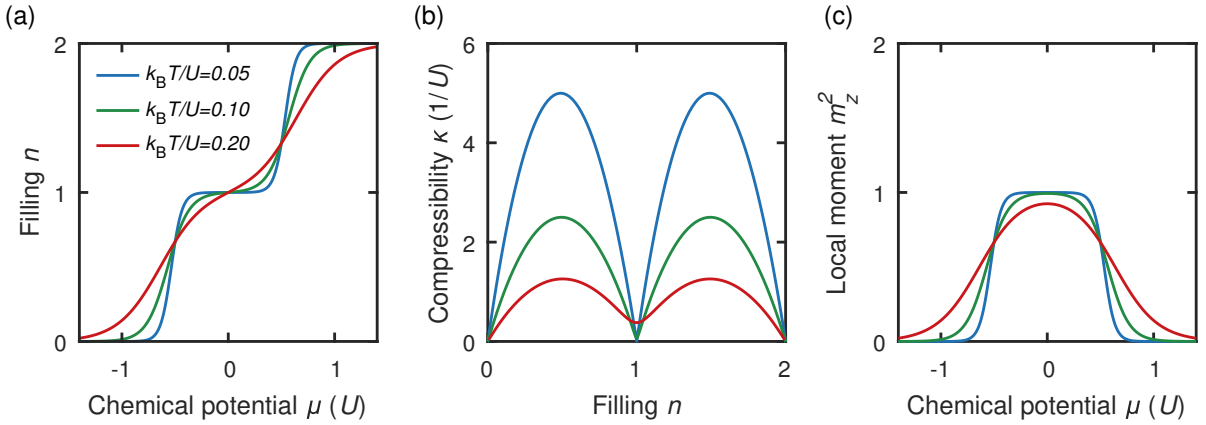

Figure 2.11: Equation of state in the atomic limit. For finite U, the density $n(\mu)$ develops a plateau around half filling, which is washed out with increasing temperature (a). This behaviour is also reflected in the compressibility, which shows a minimum at half filling indicating that the system is insulating. (c) Shows the formation of local moments with decreasing temperature.

transport requires the formation of doubly occupied sites, i.e. excitations to the upper band, which are energetically suppressed. This feature of the Hubbard model is called the *Mott plateau* after Sir Neville Mott. In the atomic limit, the width of the plateau is determined only by the strength of the on-site interaction and the temperature. The addition of a non-zero tunnelling amplitude leads to enhanced quantum fluctuations and, correspondingly, a decreasing extent of the Mott plateau. The existence of the Mott plateau at half filling introduces a new degree of freedom, since each lattice site is then filled with a (pseudo-)spin half particle. Indeed, the formation of these *local moments* $\langle m_z^2 \rangle$ is a prerequisite for localised magnetism in the Hubbard model. We define

$$\langle m_z^2 \rangle = \langle (\hat{n}_\uparrow - \hat{n}_\downarrow)^2 \rangle = \langle \hat{n} \rangle - 2 \langle \hat{n}_\uparrow \hat{n}_\downarrow \rangle \ , \tag{2.59}$$

where the last term measures the average number of atoms on doubly occupied sites $\langle \hat{d} \rangle$ and is given by

$$\langle \hat{n}_\uparrow \hat{n}_\downarrow \rangle = Z^{-1} Tr[\hat{n}_\uparrow \hat{n}_\downarrow e^{\beta \hat{H}}] = Z^{-1} e^{-\beta(U/4 - 2\mu)} \ . \tag{2.60}$$

Using these expressions, we find that the local moment is zero for both empty and doubly-occupied lattice sites, but one for singly-occupied sites. In Figure 2.11(c), the local moment at half filling is plotted as a function of temperature and on-site interaction showing that local moments increase with increasing (repulsive) interaction strength and decreasing temperature.

In conclusion, we have seen that in the atomic limit at half-filling and for sufficiently low temperature the Hubbard model is gapped against charge excitation, while two possible spin-configurations are degenerate. Therefore, we may expect that spin-excitations are accessible already at low energies. In the next section, we will reintroduce the tunnelling term of the Hubbard model and attribute an energy scale to these excitations. As a result, we will find that a finite tunnelling amplitude gives rise to antiferromagnetic correlations between lattice sites.

2.4.3 Origin of antiferromagnetic correlations in the Hubbard model - a toy model

The following paragraphs motivate how antiferromagnetic correlations originate from repulsive interactions in the Hubbard model. As a simplified model, we may consider two fermionic particles in

a double-well potential. Previously, this situation was referred to as "half filling". In this case, the basis is spanned by six states: $|\uparrow,\uparrow\rangle, |\downarrow,\downarrow\rangle, |\uparrow,\downarrow\rangle, |\downarrow,\uparrow\rangle, |\uparrow\downarrow,0\rangle$ and $|0,\uparrow\downarrow\rangle$. The states $|\uparrow,\uparrow\rangle$ and $|\downarrow,\downarrow\rangle$ are immediately identified as eigenstates of the Hubbard Hamiltonian with energy $E = 0$ since hopping is blocked by the Pauli principle and, due to the absence of double occupancy, these states carry no interaction energy. With the basis reduced to $|\uparrow,\downarrow\rangle, |\downarrow,\uparrow\rangle, |\uparrow\downarrow,0\rangle$ and $|0,\uparrow\downarrow\rangle$ the Hamiltonian reads

$$H = \begin{pmatrix} 0 & 0 & -t & -t \\ 0 & 0 & t & t \\ -t & t & U & 0 \\ -t & t & 0 & U \end{pmatrix}. \tag{2.61}$$

Proceeding with the diagonalisation of Equation 2.61, we find the following pairs of eigenstates and eigenenergies

$$\Psi_a = \frac{1}{\sqrt{2}}\left(|\uparrow,\downarrow\rangle + |\downarrow,\uparrow\rangle\right) \text{ with energy } E_a = 0,$$

$$\Psi_b = \frac{1}{\sqrt{2}}\left(|\uparrow\downarrow,0\rangle + |0,\uparrow\downarrow\rangle\right) \text{ with } E_b = U,$$

$$\Psi_c = \frac{1}{\sqrt{2}} \frac{\left(|\uparrow,\downarrow\rangle - |\downarrow,\uparrow\rangle\right) - \frac{E_c}{2t}\left(|\uparrow\downarrow,0\rangle + |0,\uparrow\downarrow\rangle\right)}{\sqrt{1+\left(\frac{E_c}{2t}\right)^2}} \text{ with } E_c = \frac{1}{2}\left(U - \sqrt{(4t)^2+U^2}\right) \text{ and}$$

$$\Psi_d = \frac{1}{\sqrt{2}} \frac{\left(|\uparrow,\downarrow\rangle - |\downarrow,\uparrow\rangle\right) + \frac{E_d}{2t}\left(|\uparrow\downarrow,0\rangle + |0,\uparrow\downarrow\rangle\right)}{\sqrt{1+\left(\frac{E_d}{2t}\right)^2}} \text{ with } E_d = \frac{1}{2}\left(U + \sqrt{(4t)^2+U^2}\right).$$

Figure 2.12 shows the eigenergies as a function of the on-site interaction. For strong repulsive interaction the energies of states with dominant single and double occupancy are gapped by an energy difference of order U, leading to a suppression of doubly occupied sites. This may be seen as a toy model of the crossover to a Mott-insulator since density excitations, and thus transport, are suppressed by the cost in interaction energy. Recently, the spectrum of the two-site Hubbard model has also been studied with cold atoms in an optical micro traps [79].

2.4.4 Superexchange

We have seen above that strong repulsive interactions suppress the formation of double occupancies and, correspondingly, empty sites. Instead, each of the wells is occupied by an unpaired spin. This hints at the possibility to minimise internal energy by a favourable alignment of spins on the different sites. Indeed, when both spins point in the same direction, as shown in Figure 2.13(a), tunnelling from one site to the other is forbidden due to the Pauli principle. On the contrary, when the spins are anti parallel as shown in Figure 2.13(b), second order tunnelling may take place. In this process, one of the spins hops to the other site forming an intermediate (virtual) double occupancy before one of the spins hops back to the empty site. Due to the cost in interaction energy for large U, the double occupancy is only formed temporarily. To understand this so-called superexchange better, we take the limit $U \gg t$ and treat tunnelling as a perturbation to the interaction Hamiltonian [11]. In this limit, the eigenstates of the

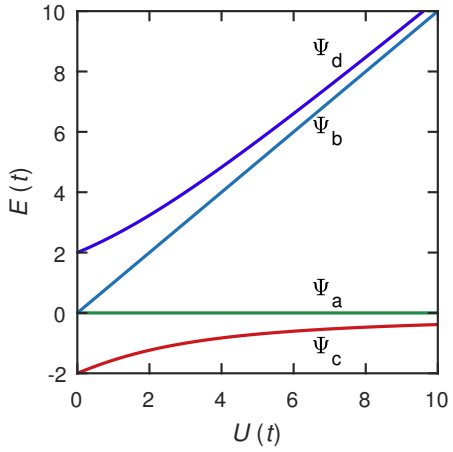

Figure 2.12: Eigenenergies of two repulsively interacting fermions in a double well as a function of the on-site interaction U.

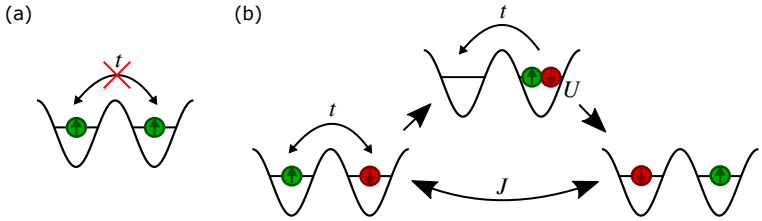

Figure 2.13: Superexchange in the double well. (a) Due to the Pauli principle tunnelling is forbidden for parallel spins. (b) Opposite spins may exchange position via an intermediate step by forming a virtual double occupancy.

interaction Hamiltonian are the following triplet and singlet states

$$\text{Triplet} \qquad \begin{cases} \Phi_{t,1} &= |\uparrow,\uparrow\rangle \\ \Phi_{t,2} &= \frac{1}{\sqrt{2}}(|\uparrow,\downarrow\rangle + |\downarrow,\uparrow\rangle) \\ \Phi_{t,3} &= |\downarrow,\downarrow\rangle \end{cases} \tag{2.62}$$

$$\text{Singlet} \qquad \Phi_s = \frac{1}{\sqrt{2}}(|\uparrow,\downarrow\rangle - |\downarrow,\uparrow\rangle)\,. \tag{2.63}$$

These states are degenerate in interaction energy. As outlined above, we introduce tunnelling as a second order perturbation. Thereby, the perturbed states are shifted in energy by

$$\delta E_n = t^2 \sum_m \frac{\left|\langle m| \sum_\sigma (\hat{c}^\dagger_{1,\sigma}\hat{c}_{2,\sigma} + \hat{c}^\dagger_{2,\sigma}\hat{c}_{1,\sigma})\,|n\rangle\right|^2}{E_n - E_m}\,. \tag{2.64}$$

In order to estimate the energy shift, we are interested in finding the matrix elements in Equation 2.64. For both $\Phi_{t,1}$ and $\Phi_{t,3}$ tunnelling is forbidden and thus $\delta E = 0$. Therefore, we now consider only the entangled states $\Phi_{t,2}$ and Φ_s. Using $|\uparrow,\downarrow\rangle = \hat{c}^\dagger_{1,\uparrow}\hat{c}^\dagger_{2,\downarrow}\,|0,0\rangle$ as well as the fermionic anti-commutation

relations we find

$$-t \sum_{\sigma} (\hat{c}^{\dagger}_{1,\sigma} \hat{c}_{2,\sigma} + \hat{c}^{\dagger}_{2,\sigma} \hat{c}_{1,\sigma}) \, |\uparrow, \downarrow\rangle = -t(|\uparrow\downarrow, 0\rangle + |0, \uparrow\downarrow\rangle) \tag{2.65}$$

$$-t \sum_{\sigma} (\hat{c}^{\dagger}_{1,\sigma} \hat{c}_{2,\sigma} + \hat{c}^{\dagger}_{2,\sigma} \hat{c}_{1,\sigma}) \, |\downarrow, \uparrow\rangle = t(|\uparrow\downarrow, 0\rangle + |0, \uparrow\downarrow\rangle) \, . \tag{2.66}$$

This shows that the symmetric triplet state $\Phi_{t,2}$ experiences no energy shift ($\delta E = 0$) due to second order tunnelling, while the energy of the singlet state is shifted by

$$\delta E = \frac{2t \cdot 2t}{0 - U} = -\frac{4t^2}{U} \, . \tag{2.67}$$

Thus, we have found that the singlet state is energetically favoured and that antiferromagnetism may arise from short-ranged repulsive interactions without the need for a direct spin-spin interaction.

2.4.5 The antiferromagnetic Heisenberg model

At half filling and for strong interactions the Hubbard model approaches the Heisenberg model of localised spins

$$H = J \sum_{\langle i,j \rangle} \hat{\mathbf{S}}_i \hat{\mathbf{S}}_j \, , \tag{2.68}$$

with local spin-$\frac{1}{2}$ operators $\hat{\mathbf{S}}_i = (\hat{S}^x_i, \hat{S}^y_i, \hat{S}^z_i)^T$ [80]. In the Heisenberg model, spins on neighbouring lattice sites $\langle i, j \rangle$ interact via spin exchange $\hat{\mathbf{S}}_i \hat{\mathbf{S}}_j$. The strength of this interaction is determined by the exchange constant $J = 4t^2/U$ [81] and the positive sign indicates that the model is antiferromagnetic. This energy scale, which we also obtained from the perturbative treatment of tunnelling in the two-site model above, yields an estimate for the temperature below which one can expect to observe magnetic order. Note, that in two-dimensional systems true long range order is forbidden at finite temperature [82]. Nevertheless, the strength of the superexchange coupling still yields an estimate for the temperature around which antiferromagnetic correlations become significant for the 2D Hubbard model.

CHAPTER 3

Experimental setup

This chapter provides an overview of the experimental apparatus in its current status. Furthermore, it summarises the production of a cold lattice gas with tunable interactions. The apparatus was originally constructed at the university of Cambridge and was moved to Bonn in 2013. Therefore, a more detailed description of many of the individual technical elements of the apparatus is found in Refs. [83], [48] and [84]. A general introduction to the creation and characterisation of degenerate Fermi gases is presented in Ref. [41] and citations therein.

Section 3.1 provides an introduction to the experimental apparatus as well as a brief summary of the cooling steps applied to achieve quantum degeneracy of fermionic Potassium-40. Thereafter, the individual cooling techniques are reviewed in greater detail: In Section 3.2 the magneto optical trap (MOT) is presented. Section 3.3 summarises the magnetic Ioffe-Pritchard trap and evaporative cooling therein. In Section 3.4 the creation of a spin balanced quantum degenerate Fermi gas in an optical dipole trap is outlined. Thereafter, the optical lattice setup is introduced in Sections 3.5.1 and 3.5.2. Finally, Section 3.6 contains a summary of the magnetic coil setup providing the Feshbach fields to manipulate the interaction between atoms in different hyperfine levels. It is further discussed how the alignment and the stabilisation of the fields to the required level of precision has been achieved.

3.1 Vacuum system

The core of the experimental apparatus is the vacuum system shown in Figure 3.1. Four sections of the system can be identified

1. A small oven provides a source of potassium atoms.
2. In the first vacuum chamber (MOT cell) a three-dimensional MOT is used to confine and cool atoms from the background pressure.
3. Then the atoms are transported through two differential pumping tubes which maintain four orders of magnitude in pressure difference between the MOT cell and the final position of the atoms.
4. The science cell provides sufficient optical access to trap the atoms in a three dimensional optical lattice and to image the density distribution using high resolution absorption imaging.

In the oven, solid potassium is heated to a temperature of 60 °C to create a background pressure of $\sim 1 \times 10^{-9}$ mbar in the MOT cell, where the atoms are trapped and cooled in a MOT. Hereafter, the pre-cooled atoms are transferred to a magnetic quadrupole trap. The magnetic trap is generated by a pair

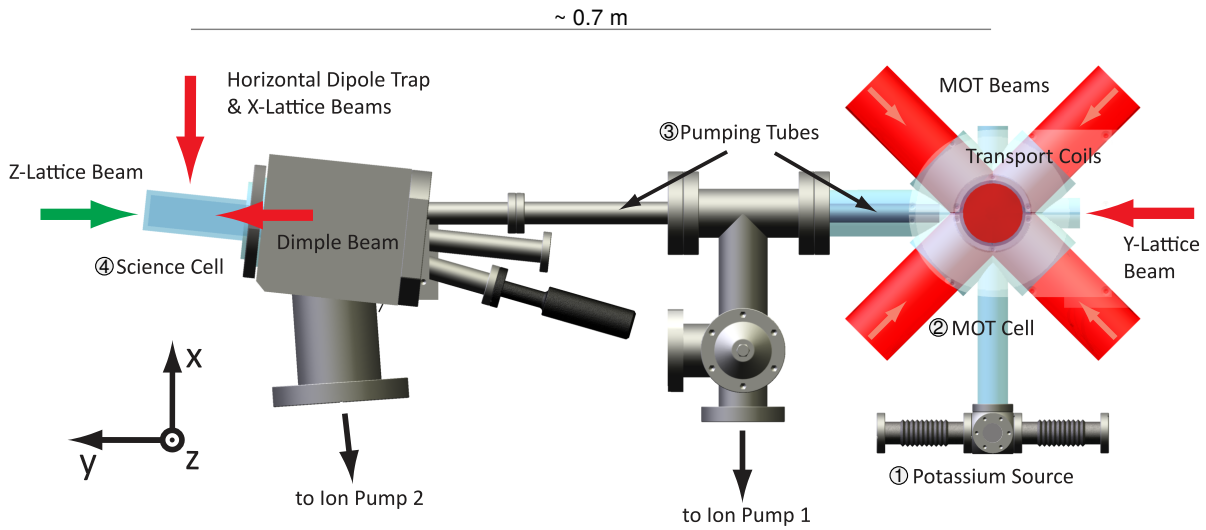

Figure 3.1: The vacuum system (viewed from above). The apparatus consists of two vacuum chambers, the MOT cell and the science cell, which are connected via two differential pumping tubes. Metallic potassium is heated to 60 °C in an oven to create a vapour pressure of approximately 1×10^{-9} mbar in the MOT cell. After trapping and primary cooling in the magneto-optical trap, the atoms are transported through two differential pumping tubes in a magnetic quadrupole trap (transport coils). In the science cell, the atoms are cooled further in a magnetic Ioffe-Pritchard trap (not shown) by microwave evaporation and, thereafter, by forced evaporation in a crossed dipole trap formed by the horizontal dipole trap and the dimple beam. Figure adapted from [85].

of coils mounted on a motorised translation stage[1], which is used to transport the atoms through two differential pumping tubes to a second vacuum chamber (science cell). In the science cell, a pressure of $\sim 1 \times 10^{-11}$ mbar is maintained to prevent heating by collisions with background atoms. Next, the atoms are loaded into a Ioffe-Pritchard trap [86] where the atoms are cooled by radio frequency (RF) evaporation. Afterwards, the temperature of the gas is low enough for optical trapping and the atoms are transferred to an optical dipole trap where a further step of evaporative cooling is applied [87] to reach quantum degeneracy. Then, a blue detuned optical lattice is ramped up along the z-direction. This deep optical lattice confines the atoms in a stack of independent two-dimensional horizontal planes. The preparation is concluded by a power increase in a pair of red detuned optical lattices in the horizontal plane. Simultaneously, the power in the dipole trap beams is decreased to compensate the change in the trap frequencies. This strategy allows to minimise heating during lattice loading, since it reduces the density redistribution, which is necessary to accommodate for the change in the density of states. After the atomic cloud has settled at the experimental lattice depth, a tenfold increase in the depth of the horizontal lattices suppresses any motion during detection. Finally, the detection involves a sequence of manipulations on the magnetic hyperfine states using RF pulses as well as an absorption imaging routine. Depending on the chosen tailored high-resolution RF spectroscopy scheme (cf. Chapter 4), either the site occupation or the magnetic hyperfine state is resolved in the images, giving access to the density and spin degrees of freedom, respectively. We employ a high resolution imaging system (cf. Chapter 5) to obtain spatially resolved images of the spin and density distributions. The following sections explain the different parts of the experimental apparatus as well as the preparation of the atomic gas in more detail.

[1] Parker Hannafin 406800 XR with Compax 3 servo drive

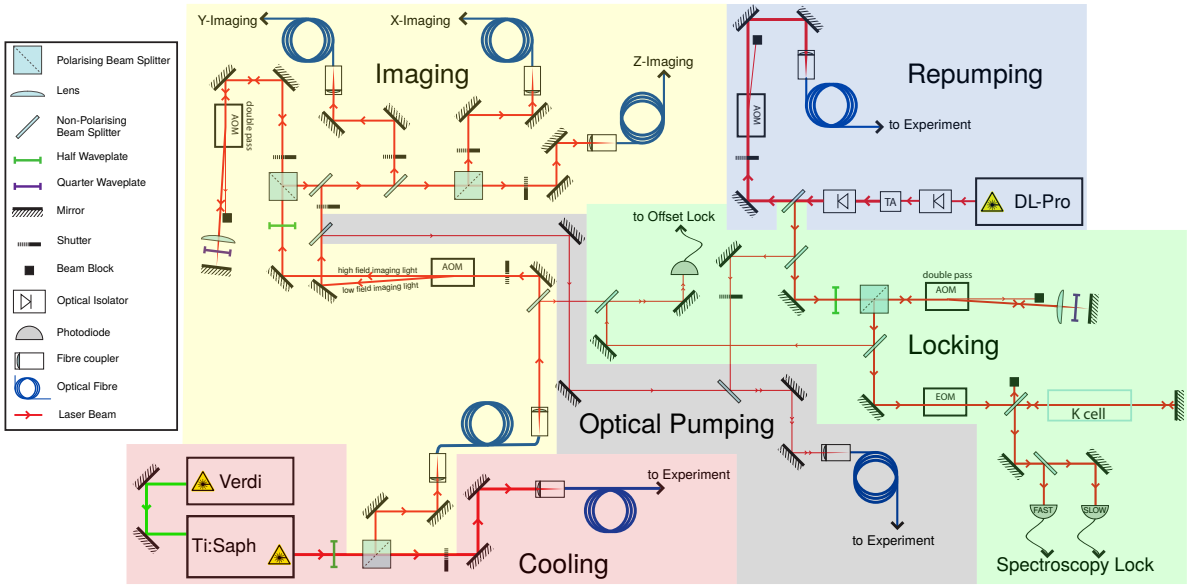

Figure 3.2: MOT and imaging laser setup

3.2 Magneto optical trap

The cooling and trapping sequence starts with a MOT. MOTs employ a combination of radiation pressure and magnetic trapping to provide a velocity as well as a position dependent force acting on an atomic cloud [46, 88, 89]. The velocity dependent force is realised by two counter propagating red detuned laser beams with σ^+ and σ^- polarisation forming an optical molasses [90]. Due to the Doppler shift, moving atoms are more likely to absorb photons from the beam in the direction they are moving towards and experience a damping force $F = -\alpha v$. However, the optical molasses alone results only in a confinement in momentum space. In order to confine the atoms in space, a small magnetic quadrupole field is applied to realise a spatially varying splitting of the Zeeman sublevels

$$E(\mathbf{r}) = g_\mathrm{F} m_\mathrm{F} \mu_\mathrm{B} B(\mathbf{r})\,. \tag{3.1}$$

Close to $z = 0$, where $B = 0$, the magnetic field varies linear with distance. Consequently, the atoms in the $m_F > 0$ ($m_F < 0$) hyperfine sublevels are gradually shifted into resonance with the red detuned beams with increasing distance in the positive (negative) z-direction. Together with the selection rules for circularly polarised light, this results in a restoring force $F = -\beta z$ acting towards the centre of the MOT.

Three dimensional trapping and cooling is achieved using three pairs of counter propagating beams, which are red detuned with respect to the atomic transition. The level scheme of ^{40}K is shown in Figure 3.3. The cooling beam is 32 MHz red-detuned to the $|F = 9/2\rangle \rightarrow |F' = 11/2\rangle$ transition. Since atoms are able to decay from $|F' = 11/2\rangle$ to $|F = 7/2\rangle$ a second laser is required to drive the repumping transition $|F = 7/2\rangle \rightarrow |F' = 9/2\rangle$ bringing the atoms back into the cooling cycle. During this thesis, home-built diode lasers providing the light for both transitions [48] have been replaced by commercial solutions. This effort resulted in an increase of the number of trapped atoms, greater stability of the prepared atom number, as well as less maintenance time for the laser system. An overview of the current optical setup is provided in Figure 3.2. The cooling light is generated by a single frequency Ti:Sapph

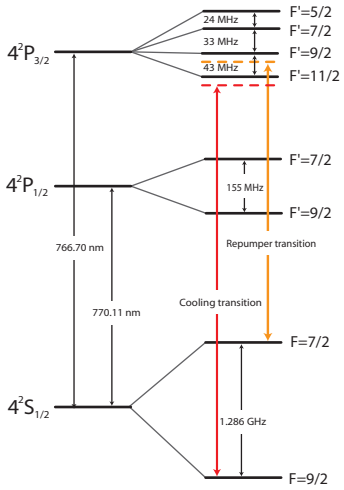

Figure 3.3: Electronic level structure of ^{40}K. The cooling and repumping transitions are shown in red and orange, respectively. The thinner black arrows on the left denote the D1 and D2 lines at 770.1 nm and 766.7 nm. Figure adopted from [48].

laser[2] providing 1.2 W of cooling light at a wavelength of 766.70 nm. In addition, a small part of the generated light is employed for optical pumping at the end of the MOT phase and to image the atomic distribution at the end of the experimental sequence. The light for the repumping transition is generated by a diode laser[3], which is amplified using a tapered amplifier system and stabilised to a ^{39}K spectroscopy cell using frequency modulation spectroscopy [91]. The cooling laser is stabilised to the repumper with an offset lock [92]. A detailed description of both locking schemes is presented in Ref. [83].

Due to the competition between cooling and heating processes, the lowest achievable temperature in the MOT is on the order of the Doppler cooling limit $T \approx T_\mathrm{D} = \hbar\Gamma/2k_\mathrm{B} \approx 145\,\mu\mathrm{K}$ [46] for Potassium. Since this temperature is still four orders of magnitude higher than the temperature to reach quantum degeneracy in our experiment, two further cooling steps are carried out. Both of these steps involve the successive removal of atoms with the highest kinetic energies and subsequent re-thermalisation of the remaining fraction of atoms. We begin by introducing the magnetic Ioffe-Pritchard trap in the next section.

3.3 Ioffe-Pritchard trap

According to Equation 3.1 magnetic traps for neutral atoms can be created using strong inhomogeneous magnetic fields. Since it is impossible to create a magnetic field maximum in free space, only atoms in *low-field seeking states*, i.e. with $g_F m_F > 0$, are magnetically trappable. Therefore, at the end of the MOT phase, we drive the $|F = 9/2\rangle \rightarrow |F' = 9/2\rangle$ transition on the $D2$-line with σ^+-polarised light to optically pump the atoms into states with positive m_F. Thereafter, the atoms are trapped in the magnetic quadrupole trap and transported to the science cell (cf. 3.1). Once the atoms have arrived at their final position, they are loaded into a Ioffe-Pritchard trap [46, 86]. This trap design combines four Ioffe bars for radial confinement with harmonic confinement in the axial direction produced by a pair of Pinch coils (see Figure 3.4). The axial bias field, provided by another pair of coils (Offset Coils) prevents losses, which

[2] MBR-110 pumped by a Verdi V18 both from Coherent.
[3] DL pro from Toptica Photonics

Property	Symbol	Value
Atomic mass of ^{40}K	m	39.96399848(21) u
Saturation Intensity	I_{sat}^{0}	17.5 W/m^2
Frequency	ν_{D2}	391.016296050(88) THz
Lifetime	τ	26.37(5) ns
Natural line width	$\Gamma/2\pi$	6.035(11) MHz
Resonant absorption cross section	σ_0	0.2807 µm^2

Table 3.1: D2-line properties of ^{40}K (extracted from Ref. [47])

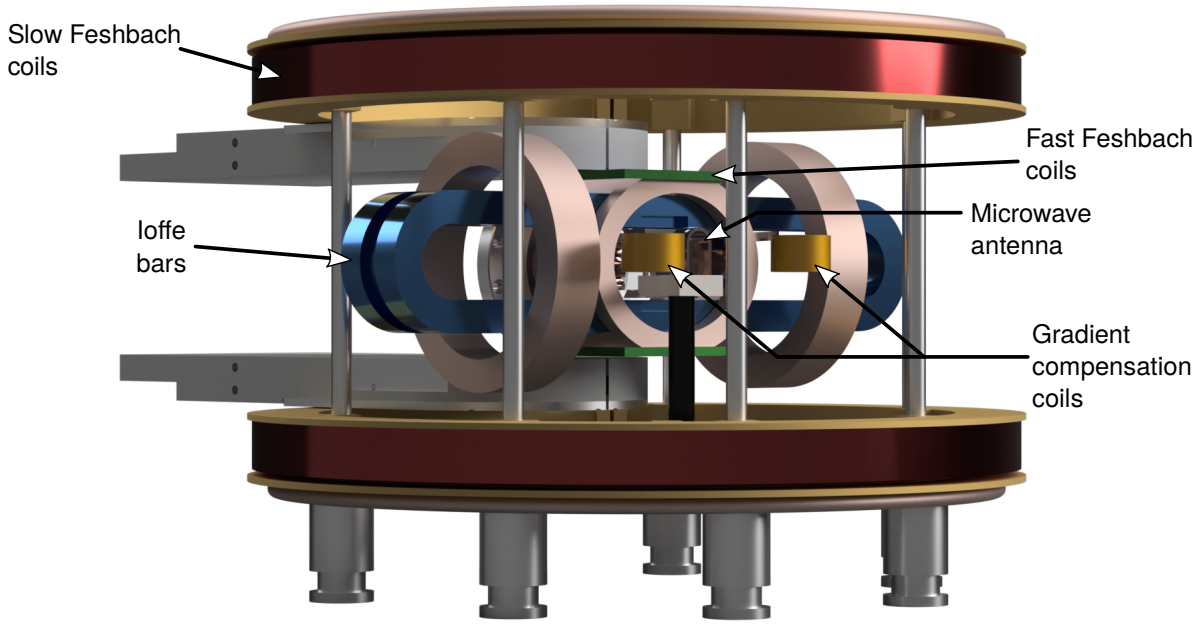

Figure 3.4: Configuration of magnetic coils around the science cell. The Ioffe-bars (blue) are used for magnetic trapping and microwave evaporation before loading the optical dipole trap. The slow (red) and fast (green) Feshbach coils are used in Helmholtz configuration to produce a magnetic bias field along the z-direction. Optionally, the fast Feshbach coils are operated in anti-Helmholtz configuration to provide a strong vertical magnetic field gradient. Residual in-plane gradients are compensated with a pair of gradient compensation coils (yellow).

occur at a magnetic field zero due to spontaneous spin flips to *high-field seeking* states. In addition, the Ioffe-Pritchard design provides good spatial overlap with the optical dipole trap used for final evaporation.

In the Ioffe-Pritchard trap, atoms can be evaporatively cooled [46] by microwave radiation. The technique exploits that atoms with higher kinetic energy explore outer regions of the trap where the magnetic field is stronger. Consequently, these atoms experience a larger Zeeman shift and, thus, can be selectively removed by addressing transitions to high-field seeking states ($g_F m_F < 0$) in the $F = 7/2$ and $F = 9/2$ manifolds. The remaining atoms thermalise to a lower temperature through elastic collisions, which redistribute kinetic energy between the atoms. At the end of the evaporation, approximately 13×10^6 atoms remain in the trap at a typical temperature around 2.5 µK. However, the gas still has to be cooled by another two orders of magnitude in order to reach quantum degeneracy. To this end the atoms are transferred to an optical dipole trap for further evaporative cooling.

3.4 A degenerate Fermi gas in an optical dipole trap

In Chapter 2.3.1, we have discussed how optical fields may be used to trap neutral atoms. In our experiment, the optical dipole trap is formed by two far-off-resonant laser beams at a wavelength of $\lambda_{\mathrm{DT}} = 1\,070\,\mathrm{nm}$[4]. The horizontal dipole trap (DTh) beam propagates along the x-direction and provides very tight confinement in the vertical direction (waist $w_z = 12.5\,\mu\mathrm{m}$) and weaker confinement along the y-axis (waist $w_y = 143\,\mu\mathrm{m}$). For confinement along the x-direction we use a second beam (dimple beam) with waists $w_x = 148\,\mu\mathrm{m}$ and $w_y = 238\,\mu\mathrm{m}$, which propagates in the yz-plane forming an angle of 45° with the xy-plane.

Preparation of a balanced spin mixture

In contrast to magnetic trapping, optical trapping is not restricted to low-field seeking states. Therefore, we may choose a pair of hyperfine states for which a convenient Feshbach resonance is available. For the experiments presented later on, we use a Feshbach resonance between the two energetically lowest sublevels $|m_F = -9/2\rangle$ and $|m_F = -7/2\rangle$ at a field of 202.13(1) G to set the two-particle interaction strength during the experiment (compare Section 2.2). To prepare the desired spin mixture, we perform an adiabatic sweep to transfer atoms to the energetically lowest hyperfine state. To this end, a homogeneous magnetic field is ramped to 60 G in order to provide a Zeeman splitting between magnetic sub levels (see Figure 2.3(a)). Afterwards, a series of three incomplete Landau-Zener sweeps is applied to create a balanced mixture of the two lowest hyperfine states. Each pulse consists of a linear frequency sweep and a square RF pulse with smooth edges to approximate the Landau-Zener limit with the transfer efficiency $p = 1 - e^{-\pi^2\Omega^2/\dot{\Delta}}$. After each of the pulses, we hold the atoms in the presence of residual gradients to allow for dephasing. We experimentally determined an optimal dephasing time of 50 ms. Thereby, each of the pulses is applied to an incoherent mixture of the two lowest spin states and the overall transfer probability may be described using the Landau-Zener formula according to Table 3.2. The advantage of using three consecutive sweeps is that the transfer is affected less by drifts of the offset field or noise, since there is a plateau of unit transfer efficiency over an approximately $0.3\,\mathrm{MHz\,ms^{-1}}$ wide window of sweep rates (see Figure 3.6(a)). As shown in Figure 3.6(b), we calibrate the transfer by measuring the ratio N_7/N_9 of atoms in the initial ($|-9/2\rangle$) and final ($|-7/2\rangle$) state versus the sweep rate $\dot{\Delta}$. In order to change the sweep rate we vary the width Δ while the duration of the linear frequency sweep is fixed to $\tau_{\mathrm{spinmix}} = 1$ ms. From a cubic fit to the data we extract an optimal sweep width of $\Delta = 1.02(6)\,\mathrm{MHz}$. The

[4] Both dipole trap beams are provided by an IPG YLM-20-LP-SC fibre laser with a short coherence length to prevent interference with possible back reflections.

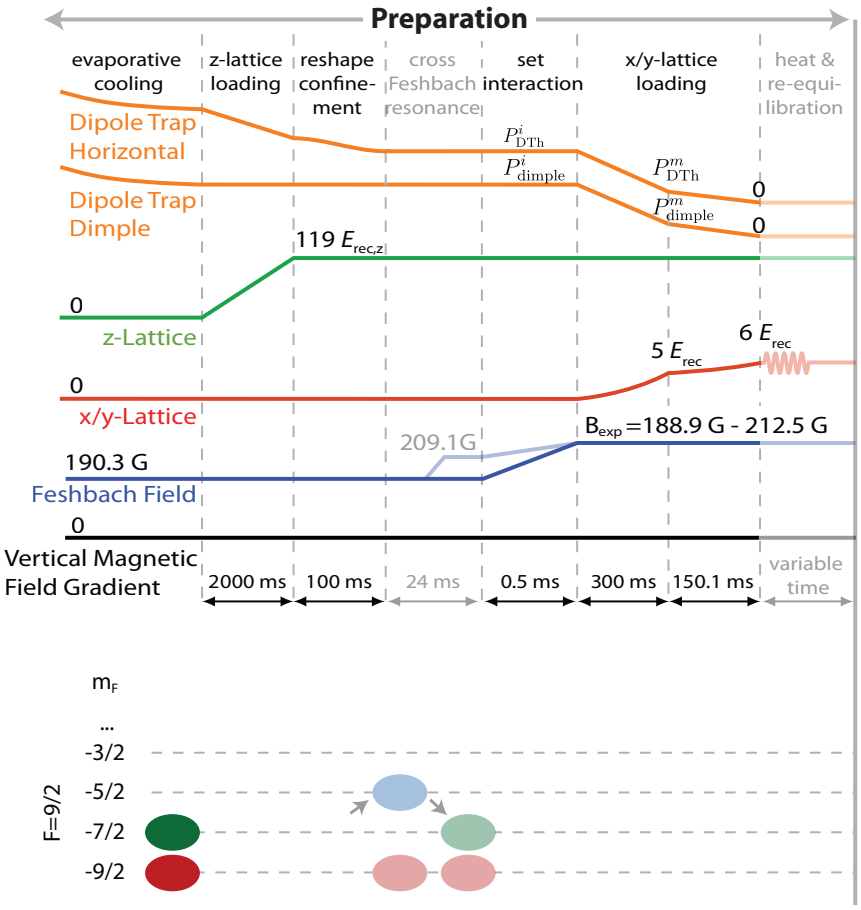

Figure 3.5: Preparation part of the experimental sequence starting after evaporation in the magnetic trap. In (a) solid lines indicate the power in the lattice beams (orange, green and red) and the magnitude of the Feshbach field (blue), respectively. To reach quantum degeneracy, a balanced mixture of the energetically lowest magnetic sub levels (lower panel) of ^{40}K is cooled to quantum degeneracy in a crossed dipole trap. Then, the gas is confined to two-dimensional planes by increasing the power in the blue detuned z-lattice. Thereafter, the scattering length is set using a Feshbach resonance at 202.13(1) G. In order to realise weakly or non-interacting systems, the resonance has to be crossed and an intermediate spin transfer is applied to avoid losses due to collisions (shown half transparent). The final step of the preparation is to ramp up the horizontal lattices. To avoid heating due to density redistribution within the trap, the power in both dipole trap beams is decreased in order to compensate the change in the trap frequencies. The lattice ramp is followed by an equilibration time. During this time step it is possible to increase the temperature by controlled heating via lattice modulation.

Number of sweeps	1	2	3
$P_{-7/2}$	p	$2p(1-p)$	$p((1-p)^2+p^2)+2p(1-p)^2$
$P_{-9/2}$	$1-p$	$(1-p)^2+p^2$	$(1-p)((1-p)^2+p^2)+2p^2(1-p)$

Table 3.2: Expected probability to find the atoms in the final (initial) state $|m_F=-9/2\rangle$ ($|m_F=-9/2\rangle$) after one, two and three consecutive Landau-Zener sweeps with identical parameters have been applied.

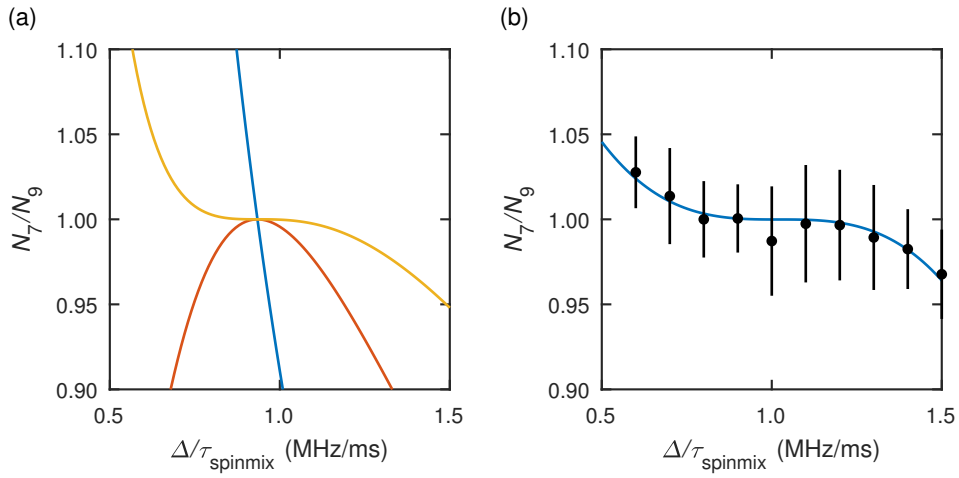

Figure 3.6: Spin-mixture calibration. (a) Expected ratio of atoms in spin-up ($|-7/2\rangle$) and spin down ($|-9/2\rangle$) states after a single Landau Zener sweep (blue) or two (orange) and three consecutive sweeps (blue). (b) Spin mixture calibration applying a series of three incomplete Landau-Zener sweeps starting from a spin polarised cloud in $|-9/2\rangle$. We measure the ratio of atoms in the two lowest hyperfine state as a function of the sweep rate for a fixed duration of each pulse of $\tau_{\text{spinmix}} = 1$ ms. A cubic fit (blue line) to the data yields an optimal sweep width of $\Delta = 1.02(6)$ MHz and an atom number ratio $N_7/N_9 = 1.00(3)$. The error bars show the standard error of three consecutive measurements.

final ratio of atoms in both hyperfine states is $N_7/N_9 = 1.00(3)$. After the balanced mixture is prepared, we wait for another dephasing time such that thermalisation via collisions among the atoms become possible again.

Evaporation in the dipole trap

For evaporation in the optical dipole trap, we set the Feshbach field to 190.3 G resulting in a scattering length of $a_s = 277(12)\,a_0$ (cf. Figure 2.5). The crossed dipole trap configuration allows us to utilise the so-called *dimple trick* [93]. By this procedure, the phase space density is increased in the centre of the trap, while hotter atoms in the outer regions of the cloud are evaporated out by lowering the power in the horizontal beam. To evaporate atoms from the trap, we lower the power of both dipole trap beams (cf. Figure 3.5) and achieve quantum degeneracy with $N \approx 173 \times 10^3$ atoms per spin state at a typical temperature of $T/T_F \approx 0.1$, which is determined from a fit to the momentum distribution after time-of-flight [17].

3.5 Optical lattices

The main experimental tool for the quantum simulation of the Hubbard model with cold atoms are optical lattices [94]. In our setup, we use an anisotropic 3D lattice configuration with a deep blue detuned lattice in the vertical (z) direction and two weaker red detuned optical lattice in the horizontal (x and y) directions. In the following, we briefly outline the optical lattice setup, the calibration of the lattice depths and the external confinement arising from the inhomogeneous intensity distribution of the beams forming the lattices.

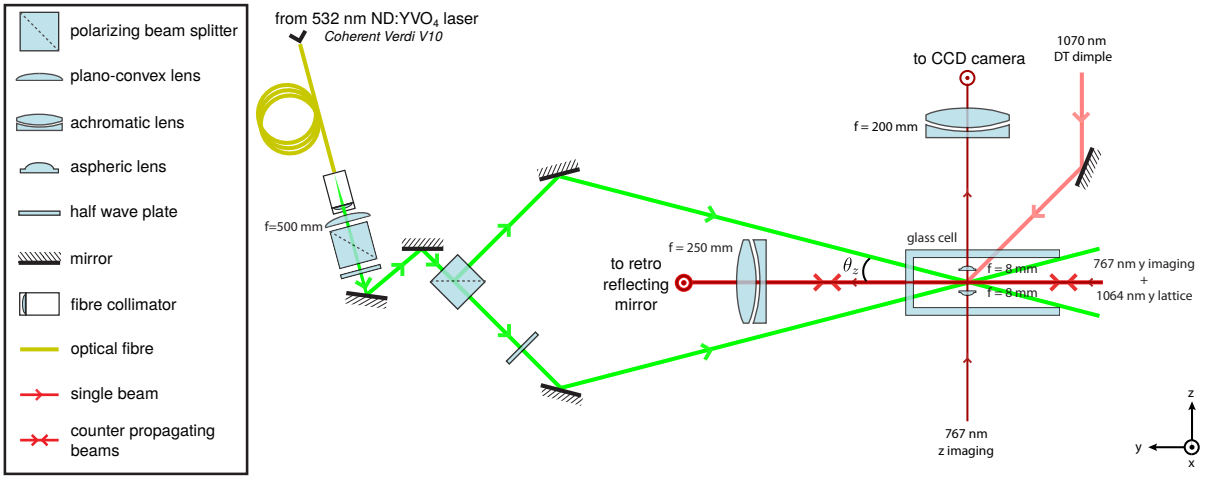

Figure 3.7: Schematic drawing of the vertical lattice setup (figure adopted from [95]).

3.5.1 Vertical lattice

Our goal is to recreate the 2D Hubbard model. To this end, we ramp up the power in a blue detuned vertical lattice. At the final lattice depth of 119 E_r, the gas is trapped in quasi two-dimensional horizontal planes with trapping frequencies $(\omega_x, \omega_y, \omega_z) \approx 2\pi \times (21\,\text{Hz}, 34\,\text{Hz}, 24.34\,\text{kHz})$. Since the nearest neighbour tunnelling rate in the vertical lattice is reduced to $t_z/h = 4 \times 10^{-4}$ Hz, any dynamics is restricted to occur within the individual planes on experimentally relevant timescales. A schematic drawing of the vertical lattice setup is presented in Figure 3.7. The blue-detuned light is provided by a frequency doubled Nd:YVO_4 laser[5] running at a wavelength of $\lambda_z = 532.2\,\text{nm}$. After the output of a single mode fibre, the polarisation is cleaned by a polarising beam splitter (PBS) and adjusted with a half wave plate such that its power is split to equal amounts into a lower and an upper path by a second PBS. Both beams are brought to a focus at the position of the atoms, where they intersect under an angle of $2 \times \theta_z = 2 \times 14.48°$ and form a lattice in the vertical direction. Together with the laser wavelength λ_z, the angle of intersection defines the lattice spacing $a_z = \lambda_z/2 \sin(\theta_z) = 1.06\,\mu\text{m}$. The running wave component (cf. 2.3.2) of the potential is controlled by a second half wave plate, which is used to adjust the polarisation of the transmitted light relative to the polarisation of the reflected upper beam. Usually, we set $\gamma_z = 1.00(5)$ such that the running wave component vanishes (cf. Equation 2.32).

Loading the vertical lattice

At the end of evaporation in the crossed dipole trap, the Fermi energy $E_F = h \times 6.9\,\text{kHz}$ is larger than the recoil energy of the vertical lattice $E_{r,z} = h \times 1.1\,\text{kHz}$. Therefore, multiple bands become populated as the power in the vertical lattice is increased, which leads to heating. However, one advantage of the blue-detuned vertical lattice is that it counteracts the confinement of the red-detuned dipole trap. For this reason, loading the lattice effectively reduces the trap depth and results in an additional step of evaporation [85]. To optimise the lattice loading, we vary the duration t_{load} of the linear ramp and determine the temperature in the lattice from a fit to a numerical simulation of the Fermi-Hubbard model (cf. Chapter 6). We find that an optimal duration of $t_{load} = 2\,\text{s}$ results in a typical temperature of $k_B T/t \approx 0.6$.

[5] *Coherent Verdi V10*

Optimising lattice loading reproducibility

The relative position between the horizontal dipole trap (DTh) and the vertical lattice determines the distribution of atoms within the vertical planes. Due to the ellipticity of the DTh, only approximately 11 sites of the vertical lattice are populated (cf. Chapter 4 and 8). However, a good relative stability of the z-lattice with respect to the DTh is crucial in order to reproduce the population in each experimental run. While, on a time scale of days, the z-lattice showed only little variation in position, the DTh was often found to drift by several micrometers over a period of a few hours. Therefore, we choose to actively stabilise the beam position of the DTh. Since the drift is rather slow, we use a CCD camera[6] to observe the beam after the glass cell and determine the position in the vertical direction by a Gaussian fit to the recorded intensity distribution. The result is used to generate an error signal which is fed back to a piezo mirror[7]. With this regulation, we typically achieve a standard deviation $\Delta z_{\mathrm{DTh}} \leq 0.67(1)\,\mu\mathrm{m}$ over more than three days, which provides a stable overlap between the z-lattice and the DTh over the time required to take a full dataset.

3.5.2 Horizontal lattices

The final step in the preparation scheme is the formation of a 2D optical lattice in the xy-plane. To this end we ramp up the power in two red-detuned beams crossing under an angle of 85.67° each forming a 1D lattice in a retro-reflected lin-lin configuration (Figure 3.8). A frequency difference between the two horizontal lattices ensures that any remaining cross interference is averaged out. To this end, we shift the frequency of the y-lattice (x-lattice) by 220 MHz (380 MHz) using acousto optical modulators (AOMs). At the same time, the AOMs are used to stabilise the intensity of the corresponding lattice beam. Both beams are derived from a 18 W Mephisto MOPA from *Innolight* running at a wavelength of $\lambda_{x,y} = 1\,064.5\,\mathrm{nm}$. This yields a lattice spacing of $a_{x,y} = \lambda_{x,y}/2 = 532.25\,\mathrm{nm}$. Due to transmission and reflection losses of the reflected beam, we measure a power imbalance of $\gamma_x = 0.84(4)$ ($\gamma_y = 0.77(4)$) for the $x(y)$-lattice. Therefore, both lattices induce an additional external confinement as outlined above (cf. Chapter 2.3.2). The calibration of this external confinement is presented below 3.5.4. Before the ramp, we match the trap frequency of the crossed optical dipole trap to the external confinement produced by the lattices alone in order to minimise the density redistribution during the ramp. Then, we reduce the power in the dipole trap beams to zero while the power in the horizontal lattice beams is increased to the final value. The duration of the ramp to the final experimental lattice depth was optimised to provide a low temperature equilibrium distribution at the final lattice depth [96].

In Chapters 6, 7 and 8, we present experimental data as a function of temperature. Two methods have been applied to heat the atomic cloud in a controlled way. The first approach involves the introduction of a variable hold time at the final lattice depth. In this case, heating occurs from off-resonant photon scattering (cf. Section 2.3.1) as well as intensity fluctuations of the lattice beams. The corresponding increase in temperature is shown in in Figure 3.9(a). The heating rate observed with this method is only as large as $93(3)\,\mathrm{Hz\,s^{-1}}$. Therefore, we choose to actively modulate the lattice. The amplitude of the modulation is 10% of the actual lattice depth at approximately twice the external trapping frequency $\omega_{\mathrm{mod}} = 2\pi \times 50\,\mathrm{Hz}$, which is far detuned both from inter-band transitions and the on-site interaction U at the experimental lattice depth. As shown in Figure 3.9(b), this method allows to access a larger range of temperatures. After the modulation, we hold the atoms in the trap for $t_{\mathrm{hold}} = 400\,\mathrm{ms}$. The long hold time ensures that possible density redistributions have settled before the measurement is carried out.

[6] Basler acA1300-30gm

[7] Using a Thorlabs MDT693B 3-channel open-loop piezo controller.

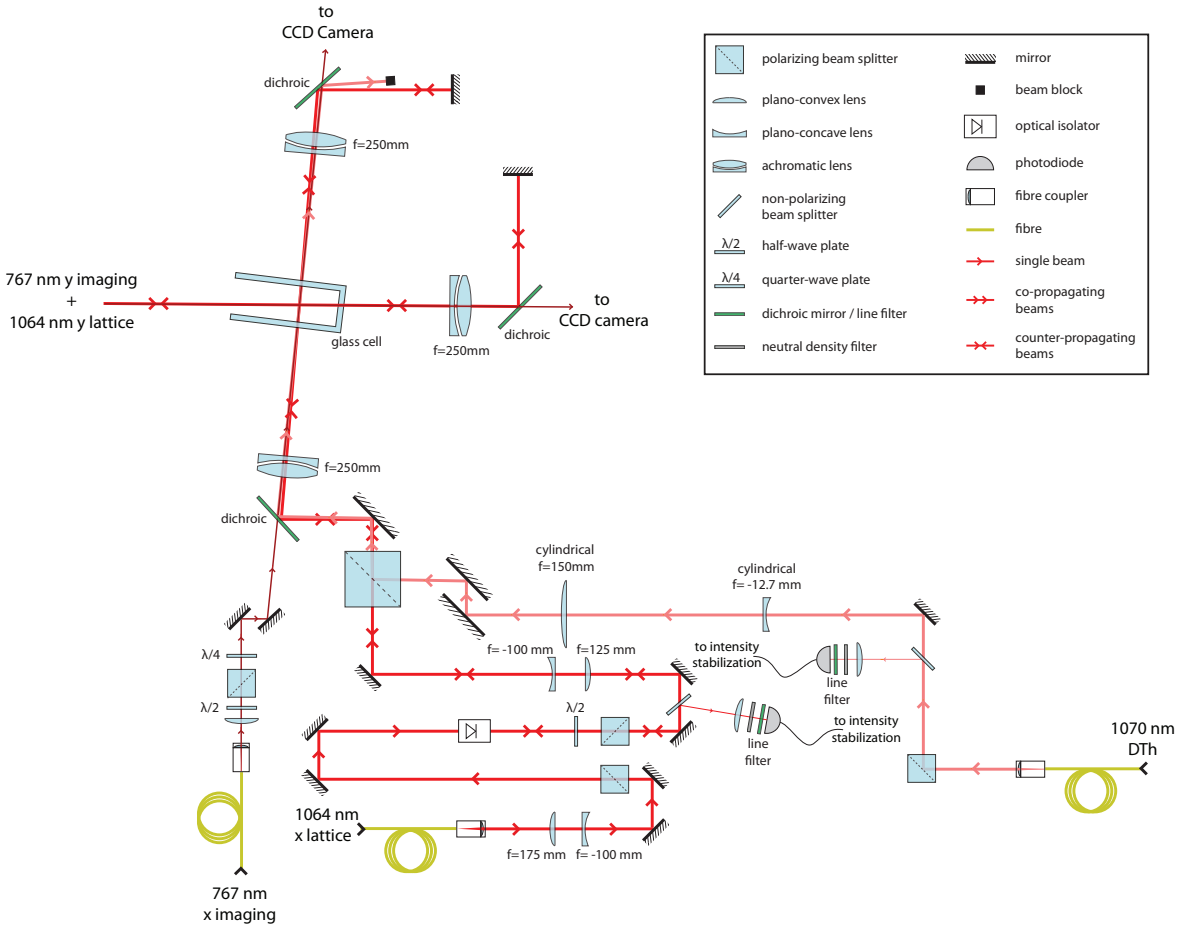

Figure 3.8: Setup of the horizontal lattice and dipole trap (figure adopted from [95])

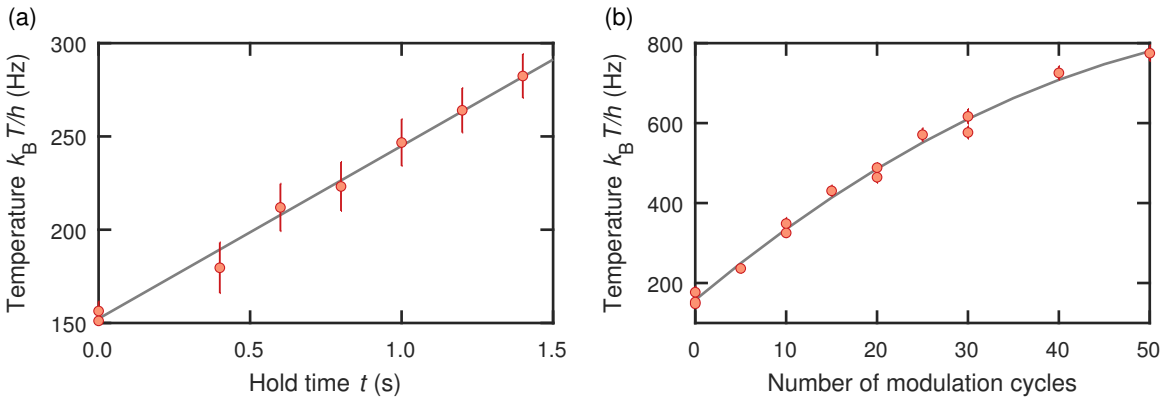

Figure 3.9: Two different methods of heating in the lattice. (a) Heating by holding in the lattice. A linear fit to the data yields a heating rate of 93(3) Hz s^{-1} (grey). (b) Higher temperatures can be achieved when the lattice depth is modulated at twice the external trapping frequency $\omega_{\mathrm{mod}} = 2\pi \times 50$ Hz with a modulation amplitude of 10 % (line is a guide to the eye). Both in (a) and (b) $U/t = 8.2$.

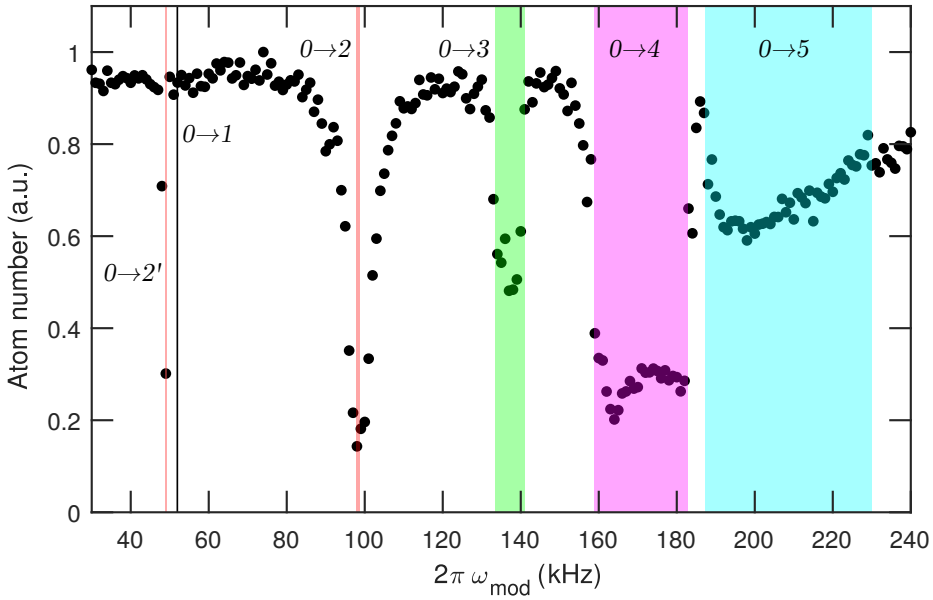

Figure 3.10: Parametric heating signal of the y-lattice. Several transitions from the lowest to excited bands are observed as a function of the modulation frequency ω_{mod} For the example chosen, the comparison to a band structure calculation (cf. Chapter 2.3.3) yields a lattice depth of $V_0 = 41.5\,E_{\mathrm{r}}$. The widths of the shaded regions indicate the expected widths of the resonances, assuming a homogeneous lattice.

3.5.3 Lattice depth calibration

The depth of each optical lattice is routinely calibrated by driving inter-band transitions [97] using parametric heating. To this end, we employ a sinusoidal modulation of the lattice depth

$$V_\nu(t) = V_\nu + \delta V_\nu \sin\left(\omega_{\mathrm{mod}} t\right) \tag{3.2}$$

to excite transitions from the ground band (cf. Figure 2.6) to higher bands. We choose an amplitude $\delta V_\nu / V_\nu = 0.1\%$ and apply the modulation for $t_{\mathrm{mod}} = 100\,\mathrm{ms}$. Atoms are excited from an initially populated band n, which is usually the lowest band, to a higher band n' when the resonance condition

$$\hbar\omega_{\mathrm{mod}} = E_{n'}(q) - E_n(q). \tag{3.3}$$

is met. Here, $E_n(q)$ denotes the energy of the nth band at quasi-momentum q. After modulating the lattice, we perform adiabatic band mapping to observe the depletion of the lowest band. To this end, we lower the lattice depth during $t_{\mathrm{bm}} = 1\,\mathrm{ms}$ to map the quasi-momentum distribution of the trapped gas to real momenta in free space [98, 99]. The band mapping is followed by a time-of-flight of $t_{\mathrm{tof}} = 4\,\mathrm{ms}$ to map momentum to position. Figure 3.10 shows a loss spectrum as a function of the modulation frequency ω_{mod} for a lattice depth of $41.5\,E_{\mathrm{r}}$. The spectrum is obtained by integrating the momentum resolved data over the first Brillouin zone. Thereby, we observe several resonances where a depletion of the lowest band occurs, indicating excitations to higher bands. The lattice depth is then obtained from a comparison of the measured spectrum to the result of a band structure calculation (cf. Chapter 2.3.3). As one would expect from the conservation of parity, the transition from the lowest band to the first excited band $0 \rightarrow 1$ is not present in the spectrum, since the corresponding wave functions have opposite parity. The most

prominent spectral feature is resonance of the $0 \longrightarrow 2$ transition (marked in red). We also observe the first sub-harmonic of this resonance (marked in light red). Note that, although naively forbidden due to parity conservation, the transitions $0 \longrightarrow 3$ as well as $0 \longrightarrow 5$ are observed experimentally. This is due to the deviation of the wave functions in higher bands from the harmonic oscillator approximation leading to a finite overlap of the wave functions and, thus, a non-zero transition matrix element for not too large lattice depths. The lattice depth calibration is a standard procedure in the alignment of the experimental apparatus and thus repeated before any experimental data is collected. The calibration of the horizontal lattices is carried out in the full three-dimensional optical potential at a fixed set beam power with a scan over a smaller range of frequencies than shown in Figure 3.10. We identify the modulation frequency of the E_{02} resonance and compare it to a band structure calculation to find the conversion from beam power to lattice depth.

3.5.4 Calibration of the external trapping potential

The Gaussian shape of the optical lattice beams leads to an inhomogeneous external trapping potential. The interpretation of the measured density distribution in the framework of the local density approximation requires an accurate calibration of this potential. At the experimental stage of the sequence, the atoms are trapped by the optical lattices in the horizontal and vertical directions alone. Therefore, only these contribute to the external confinement. Furthermore, we specifically study the 2D Hubbard model, i.e. we are interested in the physics of a single plane in the vertical direction. Therefore, we set $z = 0$ and take the contribution of each lattice $V_{\mathrm{xlat}}(x, y)$, $V_{\mathrm{ylat}}(x, y)$ and $V_{\mathrm{zlat}}(x, y)$ to the in-plane potential into account:

$$V_{\mathrm{xlat}}(x,y) = -E_{\mathrm{r}}\left[\frac{(1+\sqrt{\gamma_x})^2}{4\sqrt{\gamma_x}}|s_x|e^{-2\left(\frac{x\sin(\theta_x)+y\cos(\theta_x)}{w_x}\right)^2} - \sqrt{|s_x|}e^{-\left(\frac{x\sin(\theta_x)+y\cos(\theta_x)}{w_x}\right)^2}\right], \tag{3.4}$$

$$V_{\mathrm{ylat}}(x,y) = -E_{\mathrm{r}}\left[\frac{(1+\sqrt{\gamma_y})^2}{4\sqrt{\gamma_y}}|s_y|e^{-2\left(\frac{x\cos(\theta_y)-y\sin(\theta_y)}{w_y}\right)^2} - \sqrt{|s_y|}e^{-\left(\frac{x\cos(\theta_y)-y\sin(\theta_y)}{w_y}\right)^2}\right], \tag{3.5}$$

$$V_{\mathrm{zlat}}(x,y) = E_{\mathrm{r},z}\sqrt{|s_z|}e^{-\frac{x^2+y^2\sin^2(\theta_z)}{w_z^2}}, \tag{3.6}$$

where γ_ν describes the power imbalance of the beams forming a lattice in the ν-direction. In Equation 3.6 we have used $\gamma_z \approx 1$. In addition, the exact arrangement of the beams has to be known. The angle between both beams forming the vertical lattice $\theta_z = 14.45°$ is defined by the setup. The angles formed by the horizontal x(y)-lattice beams with the $x(y)$-direction of the high resolution image frame $\theta_x = -4.85(4)\,°$ ($\theta_y = -0.42(6)\,°$), respectively, from a measurement of noise correlations in a time-of-flight experiment revealing the reciprocal lattice vectors [100] (cf. Chapter 5.6.1). Direct images of the beams yield beam waists of $w_x = 175(10)\,\mu\mathrm{m}$, $w_y = 165(10)\,\mu\mathrm{m}$ and $w_z = 140\,\mu\mathrm{m}$. However, in order to account for small misalignments of the lattice beams, we characterise the potential prior to each experiment with trap frequency measurements. To this end, we excite dipole oscillations in an array of one dimensional tubes perpendicular to x(y)-lattice beam to obtain ω_y (ω_x). The tubes are created by blocking the retro reflecting mirror in the direction to be probed. At the same time, we increase the power in the blocked beam to compensate for the fourfold increase in the depth of the lattice potential, which would arise from the constructive interference of the (non-blocked) lattice beam. To induce oscillations, we load the lattice in the presence of a magnetic in-plane gradient which displaces the cloud from the centre of the trap. The gradient is created by a pair of coils, whose main purpose is the compensation of in-plane gradients

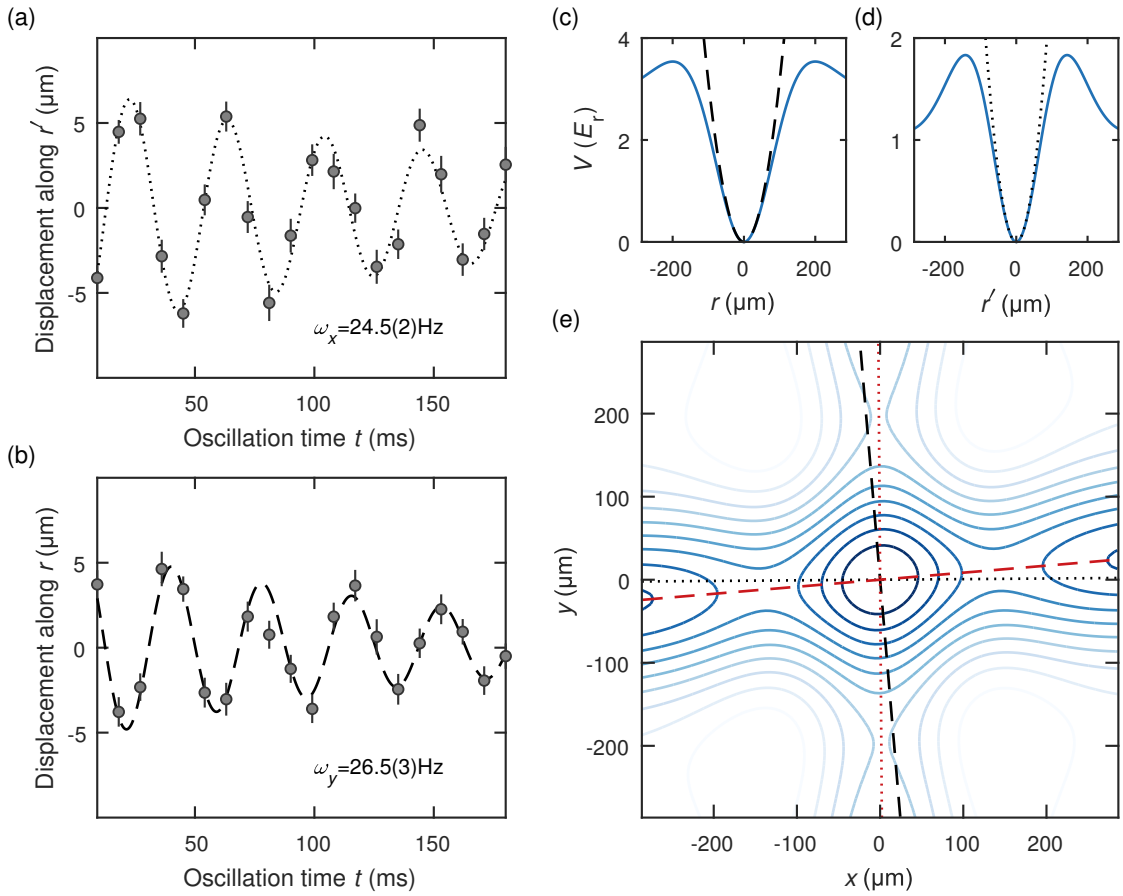

Figure 3.11: Calibration of the external confinement. (a,b) Typical results of a trap frequency measurement at a horizontal lattice depth of $6\,E_\mathrm{r}$. To determine the trap frequencies, we induce dipole oscillations perpendicular to the y-lattice (a) and x-lattice (b). Then, we record a time series of in-situ images of the moving cloud and determine the centre-of-mass displacement as a function of the oscillation time t. A damped sinusoidal fit to the data yields the trap frequencies $\omega_x = 2\pi \times 24.5(2)\,\mathrm{Hz}$ and $\omega_y = 2\pi \times 26.5(3)\,\mathrm{Hz}$. (c,d) In a numerical optimisation we compare the measured trap frequency to harmonic fits (dashed and dotted lines) of the calculated in-plane potential (solid line) to find the effective beam waist. For the example shown, we obtain $w_x = 172\,\mu\mathrm{m}$ (c) and $w_y = 154\,\mu\mathrm{m}$ (d). (e) shows a map of the in-plane potential with equipotential lines. The direction of the x-lattice (y-lattice) is indicated by the red dashed (dotted) line and the black dashed and dotted lines show the corresponding perpendicular directions along which the dipole oscillations are excited for the measurement shown in (b) and (a), respectively.

during the experiment. However, we can also use the same coils to induce a force on the atomic cloud. By finely tuning the relative currents in the coils, both amplitude and direction of the displacement may be adjusted. Consecutively, the gradient is rapidly switched off to excite oscillations along the tubes. To observe the dipole mode, we repeat the measurement several times and vary the time after the excitation before an in-situ image of the cloud is recorded and fitted to a two-dimensional Gaussian distribution to determine the centre-of-mass position (see Figure 3.11 for an exemplary measurement). Finally, the observed centre-of-mass oscillation is fitted to a damped sinusoidal to extract the trap frequency (solid lines). The data shown in Figure 3.11(a) and (b) correspond to a typical experimental lattice depth of $6\,E_\mathrm{r}$ and yield trap frequencies of $\omega_x = 2\pi \times 24.5(2)\,\mathrm{Hz}$ and $\omega_y = 2\pi \times 26.5(3)\,\mathrm{Hz}$, respectively. The measured trap frequency serve as an input for an optimisation routine using the waists of the horizontal

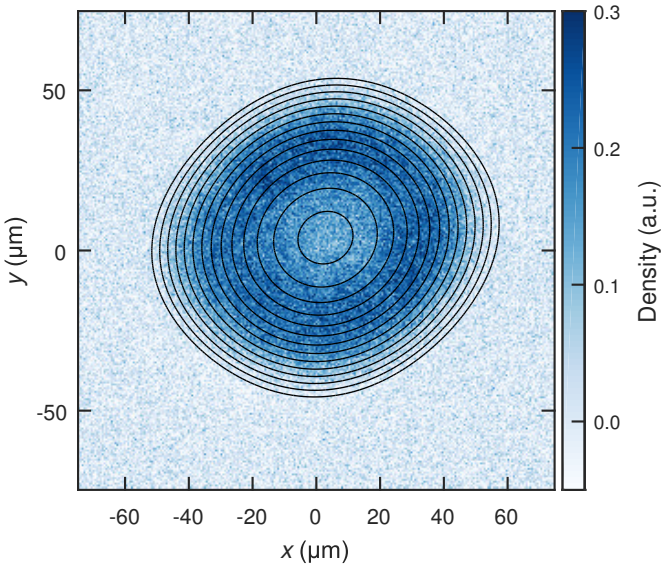

Figure 3.12: Spatial distribution of singly occupied sites (colour coded) together with equipotential lines of the external potential (cf. Figure 3.11) (solid black lines) averaged over 66 experimental realisations. The contour lines are spaced by $h \times 224\,\mathrm{Hz}$ and extend to $h \times 3\,000\,\mathrm{Hz}$ at the edge of the cloud. The reduced density in the centre of the image is due to the formation of doubly occupied sites.

lattices as free parameters to model the combined potential $V(x, y) = V_{\mathrm{xlat}}(x, y) + V_{\mathrm{ylat}}(x, y) + V_{\mathrm{zlat}}(x, y)$. For the exemplary measurement shown in Figure 3.11 the optimisation yields waists of $w_x = 172\,\mu\mathrm{m}$ and $w_y = 154\,\mu\mathrm{m}$, which are in good agreement with the directly imaged beams. Figure 3.12 shows the external confinement in the horizontal plane together with a corresponding measurement of the in-situ density distribution of singly occupied sites averaged over 66 individual experimental realisations. Since we average the spatially resolved density distribution along equipotential lines to obtain the equation of state and, by comparison to numerical data, the temperature of the prepared many-body state, the precise knowledge of the external potential is a crucial input to our data analysis. Therefore, we perform trap frequency measurements before taking data in order to provide an accurate mapping between space and external potential. Furthermore, a deviation from the expected trap frequencies signals a misalignment of the lattice beams.

3.6 Feshbach fields

While magnetic fields are indispensable for magnetic trapping of neutral atoms as described above, they also provide the means to control the interaction between atoms by tuning the scattering length as outlined above (cf. Section 2.2). To this end, large bias fields are required to adjust the field in the vicinity of a magnetic Feshbach resonance. At the same time, our aim is to perform high resolution RF spectroscopy. This requires both a low level of noise on the magnetic fields as well as excellent control over magnetic gradients. Figure 3.4 shows the arrangement of coils in our experiment. A large homogeneous offset field is produced by the combined fields of two pairs of coils in Helmholtz (HH) configuration. The major contribution is provided by the *slow Feshbach coils* (slow FB; shown in red) and a smaller field is added by the *fast Feshbach coils* (fast FB; shown in green). Operating the latter in anti-Helmholtz (AHH) configuration instead, leads to a large gradient perpendicular to the horizontal planes. This gradient induces a spatially varying Zeeman shift, which we employ to resolve the vertical lattice sites with a

high resolution spectroscopy technique. Furthermore, precise control over stray magnetic gradients is facilitated by two additional gradient compensation coils (shown in yellow), which were implemented during this thesis. In the following, we will address the individual components and outline the strategy employed to achieve low-noise magnetic field control as well as a method to compensate in-plane gradients at the place of the atoms during the experiment.

3.6.1 Slow Feshbach field

A homogeneous offset field is required to define a quantisation axis parallel to the axis of the high resolution imaging system and to control the two-particle interaction by tuning the magnetic field in the vicinity of a Feshbach resonance. The main contribution to this field is provided by the slow FB coils exhibiting a large inductance $L_{\mathrm{slow}} = 5.2\,\mathrm{mH}$. Direct water cooling of the coils ensures stable operation at a temperature of $T_{\mathrm{slow}} = 18(1)\,^{\circ}\mathrm{C}$. Due to the large magnetic field produced by the slow Feshbach coils, noise on their driving current contributes most to magnetic field noise and has to be suppressed to a level of $\frac{|B|}{B} \leq 10^{-5}$ especially during the field sensitive high resolution spectroscopy. To achieve this, a modified version of the proportional-integral-derivative controller (PID) described in [57] is used.

Slow feedback – PID

The current for the slow Feshbach field is provided by a voltage controlled power supply[8]. To begin with, the 16 bit digital output is divided by 5 and low pass filtered to reduce the error due to the least significant bit. This signal is then added to a voltage reference. The voltage reference is switch between 0 V for low magnetic fields ($B_{\mathrm{ref}} = 0\,\mathrm{G}$) and a stable 5 V source to generate high magnetic fields ($B_{\mathrm{ref}} = 177.1\,\mathrm{mG}$). To generate an error signal, the output current of the power supply is measured with a current transducer[9]. The error signal is processed by a PID to regulate the power supply. This suppresses the magnetic field noise to a level of $\Delta B_{\mathrm{p-p}} \approx 10\,\mathrm{mG}$.

Automatic battery switcher

For stable operation, the PID itself has to be powered by a noise free power supply. Therefore, we use lead-acid batteries as a stable voltage source for the PID electronics as well as the reference voltage. To compensate for the voltage drop as the batteries are drained, we use two pairs of batteries and employ an automatic battery switcher which is based on an Arduino microcontroller. While one of the pairs is in use, the other one is charged until the voltage of the used pack drops below a threshold value. After this event, the role of the packs is exchanged. A rather high threshold value ensures that the change in voltage after the exchange of the battery packs does not lead to a loss of the spectroscopy signal in tomography due to the resulting change in the magnetic field value. This strategy is used for both the slow and fast Feshbach field PID electronics.

3.6.2 Fast Feshbach field

Often, relatively quick changes in the magnetic field are required, for example in order to cross the Feshbach resonance at 202.13 G (cf. Figure 2.5) to investigate non-interacting or weakly interacting systems. These fast ramps are enabled by the a second pair of coils (fast Feshbach coils) with an inductance of $L_{\mathrm{fast}} = 75\,\mu\mathrm{H}$. In Helmholtz configuration the fast FB add a homogeneous field to the Slow

[8] Delta Elektronica SM-60-100

[9] Danfysik Ultrastab Saturn STH-600

FB field. Furthermore, they can be switched to anti-Helmholtz configuration using a double-H-Bridge circuit in order to produce a strong B-field gradient $\partial B_z/\partial z = 33.3(5)\,\mathrm{G/cm}$ in the vertical direction. This allows to selectively address different planes in the vertical direction by means of RF spectroscopy. In this configuration typically $B_{\mathrm{sFB}} = 212.5\,\mathrm{G}$ and, since the zero of the magnetic quadrupole field does not coincide with the position of the atoms, they experience an additional field of $B_{\mathrm{fFB}} = 1.25\,\mathrm{G}$. Around the total offset field of $B = 213.75\,\mathrm{G}$ (cf. Figure 2.5) the derivative of the $|-3/2\rangle \rightarrow |-5/2\rangle$ transition frequency with respect to the B-field is $\partial\nu_{35}/\partial B = 180\,\mathrm{Hz/mG}$. Therefore, the applied gradient induces a frequency shift of $\Delta\nu_{a_z} = 640(10)\,\mathrm{Hz}$ for the transition of atoms trapped in neighbouring planes allowing to spectrally resolve the vertical lattice sites.

Fast feedback – active load

A comparison of the noise level achieved with the PID regulating the slow Feshbach field alone to the separation of the vertical planes in the vertical B-field gradient $\Delta B_{a_z} \approx 3.3\,\mathrm{mG}$ indicates that a further reduction of the noise level is required. Therefore, we employ an active load circuit to cancel most of the remaining noise. The active load consists of a controlled resistive load running in parallel to the coils. The working principle is as follows, the total current $I_{\mathrm{tot}} = I_{\mathrm{sFB}} + I_{\mathrm{AL}}$ provided by the power supply is diverted into the current flowing through the slow FB coils I_{sFB} and the current flowing through the active load I_{AL} circuit. When the active load is controlled in such a way that I_{AL} agrees with the modulation of I_{tot} due to the noise, this noise will be removed from I_{sFB}. To this end, the resistive load is steered using a second current transducer sensing the current through the slow FB coils. The measured signal is high pass filtered to block the dc-component before it is fed into a programmable filter stage[10] for further filtering and amplification. The amplified signal is added to a stable 5 V reference to allow for bipolar regulation. With the active load the 50 Hz noise is suppressed to a peak-to-peak level of $\Delta B_{\mathrm{p-p}} \lesssim 2\,\mathrm{mG}$. The upper left inset of Figure 3.13 shows a comparison of traces of the slow FB field during the experiment recorded with (blue) and without (green) the active load acting on the current and highlights the reduction of noise with a frequency of 50 Hz and higher harmonics thereof. The main plot in Figure 3.13 shows the average of 64 consecutively recorded field traces. The standard error of 0.8 mG reflects the high reproducibility of the prepared magnetic fields. In order to further reduce the influence of magnetic field noise on the high-resolution RF spectroscopy scheme, we chose a time-window in which the noise level is approximately flat for the duration of the pulse.

Improvement of thermal stability

In contrast to the slow FB coils, the fast FB coils are not water cooled directly. Instead, we rely on passive cooling by the water cooled Ioffe bars, to which the fast FB coil mounting structure is attached. We observed that the experimental cycle results in a periodic modulation of the cooling water temperature with a peak-to-peak amplitude of $\Delta T_{\mathrm{p-p}} = 6.6\,\mathrm{K}$. More dramatically, slow drifts of the cooling water temperature lead to a corresponding drift of the temperature at the time of RF tomography in between sequences. Due to the thermal expansion coefficient of the Ioffe bar holder, this leads to a drift of the fast FB coils' position. In anti-Helmholtz configuration, this results in a translation of the magnetic field zero and a change of the magnetic field at the position of the atoms. The relation between the tomography frequency and the cooling water temperature can be expressed by the coefficient $\partial\nu_{35}/\partial T = 1.6\,\mathrm{kHz\,K^{-1}}$ indicating the requirement of an improved thermal stability of the cooling water in order to realise single plane tomography. Therefore, we actively stabilise the cooling water temperature using a 2 kW thermostat inserted on the laboratory side of the cooling circuit, which is PID controlled by an Arduino

[10] Stanford Research System SR600

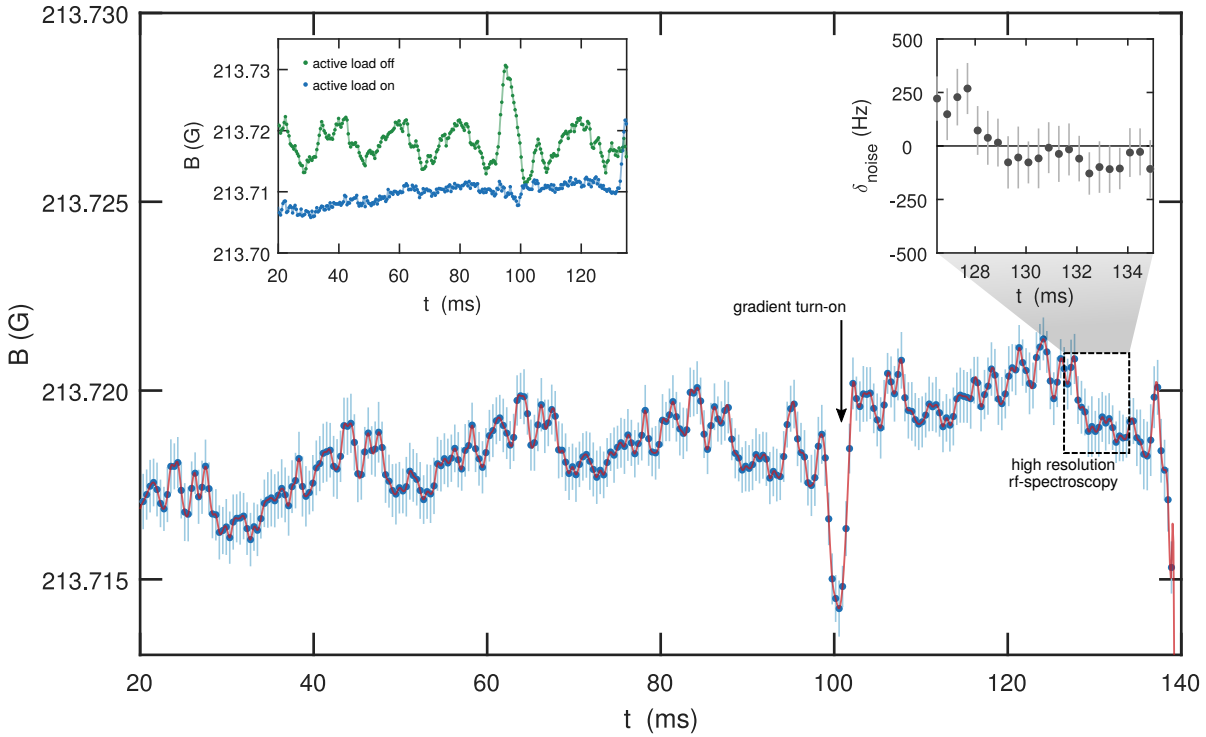

Figure 3.13: (Main) Time trace of the slow Feshbach field averaged over 64 individual realisations revealing residual modulations with a frequency 50 Hz and higher harmonics. The error bars show the standard error and reflect the high inter-sequence stability with a mean standard error 0.8(2) mG. The solid red line is an interpolation using 5th order polynomials.The dip around 100 ms is due to the turn on of the vertical B-field gradient. (Inset, upper left) Magnetic field noise with (without) the active load stabilising the current shown in blue (green). Data points are the statistical average of three measurements. Note the different y-axis scale as compared to the main graph. (Inset, upper right) Magnetic field fluctuations during the tomography pulse converted to the drift of the detuning.

microcontroller. With this approach, we achieve a thermal stability of $\Delta T_{\mathrm{p-p}} = 1\,\mathrm{K}$ within a sequence and inter-sequence variation of the temperature at the point of RF tomography of $\Delta T_{\mathrm{rms}} = 50\,\mathrm{mK}$.

3.6.3 In-plane gradient compensation

In addition to magnetic field noise, a further complication arises from the presence of stray magnetic field gradients. These can originate from metallic parts in the experimental setup, the inhomogeneity of the Feshbach fields or, during tomography, from a misalignment of the vertical magnetic field gradient. We have to compensate these gradients, since, on the one hand, they lead to a hyperfine state dependent potential and to a displacement and reduced overlap of the two spin components during the experimental part of the sequence. On the other hand, during tomography, the presence of horizontal gradients leads to a broadening of the spectroscopy signal, which easily compromises the tomography of a single plane. To minimise these gradients, two additional coils[11] where installed during this thesis (see Figure 3.4). Each of the coils produces a magnetic field $B \propto 1/r^2$, leading to an approximately linear gradient at the position of the atoms. The gradients produced are approximately orthogonal to each other (cf. Table 3.3 for the specifications of the two coils). The current of each coil is controlled individually[12] to allow for

[11] The same coils are used to excite the dipole mode for the trap frequency measurements presented in Chapter 2.

[12] Using current controlled Delta Elektronica ES-015 power supplies

Property	Coil 1	Coil 2
wire diameter d	1 mm	0.5 mm
windings N	165	672
resistance R	0.25 Ω	3.6 Ω
in-plane gradient angle α	24.4°	129.0°
in-plane gradient magnitude $\left\|\nabla B^z\right\|$	0.0495 G/cmA	0.0464 G/cmA

Table 3.3: Properties of the gradient compensation coils.

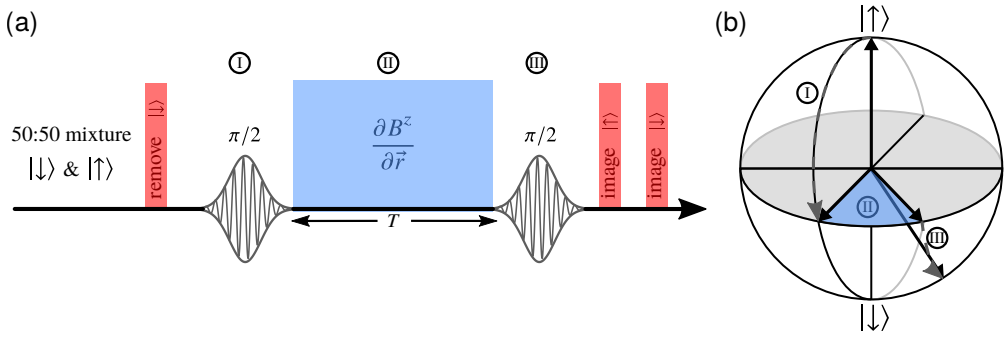

Figure 3.14: (a) Schematic Ramsey spectroscopy sequence and (b) Bloch sphere representation of the same sequence. The atoms are prepared in a quantum degenerate spin balanced Fermi gas. Thereafter, one spin component is removed to obtain a cold spin polarised gas. A first $\pi/2$-pulse creates a coherent superposition of up and down spins moving the Bloch vector to the equator of the Bloch sphere. Then, a magnetic field gradient is applied for the duration T, which leads to a precession around the z-axis. The second $\pi/2$-pulse rotates the population around the x-axis again. The final superposition is detected with two consecutive images of both spins and depends on the phase collected during the evolution time T.

precise alignment of the in-plane gradient angle in the accessible range $24.4° < \alpha < 129.0°$.

Ramsey sequence and in-plane gradient minimisation

The technique to determine the in-plane gradients present during the experiment follows the idea of Ramsey spectroscopy. To this end two $\pi/2$-pulses are placed around the time step during which we want to infer the gradient. Figure 3.14(a) presents the Ramsey spectroscopy sequence schematically. As usual, we prepare a balanced mixture of atoms in $|\uparrow\rangle = |-7/2\rangle$ and $|\downarrow\rangle = |-9/2\rangle$. We then apply a resonant pulse of imaging light to remove all atoms in $|\downarrow\rangle$ and obtain a spin polarised cloud of atoms in $|\uparrow\rangle$. Afterwards, the first $\pi/2$-pulse is applied using a Gaussian pulse with a bandwidth of 3.3 kHz. In the Bloch sphere picture (Figure 3.14), this pulse rotates the Bloch vector around the x-axis and transfers the population into a superposition $a\,|\uparrow\rangle + b\,|\downarrow\rangle$, with weights a, b. Then, during an evolution time T the Bloch vector precesses around the z-axis with the Larmor frequency $\omega = \delta\gamma B^z$ until the final pulse rotates the Bloch vector again around the x-axis. The probability to find the population in the excited state at the end of the sequence is described by [62]

$$P_{|\uparrow\rangle} = \cos^2\left(\frac{\Delta T}{2}\right) \tag{3.7}$$

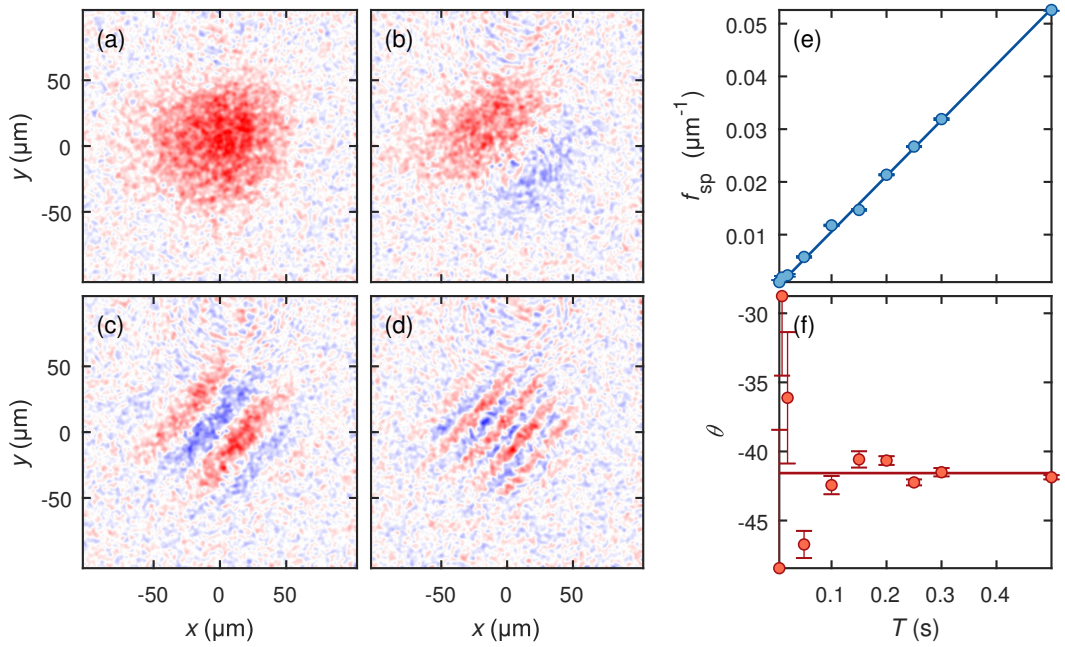

Figure 3.15: Magnetisation pattern $S^z(\mathbf{r})$ measured after free evolution times of (a) $T = 5$ ms, (b) $T = 50$ ms, (c) $T = 200$ ms and (d) $T = 500$ ms. From a sinusoidal fit to the data, we extract the spatial frequency (e) and the angle (f) of the magnetisation pattern. According to Eq. 3.9, the linear dependence (blue solid line) of the spatial frequency on the evolution time yields the magnetic field gradient $\left|\frac{\partial B^z}{\partial r}\right| = 6.5(6)$ mG/cm. Error bars show the error of the sinusoidal fit. Note that for low frequencies the determination of the angle by the fit is not reliable and we use the average of times $T > 0.1$ s to determine the angle $\theta = -41.6(7)\,^\circ$ (red solid line).

and depends only on the detuning Δ during the free phase evolution during the time T. In the presence of in-plane gradients $\frac{\partial B^z}{\partial r}$, the detuning becomes spatially dependent

$$\Delta \longrightarrow \Delta(r_i) = \delta\gamma \frac{\partial B^z}{\partial r} r_i\,, \tag{3.8}$$

which leads to different precession speeds of the Bloch vector at different lattice sites r_i. A solution of Equation 2.13 yields the differential gyromagnetic ratio $\delta\gamma = \frac{1}{\hbar}\frac{\partial(E_{-7/2}-E_{-9/2})}{\partial B} = 2\pi \times 161.875(3)$ kHz/G at a homogeneous offset field $B_0 = 190.300(6)$ G. To investigate the influence of magnetic gradients, two consecutive images of the in-situ distribution $n_\uparrow(\mathbf{r})$ ($n_\downarrow(\mathbf{r})$) of atoms in $|\uparrow\rangle$ ($|\downarrow\rangle$) are recorded (cf. Chapter 4) and yield the spatially alternating magnetisation $S^z(\mathbf{r}) \propto n_\uparrow(\mathbf{r}) - n_\downarrow(\mathbf{r})$. Figures 3.15(a,b,c,d) present exemplary measurements of the magnetisation pattern for four evolution times at fixed currents I_{C1} and I_{C2} running though each of the gradient compensation coils. From a sinusoidal fit to the data, we extract the wavelength of the spin spiral pattern

$$\lambda_{sp} = \frac{2\pi}{\delta\gamma \frac{\partial B^z}{\partial r} T}\,, \tag{3.9}$$

as well as the direction of the gradient θ shown in Figure 3.15(e). Since, for low spatial frequencies the determination of the gradient angle is not accurate, we average the angle for evolution times $T > 100$ ms. Figure 3.15(d)) shows the spatial frequency of the magnetisation pattern $f_{sp} = 1/\lambda_{sp}$ as a function of the devolution time T. As expected, we find a linear dependence. Therefore, we may extract the

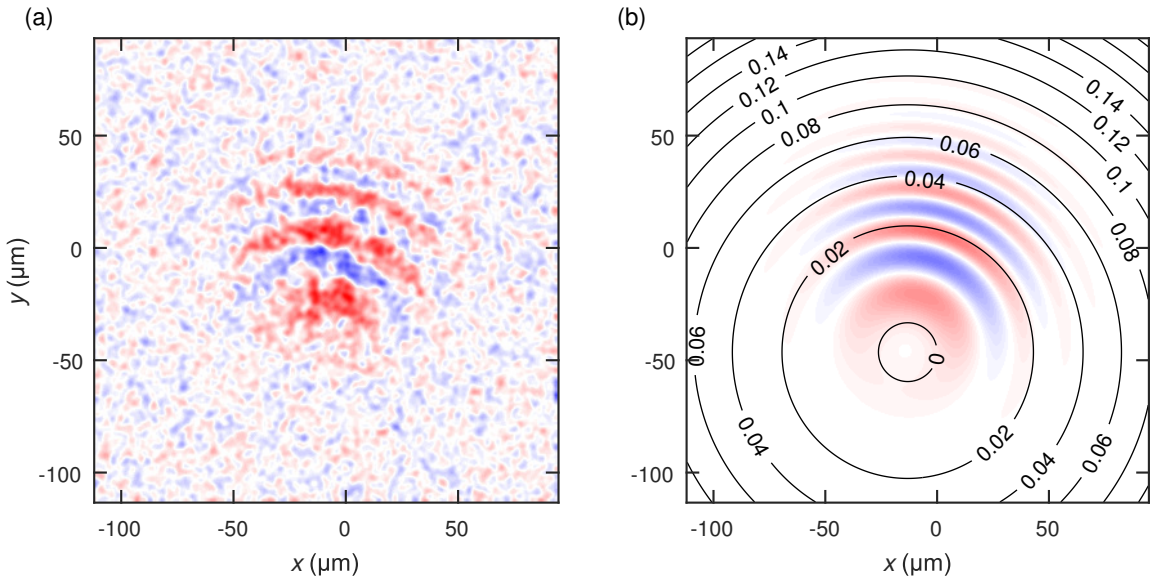

Figure 3.16: (a) Magnetisation pattern measured after a free evolution time of $T = 400\,\mathrm{ms}$. The origin of the imaging frame corresponds to the centre position of the atomic cloud. (b) Sinusoidal fit to the data shown in (a). The contours show lines of constant magnetic field in units of mG extracted from the fit.

strength of the gradient by a linear fit of the data to Equation 3.9. In the example shown, the currents of the two gradient compensation coils are set to $I_{\mathrm{C1}} = 2.313\,\mathrm{A}$ and $I_{\mathrm{C2}} = 0.5\,\mathrm{A}$ yielding a gradient of $\left|\frac{\partial B^z}{\partial r}\right| = 6.5(6)\,\mathrm{mG/cm}$ with an angle of $\theta = -41.6(7)\,^\circ$. Repeating the measurements outlined above for varying currents, allows to find an optimal pair of I_{C1} and I_{C2} for each value of the magnetic field during the experiment, which minimises the in-plane gradient. After a careful optimisation we measure residual stray gradients on the order of $\left|\frac{\partial B^z}{\partial r}\right| \lesssim 15\,\mathrm{mG/m}$ for all fields during the experimental stage. Thereby, we reduce the centre of mass displacement of atoms in different hyperfine states to below a lattice spacing. The compensated in-plane gradients allow to observe the curvature of the slow Feshbach field. Figure 3.16(a) and (b) shows the magnetisation pattern for an evolution time of 400 ms and the corresponding fit together with contours of the extracted magnetic field, respectively.

Finally, we must parallel the vertical tomography gradient with the vertical lattice direction in order to avoid a varying energy shift within horizontal planes. To this end, the minimisation procedure described above is repeated in the presence of the gradient. Then, using two additional pairs of coils (light red in Figure 3.4) producing homogeneous fields along the x- and y-direction we position the zero of the fast Feshbach field to minimise in-plane gradients resulting from a misplacement of the quadrupole field. Proceeding along these lines we achieve a reduction of the angle to $\theta_{\mathrm{AHH}} \lesssim 0.20\,\mathrm{mrad}$.

The excellent control over the magnetic field, which we have described in the preceding paragraphs is the precondition to achieve high resolution RF spectroscopy with the goal to address a single site of the vertical lattice. A summary of the applied spectroscopy techniques will be presented in the next chapter.

CHAPTER 4

Occupation and spin resolved detection of atoms in a single vertical layer

In this chapter, I will present a spectroscopic method for stable and high contrast RF tomography of the atomic cloud in the vertical optical lattice using tailored pulse shapes. Section 4.1 recapitulates the manipulation of internal states by Rabi oscillations and adiabatic population transfer. In Section 4.2.2 the optimisation of a tailored RF pulse for high-resolution tomography is outlined. Together with a scheme to resolve the energy splitting between singly and doubly occupied sites, this yields the occupation resolved distribution of atoms in the lattice. Then, Section 4.3 presents a modified spectroscopy scheme, which allows to access the spin-degree of freedom. Absorption imaging is a destructive detection method. Therefore, in order to record consecutive images in a single experimental run, the atoms have to be protected from the imaging light. A scheme for this purpose is presented in Section 4.4.

4.1 Coherent manipulation of a two-level system

The interaction of an atomic two-level system with a coherent electric field $E(t) = E_0(t)\cos(\omega t)$ can be described using the Schrödinger equation. In a rotating frame oscillating at the frequency of the driving electromagnetic field, we may write [62]

$$\frac{\mathrm{d}}{\mathrm{d}t}\begin{bmatrix} a_1(t) \\ a_2(t) \end{bmatrix} = -i\begin{bmatrix} 0 & \frac{1}{2}\Omega_0(t) \\ \frac{1}{2}\Omega_0(t) & \Delta(t) \end{bmatrix}\begin{bmatrix} a_1(t) \\ a_2(t) \end{bmatrix}, \tag{4.1}$$

where $\left|a_1(t)\right|^2$ and $\left|a_2(t)\right|^2$ are the time dependent populations in the ground and excited state of the two-level system, respectively. The off-diagonal element $\Omega_0(t) \propto \left|E_0\right|^2$ describes the interaction of the two-level system with the radiation and is called the Rabi frequency. Finally, the detuning of the driving field from the atomic resonance is given by $\Delta = \omega - \omega_0$. Together, these yield the time-dependent, effective Rabi frequency $\Omega(t) = \sqrt{\Omega_0(t)^2 + \Delta(t)^2}$. The time dependent Rabi frequency and detuning in Equation 4.1 allow to describe pulses with shaped amplitude as well as frequency sweeps.

4.1.1 Rabi oscillations

The interaction between a two level atom and an electromagnetic driving field with constant detuning and amplitude leads to an oscillation of the population between the ground and excited state. The corresponding dynamics of the population is found by a solution of Equation 4.1. For a constant Rabi

frequency $\Omega(t) = \Omega$, the evolution of the state populations for an atom prepared in the ground state $|1\rangle$ ($\left|a_1(0)\right|^2 = 1, \left|a_2(0)\right|^2 = 0$) is described by the probabilities

$$P_{|1\rangle}(t) = \left|a_1(t)\right|^2 = \cos^2\left(\frac{1}{2}\Omega t\right),$$
$$P_{|2\rangle}(t) = \left|a_2(t)\right|^2 = \sin^2\left(\frac{1}{2}\Omega t\right). \tag{4.2}$$

In the case of a constant Rabi frequency, full transfer of the population is achieved for $\Omega t = \pi$ (a so called *π-pulse*). A simple square pulse in the time domain has the disadvantage of relatively strong side bands because of its sinc-shaped spectrum in the frequency domain. Therefore, we numerically optimised the time dependent Rabi frequency $\Omega(t)$ taking into account the energy splitting between different sites of the vertical lattice as well as the measured magnetic field noise, which we have discussed in Chapter 3. In the general case of a resonant pulse with time dependent amplitude $\Omega(t)$, the population transfer is maximised for $\int \Omega(t)\,\mathrm{d}t = \pi$.

4.1.2 Adiabatic passage

A different way to excite an atom from the ground to the excited state is the *adiabatic passage* using a frequency sweep of the driving field [62]. When the frequency is changed slow enough, the population will be transferred between the two states with high fidelity. To understand the process qualitatively, we consider the dressed states arising from the atom-field interaction. The interaction induces a coupling of the diabatic states $|1\rangle$ and $|2\rangle$ yielding new adiabatic eigenstates

$$|-\rangle = \sin\left[\theta(t)\right]|1\rangle - \cos\left[\theta(t)\right]|2\rangle\ ,$$
$$|+\rangle = \cos\left[\theta(t)\right]|1\rangle + \sin\left[\theta(t)\right]|2\rangle\ . \tag{4.3}$$

Here, $\theta(t) = \frac{1}{2}\arctan(-\Omega/\Delta)$ is called the *mixing angle*. The presence of the driving field leads to an *avoided crossing* of the adiabatic energy levels. Adiabatic passage works as follows: When the detuning is changed slowly with respect to the splitting of the adiabatic eigenstates, the population follows the adiabatic states. Starting in $|+\rangle$ at $\Delta = -\infty$ this leads to a complete population transfer from $|1\rangle$ to $|2\rangle$, when the detuning is changed from $-\infty$ to ∞. In the Landau-Zener limit, the probability to excite the atom is given by

$$P_{|2\rangle} = 1 - p, \text{with } p = \exp\left\{-\frac{\pi^2\Omega^2}{2\left|\dot{\Delta}(t)\right|}\right\}. \tag{4.4}$$

In the opposite case, when the rate at which the detuning changes is large, the population is exchanged between the adiabatic eigenstates leaving the population in the initial states. Although Equation 4.4 is only exact for a constant amplitude and linearly varying detuning, it can often be used to describe the population transfer of more general pulses approximately. In fact, we have already applied this in Chapter 3.4 where we described the fidelity with which a balanced spin mixture is realised from an initially polarised gas of atoms. An advantage of adiabatic population transfer is its insensitivity to small changes in the Rabi frequency and detuning (amplitude fluctuations of the driving field) as well as to moderate drifts and noise of the magnetic bias field.

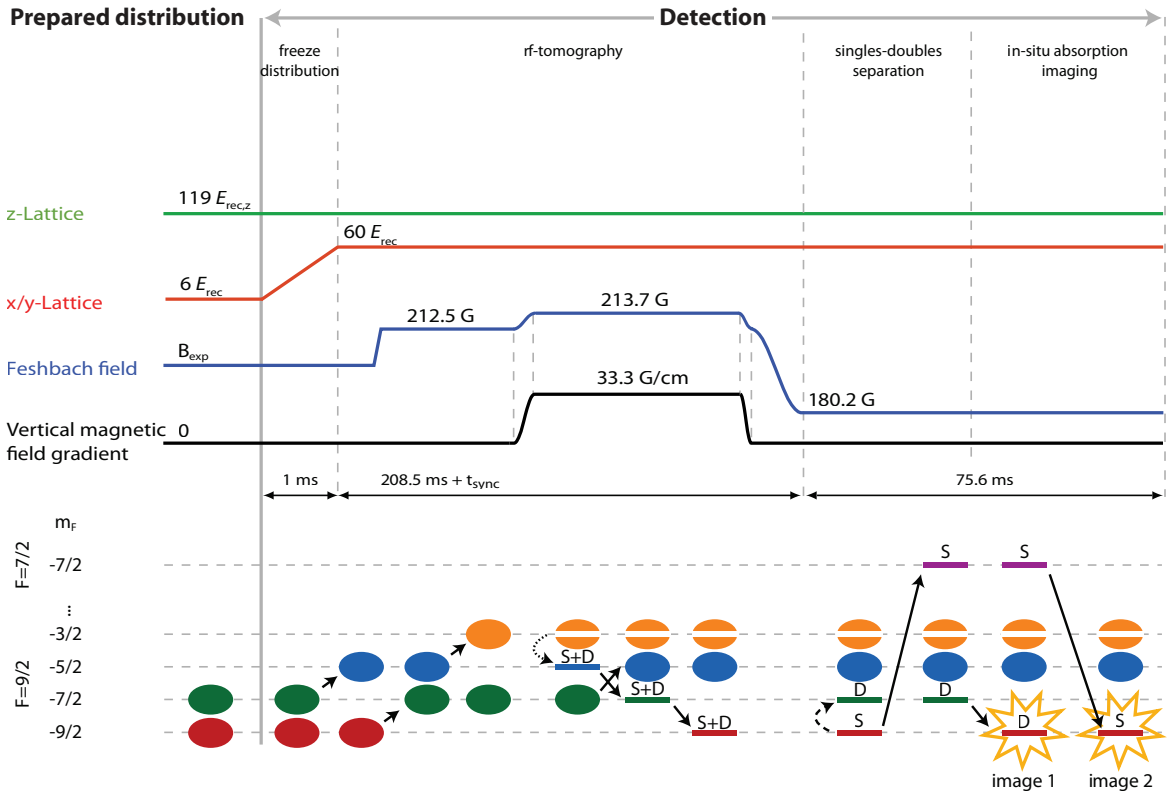

Figure 4.1: Detection part of the experimental sequence. To begin with, tunnelling of the atoms is suppressed by a ramp to a horizontal lattice depth of 60 E_r. The Feshbach resonance is crossed to reach $B = 213.8\,\mathrm{G}$ where the on-site interaction difference of the relevant spin mixtures vanishes. To avoid losses during the ramp, atoms in $|-7/2\rangle$ are transferred to $|-5/2\rangle$. Then, $|-9/2\rangle$ atoms is transferred to $|-7/2\rangle$. RF tomography is performed in a vertical magnetic gradient addressing the $|-5/2\rangle$ to $|-3/2\rangle$ transition. The variable synchronisation time t_{sync} is adjusted to yield the highest contrast in a vertical tomography of the full atomic cloud. Atoms remaining in $|-7/2\rangle$ are transferred to $|-5/2\rangle$ to avoid off-resonant scattering of imaging light, while atoms in $|-5/2\rangle$ are successively transferred to $|-9/2\rangle$. At a magnetic field of 180.2 G, we exploit the differential on-site interaction to separate singly- and doubly-occupied sites in the $|-9/2\rangle$ $|-5/2\rangle$ mixture. Before the distribution of doubly-occupied sites is recorded, the atoms on doubly occupied sites are transferred to the $|7/2, 7/2\rangle$ state and transferred back before the second image is recorded. Finally, an image recording the intensity distribution of the imaging beam without atoms is recorded (not shown).

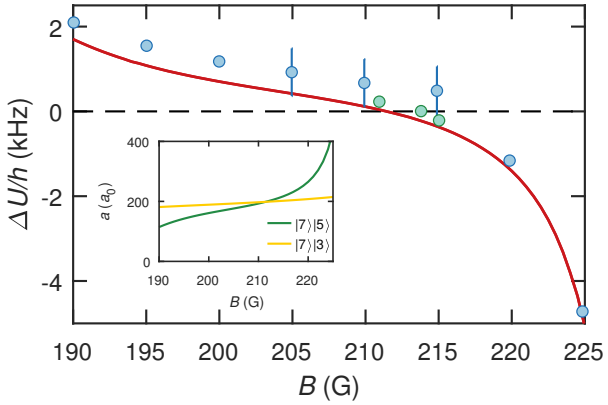

Figure 4.2: Calibration of the differential on-site interaction energy. We determine the magnetic field were the differential on-site interaction energy ΔU between sites occupied by pairs $|-7/2\rangle\,|-5/2\rangle$ and $|-7/2\rangle\,|-3/2\rangle$ vanishes using global RF spectroscopy and find $B(\Delta U = 0) = 213.8\,\mathrm{G}$. At magnetic fields where resonances from singly and doubly occupied sites are well resolved, a Gaussian pulse with a full width at half maximum FWHM = 1 ms is used to address the $|-5/2\rangle \rightarrow |-3/2\rangle$ transition (blue data points). Close to the zero crossing (green data points) the individual peaks are considerably overlapping. Therefore, we use a longer Gaussian pulse (FWHM = 3 ms) to increase the spectral resolution and differentiate between singly and doubly occupied sites using an additional adiabatic frequency sweep. The red curve shows the expected dependence of ΔU on the magnetic field calculated from an interpolation of the Feshbach resonances between $|-7/2\rangle\,|-5/2\rangle$ and $|-7/2\rangle\,|-3/2\rangle$ (see inset).

4.2 Occupation resolved detection

The most prominent feature of the Hubbard model is the crossover from a metallic to a Mott-insulating state for finite repulsive on-site interactions as a function of the doping and the temperature. This crossover is signalled by a uniform density distribution and a vanishing compressibility around half filling as well as a suppression of doubly occupied sites. Therefore, in order to study the density sector of the Hubbard model, we developed an occupation resolved detection technique.

4.2.1 Interaction shift

Extracting the *in-situ* density distribution of a single plane in the vertical direction requires a reliable addressing scheme. Aside from stable magnetic fields and precisely controlled gradients, this requires a scheme which addresses both singly and doubly-occupied sites in a single vertical layer at the same time. Due to the intensity envelope of the lattice beams, the lattice depth is spatially varying. Correspondingly, the on-site interaction varies across the trap as well. For these reasons, it is desirable to apply a detection scheme, which is independent of the different scattering length in the initial and final states. The Feshbach resonances of ^{40}K allow to identify a magnetic field, where the difference in the scattering length for mixtures $|-7/2\rangle\,|-5/2\rangle$ and $|-7/2\rangle\,|-3/2\rangle$ vanishes between the corresponding Feshbach resonances. From the interpolated scattering length in the crossover region in between the Feshbach resonances, we expect the scattering lengths a_{75} and a_{73} to be equal and, correspondingly, the difference in the initial and final on-site interaction $\Delta U = U_{75} - U_{73}$ to vanish at $B(\Delta U = 0) \approx 211.8\,\mathrm{G}$ (see Figure 2.5). Note, however, that the values for the scattering lengths at magnetic field in between the Feshbach resonances were obtained from an interpolation and are possibly inaccurate. To determine the correct magnetic field experimentally, we measure $\Delta U(B)$ as presented in Figure 4.2. We take spectra at different magnetic fields and determine the spectral separation $\Delta U(B)$ of two features corresponding to singly and doubly-occupied lattice sites. When ΔU becomes smaller than the Fourier limited width of the Gaussian

pulse, the two features cannot be resolved any more. In this case, we use a longer Gaussian pulse to increase the resolution and, more importantly, apply an additional RF sweep to separate the signals from singly and doubly-occupied sites, which are then measured consecutively (cf. Section 4.2.3) in a single realisation of the experiment. While the observed trend agrees well with the expected behaviour, we observe the differential on-site interaction to vanish at a slightly higher bias field than expected at $B(\Delta U = 0) = 213.8\,\mathrm{G}$.

4.2.2 Optimised radio-frequency pulses for high-resolution tomography

In the last chapter, we described the preparation of a degenerate Fermi gas in an anisotropic 3D optical lattice. Since tunnelling in the vertical direction is negligible, each of the planes in the vertical direction can be thought of as an individual realisation of the 2D Hubbard model. However, to make full advantage of the high resolution imaging capabilities of our experimental setup, and also to avoid averaging over different fillings across the vertical lattice, we need to select a single site of the vertical lattice. First of all, this requires a way to distinguish different sites of the vertical lattice. To this end, we apply a strong magnetic field gradient $\frac{\mathrm{d}B}{\mathrm{d}z} = 33.3\,\mathrm{G/cm}$ in the vertical direction. In the presence of a spatially varying Zeeman splitting, the energy of atoms in the same magnetic hyperfine state depends on their position along the vertical direction (cf. Chapter 3). Furthermore, since the magnetic moments $\mu_{\mathrm{F},\mathrm{m_F}} = \partial E_{\mathrm{F},\mathrm{m_F}}/\partial B$ depends on the hyperfine state, the resonance frequency of the transition between neighbouring Zeeman sublevels varies spatially as well. The precise value of the shift of the resonance depends on the internal states involved and the magnitude of the homogeneous offset field (cf. Chapter 3.6). For the $|-3/2\rangle \rightarrow |-5/2\rangle$ transition at a bias field of $B_0 = 213.8\,\mathrm{G}$, the differential gyromagnetic ratio of $\delta\gamma = \partial\left(E_{\mathrm{F}',\mathrm{m}'_\mathrm{F}} - E_{\mathrm{F},\mathrm{m_F}}\right)/\partial B = 2\pi \times 180.9\,\mathrm{kHz/G}$ results in a frequency difference of $\delta_z = 642\,\mathrm{Hz}$ for neighbouring planes with the lattice spacing a_z. While a stronger gradient would relax the requirement on the spectral width of the pulse, we are currently limited by the current available to create the gradient. Therefore, a compromise between spectral resolution and inter-sequence stability has to be found. Naively, one might choose a Gaussian pulse due to its narrow line shape. However, in the present application there is a trade-off between spectral resolution and vulnerability to magnetic field fluctuations. The ideal pulse shape would thus yield a narrow flat top spectrum. The time dependent amplitude of such a pulse is described by the Fourier-series

$$A(t) = A_0 \sum_{n=1}^{5} a_n \sin\left((2n-1)\,\pi\,\frac{t}{\tau_\mathrm{p}}\right). \tag{4.5}$$

A_0 denotes the amplitude of the pulse; $\tau_\mathrm{p} = 7.5\,\mathrm{ms}$ is the pulse duration; The Fourier coefficients a_n define the temporal and spectral shape of the pulse. To optimise the pulse shape, we aim to find Fourier components that yield high and uniform transfer in a 200 Hz wide region around the resonance. At the same time transfer in a 200 Hz wide region around neighbouring planes, i.e. with a detuning ±640 Hz from the resonance, should be suppressed to avoid that atoms in neighbouring planes are off-resonantly addressed by the pulse. The a_n are found by a numerical solution of the Schrödinger equation of the driven two-level system (Equation 4.1). The numerical optimisation was carried out with Mathematica and yields the values listed in Table 4.1. The resulting pulse shape[1] is shown in Figure 4.3(a). The expected spectrum for a realistic distribution of atoms over the vertical lattice is shown in Figure 4.3(c). From the numerical simulation, we expect an average fidelity of 0.98(1) in a region ±100 Hz around the resonance

[1] Flat-top pulses for spin and occupation resolved detection are created using a *Tabor WW1281A Arbitrary Waveform Generator* offering both phase and amplitude control.

Fourier coefficients	$\|-3/2\rangle \rightarrow \|-5/2\rangle$
a_1	0.0956
a_2	−0.091
a_3	0.0483
a_4	−0.005
a_5	0.002

Table 4.1: Optimised Fourier coefficients of Equation 4.5 for high resolution RF tomography.

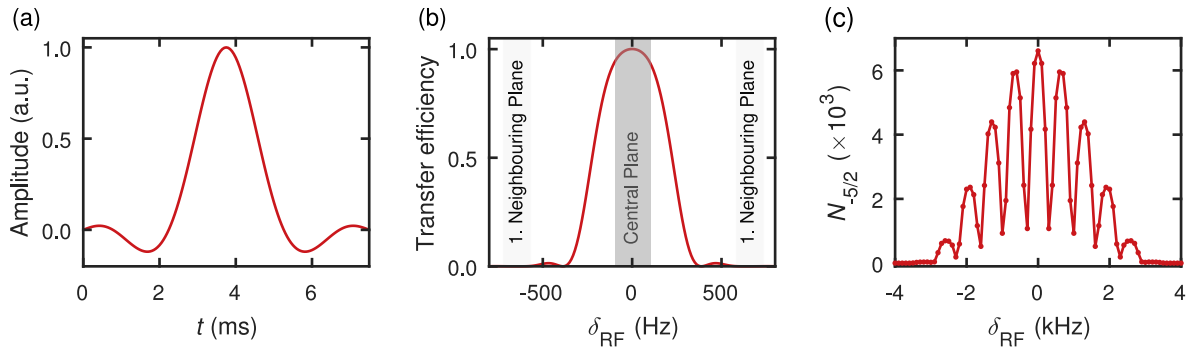

Figure 4.3: (a) Optimised flat-top pulse for high-resolution tomography. The spectrum shown in (b) results from a numerical simulation of the driven two-level system. The shaded regions indicates the 100 Hz wide regions where a uniform transfer (green) and a suppressed transfer (light red) is achieved using the numerically optimised pulse parameters. (c) Expected tomography contrast using the Thomas-Fermi approximation and an harmonic external potential.

and a contribution from neighbouring planes smaller than a tenth of a percent. The actual spectrum shown in Figure 4.8 displays a reduced contrast, which could be reproduced assuming a Gaussian broadening with a width of 145 mG. We attribute the broadening to B-field noise and/or residual magnetic field gradients and drifts during the pulse. Taking the spectral broadening into account, we find an average fidelity of 0.96 around the central region, while the expected contribution from neighbouring planes increases to 1.3%.

In order to calibrate the amplitude A_0 of the spectroscopy pulse, we observe Rabi oscillations of the transferred number of atoms in the absence of the vertical gradient (Figure 4.4). Within our experimental error, the transfer of atoms on either singly (red) or doubly (blue) occupied lattice sites is maximised for the same amplitude.

Power line synchronisation

In spite of the regulation of the magnetic field outlined in Section 3.6.1, low-amplitude noise with a frequency of 50 Hz and higher harmonics thereof originating from the power line are visible on the magnetic bias field (cf. Figure 3.13). In order to further improve the inter-sequence stability, we synchronise the timing of the high resolution RF tomography to the 50 Hz oscillations of the power line. To this end we sample the power line signal and convert it to a square wave "LineCLK". Upon a trigger before the pulse, we pause the sequence by disabling the 10 MHz clock serving as a time reference for

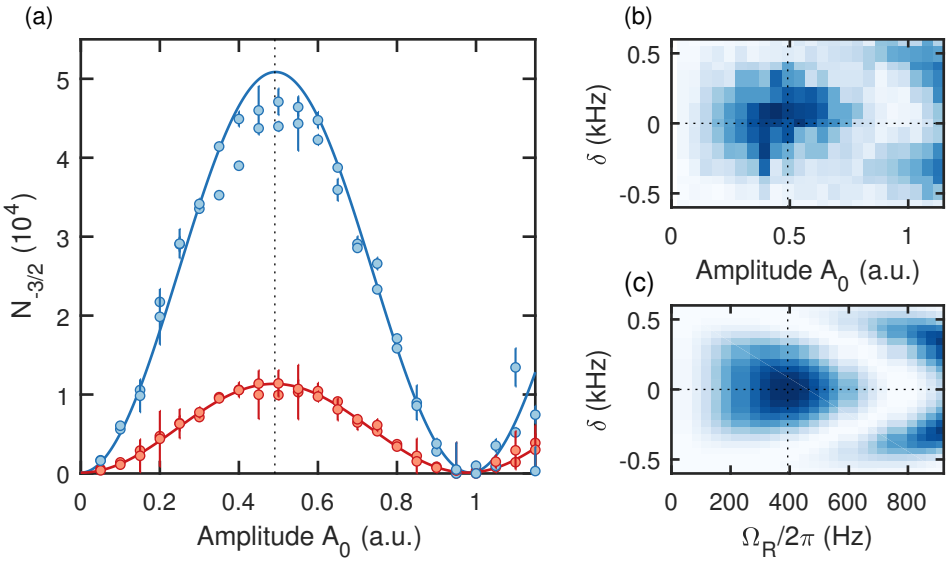

Figure 4.4: (a) Rabi oscillations of atoms on singly (blue points) and doubly (red points) occupied lattice sites driven by the high resolution spectroscopy pulse. Error bars denote the standard error of two measurements. The amplitude required for a π-pulse is extracted from sinusoidal fits to the data (solid lines). At an offset field of $B_0 = 213.75$, we observe full transfer for equal amplitudes irrespective of the occupation within error. This observation reflects that the on-site interactions for a pair of atoms in the initial and final states are the same at this field. (b) Map of the population transfer as a function of amplitude and detuning. For comparison (c) shows the expected transfer as a function of the Rabi frequency and detuning. The observed π-amplitude (dotted line) corresponds to a Rabi frequency $\Omega_R/2\pi \approx 400\,\mathrm{Hz}$.

the analogue and digital cards controlling the experiment. Upon the next rising edge of the "LineCLK" the clock input is enabled again setting a well defined phase for the continuing sequence. Ideally, the tomography will thereafter occur at an extremum of the 50 Hz cycle such that only little phase accumulates during the radio-frequency pulse. We experimentally determined the optimal timing of the tomography pulse with respect to the phase of the power line. To this end, we introduce a variable delay time t_{sync} for which the sequence is paused after the synchronisation and maximise the contrast in tomography by varying t_{sync} (cf. Figure 4.5).

Magnetic field tracking

In a typical measurement, we scan over a large range of frequencies to find the maximally populated plane in the vertical lattice first. Then, we repeatedly scan over this resonances to gather enough data to perform a statistical analysis of the dataset for a chosen set of Hubbard parameters. However, we typically observe drifts of the tomography resonance by more than one lattice spacing over a time scale of hours. This drift is caused by slow variations of the magnetic bias field produced by the slow Feshbach coils. In order to compensate the drift, we have implemented a feedback on the frequency applied in the spectroscopy scan. To this end, we monitor the current flowing through the slow Feshbach coils and average over 13 consecutively recorded values of the current recorded at the time of the spectroscopy pulse. The measured current is converted to a magnetic field and further, using the Breit-Rabi formula and the magnetic field at the beginning of the scan, to a frequency difference, which is added to the frequency set in the experimental control.

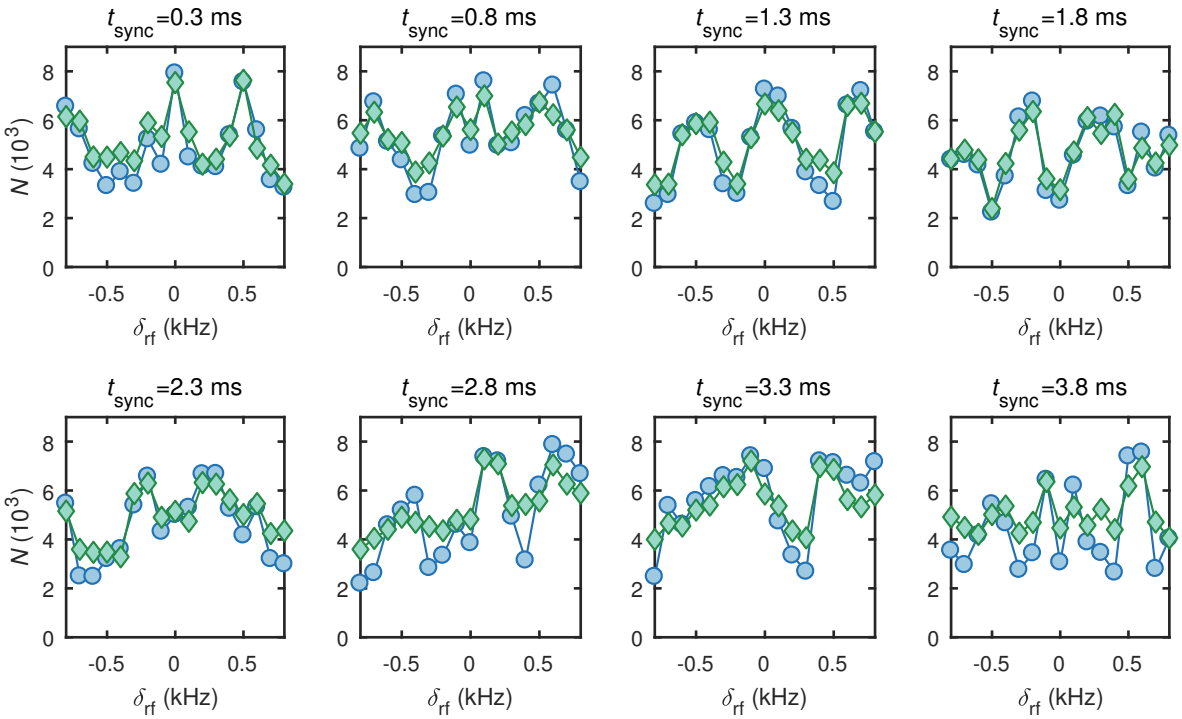

Figure 4.5: Optimisation of tomography timing. To reduce the influence of B-field drifts (cf. 3.6.1), we maximise the tomography contrast by varying the synchronisation time t_{sync}. While a similarly good contrast is observed for $t_{sync} = 1.3$ ms and $t_{sync} = 1.8$ ms, it is difficult to distinguish the vertical lattice sites for other synchronisation times.

4.2.3 Selective addressing of singly and doubly occupied sites

In the last section, we described how we simultaneously transfer atoms on singly- and doubly occupied lattice sites in a single site of the vertical lattice using a spectrally narrow flat-top RF pulse. The remaining task for occupation resolved detection is now to distinguish between singly and doubly-occupied sites. To this end, we ramp the B-field from 213.75 G to 180.2 G where the differential on-site interaction between pairs of $|-9/2\rangle\,|-5/2\rangle$ and $|-7/2\rangle\,|-5/2\rangle$ is $\Delta U = -6.6$ kHz. To distinguish between singly and doubly occupied sites, we address the $|-9/2\rangle \rightarrow |-7/2\rangle$ transition with a wide RF-sweep. To achieve a nearly box like transfer spectrum, we use a hyperbolic secant (HS1) pulse combining a shaped amplitude (see Figure 4.6(a))

$$E_{\mathrm{HS1}}(t) = E_0\,\mathrm{sech}\left(\left[C_{\mathrm{trunc}}\left(\frac{2t}{T_{\mathrm{pulse}}} - 1\right)\right]\right) \tag{4.6}$$

with a chirped frequency sweep (see Figure 4.6(b))

$$\Delta_{\mathrm{HS1}}(t) = \frac{\Delta_0}{2}\tanh\left(\left[C_{\mathrm{trunc}}\left(\frac{2t}{T_{\mathrm{pulse}}} - 1\right)\right]\right) \tag{4.7}$$

In Equation 4.6 E_0 is the amplitude of the pulse; $\Delta_0 = 4$ kHz denotes the width of the frequency sweep and $C_{\mathrm{trunc}} = 5.3$ is a truncation parameter [101] scaling the pulse within the total pulse duration $T_{\mathrm{pulse}} = 3$ ms. With the chosen parameters, the HS1 pulse yields an approximately 400 kHz wide window of uniform transfer efficiency $\eta_{HS1} = 1.003(8)$ (cf. Figure 4.6(c)). Importantly, the transfer efficiency is insensitive to drifts and noise of the magnetic field as well as a spatially varying ΔU arising from the

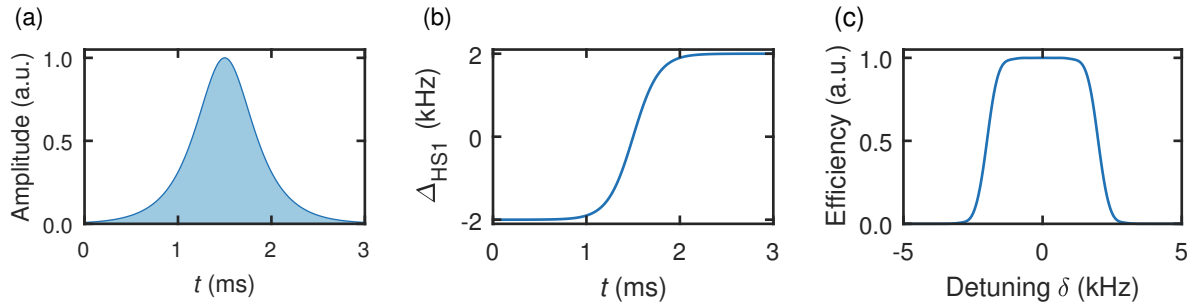

Figure 4.6: HS1 pulse combining an amplitude modulation (a) with a frequency sweep over 4 kHz (b). From a numerical simulation of the Schrödinger equation, we expect a flat population transfer (c) with negligible off-resonant contribution for a detuning larger than 3 kHz.

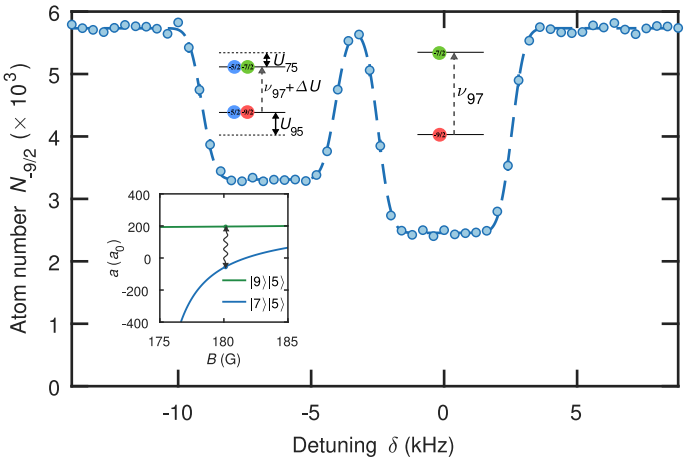

Figure 4.7: Calibration of the spectroscopic separation of atoms on singly- and doubly-occupied lattice sites. We measure the number of atoms remaining in the initial state as a function of the centre frequency ν_{HS1} of the adiabatic frequency sweep. The data points (blue) are the statistical average of 14 measurements which is additionally binned with a bin size of 400 Hz. The standard error is smaller than the marker size. The centre positions of the two features are extracted from a fit to a symmetric two-sided error function (dashed blue line). While atoms on singly-occupied sites are resonantly addressed at the bare atomic frequency of ν_{97}, atoms on doubly-occupied sites experience a shift due to the differential on-site interaction $\Delta U = U_{75} - U_{95}$.

varying lattice depth across the trap (cf. Chapter 2). The second feature of the transfer spectrum is a sharp drop of transfer efficiency at the edges of the frequency window. Figure 4.7 presents the number of atoms remaining in the initial $|-9/2\rangle$ state as a function of the centre frequency of the adiabatic sweep. While atoms on singly-occupied sites are resonantly addressed at the bare atomic frequency $\nu_{97} = (E_{-7/2} - E_{-9/2})/h = 41.2756(1)\,\mathrm{MHz}$, atoms on doubly-occupied sites experience a shift due to the difference of the on-site interaction $\Delta U = U_{75} - U_{95}$ between the initial and final state. The observed shift is in agreement with the calculated value $U_{75} - U_{95} = -h \times 6.6\,\mathrm{kHz}$. As the spectrum shows, the signals from singly- and doubly-occupied sites are well separated at the chosen field. Therefore, to discriminate between atoms on singly- and doubly-occupied sites, we may now selectively address atoms in $|9/2, -9/2\rangle$ on doubly-occupied sites with a fixed centre frequency $\nu_{97} + \Delta U/h$.

Combining the methods discussed in this section, we are able to reconstruct the occupation distribution in the vertical direction by varying the center frequency of the high resolution spectroscopy pulse. Figure 4.8 shows a tomography spectrum of the full cloud and resolves the occupation of the individual

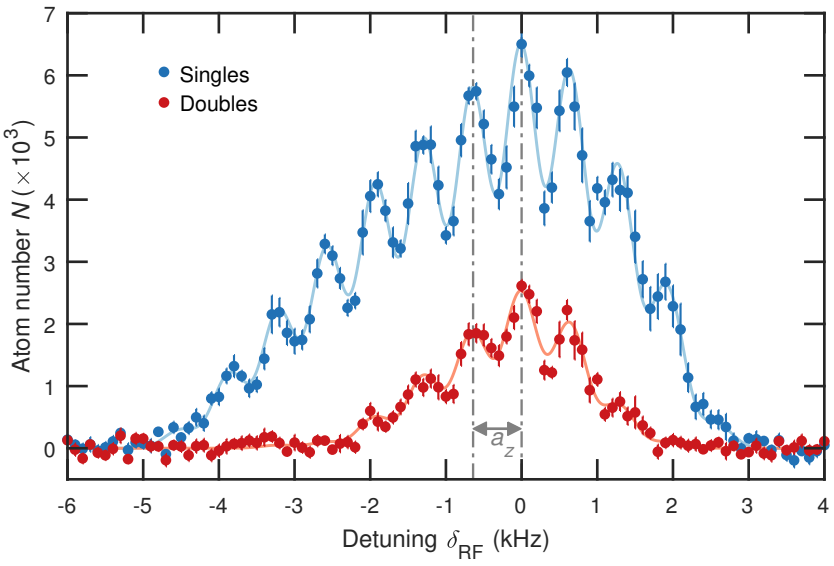

Figure 4.8: Spatially resolved standing-wave structure in the vertical direction. The data shown are the averages of nine consecutive measurements and we have used the monitored magnetic field to correct for residual drifts of the resonance between consecutive measurements. Error bars denote the standard deviation. The solid lines are fits to the data based on a numerical simulation of Equation 4.1 and take into account the optimised pulse shape as well as an additional Gaussian broadening.

lattice sites of the vertical lattice. The data is averaged over nine consecutive measurements. Additionally, we have used the monitored magnetic field to post-process the data in order to correct for residual drifts of the magnetic bias field between measurements. The observed envelope arises from the combined effect of the Gaussian envelopes of the laser beams forming the 3D optical lattice. The asymmetric shape of the spectrum is caused by the gravitational force.

4.3 Spin resolved detection

In the previous sections, we described a high resolution spectroscopy scheme to resolve the spatial distribution of the lattice site occupation within a single two-dimensional plane of the vertical lattice. As we will see in Chapter 6 this method allows to fully determine the thermodynamic properties of the Hubbard model in the density sector. However, in order to access to the low temperature phase diagram, which is characterised by the antiferromagnetic alignment of spins, we require a modified detection scheme, which is able to distinguish between atoms in different hyperfine states.

The magnetisation on a lattice site i is given by

$$\langle \hat{S}_i^z \rangle = \langle \hat{n}_{\uparrow,i} - \hat{n}_{\downarrow,i} \rangle /2, \tag{4.8}$$

where $\hat{n}_{\uparrow,i}$ ($\hat{n}_{\downarrow,i}$) is the total number of atoms in spin-up (spin-down). Together with the definition for the expectation value of the number operator of atoms with spin σ on singly occupied sites

$$\langle \hat{s}_{i,\sigma} \rangle = \langle \hat{n}_{i,\sigma} \rangle - \langle \hat{n}_{i,\uparrow} \hat{n}_{i,\downarrow} \rangle \,, \tag{4.9}$$

we find that the magnetisation may be expressed as the difference of atoms in spin-up and spin-down on

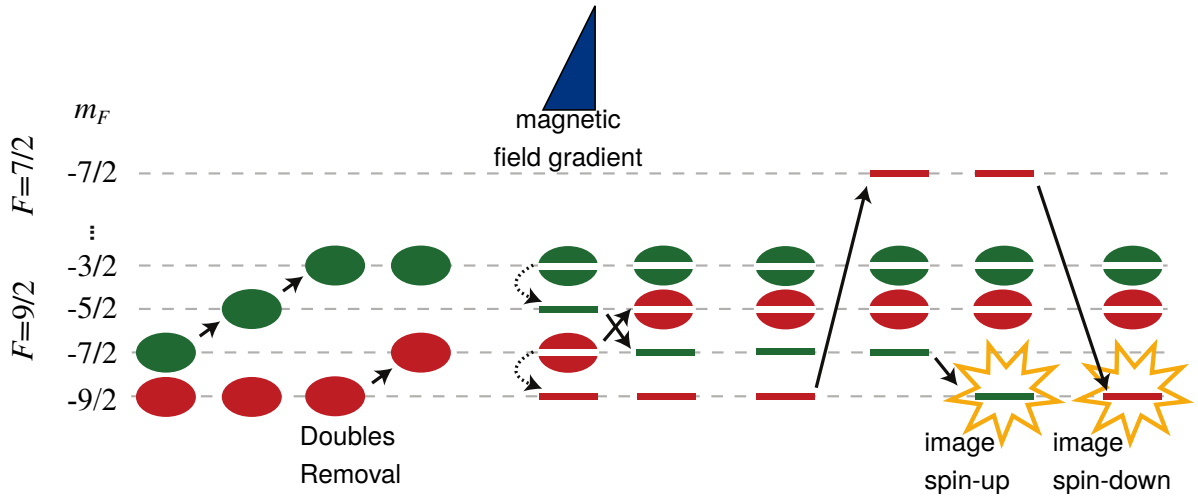

Figure 4.9: Spin resolved detection scheme. The experiment is performed with a balanced mixture of the states $|\uparrow\rangle = |9/2, -7/2\rangle$ (green) and $|\downarrow\rangle = |9/2, -9/2\rangle$ (red). After the experiment, atoms residing on doubly-occupied sites are removed by spin-changing collisions between the states $|9/2, -9/2\rangle$ and $|9/2, -3/2\rangle$. Subsequently, simultaneous RF tomography in a vertical magnetic field gradient is used to address both spin components in a single horizontal layer. Finally, consecutive absorption images of both distributions are recorded.

singly occupied sites

$$\langle \hat{S}_i^z \rangle = \langle \hat{s}_{\uparrow,i} - \hat{s}_{\downarrow,i} \rangle / 2 \,. \tag{4.10}$$

Therefore, in order to obtain the in-situ distribution of the magnetisation, it is sufficient to determine the distribution of atoms in both spin states on singly-occupied sites in a single experimental run. Hence, we need to modify the detection sequence to meet two requirements:

- To access the magnetisation in a single experimental run, we need to implement a spectroscopy scheme, which is able to address two hyperfine transitions in the tomography gradient simultaneously.
- In order to address only atoms on singly occupied sites, we have to remove all atoms on doubly-occupied sites.

Figure 4.9 shows the corresponding detection sequence schematically. Directly after suppressing tunnelling, we selectively remove atoms on doubly occupied sites by exothermic spin-changing collisions. Thereafter, spin resolved high resolution RF tomography of the vertical planes in a magnetic field gradient is performed before two consecutive images are recorded. Again atoms in $|9/2, -7/2\rangle$ are protected from off-resonantly scattered light during the first imaging pulse using a microwave sweep to $|7/2, -7/2\rangle$. In the next subsection, we will describe the removal of atoms on doubly occupied sites as well as the spin-resolved spectroscopy technique in more detail.

4.3.1 Removal of atoms on doubly occupied lattice sites

To access the magnetisation, we employ spin-changing collisions to remove all atoms on doubly occupied sites. In a spin-changing collision of two atoms the initial internal states $|m_{F,2}\rangle\,|m_{F,2}\rangle$ differ from the final states $|m'_{F,2}\rangle\,|m'_{F,2}\rangle$ while the total magnetic quantum number is conserved $M_F = m_{F,1} + m_{F,2} = m'_{F,1} + m'_{F,2}$. In an inelastic collision, the sum of internal energies in the initial and final states are different.

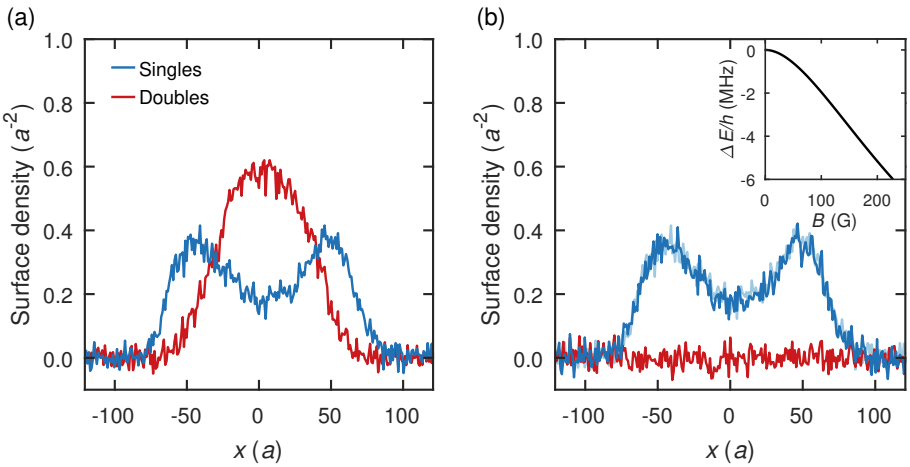

Figure 4.10: Removal of atoms on doubly occupied lattice sites. We show a comparison of a measurement of the distribution of singly occupied sites (blue) and doubly occupied sites (red) without (a) and with (b) spin changing collisions. When spin-changing collisions are enabled the atoms on doubly occupied sites are selectively removed by spin-changing collisions (b). At the same time, the singles density remains unaffected. For comparison, the distribution of singly occupied sites without spin-changing collisions is shown again (light blue). The data shown in both graphs have been averaged over 60 experimental realisations.

The removal scheme works as follows. Directly after the desired many-body state has been prepared in the lattice, the horizontal lattice depth is increased to 60 E_r to suppress tunnelling. Then, the spin-up atoms in $|9/2, -7/2\rangle$ are adiabatically transferred to $|9/2, -3/2\rangle$. Now, atoms on doubly occupied sites undergo exothermic spin-changing collisions. The difference in the internal energies

$$\Delta E = (E_{|7\rangle} + E_{|5\rangle}) - (E_{|9\rangle} + E_{|3\rangle}) \tag{4.11}$$

is shown in the inset of Figure 4.10 and depends strongly on the magnetic field. Upon a collision this energy difference is converted to kinetic energy. At the chosen field of $B = 212.5$ G the released energy is approximately $\Delta E/h = -5$ MHz exceeding the trap depth by more than a factor of 20. Therefore, the inelastic collision results in a fast loss of doubles. In order to verify the method, we record the density distributions of singly and doubly occupied sites with and without spin-changing collisions. To increase the sensitivity to the loss of atoms on doubly occupied sites we prepare the sample at a Feshbach-field of 212 G and a lattice depth of 6 E_r is applied to realise the Hubbard model with weakly repulsive interactions $U/t = 1.6$ (compare Chapter 6). This results in a large number of doubly occupied sites in the centre of the trap surrounded by a ring of singly occupied lattice sites as shown in Figure 4.10(a). Figure 4.10(a) shows the prepared distribution, which have been recorded in the usual way. Figure 4.10(b) shows a distribution which was prepared in the same way, but this time with spin-changing collisions enabled. The measurement shows that, on the one hand, all atoms on doubly-occupied sites are lost due to the inelastic collisions, while, on the other hand, the spatial distribution of singly-occupied sites remains unaffected. Thereby, the observation also confirms that negligible heating is introduced by the process.

4.3.2 Spin resolved radio-frequency tomography

In order to simultaneously extract the distribution of both spin components in a single plane of the vertical lattice, we adopt the tomography scheme described above with the difference that here we apply two RF pulses simultaneously to detect atoms in two spin states. At a magnetic bias field of 213.8 G transitions

Fourier coefficients	$\|-3/2\rangle \rightarrow \|-5/2\rangle$	$\|-7/2\rangle \rightarrow \|-9/2\rangle$
a_1	0.0956	0.0950
a_2	–0.1010	–0.0945
a_3	0.0483	0.0350
a_4	0.0000	–0.0100
a_5	0.0025	0.0036

Table 4.2: Numerically optimised Fourier coefficients a_n (Equation 4.5) for spin-resolved high resolution tomography.

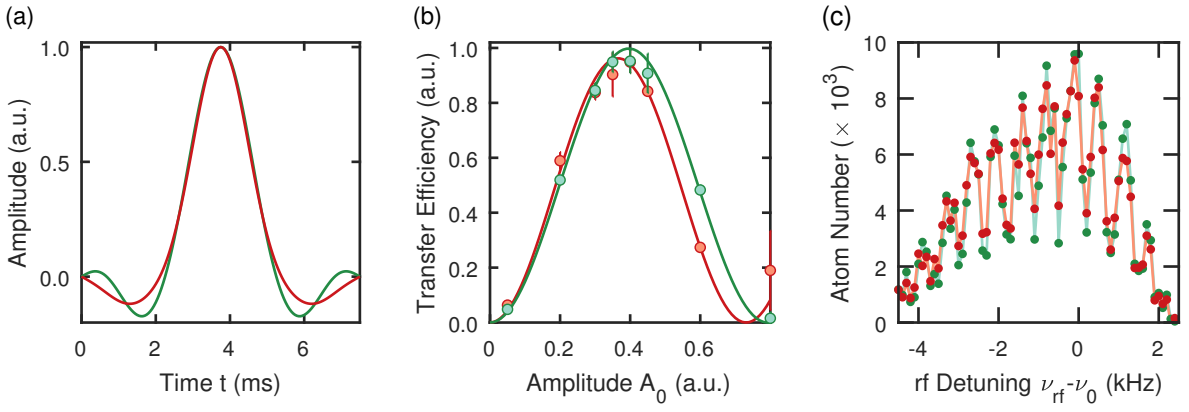

Figure 4.11: Spin-resolved RF tomography. (a) Optimised pulse shape for the addressed transitions $|-3/2\rangle \rightarrow |-5/2\rangle$ (green) and $|-7/2\rangle \rightarrow |-9/2\rangle$ (red). (b) Amplitude calibration using Rabi oscillations in the absence of the vertical magnetic field gradient (circles). The error bars show the statistical uncertainty from three consecutive measurements. The solid lines are sinusoidal fits to the data, from which we extract the amplitude required for a π-pulse. (c) Full tomography spectrum in the presence of a vertical magnetic field gradient. For (b) and (c) the colour code is the same as in (a).

with $\Delta m_F = \pm 1$ between different magnetic sublevels are easily resolved, since they are separated by about 1 MHz in frequency. However, the spatially varying energy shift of the driven transitions due to the magnetic field gradient $\mathrm{d}E/\mathrm{d}B$ depends on the driven transition since the linear Paschen-Back regime is not reached at this magnetic field. Therefore, the two pulses have to be shaped independently in order to yield comparable contrasts and transfer efficiencies. A numerical optimisation following the same procedure as presented in Section 4.2.2 yields the optimal Fourier coefficients stated in Table 4.2. Figure 4.11 shows the corresponding pulse shape (a) together with a calibration of the amplitude required for a π-pulse (b). Finally, Figure 4.11(c) presents the full, spin-resolved, tomography spectrum of the cloud.

4.4 Protection against off-resonant photon scattering

The $D2$-line of Potassium 40 shows a broad natural line width (cf. 3.1), which is comparable to the spacing between adjacent magnetic hyperfine states at the magnetic fields applied during imaging. Therefore, the off-resonantly imaged population of neighbouring magnetic hyperfine states contributes to the absorption signal. At the same time, off-resonantly imaged atoms are optically pumped into the lowest hyperfine

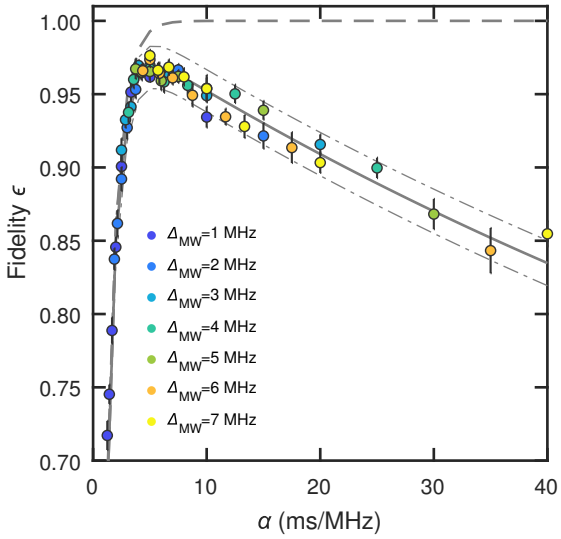

Figure 4.12: Microwave transfer. We measure the fidelity ϵ for varying sweep width as a function of the inverse sweep rate α. For a fixed amplitude Ω_{MW} the fidelity depends on α only. The solid line is a fit to Equation 4.13 and describes the transfer probability in the presence of noise on the driving field. For comparison the Landau-Zener limit is shown (dotted line). Dashed-dotted lines show the standard error of the fit.

state. Both effects result in an overestimated (underestimated) density of the state imaged in the first (second) image. Therefore, we employ an intermediate transfer of the atoms in $|-9/2\rangle$ to the $|7/2,-7/2\rangle$ state with a broad adiabatic microwave sweep before the first image is recorded and consecutively transfer the atoms back to the $|9/2,-9/2\rangle$ state just before the second image is recorded. In the following, we outline the optimisation of the transfer efficiency. When the atom number in $|9/2,-9/2\rangle$ is $N_{9/2}$, the atom numbers recorded in the first and second image are $N_1 = (1-\epsilon)N_{9/2}$ and $N_2 = \epsilon^2 N_{9/2}$, respectively. Solving for the single path transfer efficiency yields

$$\epsilon = \frac{N_2}{2N_1}\left(\sqrt{1+4\frac{N1}{N2}}-1\right). \tag{4.12}$$

Figure 4.12 shows an exemplary measurement of the MW-transfer fidelity ϵ. As expected, the data collapses on a single curve when plotted as a function of the inverse sweep rate $\alpha = \tau_{\mathrm{MW}}/\Delta_{\mathrm{MW}}$. However, we observe a lower efficiency than expected in the Landau-Zener limit $P_{\mathrm{LZ}}(\alpha) = 1-\exp\left\{-\pi^2\Omega_{\mathrm{MW}}^2\alpha\right\}$ (dotted line in Figure 4.12), where Ω_{MW} is the Rabi frequency. In particular, while a saturation of the fidelity to one is expected for $\alpha \gg \Omega_{\mathrm{MW}}^2$, the data shows a decaying fidelity. We attribute this observation to the presence of noise on the driving field. Following the approach presented in Refs. [102, 103], the transfer probability can be analytically approximated by

$$P(\alpha) = \frac{1}{2}\left(1-\exp\left\{-2\pi\Gamma_{\mathrm{MW}}\Omega_{\mathrm{MW}}\alpha\right\}\right) + \exp\left\{-2\pi\Gamma_{\mathrm{MW}}\Omega_{\mathrm{MW}}\alpha\right\}P_{\mathrm{LZ}} \tag{4.13}$$

and extract the Rabi frequency $\Omega_{\mathrm{MW}} \approx 2\pi\times 9.9(4)\,\mathrm{kHz}$ and a dephasing rate $\Gamma_{\mathrm{MW}} \approx 2\pi\times 51(1)\,\mathrm{Hz}$ (solid line in Figure 4.12). Finally, we choose $\Delta_{\mathrm{MW}} = 2.5\,\mathrm{MHz}$, $\tau_{\mathrm{MW}} = 5\,\mathrm{ms}$ yielding a fidelity $\epsilon = 0.98(3)$.

CHAPTER 5

High resolution absorption imaging

In quantum gas experiments, results are typically accessed through images of atomic distributions. Over the last two decades, several techniques have been developed to infer physical observables from these images. In time-of-flight experiments, the momentum distribution of quantum gases is obtained from a measurement of the density distribution measured after ballistic expansion. This detection technique has been employed to observe the formation of Bose-Einstein condensates [16] and degenerate Fermi gases [17]. Time-of-flight imaging of bosonic atoms in optical lattices led to the observation of a phase transition from an incoherent Mott-insulating state to a coherent superfluid many-body state [22]. An alternative approach are *in-situ* imaging techniques, which yield the real space density distribution of a trapped atomic cloud. Sufficient optical resolution provided, these techniques allow to measure local properties of the system instead of integrating over different regions of the spatially varying trapping potential. The additional knowledge of the trapping potential allows to study the equation of state, which fully determines the thermodynamic properties of the many-body system. In previous studies, this approach was used to investigate the unitary Fermi gas [104] and to study the BEC-BCS crossover in a two-dimensional Fermi gas [105]. Recently, a number of groups implemented quantum gas microscopy in Fermi gas experiments, which is based on the detection of atomic fluorescence [33–35, 106]. In parallel to the work presented in this thesis, several of these groups reported on site resolved investigations of the two-dimensional Hubbard model [37, 107].

The following sections focus on our high resolution absorption imaging system. To begin with, Section 5.1 explains the working principle of absorption imaging, which is based on the Beer-Lambert law. Corrections of the Beer-Lambert law in the saturated imaging regime and their calibration are presented. Thereafter, Section 5.2 introduces the imaging setup. Finally, Section 5.6 presents a characterisation of the imaging system's performance in terms of the magnification and the modulation transfer function.

5.1 The modified Beer-Lambert law

In Chapter 2, we have discussed the interaction between light and matter to derive the optical dipole force. We also observed the existence of a dissipative term, which we associated with heating due to the absorption and emission of photons 2.19. The very same mechanism is also routinely applied in order to infer atomic densities via the absorption of resonant light from a probe beam. To probe the atoms, we resonantly excite the $|F = 9/2, m_F = -9/2\rangle \rightarrow |F = 11/2, m_F = -11/2\rangle$ transition on the D2-line $4^2S_{1/2} \rightarrow 4^2P_{3/2}$ using σ^- polarised light. Since this transition is closed, the imaging process may be

described as a resonantly driven two-level system with the intensity dependent cross section [62]

$$\sigma(I) = \frac{\sigma_0}{1 + (2\Delta/\Gamma)^2 + s} \,. \tag{5.1}$$

Here, $\Delta = \omega_L - \omega_0$ is the detuning between imaging beam with angular frequency ω_L to the atomic transition with an energy difference $\hbar\omega_0$; Γ is the natural line width of the D2-line and the imaging saturation $s = I/I_{sat}$ is the ratio between the probe beam intensity I and the saturation intensity

$$I_{sat} = \frac{\hbar\omega_0\Gamma}{2\sigma_0} \,, \tag{5.2}$$

where the resonant cross section σ_0 depends on the imaging wavelength λ_{D2} via

$$\sigma_0 = \frac{3\lambda_{D2}^2}{2\pi} = 0.2807\,\mu m^2 \,. \tag{5.3}$$

This yields a saturation intensity of $I_{sat} = 17.50\,W\,m^{-2}$.

In the following, we derive the Beer-Lambert law and take into account saturation effects, which are important for intense probe beams. To this end, we consider a beam of intensity I which propagates through a medium of density $n(x, y, z)$ on a path dz. The resulting change of intensity due to absorption in the medium is described by the differential equation

$$\frac{dI(x, y, z)}{dz} = -\sigma(I)n(x, y, z)I(x, y, z) \,. \tag{5.4}$$

In the limit of negligible saturation, Equation 5.4 yields the usual Beer-Lambert law relating the optical density to the logarithm of the transmission through the medium [46]. However, when the saturation is *not* negligible, the intensity dependence of the cross section introduced in Equation 5.1 has to be taken into account. Upon integrating Equation 5.4, the optical density $od(x, y)$ is expressed by the modified Beer-Lambert law [108]

$$od(x, y) = \sigma_0 n(x, y) = -\alpha \ln\left(\frac{I_f(x, y)}{I_i(x, y)}\right) + \frac{I_i(x, y) - I_f(x, y)}{I_{sat}^0} \,. \tag{5.5}$$

In this expression, $n(x, y) = \int n(x, y, z)\,dz$ is the column integrated density; I_i and I_f are the intensities of the probe beam before and after being transmitted through the optical cloud, respectively; In addition, we have introduced the factor α to account for possible modifications of the optical cross section due to, e.g. imperfect polarisation of the probe beam or the collection of forward scattered light. An independent calibration of α is presented in Section 5.3.

5.2 High resolution imaging system

The imaging setup is shown schematically in Figure 5.1. Spatially resolving the density resolution of an atomic cloud trapped in an optical lattice requires a good imaging resolution and, consequently, an objective lens with a high numerical aperture (NA). To achieve this in a cost efficient way, a commercially available aspheric lens[1] with a clear aperture of 8 mm is mounted inside the science cell. Due the small

[1] Thorlabs: Unmounted Geltech Aspheric Lens 352240-B

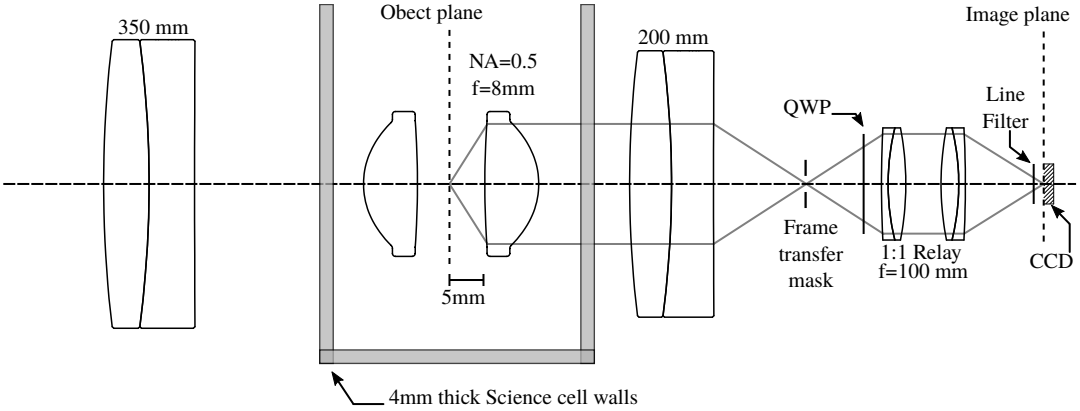

Figure 5.1: Vertical imaging system. A aspheric lens is mounted inside the science cell to image the atomic cloud. The light is brought to a primary focus at a mask to illuminate only a section of a CCD sensor. Then, a secondary focus is formed at the chip surface using a 1:1 relay.

clear aperture, the short working distance of only 5.92 mm is required to achieve a numerical aperture of NA = 0.5. As a rough estimate of the imaging quality the Rayleigh criterion[2] yields a diffraction limited resolution of $r = 1.22\lambda/\mathrm{NA} = 0.94\,\mu\mathrm{m}$. Outside the vacuum chamber, an achromatic doublet is used to set the magnification and to bring the collimated beam to a focus to form a primary image. At this focus, a mask formed by a pair of razor blades is used to define the image frame. This image is then relayed to the image plane using a 1:1 relay consisting of a pair of achromatic doublets with a focal length of 100 mm. Thereby, only a section of the sensor of a CCD camera[3] is illuminated by the imaging light. In front of the sensor, a laser line filter with a measured transmission of $T_{\mathrm{Filter}} = 0.976(4)$ at the imaging wavelength is used to filter out non-resonant light.

Frame transfer scheme

The Andor iXon888 offers a fast kinetics mode. This mode allows to record multiple images in a single experimental run. To this end, the camera is equipped with a large 1 024 pixel × 2 048 pixel CCD sensor, half of which is covered and serves as a storage area. In order to record three consecutive images, the image frame defined at the primary focus is chosen to cover only a third of the full chip. Before the image acquisition starts, the CCD chip is potentially exposed to stray light. To avoid the accumulation of background signal during this time, the camera employs a "keep clean cycle". In this mode, the chip is constantly read out and thereby cleaned of charges until the exposure starts. Figure 5.2 shows the imaging sequence schematically. Just before the image acquisition starts, atoms in $|-9/2\rangle$ are transferred to the $F = 7/2$ manifold using an adiabatic frequency sweep (cf. Section 4.4). Then, a RF sweep is applied to transfer atoms in $|-7/2\rangle$ to $|-9/2\rangle$. Upon the first trigger, the chip cleaning stops and the first image of the resonant probe beam transmitted through the atomic cloud is recorded in the illuminated section of the chip. After an exposure time T_{exp}, the acquisition stops and the accumulated charges are vertically shifted by 512 pixels such that a new image can be recorded in the illuminated section. We found that using a rather slow vertical shift speed (6.5 µs/row) results in the best signal-to-noise ratio. During the time between the end of the first exposure and the next trigger event, atoms are transferred from the $F = 7/2$ manifold back to $|F = 9/2, m_F = -9/2\rangle$ (4.4). Upon the second camera trigger, another acquisition and

[2] Strictly speaking, the Rayleigh criterion in this form applies to incoherent fluorescence imaging. A more accurate estimate of the resolution in the case of absorption imaging is presented in Section 5.6.2.

[3] Andor iXon888

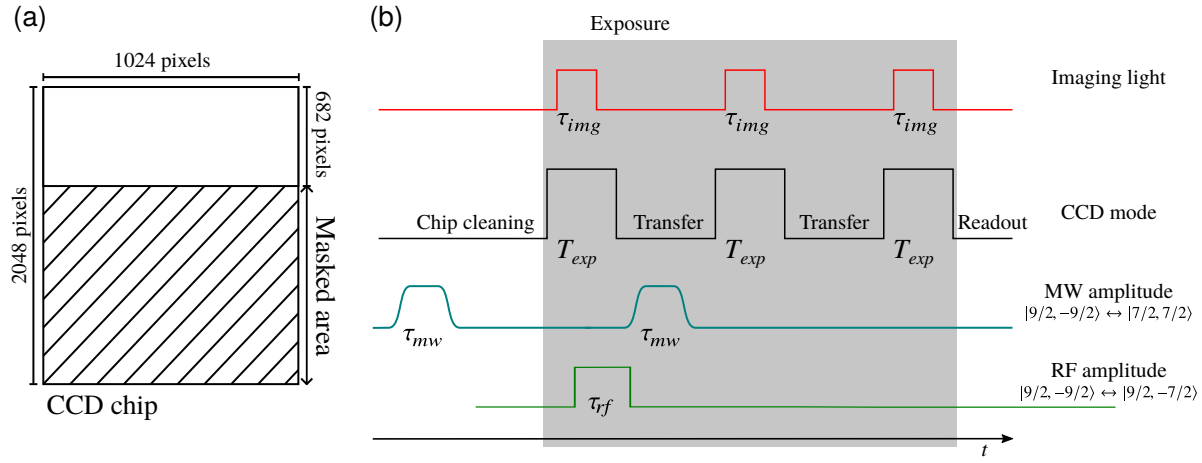

Figure 5.2: Illustration of the fast kinetics scheme. In order to take three consecutive images in each experimental run, only a third of the sensor (e2v CCD201-20) is illuminated (a). (b) Shows details of the fast kinetics imaging scheme. After each exposure, the signal in the illuminated part of the CCD chip is vertically shifted in 6.5 µs into the masked region for storage. After three exposures the full chip is read out.

transfer cycle starts. Again, the transmitted light is recorded. In a third and final image, the intensity distribution of the imaging beam in the absence of atoms is recorded. Afterwards, the full chip is read out. Note that in between the images the chip is not cleaned, which leads to an accumulation of dark current (counts) and background charges. We account for this with a set of dark images, which are recorded in the absence of imaging light but otherwise equal experimental conditions. This set of dark images is acquired in a separate measurement to obtain a dark image for each of the three images recorded in a normal measurement. In order to suppress technical noise in the dark images, we average over a large number of images and determine the average distribution of counts in the absence of imaging light.

5.3 Imaging calibration

CCD cameras yield a discretised image of the intensity distribution. Due to the linear relation between the number of counts C per pixel and the incident intensity I, Equation 5.5 may be rewritten as

$$od(x,y) = \sigma_0 n(x,y) = \sigma_0 n(x,y) = -\alpha \ln\left(\frac{C_\mathrm{f}(x,y)}{C_\mathrm{i}(x,y)}\right) + \frac{C_\mathrm{i}(x,y) - C_\mathrm{f}(x,y)}{C^0_\mathrm{sat}}. \tag{5.6}$$

In order to apply the Beer-Lambert law in the form of Equation 5.6, we calibrate the conversion from intensity in the atomic plane to number of counts at the camera. This conversion lets us express the saturation intensity I^0_sat in the number of counts C^0_sat collected during the exposure time τ_img. To find the relation between the probe beam intensity incident on the atoms and the corresponding number of counts per pixel in the recorded image, we need to know two quantities: On the one hand, the effective quantum efficiency QE_eff is needed to relate counts to photons incident on the camera chip. On the other hand, the transmission losses along the imaging path, in order to infer the intensity at the position of the atoms from the intensity measured at the position of the camera. To access the latter, we determine the transmission losses of light travelling from the atoms to a laser line filter in front of the camera (cf. Figure 5.1). We find an overall transmission of $T_\mathrm{Path} = 0.847$ at the imaging wavelength $\lambda_\mathrm{img} = 766.7\,\mathrm{nm}$. Next, we calibrate the effective quantum efficiency of the CCD chip. To this end, we create a small beam

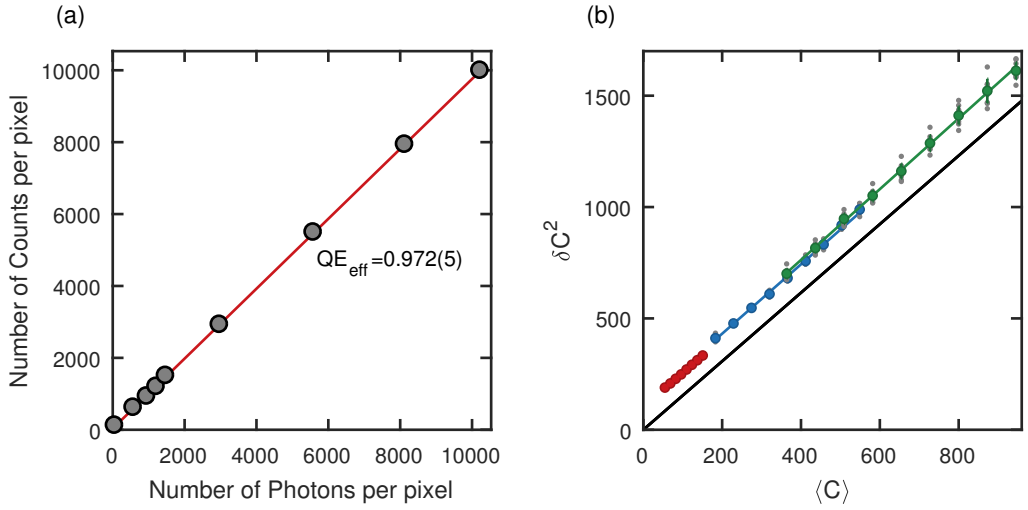

Figure 5.3: CCD camera characterisation. (a) Shows the calibration of the effective quantum efficiency of the CCD camera. (b) The pre-amplifier gain is determined from a measurement of the on imaging noise in relation to the intensity of the imaging beam. Different colours represent measurements with different total power in the imaging beam.

of uniform intensity to calibrate the voltage V_{PD} measured on a photo diode after the imaging fibre output to the power measured in front of the line filter P_{LF} and obtain a conversion factor $V_\gamma = V_{\mathrm{PD}}/P_{\mathrm{LF}}$. Now, we simultaneously record the number of counts C and the voltage during the pulse to obtain the number of photons

$$N_\gamma = \frac{V_\gamma \int_0^\tau V_{\mathrm{PD}}(t)\,\mathrm{d}t}{T_{\mathrm{Path}}} \frac{1}{\hbar\omega} \,. \tag{5.7}$$

in the atomic plane. Finally, for N_γ photons in the object plane the number of recorded counts is

$$C = \mathrm{QE}_{\mathrm{eff}} N_\gamma T_{\mathrm{Path}} T_{\mathrm{LF}} + \mathrm{const.}\,, \tag{5.8}$$

where $\mathrm{QE}_{\mathrm{eff}}$ is the effective quantum efficiency of the camera. Figure 5.3 shows the determination of $\mathrm{QE}_{\mathrm{eff}}$ from a measurement of the number of counts as a function of the photon number. For the measurement, we vary the power of the probe beam, while keeping the pulse duration $\tau_{\mathrm{img}} = 5\,\mu\mathrm{s}$ fixed. In addition, we remove a constant background using the number of counts in a region outside the apertured beam. A fit to Equation 5.8 yields

$$\mathrm{QE}_{\mathrm{eff}} = 0.972(5)\,. \tag{5.9}$$

With the effective pixel size $A = (13\,\mu\mathrm{m})^2/M = (0.574\,\mu\mathrm{m})^2$[4] in the object plane, we find that $C^0_{\mathrm{sat}} = 92(9)$ counts per pixel correspond to the saturation intensity I^0_{sat}. In order to validate this result, we compare the measured effective quantum efficiency to the quantum efficiency QE of the chip. The effective quantum efficiency is the quantum efficiency of the chip enhanced by the gain stage of the camera $\mathrm{QE}_{\mathrm{eff}} = g\mathrm{QE}$, where g is the pre-amplifier gain. We determine g with an independent measurement of the imaging shot noise. Provided that photon shot noise dominates over technical noise sources, we expect the photon statistics to follow the Poisson distribution of a coherent light source and, thus, $\delta N_\gamma^2 = N_\gamma$. The quantum efficiency is the likelihood that a photon incident on the chip surface will create a photo electron $\langle N_{\mathrm{e}}\rangle = \mathrm{QE} \times \langle N_\gamma\rangle$. This is a stochastic process, which preserves the original Poisson statistics, i.e.

[4] An independent measurement of the magnetisation M is presented in Section 5.6.1.

$\delta N_e^2 = N_e$. Secondary electrons are created in an amplifying stage with a gain factor g to enhance and digitalise the signal into counts $\langle C \rangle = g \times \langle N_e \rangle$. Now however, since the gain is just a multiplicative factor, the statistics of the counts is not described by a Poisson distribution any more. Instead, we find $\delta C^2 = g \times \langle C \rangle$ [109]. To verify this relationship, we illuminate the CCD with a diverging beam of imaging light and determine the noise characteristics. To compensate optical etaloning effects arising from the window in front of the CCD chip, we evaluate the noise on the difference of two consecutively recorded images. To this end, we bin the spatially varying intensity into classes of homogeneous average intensity and compute the variance in these bins. Figure 5.3 displays the result of such a measurement. We find that the variance depends linearly on the average number of counts and scales with the expected gain of $g = 1/0.65$. With this measurement, the quantum efficiency of the chip becomes $\mathrm{QE} = \mathrm{QE}_{\mathrm{eff}}/g = 0.63$, which agrees well with the value reported in Ref. [110] for our camera model.

Effective saturation intensity

In the experiment, the observed cross section σ_{eff} may be reduced from the ideal cross section $\sigma_0 = 3\lambda^2/2\pi$ for a variety of reasons. For example, due to the high numerical aperture of our high-resolution imaging system, we expect to collect a fraction

$$\Omega = 2\pi \left[1 - \cos\left(\sin^{-1}(\mathrm{NA})\right)\right] /4\pi \tag{5.10}$$

of forward scattered light. This can be taken into account as a reduction of the scattering cross section by $(1 - \Omega)$ In the modified Beer-Lambert law [111]. For our NA = 0.5, we find $\Omega \approx 0.07$. In addition, we image atoms which are trapped in a lattice and should consider the Franck-Condon factors given by the overlap of the wave functions of the initial and final state. The relevant Wannier functions vary, since the ground and excited state of the imaging transition experience different trapping potentials at the chosen lattice wavelength. Again, we may expect that this effect leads to a reduction of the cross section. Other relevant effects include the pureness of the imaging beam polarisation, the linewidth of the imaging laser and the dynamic change of the detuning due to the Doppler shift experienced by the atoms during imaging. As a consequence, we have to calibrate the effective saturation intensity $I_{\mathrm{sat}}^{\mathrm{eff}} = \alpha I_{\mathrm{sat}}^0$ in the Beer-Lambert formula 5.6. For this purpose, we repeatedly image atomic distributions prepared under identical conditions with a range of different imaging intensities [108]. We vary the intensity by choosing the imaging pulse duration in the range $1.5\,\mu\mathrm{s} \leq \tau_{\mathrm{img}} \leq 10\,\mu\mathrm{s}$ while keeping the total number of incident photons constant. In order to calibrate α under typical experimental conditions, we realise the repulsively interacting Hubbard model at a field of 189 G ($U/t \approx 8.2$) and record the distribution of singly occupied lattice sites. In this configuration, the recorded density reaches an occupation of almost one atom per lattice site (Mott insulator) in a ring surrounding the centre of the trap and gradually changes to zero in the wings of the distribution. Figure 5.4 shows the low intensity term in Equation 5.6 as a function of the high intensity term. The data have been binned into classes according to regions of equal potential, in which the density is expected to be constant. Finally, we fit a line to the data in each of the bins. The slope of this fit yields the effective saturation intensity expressed in counts $C_{\mathrm{sat}}^{\mathrm{eff}}$ per 5 µs. However, for optical densities realised in our experiment, we find $C_{\mathrm{sat}}^{\mathrm{eff}} = \text{const.}$ (see Figure 5.4(b)). A weighted average over $od \geq 0.1$ yields

$$C_{\mathrm{sat}}^{\mathrm{eff}} = 115(2)\,. \tag{5.11}$$

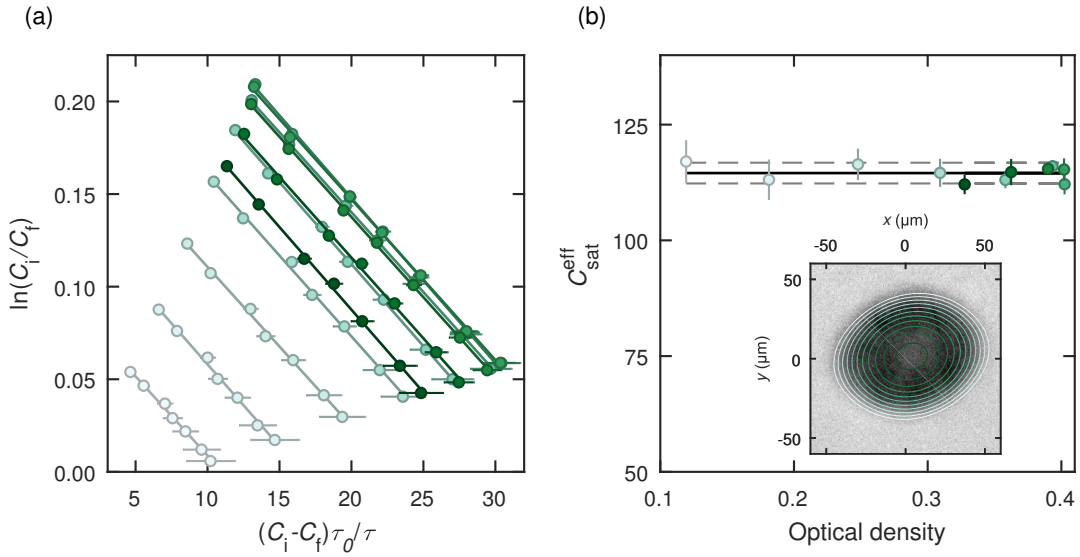

Figure 5.4: Calibration of imaging parameters. In (a), we plot the low intensity term as a function of the linear high intensity correction binned according to the apparent optical density (different colours). The data in each bin is fitted by a straight line to extract the number of counts $C_{\mathrm{sat}}^{\mathrm{eff}}$ corresponding to the effective saturation intensity. (b) $C_{\mathrm{sat}}^{\mathrm{eff}}$ as a function of the optical density. The solid and dashed lines indicate the weighted mean and standard deviation from averaging over all optical density bins with $od \geq 0.1$. Error bars are obtained from the fit error of the linear fit to the data in (a). The inset in (b) shows a map of the average optical density; the contours show regions of equal potential according to which we bin the optical density.

Together with the calibrated value of C_{sat}^{0}, this results in the high intensity correction factor

$$\alpha = \frac{C_{\mathrm{sat}}^{\mathrm{eff}}}{C_{\mathrm{sat}}^{0}} = \frac{115(2)}{91(9)} = 1.3(1)\ . \tag{5.12}$$

The dominating uncertainty on the calibrated value results from the estimated error of 10% on absolute intensities measured with the commercial power meter used to calibrate C_{sat}^{0}.

5.4 Contributions to noise in absorption images

When choosing imaging parameters, one figure of merit is the minimisation of noise arising from the imaging process. Several sources contribute to the overall noise: First, the electronic properties of the CCD camera lead to read out noise, which is only a small contribution to the overall noise for the chosen camera model. Second, small particles on elements in the beam path give rise to complicated patterns. Ideally, these would vanish in the calculated transmission maps. However, the patterns in two successively recorded images may vary. Usually, this is caused by mechanical vibrations of optical elements in the setup or insufficient frequency stability of the imaging laser. The variation of the pattern is often a dominant contribution to the overall noise. By reducing the time in between the first and third (second and third) exposures to 21.4 ms (7.6 ms), we were able to reduce the visibility of fringes. As an alternative procedure, numerical post processing of the images could be applied to reduce the visibility of these patterns further[112].

The remaining source of noise is photon shot noise. Photon shot noise arises from the statistics of the

imaging beam itself and is therefore unavoidable. However, apart from averaging over a large dataset, we may reduce its impact on the measurements by a suitable choice of imaging parameters. To this end, we derive the variance of the optical density from Equation 5.5 using Gaussian error propagation and find

$$\delta od^2 = \left[\frac{\alpha}{C_\mathrm{i}} + \frac{1}{C_\mathrm{sat}^0}\right]^2 \delta C_\mathrm{i}^2 + \left[\frac{\alpha}{C_\mathrm{f}} + \frac{1}{C_\mathrm{sat}^0}\right]^2 \delta C_\mathrm{f}^2 \,. \tag{5.13}$$

To understand the contribution of the shot noise to the variance of the optical density, we will now consider the case without atoms, i.e. $C = C_\mathrm{i} = C_\mathrm{f}$. In this limit, Equation 5.13 simplifies to

$$\delta od^2 = 2\left[\frac{\alpha}{C} + \frac{1}{C_\mathrm{sat}^0}\right]^2 \delta C^2 \,. \tag{5.14}$$

The photonic contribution to the variance of the optical density is evaluated on a set of images recorded with varying intensity and exposure time in the absence of atoms. These images are processed according to Equation 5.5 to yield the optical density. The variance of the optical density is then determined from a central region within the images, where the intensity is approximately constant. In Equation 5.14, the variance of the measured counts $\delta C^2 = \delta C_0^2 + \delta N_\mathrm{d}^2$ includes both the variance of counts δC_0^2, which reflects the statistics of the imaging beam and technical noise sources, as well as a contribution from the variance of dark counts δN_d^2. We independently measure a mean number $N_\mathrm{d} = 87$ of dark counts per pixel, which we subtract from all images in the data analysis and $\delta N_\mathrm{d}^2 = 77(4)$. Figure 5.5 shows the measured variance of the optical density for different imaging times τ_img and saturations $s = I/I_\mathrm{sat}^\mathrm{eff}$. For the comparison to Equation 5.14 in Figure 5.5 we assume a shot noise limited imaging beam, i.e. $\delta C^2 = g\,\langle C\rangle$. In general, we observe a reduction of noise with increasing τ_img, which is associated to the suppression of the linear term in Equation 5.6 for longer imaging pulse durations due to the increase in C_sat^0. In addition, each of the curves shows a minimum around $s \approx 1.5$, which is identified as the optimal imaging intensity in terms of shot noise. In our experiment, the contribution from atoms to the shot noise is almost negligible due to the small densities realised in the optical lattice. Therefore, applying Equation 5.14 gives a good estimate of the signal-to-noise ratio (SNR). At half filling and for an imaging beam with $s = 1.5$ and $\tau_\mathrm{img} = 10\,\mu\mathrm{s}$, we estimate $\mathrm{SNR} = \frac{od}{\delta od} \approx 1.3$. From the observations presented in this section, it is straight forward to conclude that long imaging pulses are ideal to achieve a low level of noise and, thus, a high signal-to-noise ratio. However, we must respect the dissipative nature of the imaging process to find adequate imaging parameters.

5.5 A suitable choice of imaging parameters

The absorption of photons from the imaging beam leads to a momentum transfer to the atoms. Therefore, the atom is accelerated and experiences a Doppler shift. To estimate the corresponding displacement, we consider the momentum transfer from an imaging beam to a free atom at rest [113]. Each absorbed photon transfers a momentum $\hbar k_\mathrm{img}$. Together with the scattering rate

$$\gamma = \frac{\Gamma}{2}\frac{s}{1 + s + 4\delta^2/\Gamma^2}\,, \tag{5.15}$$

this yields the acceleration $a = \hbar k_\mathrm{img}^2 \gamma/2m$. At the end of the imaging pulse, the atoms have acquired a velocity $v = a\tau$ and, thus, experienced a Doppler shift of $k_\mathrm{img} v$. To avoid that the atoms are shifted out

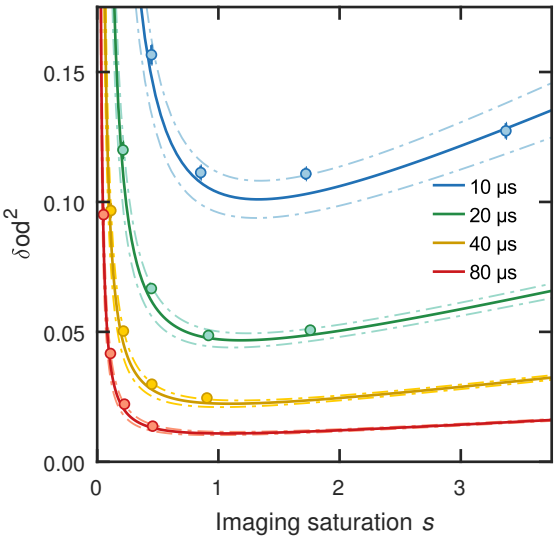

Figure 5.5: Shot noise contribution to the variance of the optical density δod^2 as a function of the imaging beam saturation s for different imaging pulse durations τ_{img} (legend). Error bars denote the standard error of the variance. Solid lines show the prediction of Equation 5.14 applying the imaging beam parameters as well as the calibrated values for α, C^0_{sat}, the measured dark current noise δN_{d} and assuming a shot noise limited imaging beam. Dashed dotted lines show the standard error of the model propagating the error on α and C^0_{sat}.

of resonance with the imaging laser, we need to restrict the imaging time and intensity, such that the Doppler shift remains well below the power broadened line width $\Gamma\sqrt{1+s}$. Solving $k_{\mathrm{img}}v = \Gamma\sqrt{1+s}/4$ for τ_{img} yields a Doppler limit of

$$\tau_{\mathrm{D}} = \frac{1}{4}\frac{2m}{\hbar k^2_{\mathrm{img}}}\sqrt{s(1+1/s)^3}, \tag{5.16}$$

For an intensity of $2I^{\mathrm{eff}}_{\mathrm{sat}}$, this yields an upper limit of $\tau_{\mathrm{D}} = 12.78\,\mu\mathrm{s}$ for the imaging pulse duration.

A second bound on the imaging parameters is set by the diffraction limited depth of focus $d_{\mathrm{dof}} = \lambda/\mathrm{NA}^2 = 3.1\,\mu\mathrm{m}$. The radiation force displaces the atom by $d = v\tau_{\mathrm{img}}$. Solving $d_{\mathrm{dof}} = v\tau_{\mathrm{img}}$ yields a displacement limit on the imaging time of

$$\tau_{\mathrm{dof}} = \sqrt{\frac{4}{\Gamma}\frac{m}{\hbar k}}\sqrt{1+1/s}\sqrt{d_{\mathrm{dof}}} \tag{5.17}$$

and we choose imaging parameters for which the displacement does not largely exceed this bound. In general, for our parameters $\tau_{\mathrm{dof}} < \tau_{\mathrm{D}}$. In fact, we should pause a moment to consider that, due to the constant acceleration, also the scattering rate changes during the imaging pulse. This behaviour is illustrated by the measured change of the imaging resonance as a function of both the saturation s and the imaging pulse duration τ_{img} as shown in Figure 5.7(a). For $\tau_{\mathrm{img}} \geq 10\,\mu\mathrm{s}$, we observe a blue shift of the resonance as the number of scattered photons increases with increasing saturation. This is in qualitative agreement with a numerical simulation of the line shape taking into account the dynamic change of the scattering rate

$$\frac{\mathrm{d}v}{\mathrm{d}t} = \frac{\hbar k_{\mathrm{img}}}{m}\frac{\Gamma}{2}\frac{s}{1+s+4(\delta_{\mathrm{L}} - k_{\mathrm{img}}v(t))^2/\Gamma^2} \tag{5.18}$$

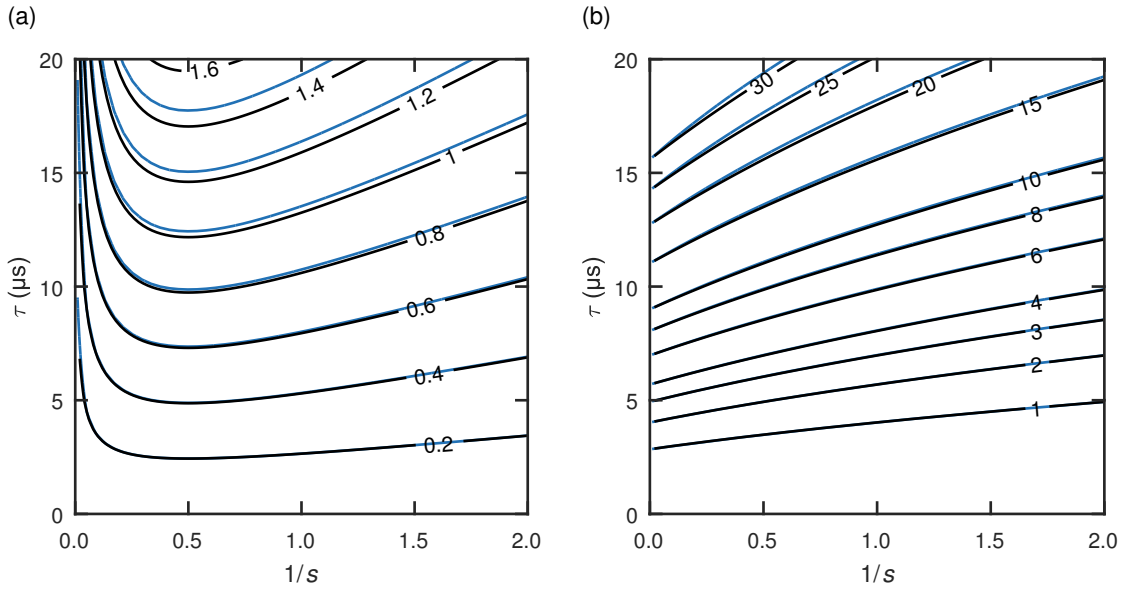

Figure 5.6: Limits on the imaging parameters for a free atom. (a) Detuning contours as a function of the inverse imaging saturation $1/s$ and the pulse duration τ. The detuning is expressed in units of $\Gamma\sqrt{(1+s)}/4$. (b) For the same parameters as in (a), we show lines of equal displacement in units of 1 µm. Black lines show the case of a static scattering rate as discussed in the main text. Blue lines show a numerical solution of Eq. 5.18.

presented in Figure 5.7(b). The experimentally observed slower initial increase of the resonance position is most likely due the reduced overlap of the wave functions in the initial and final state since the excited state experiences an approximately tenfold weaker repulsive potential of the blue detuned vertical lattice than the ground state. To estimate the influence of the changing scattering rate on the atomic dynamics, Figure 5.6 additionally shows the displacement and detuning at the end of the imaging pulse according to Equation 5.18. When the shift of the resonance is taken into account, the disagreement of the two cases is negligible for the imaging parameters applied in all the experiments presented in this thesis. Now, we consider imaging pulse durations $\tau_{\mathrm{img}} \leq 5\,\mu\mathrm{s}$ to notice a red shift of the resonance for the shortest imaging pulse durations. This may be qualitatively understood, when we remind ourselves that the atoms are actually imaged in the presence of the optical lattice potential. Therefore, the atoms are trapped at least at the beginning of the imaging pulse. Only after a number of scattering events, the atoms are heated out of the lowest band of the lattice and start to behave like free atoms. The implication of this finding is that the displacement criterion formulated above can be relaxed to some degree to allow for slightly longer and/or more intense pulses, which yield the better signal-to-noise ratio (cf. Section 5.4).

5.6 Characterisation of the imaging system

The following subsections present a characterisation of the high resolution imaging system. First, the magnification is obtained from a time-of-flight measurement of the second-order correlation function revealing the reciprocal lattice vectors. Second, the modulation transfer function (MTF) is determined through a measurement of density fluctuations of a trapped ensemble of atoms. Furthermore, we will outline the procedure to find the optimal camera position and discuss the influence of the duration of the imaging pulse on the performance of the imaging system.

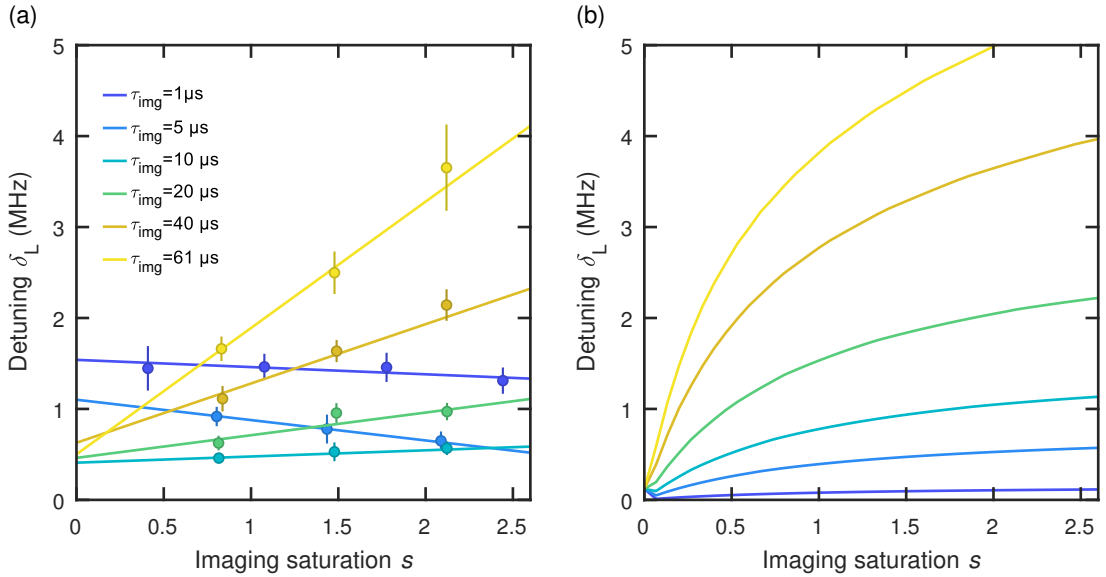

Figure 5.7: (a) We measure the line shape as a function of the saturation for variable imaging pulse durations and extract the detuning δ_L which maximises the absorption. Error bars denote the standard errors of a Lorentzian fit to the line shape. Solid lines are guides to the eye. (b) For comparison we extract the expected dependence for an initially free atom. To this end we model the effective line shape using Eq. 5.18. The maximum of the shifted line yields δ_L.

5.6.1 Magnification

In order to relate the observed optical density to the filling factor of the lattice, we must know the magnification M of the imaging system. We experimentally calibrate the magnification using a time-of-flight measurement. The scheme is based on a measurement of the fermionic anti-bunching at the reciprocal lattice vectors, which is revealed in the second-order correlation function [100, 114]. We prepare a non-interacting atomic cloud in a three-dimensional optical lattice. Before we image the cloud, the horizontal lattices are switched of rapidly and the cloud is left expanding for a variable time-of-flight. Thereby, the Bloch functions describing particles with well defined quasi-momentum $\hbar q$ in a periodic potential are projected onto plane waves propagating with real momenta $p_n = \hbar q \pm 2n\hbar k_L$. To ensure that the atomic cloud stays in the focal plane during expansion, we use a magnetic field to compensate gravity. When the ensemble is allowed to expand for a variable time t_{ToF}, the interference of the overlapping plane wave components leads to characteristic dips at positions $x_n \propto p_n t_{ToF}$. Finally, the position of the dips in the image plane depends only on the reciprocal lattice wave vectors, the magnification and the (known) time-of-flight duration (cf. Figure 5.8(a)-(d)). From a set of recorded images of the density distribution after time-of-flight, we obtain the integrated second-order correlation signal

$$C(\mathbf{d}) = \frac{\int \mathrm{d}^2\mathbf{x}\, \langle n(\mathbf{x}-\mathbf{d}/2)n(\mathbf{x}+\mathbf{d}/2)\rangle}{\int \mathrm{d}^2\mathbf{x}\, \langle n(\mathbf{x}-\mathbf{d}/2)\rangle \langle n(\mathbf{x}+\mathbf{d}/2)\rangle}\,. \tag{5.19}$$

Here, $\langle \ldots \rangle$ denote the average over multiple experimental realisations. Instead of calculating the integrals in Equation 5.19 directly, both the numerator and denominator are more efficiently evaluated using the Wiener–Khinchin theorem [115], which relates the autocorrelation function $A(\mathbf{d}) = \int S(\mathbf{x}-\mathbf{d}/2)S(\mathbf{x}+$

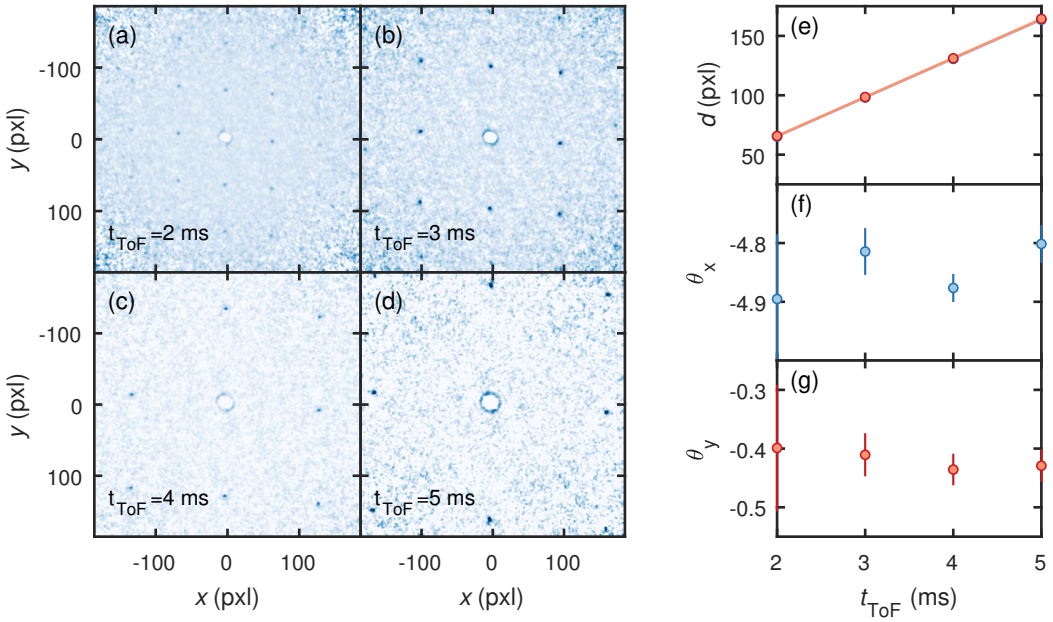

Figure 5.8: Calibration of magnification and lattice angles using the second-order correlation function. (a)-(d) show the measured second order correlation function $C(\mathbf{d})$ for varying time-of-flight duration t_{ToF}. The positions of the antibunching dips directly yield the reciprocal lattice vectors. and, thus, the angle $\theta_{\mathrm{x}}(\theta_{\mathrm{y}})$ formed by the x- and y-lattice beams with respect to the image frame. (e) The magnification along x and y is obtained from a linear fit to the displacement of the dips measured as a function of t_{ToF}. We measure $M_x = 22.64(1)$ and $M_x = 22.75(2)$. Note, that different colour scales have been used for (a,b) and (c,d) to increase the visibility of the antibunching signal. (f,g) Show the angle of the lattice beams with respect to the image frame, which was extracted from the position of the antibunching dips. These values have already been as an input in the characterisation of the external confinement in Chapter 3.

/2) d$\mathbf{x}$ of a signal $S(\mathbf{x})$ to the inverse Fourier transform of its power spectral density

$$A(\mathbf{d}) = \mathcal{F}^{-1}|\mathcal{F}[S(\mathbf{x})]|^2 \,. \tag{5.20}$$

Since the amplitude of the correlation signal depends inversely on the square root of the number of images, we typically average over around 200 experimental realisations to obtain a strong correlation signal. To evaluate the signal, we fit regularly spaced Gaussian functions, with free distance and amplitude to the two-dimensional correlation signal. The observation of dips ($C(\mathbf{d}) < 1$) is characteristic for fermionic antibunching due to the Pauli principle. Since the difference in the velocity components of a wave packet is accurately known from the wavelength of the lattice laser, the magnification of the imaging system is directly obtained from a measurement of the displacement d of the dips as a function of t_{ToF} (Figure 5.8(e)). We measure almost equal magnifications $M_x = 22.64(1)$ and $M_y = 22.75(2)$ along both axis of the imaging frame. In all of the data analysis presented later on, we use the mean $M = 22.69(1)$ of the two values. In addition, the measurement serves as a precise calibration of the angle $\theta_x = -4.85(4)\,^\circ$ ($\theta_y = -0.42(6)\,^\circ$) formed by the horizontal x-lattice (y-lattice) beam and the x (y) axis defined by the imaging frame as shown in Figure 5.8(f,g). These are a crucial ingredient to the full characterisation of the external trapping potential (cf. Chapter 3.5.4).

It has been proposed to use noise-correlations in momentum space to characterise more complex phases in cold atoms experiments. Especially for repulsively interacting fermions in optical lattices, one would expect that a doubling of the unit cell by the presence of antiferromagnetic (quasi) long-range

order manifests in the appearance of additional correlation dips at half the reciprocal lattice vectors [116, 117]. Indeed, we have recently used this signature to calibrate a method that coherently manipulates the spin-correlations using a technique building upon the Ramsey interferometry presented in Section 3.6.3. In this calibration measurement, we prepared a spin-polarised gas and imprinted a chequerboard spin pattern using the precession of the transverse spin components in a magnetic field gradient aligned to the lattice diagonal [118].

5.6.2 Measuring the modulation transfer function with density fluctuations

As mentioned above, a spatially resolved detection scheme is crucial to resolve the *in-situ* density distribution. In order to extract local thermodynamic quantities, the imaging system has to resolve variations of the density on length scales much smaller than the variation of the underlying inhomogeneous trapping potential. Even more importantly, the convolution with the point spread function obscures the correlation functions of the many-body system. Therefore, an accurate characterisation of the imaging system serves as a central input for the data analysis presented in Chapter 7.

Following Ref. [119] the modulation transfer function (MTF) can be obtained from a measurement of the power spectral density of in-situ density fluctuations. In addition, we apply this method to find the best focus of the imaging system and to determine the influence of the imaging light itself on the imaging performance.

The point spread function and optical aberrations

The result of a measurement on an ultracold gas is available as an image representing the atomic density distribution. The observed density distribution in the image plane $n_{\mathrm{exp}}(\mathbf{r})$ is thus the convolution of the actual density distribution in the lattice n_i with the point spread function $\mathcal{P}(r)$

$$n_{\mathrm{exp}}(\mathbf{r}) = \int \mathrm{d}\mathbf{r}'\, n(\mathbf{r}')\mathcal{P}(\mathbf{r}-\mathbf{r}'). \tag{5.21}$$

The CCD camera yields a discretised representation of the image. As long as the pixel area A is much smaller than the resolution spot size we may write

$$n_{\mathrm{img}}(\mathbf{r}_j) = \frac{N_j}{A} = \int \mathrm{d}\mathbf{r}'\, n(\mathbf{r}')\mathcal{P}(\mathbf{r}_j-\mathbf{r}'), \tag{5.22}$$

where $\mathbf{r}_j$ is the centre position of pixel j and N_j the atom number on this pixel. To understand the origin of the point spread function in absorption imaging, we have to recall the how the image of the atomic density is formed. To this end, we consider a single atom illuminated with a uniform light field. The incoming probe field E_0 is scattered by the atom and the resulting spherical wave is then focused by the imaging system yielding $E_{\mathrm{scatt}} = \epsilon E_0 e^{i\delta} p(\mathbf{k})$, where $p(\mathbf{k})$ is the Fourier transform of the pupil function of the imaging system, ϵ is the fraction of the scattered light collected by the objective and δ is the detuning of the probe beam with respect to the atomic transition. The interference pattern of the probe field and the scattered field $\left|E_0 + E_{\mathrm{scatt}}\right|^2$ is recorded on a CCD camera, yielding a "shadow image" of the atom. Thus, the recorded transmission through the atomic sample becomes

$$t = \frac{I_{\mathrm{f}}}{I_{\mathrm{f}}} = \left|\frac{E_0 + E_{\mathrm{scatt}}}{E_0}\right|^2 \approx 1 + \epsilon 2\,\mathrm{Re}\left\{e^{i\delta} p(\mathbf{k})\right\}. \tag{5.23}$$

The logarithm of Equation 5.23 yields the point spread function for low probe beam intensity. For non-negligible saturation, the linear term in the modified Beer-Lambert law has to be taken into account. The term may be written as

$$s(1-t) \approx s\epsilon 2\,\mathrm{Re}\left\{e^{i\delta}p(\mathbf{k})\right\}. \tag{5.24}$$

In the above approximations we assumed $\epsilon \ll 1$, which is valid for low densities and not too large NA. Further approximating $\ln(t)$ for $t \approx 1$, and combining the Equations 5.23 and 5.24, the point spread function for the optical density is found to be $\mathcal{P}(\mathbf{r}) \propto \mathrm{Re}[e^{i\delta}p(\mathbf{k})]|_{\mathbf{k}=\mathbf{r}/ad}$ [120]. In polar coordinates, the pupil function is given by

$$p(\rho,\theta) = U(\rho)e^{-\rho^2/\tau^2}e^{W(\rho,\theta)}. \tag{5.25}$$

where $U(\rho)$ describes the ideal pupil, which is constant within the aperture radius R and zero outside; The first exponential factor describes a reduced transmittance at the edge of the limiting aperture and $W(\rho,\theta)$ is the wave front of the imaging beam after passing the imaging system. For an ideal imaging system $W(\rho,\theta) = 0$ and $\tau = \infty$. In this case, the Fourier transform of the pupil function is $J_1(r/\sigma)/(r/\sigma)$, where $J_1(x)$ is the Bessel function of first kind and $\sigma = (k\mathrm{NA})^{-1}$. However, optical aberrations lead to deformations of the wave front. For typical experimental conditions, i.e. short imaging pulses and a saturation $s \approx 2$ the wave front can be approximated by

$$W(\rho,\theta) = S_0\rho^4 + \beta\rho^2 + \alpha\rho^2(\cos(2\theta - 2\phi)). \tag{5.26}$$

The individual terms in Equation 5.26 correspond to low order optical aberrations; S_0 describes spherical aberration, β the effect of defocus and α the strength of astigmatism with an angle ϕ. In the next section, we will describe a method extract the modulation transfer function from repeated images of the in-situ density distribution. Equation 5.25 fully determines the quality of the imaging system and can be used to model either the point spread function $\mathcal{P}(\mathbf{r})$ or, equivalently, the modulation transfer function $\mathcal{M}(\mathbf{k}) = |\mathcal{P}(\mathbf{k})|$ to compare to experimental measurements. While a direct measurement of the point spread function is difficult since it requires an isolated point source — for example a single atom — the modulation transfer function is more easily accessible through a measurement of the power spectral density of atom number fluctuations. Similar to Equation 5.22 connecting the real density distribution to its image, the relationship between the experimentally observed atom number fluctuation δN_j^2 at pixel j and the actual correlations is given by a convolution with the point spread function

$$\langle \delta N_j^2\rangle = \langle N_j^2\rangle - \langle N_j\rangle^2 = A^2\int\int \mathrm{d}\mathbf{r}\,\mathrm{d}\mathbf{r}'\,\langle \delta n(\mathbf{r})\delta n(\mathbf{r}')\rangle\,\mathcal{P}(\mathbf{r}_j-\mathbf{r})\mathcal{P}(\mathbf{r}_j-\mathbf{r}') \tag{5.27}$$

A discrete Fourier transform of the atom number fluctuations yields

$$\langle\left|\delta n(\mathbf{k}_l)\right|^2\rangle \approx NS(\mathbf{k}_l)\mathcal{M}^2(\mathbf{k}_l), \tag{5.28}$$

where we have introduced the density structure factor $S(\mathbf{k}) = \frac{\langle|\delta n(\mathbf{k})|^2\rangle}{N}$. In order to determine the modulation transfer function we usually measure the noise power spectrum of a non-interacting Fermi gas on a square lattice prepared at a temperature of $k_\mathrm{B}T/t = 3.5$. This yields an approximately flat structure factor up to the spatial cutoff frequency $f_\mathrm{c} = \mathrm{NA}/\lambda \approx 0.65\,\mu\mathrm{m}^{-1}$ for NA = 0.5.

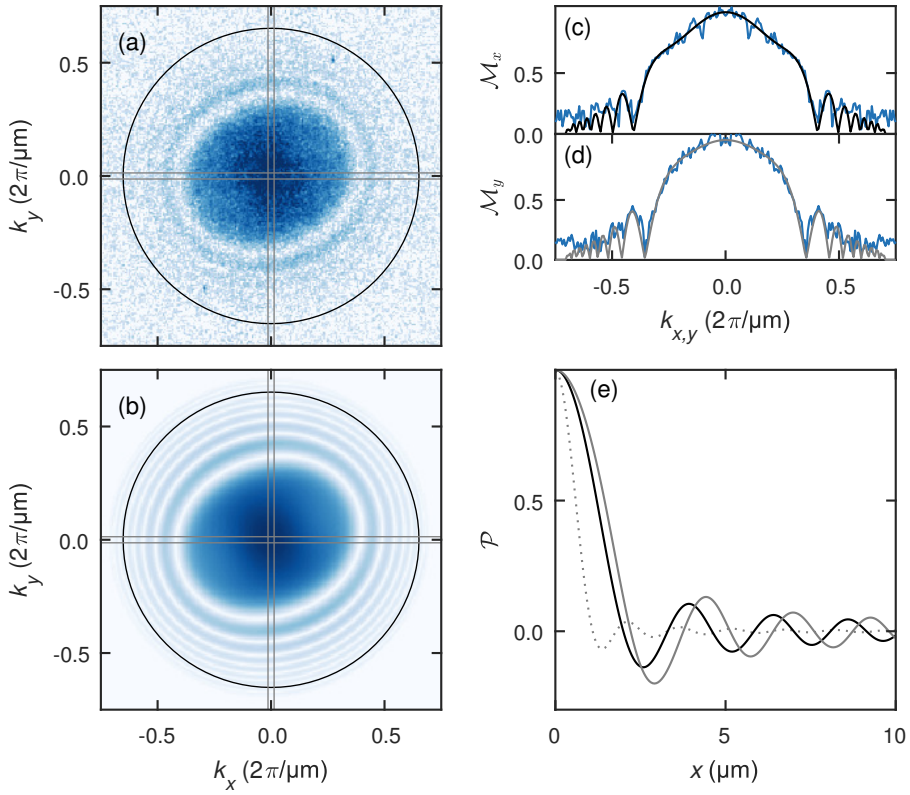

Figure 5.9: Modulation transfer function and point spread function. (a) Measured power spectral density and (b) corresponding fit to the MTF. The solid black circle in (a,e) depicts the cutoff frequency of a coherent imaging system with NA = 0.5. (c) and (d) show cuts through both the data and the fitted MTF along x and y averaged over 0.0336 µm^{-1} wide regions (grey solid lines in (a,b)). In (e), we plot cuts through the normalised PSF along x (black) and y (grey) evaluated on a fine grid using the coefficients extracted from (b) yielding a resolution of 1.25 µm (HWHM). The grey dotted line is a comparison to the diffraction limited point spread function.

Finding the optimal camera position

Having introduced a method to measure the MTF, we proceed by determining the focal position of the camera. To this end, we measure the power spectral density of the atom number fluctuations as a function of the camera position along the optical axis. Figure 5.10 presents a result of this measurement evaluating the in-situ density noise on a set of 60 images at each position together with a fit to to determine the defocus parameter β. We find that β scales approximately linear with the camera position (Figure 5.10(k)). Furthermore, we determine $S0 = 25.5(8)$, $\alpha = 2.4(1)$, $\phi = 1.9(1)$. Note, that the optimal focal position is not where $\beta = 0$. Instead, a finite amount of defocus ($\beta \neq 0$) is required to compensate for the observed spherical aberrations. We determine the best focal position by varying the position of the Andor camera along the optical axis in order to optimise the measured MTF. In daily operation, we average over only 10 images to accelerate the procedure and use the size and homogeneity of the central region of the power spectral density as a figure of merit for the resolution to find the best focus. We routinely check the focal position before performing experiments and calibration measurements.

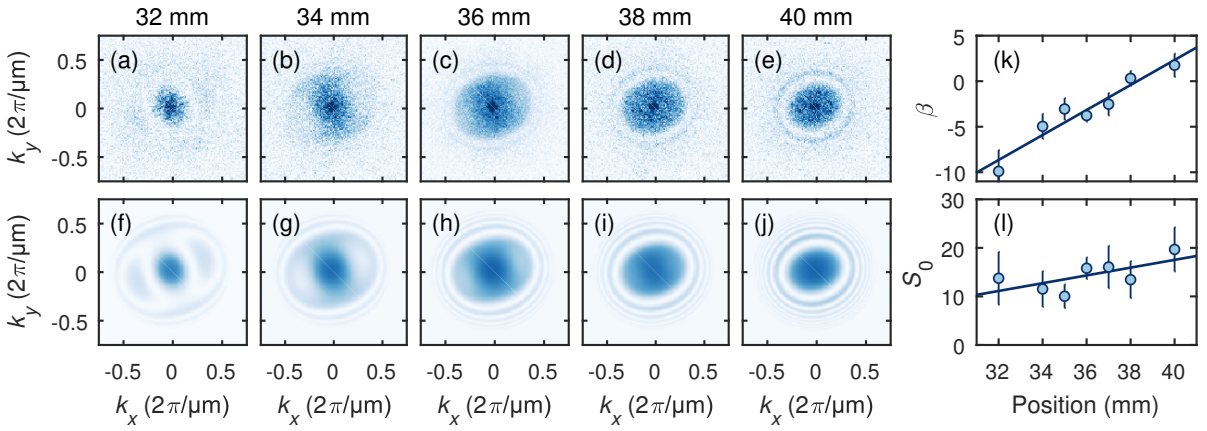

Figure 5.10: Illustration of the focusing technique. In (a), the response of the measured power spectrum (a-e) to a change of camera position and the corresponding fits to the squared MTF $\mathcal{M}^2$ (f-j) are shown. In (k), we demonstrate the linear dependence of the defocus parameter β on the position of the camera along the imaging beam propagation. The solid line is a guide to the eye.

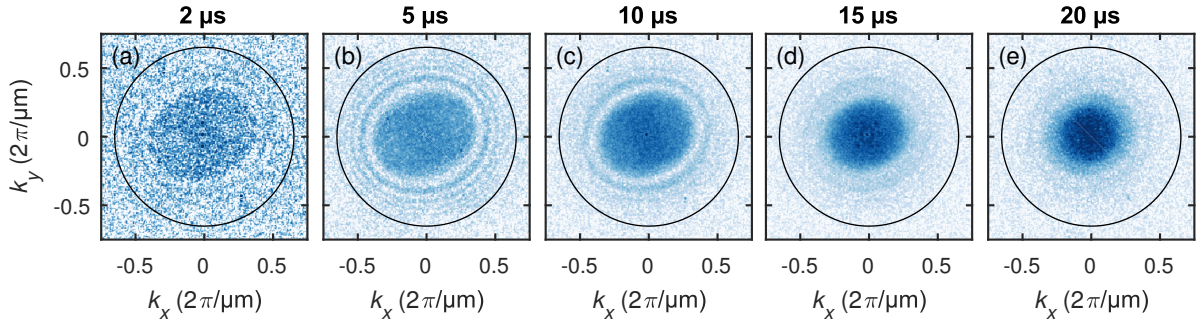

Figure 5.11: Influence of the pulse duration on the resolution. (a-e) show the MTF for varying imaging pulse duration. The diffraction limited cutoff frequency is indicated by black black circles.

Influence of the atomic motion on the modulation transfer function

Not only optical aberrations but also the dynamics of the imaged atoms influence the imaging quality. In Section 5.5, we discussed the acceleration of free atoms in the direction of the objective lens due to the resonant interaction with the probe light. Here, we concentrate on the consequences of these dynamics on the resolution. To this end, Figure 5.11 presents a measurement of the square root of the *in-situ* density noise power spectrum as outlined above. We vary the imaging pulse duration for approximately fixed imaging intensity. We observe that longer pulses result in a suppression of larger spatial frequencies. This can be explained with the displacement of the atomic cloud towards the objective lens resulting in increased defocusing for longer imaging pulses. At the same time, we recover the statement that a longer imaging pulse duration results in a better signal-to-noise level, since the number of photons contributing to the signal is increased. However, in order to make full advantage of the high-resolution imaging system we must find a compromise between resolution and noise. Therefore, we restrict the imaging pulse duration to $5 \leq \tau \leq 10\,\mu s$ for all the experiments presented later on.

CHAPTER 6

Probing the equation of state of the two-dimensional Hubbard model

This chapter presents results published in "Equation of State of the Two-Dimensional Hubbard Model" by E. Cocchi, L. A. Miller, J. H. Drewes, M. Koschorreck, D. Pertot, F. Brennecke and M. Köhl (see Ref. [96]) and closely follows the presentation therein.

The following chapter presents a measurement of the equation of state of the two-dimensional Hubbard model. Our approach combines the precise control over the Hamiltonian offered by optical lattices with a high resolution imaging system. This allows to probe the many-body system locally in order to study the quantum phases and thermodynamic properties of the trapped gas in a quantitative way. Furthermore, the results presented in this chapter provide the basis for thermometry in Chapters 7 and 8.

Section 6.1 motivates our work and highlights its relation to previous studies. Section 6.2 presents the measurement scheme and summarises the data analysis. An in-depth discussion of the data analysis and, in particular, the fitting procedure to compare our results to numerical data are presented in the theses of my co-workers L. A. Miller [85] and E. Cocchi [95]. In Section 6.3 the results of the measurement are presented.

6.1 Motivation and previous work

Ultracold fermionic atoms have emerged as a versatile platform to study strongly-correlated spin-1/2 fermions since they submit to a precise microscopic description and superbly sensitive detection. This approach has shed new light, for example, on the crossover between a Bose-Einstein condensate (BEC) of dimers and a Bardeen-Cooper-Schrieffer (BCS)-type superconductor as well as on the universal physics of the unitary Fermi gas [121]. Among the remaining open questions are the properties of strongly-interacting fermions in lattices, which have begun to be explored [23, 24, 26, 94, 122–124].However, these investigations have not yet achieved the same level of accuracy in determining quantum phases and thermodynamic properties as those without lattice [31, 32]. The experimental determination of the equation of state of the Hubbard model is of particular importance because, even with the most advanced theoretical methods, strongly-correlated lattice models are notoriously hard to tackle [13, 125]. Recently developed numerical approximations of the two-dimensional Hubbard model [74, 126] provide predictions for a range of parameters. However, the inherent difficulty of simulating strongly-correlated fermions has yet precluded the determination of a general phase diagram, and the predictions resulting from the approximations still require experimental verification.

Previously, investigations of the Hubbard model with ultracold atoms have mostly focused on the Mott insulator in three dimensions by detecting the global disappearance of doubly occupied sites [23, 123, 127], the response to an external compression [24], the analysis of reconstructed density profiles [124], and global detection of local spin correlations [25, 128]. However, unlike homogeneous solid state systems, ultracold atoms are usually confined by an external trapping potential $V(\mathbf{r})$ leading to a spatially varying density distribution $n(\mathbf{r})$. Therefore, different quantum phases coexist in different regions of the trap and their unique identification using global observables is often impossible. Conversely, with sufficient local resolution, the coexistence of different phases can in principle be used to sample a range of the phase diagram in a single experimental realisation. For bosonic [28–30] and, recently, fermionic [107, 124, 129] atoms in optical lattices the coexistence of different phases has been observed.

6.2 Measurement scheme

In the experiment presented here, we demonstrate high-resolution in-situ absorption imaging of a spin-balanced mixture of interacting spin-1/2 fermionic atoms in a single, two-dimensional layer of an optical lattice (see Fig. 6.1(a)). By combining narrow linewidth RF spectroscopy (cf. Chapter 4.2.3) and absorption imaging (cf. Chapter 5) we detect the density distributions of singles $\langle \hat{n}_\uparrow - \hat{n}_\uparrow \hat{n}_\downarrow \rangle$ and doubles $\langle \hat{n}_\uparrow \hat{n}_\downarrow \rangle$. The analysis of the spatially resolved density distribution gives direct access to the equation of state [27] $n(\mu)$. In particular, our technique does not rely on density reconstruction through inverse Abel transforms [124], which introduce numerical noise at small radii. Our experiments cover the regimes from weak ($U/t \simeq 0$) to strong ($U/t \simeq 20$) interactions and, where available, we compare to state-of-the-art numerical results.

Figure 6.1 shows examples of the recorded singles and doubles density profiles for different interaction strengths. For each of the figures shown the data have been averaged over approximately 35 individual experimental realisations. For weak interactions, $U/t = 1.6(2)$, we observe an inhomogeneous density distribution (Figure 6.1a). In the centre of the trap, where the density is largest, we find an accumulation of doubles. This dense core is surrounded by a low-density ring where predominantly singles form. For intermediate interactions, $U/t = 8.2(5)$, the doubles are suppressed by the increased interaction energy and, correspondingly, the size of the cloud increases (Figure 6.1(b)). Finally, for strong interactions, $U/t = 12.0(7)$, we do not observe any doubles and a pronounced plateau forms around half filling, which signals the appearance of the Mott insulator (see Figure 6.1(c)). Employing the precise knowledge of the slowly varying trapping potential $V_T(x, y)$ caused by the finite Gaussian waists of the optical lattice beams (cf. Chapter 2) enables us to average the measured density along equipotential contours, see Figures 6.1(d-f).

6.3 The equation of state and the crossover from a metal to a Mott-insulator

6.3.1 From the in-situ density distribution to the equation of state

In order to access the equation of state of the 2D Hubbard model and to directly determine local thermodynamic properties of the gas [27, 29, 31, 130], we analyse our data in the framework of the local density approximation (LDA). We noted above that the local chemical potential $\mu(x, y)$ results from the chemical potential at the centre ($x = y = 0$) of the cloud μ_0 and the trapping potential by $\mu(x, y) = \mu_0 - V(x, y)$. LDA state that the properties of the homogeneous system with $\mu(x, y)$ can be locally applied as long as the change in the potential is small compared to characteristic length scales of

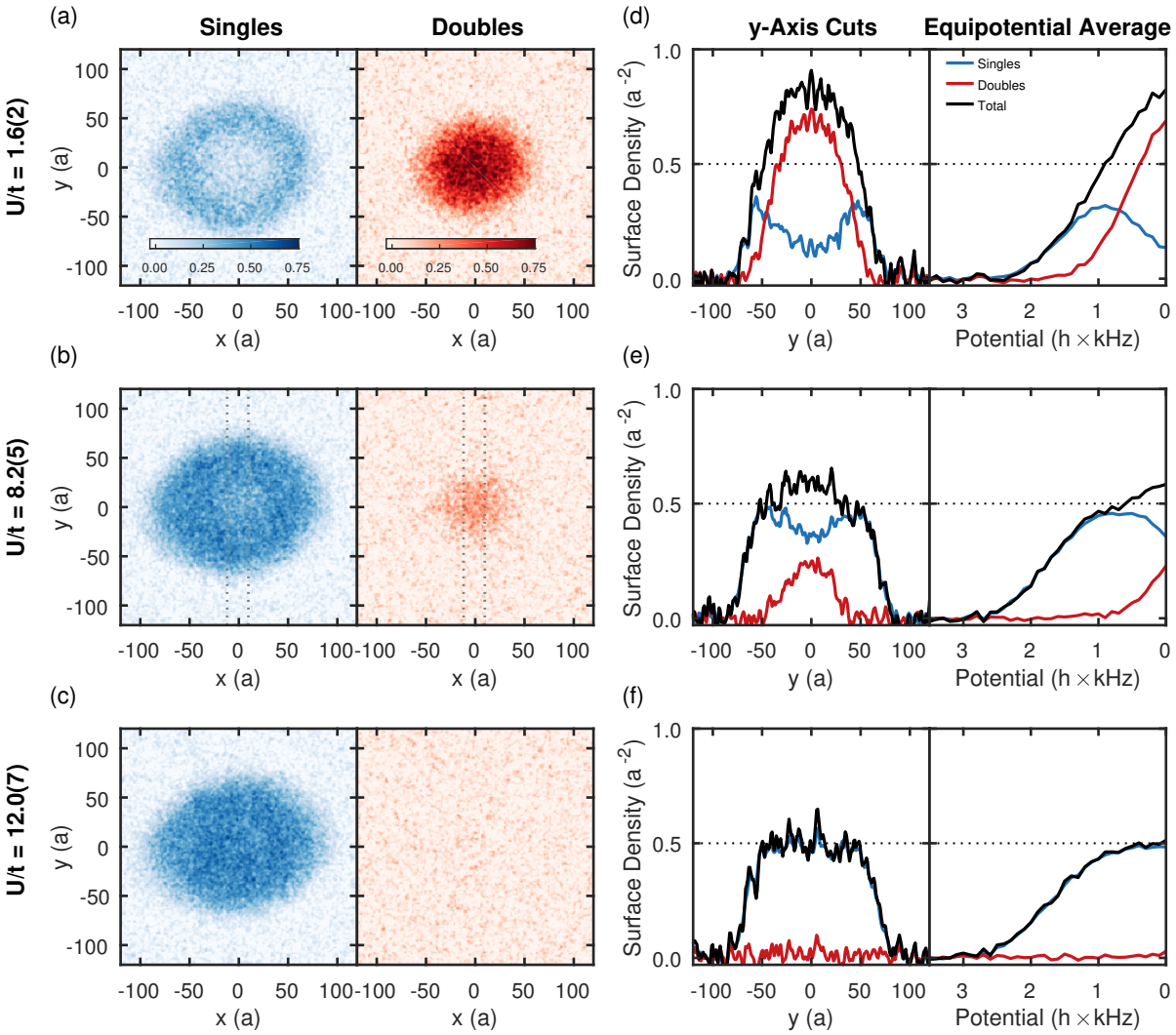

Figure 6.1: In-situ distribution of singly and doubly occupied lattice sites. (a-c) Maps of the in-situ density of singles and doubles in the two-dimensional Hubbard model for different interaction strengths. The images are averaged over ~ 35 repetitions of the experiment. The density profiles show the crossover from a metal at weak interactions, $U/t = 1.6$, to a flat-top Mott insulator without doubles at strong interaction $U/t = 12.0$. (d-f) Singles, doubles, and total density averaged over $-10a \leq x \leq 10a$ (see dashed lines in (b)) as well as evaluated along equipotential contours of the trapping potential.

the many-body system, e.g. the correlation length. In the following list, we translate the recorded density maps $n(x, y)$ to the equation of state $n(\mu)$ and the comparison thereof to numerical data will be outlined.

1. The precise knowledge of the external potential $V(x, y)$ allows to average the recorded spatial maps of the singles and doubles density distributions along equipotential contours. Note, that we independently calibrated a reduced relative fidelity $\eta_\mathrm{d} = 0.82(2)$ in the detection of doubles as compared to the detection of singles. We assign this behaviour to losses induced by the presence of a broad $|-9/2\rangle\,|-5/2\rangle$ p-wave resonance at 215(5) G [53] during the detection part of the sequence.

2. To convert further from the external potential to chemical potential we need to determine the chemical potential in the centre of the trap μ_0. This is facilitated by a consequence of the particle-hole symmetry of the Hubbard model. Due to this symmetry the singles density always assumes its maximum at half-filling $\mu_0 = U/2$. Therefore, the peak in the singles density provides a method to calibrate the chemical potential axis and we obtain the equation of state $n(\mu) = s(\mu) + d(\mu)/\eta_\mathrm{d}$.

3. Now, the singles and doubles profiles $s(\mu)$ and $d(\mu)/\eta_\mathrm{d}$ from each dataset are fitted to interpolated data from numerical linked cluster expansion (NLCE) calculations [74] $\eta_\mathrm{det} s_\sigma^{NLCE}(\mu, k_\mathrm{B}T)$ and $\eta_\mathrm{det} d_\sigma^{NLCE}(\mu, k_\mathrm{B}T)$, to obtain the overall detection fidelity η_det and the temperature $k_\mathrm{B}T$. Afterwards, the data is filtered for the fidelity in the range $0.95 \leq \eta_\mathrm{det} \leq 1.05$ to reject experimental realisations with a large deviation from the average fidelity.

4. Due to fluctuations of the prepared total atom number, individual measurements of the density distribution sample slightly different intervals in chemical potential. Instead of rejecting large amounts of data based on atom number, we combine the filtered data from a full dataset, and use the individual values of μ_0 to re-bin the data in chemical potential. Thereby, we obtain a precise average of the equation of state $\bar{n}(\mu)$. Finally, we fit the average profiles $\bar{s}(\mu)$ and $\bar{d}(\mu)$ to NLCE data to determine the average values of temperature and central chemical potential of the dataset.

Figure 6.2(a) shows the measured equation of state $\bar{n}(\mu)$ for different interaction strengths. The data show the crossover from a metal for weak interactions with a strong density variation across the region of half filling, to a Mott-insulator with a density plateau around half-filling for strong interactions. While the atom number remains approximately constant at $N \simeq 8.8(6) \times 10^3$ across different interaction strengths, there is a marked increase of the extent of the Mott-insulating region for larger U/t. Our lowest temperature, $k_\mathrm{B}T/t = 0.63(2)$ at $U/t = 8.2$, is already at the limit of validity of the numerical approximation, which is evident from weak artificial oscillations of the theoretical $n(\mu)$ data near $n = 0.25$ and above $n = 1$. We also compare our data with numerical calculations using dynamical cluster approximation (DCA) [126] for $U/t = 8$ (see inset of Figure 6.2(a)), which confirms that they fall into the temperature interval $0.55 \leq k_\mathrm{B}T/t \leq 0.82$. However, the available DCA data are too coarsely spaced in order to fit the temperature more accurately.

6.3.2 Compressibility

As discussed above, the compressibility provides an observable to determine transport properties of many-body system in order to determine weather it behaves metallic or insulating. In the experiment, we obtain the compressibility from numerical derivative of the measured equation of state with respect to the chemical potential

$$\kappa = \frac{1}{a^2} \frac{\partial \langle \hat{n}(\mu) \rangle}{\partial \mu} \tag{6.1}$$

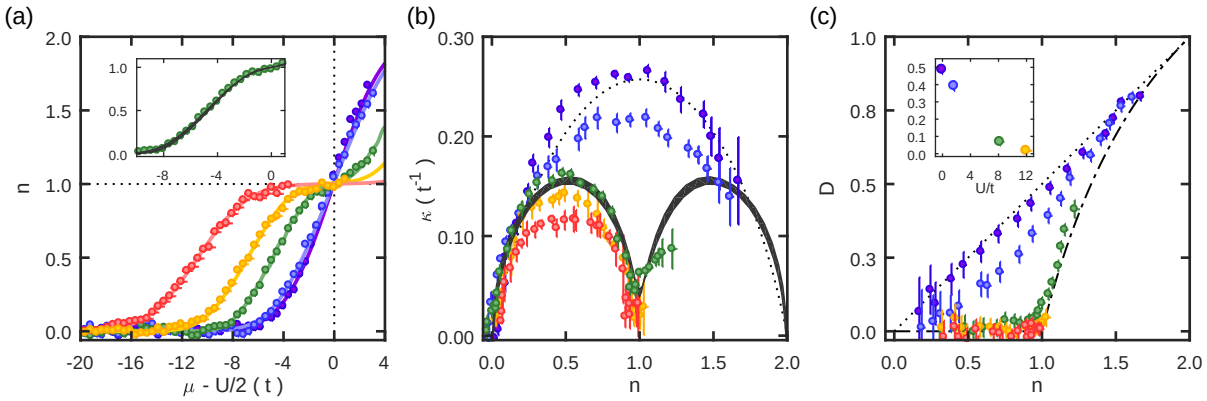

Figure 6.2: Equation of state of the two-dimensional repulsive Hubbard model. Purple: $U/t = -0.2(3)$ for $k_B T/t = 1.35(4)$; blue: $U/t = 1.6(2)$ for $k_B T/t = 1.19(4)$; green: $U/t = 8.2(5)$ for $k_B T/t = 0.63(2)$; yellow $U/t = 12.0(7)$ for $k_B T/t = 0.92(6)$; red: $U/t = 19.5(1.3)$ for $k_B T/t = 1.41(5)$. (a) Equation of state $n(\mu)$ for varying interaction strength U/t. Solid lines show fits using NLCE data [74] (purple: non-interacting Hubbard model) from which the temperature has been extracted. The inset shows the comparison with DCA data [126] for the temperature interval $0.55 \leq k_B T/t \leq 0.82$ at $U/t = 8$. (b) Compressibility κ versus filling. The dashed line shows the prediction of the non-interacting Hubbard model at $k_B T/t = 1.4$ and the grey band the prediction from DCA as in (a). (c) Doubles fraction versus filling. The theoretical predictions for the non-interacting (dashed line) and infinitely repulsive (dashed-dotted line) Hubbard model are shown. The inset shows the behaviour at half filling as a function of the on-site interaction strength. The error bars show the standard errors.

Figure 6.2(b) shows the compressibility as a function of the filling for different interaction. The non-interacting gas ($U/t = -0.2(3)$) exhibits a maximum compressibility of $\kappa = 0.266(6)\, t^{-1}$ at half filling $n = 1$, which signals metallic behaviour and is in agreement with the numerical simulation of the homogeneous non-interacting Hubbard model at a temperature of $k_B T/t = 1.4$ (dashed line). At finite temperatures the approach from the metal to the Mott insulator is a crossover and therefore we expect a smooth change of the thermodynamic properties as the interaction strength or density changes. For intermediate interactions, $U/t = 8.2$, we already observe a significant reduction of the compressibility at $n = 1$ and a return to a more compressible phase at fillings $n > 1$. A comparison of the compressibility with data from DCA calculations [126] shows very good agreement (shaded area in Fig. 6.2(b)). For strong interactions, $U/t \geq 12.0$, the compressibility is close to zero at half filling. For a system without disorder, a vanishing compressibility implies a gap against density excitations, and hence, combined with the observation of a plateau at half-filling, unequivocally demonstrates the observation of the Mott insulator in two dimensions.

6.3.3 Doubles fraction

As noted above, our occupation detection scheme gives access to the distribution of doubly occupied sites. Figure 6.2(c) shows the measured doubles fraction

$$D = \frac{2\langle \hat{n}_\downarrow \hat{n}_\uparrow \rangle}{\langle \hat{n}_\uparrow \rangle + \langle \hat{n}_\downarrow \rangle} \tag{6.2}$$

versus filling and interaction strength. For the non-interacting gas, the spin-up and spin-down fillings are uncorrelated, hence the doubles fraction simplifies to $D = n$ (dashed line in 6.2(c)). The data for the non-interacting gas agree with this prediction. In the limit of infinitely strong repulsive interactions,

the number of doubles is completely suppressed if there are more lattice sites than particles, i.e. $D = 0$ for $n \leq 1$, while for $n > 1$ the number of doubles equals the excess of atoms above half filling, i.e. $D = 2 - 1/n$ (dashed-dotted curve in Figure 6.2(c)). We observe that even for $U/t = 8.2$ the data is close to the infinite-interaction limit. For interaction strengths above this, the external compression provided by the trap is too weak to observe fillings $n > 1$. The inset shows the measured doubles fraction at half filling as a function of interaction strength U/t.

6.3.4 Melting of the Mott-insulator

Finally, we investigate the repulsive Hubbard model as a function temperature at $U/t = 8.2$ where antiferromagnetic ordering is expected to occur at the highest transition temperature [131] of $k_B T/t \sim 0.3$. In order to experimentally adjust the temperature, we heat the gas using a weak periodic modulation of the intensity of the horizontal lattice beams with a frequency close to twice the horizontal trapping frequency, followed by an equilibration time of 400 ms (cf. Chapter 3.5.2). Figure 6.3 displays the variation of $n(\mu)$ with temperature. In general, the distribution $n(\mu)$ gets broader and varies more smoothly with increasing temperature. This is directly reflected by the compressibility at half-filling (Fig. 6.3(b)) which shows how the Mott insulator gradually becomes metallic and its compressibility increases from $\kappa = 0.02\,t^{-1}$ at low temperature to $\kappa = 0.06\,t^{-1}$ at high temperature, in agreement with NLCE calculations (solid line) within error. Moreover, Figure 6.3(c) shows the doubles fraction D versus filling n for varying temperatures. The data illustrate a considerable increase of doubles with temperature across all fillings. Some deviations between our experimental and the theoretical NLCE data are observed at low filling for low temperatures even though the total filling n is in good agreement. In Figure 6.3(d) we plot the doubles at half filling versus temperature and find that it increases from 0.054(5) at the lowest temperatures $k_B T/t = 0.67(3)$ to 0.13(3) at $k_B T/t = 3.25(7)$, in agreement with the results from NLCE [74], DCA [126], and quantum Monte-Carlo (QMC) simulations [131]. Both, the increase of the compressibility and the increase in doubles, signal the creation of thermally activated density excitations out of the lower Hubbard band.

6.4 Conclusion

The results presented in this chapter provide a precise characterisation of the density equation of state of the two dimensional Hubbard model. Using a spatially as well as occupation resolved detection technique, we observed the crossover from a metal to a Mott insulator which is signalled by a plateau of constant density at half filling, a suppression of doubly occupied sites and a vanishing compressibility at half filling. Furthermore, we studied the gradual disappearance of the Mott-insulator as the temperature of the system is increased by controlled heating (cf. Chapter 3.5.2). Our experimental platform provides access to the full doping range, which is impossible to achieve in solid state experiments.

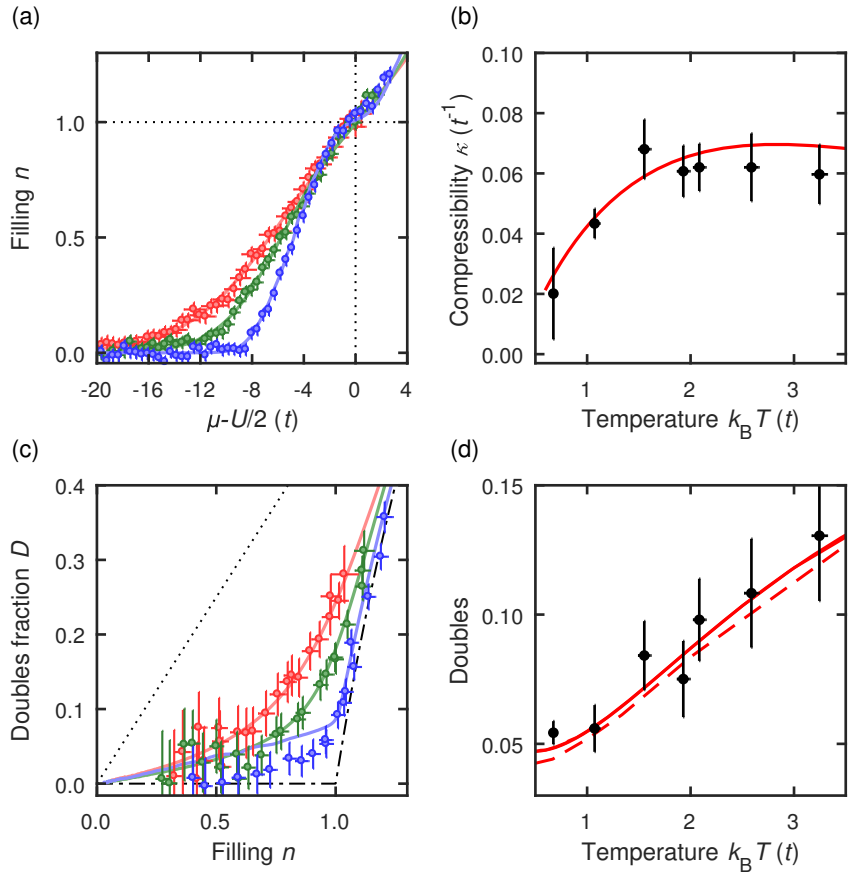

Figure 6.3: Melting of the Mott-Insulator. Blue: $k_B T/t = 0.67(3)$, green: $k_B T/t = 1.55(6)$, red: $k_B T/t = 3.25(7)$. (a) Equation of state $n(\mu)$ for different temperatures with fits using NLCE data. (b) Compressibility at half filling versus temperature together with NLCE data. (c) Doubles fraction D versus filling for different temperatures. (d) Doubles $\langle \hat{n}_\uparrow \hat{n}_\downarrow \rangle$ at half filling vs. temperature. The solid line shows the coinciding predictions of NLCE [74] and DCA [126], and the dashed line the QMC prediction [131]. The error bars show the standard errors.

CHAPTER 7

Thermodynamics versus local density fluctuations in the two-dimensional Hubbard model

The results presented in this chapter have been published in "Thermodynamics versus Local Density Fluctuations in the Metal–Mott-Insulator Crossover" by J. H. Drewes, E. Cocchi, L. A. Miller, C. F. Chan, D. Pertot, F. Brennecke and M. Köhl (see Ref. [132]).

A key requirement to fully understand the phase diagram strongly-correlated many-body systems is the establishment of a link between the microscopic physics and macroscopic observables. In the last chapter, we studied the equation of state and observed the crossover from a metal to a Mott insulator. On the microscopic level, strong repulsive interactions lead to a suppression of doubly-occupied lattice sites and to a localisation of atoms at the lattice sites. On a macroscopic level, this is reflected in the vanishing compressibility and conductivity of the Mott insulator. In this chapter, we start from precise measurements of the equation of state and apply the fluctuation-dissipation theorem to study the disappearance of non-local correlations as the system approaches the Mott insulator.

Section 7.1 provides a short introduction to the fluctuation-dissipation theorem. In Section 7.2 the origin of fluctuations from the inherent microscopic correlation functions is discussed using the example of a uniform non-interacting Fermi gas on a square lattice. Finally, our measurement and results obtained are presented in Section 7.3 and Section 7.4.

7.1 Fluctuation dissipation theorem

The fluctuation-dissipation theorem (FDT) [133] provides a conceptual link between thermodynamic and microscopic observables. The FDT quantifies how the presence of microscopic fluctuations in thermal equilibrium is linked to the response of a system to a (weak) external perturbation. The FDT has been applied to a variety of linked thermodynamic/microscopic observables. Examples are Johnson-Nyquist noise in an electrical conductor or the Brownian motion of particles suspended in a fluid. This chapter presents a study of the crossover between a metal and a Mott-insulator, which is observed in density ordering. A change in the density $n = \langle N \rangle / V$ is related to a variation of the chemical potential μ. The response of the particle number to a variation of the chemical potential is governed by the isothermal compressibility

$$\kappa = \frac{1}{V} \frac{\partial \langle N \rangle}{\partial \mu} \,. \tag{7.1}$$

The average particle number is given by

$$\langle N \rangle = k_{\mathrm{B}} T \left(\frac{\partial}{\partial \mu} \ln Z \right)_{V,T} . \tag{7.2}$$

Further, the fluctuations of the particle number are

$$\langle \delta N^2 \rangle = (k_{\mathrm{B}} T)^2 \left(\frac{\partial^2}{\partial \mu^2} \ln Z \right)_{V,T} . \tag{7.3}$$

Combining the last three equations we arrive at the static form of the fluctuation-dissipation theorem [134] which, in thermal equilibrium, relates the compressibility to the particle number fluctuations

$$\frac{\kappa}{n} = \frac{1}{k_{\mathrm{B}} T} \frac{\langle \delta N^2 \rangle}{\langle N \rangle} \tag{7.4}$$

Importantly, the proportionality factor between the thermodynamic variable κ and the microscopic density correlations in the fluctuation-dissipation theorem is the temperature. In the context of cold atom experiments, this property has been employed to conduct fluctuation-based thermometry [135–137] when compressibility and density-fluctuations can be independently measured.

7.2 Fluctuations, correlations and the static structure Factor

In this section, we will outline the connection between fluctuations, correlation functions and the static structure factor. Specifically, we will study the case of a non-interacting Fermi gas on a square lattice to show the equivalence between the static structure factor and the compressibility. In a homogeneous system, atom number fluctuations are expressed by the statistical variance

$$\langle \delta N^2 \rangle = \langle N^2 \rangle - \langle N \rangle^2 = \iint \left(\langle \hat{n}(\mathbf{r}) \hat{n}(\mathbf{r}') \rangle - \langle \hat{n}(\mathbf{r}) \rangle \langle \hat{n}(\mathbf{r}') \rangle \right) \mathrm{d}\mathbf{r}\, \mathrm{d}\mathbf{r}' . \tag{7.5}$$

In the equation above, $\langle \hat{n}(\mathbf{r}) \rangle$ yields the average total surface density at position $\mathbf{r}$. In a homogeneous system $\langle \hat{n}(\mathbf{r}) \rangle = n$. In principle, density fluctuations at all length scales contribute to the thermodynamic compressibility. Previous work has focussed on column-integrated densities [136, 138] or on local measurements [106], such that long-range density correlations were either integrated out or not detected. The integrand in Eq. 7.5 is related to the *density-density correlation function* $\nu(\mathbf{r}, \mathbf{r}')$ via

$$\begin{aligned} \langle \hat{n}(\mathbf{r}) \rangle \, \nu(\mathbf{r}, \mathbf{r}') &= \langle \hat{n}(\mathbf{r}) \hat{n}(\mathbf{r}') \rangle - \langle \hat{n}(\mathbf{r}) \rangle \langle \hat{n}(\mathbf{r}') \rangle \\ &= \langle \hat{n}(\mathbf{r}) \rangle \, \delta(\mathbf{r}, \mathbf{r}') + \langle \hat{n}(\mathbf{r}) \rangle \langle \hat{n}(\mathbf{r}') \rangle \left(g^{(2)}(\mathbf{r} - \mathbf{r}') - 1 \right) . \end{aligned} \tag{7.6}$$

Here, we have introduced the pair distribution function $g^{(2)}(\mathbf{r} - \mathbf{r}')$, which describes the probability to find two particles at distance $|\mathbf{r} - \mathbf{r}'|$. Note, that in general $g^{(2)}(x) = \frac{1}{2} \sum_{\sigma,\sigma'} g^{(2)}_{\sigma,\sigma'}(x)$. For non-interacting fermions however different spins are uncorrelated, and for $\sigma \neq \sigma'$, $g^{(2)}_{\sigma,\sigma'}(x) = 1$. Therefore, in the following the discussion is limited to the case $\sigma = \sigma'$ and we omit the spin index. Expressing the pair

distribution function in fermionic field operators yields

$$\left(\frac{n}{2}\right)^2 g^{(2)}(\mathbf{r}-\mathbf{r}') = \langle \hat{\Psi}^\dagger(\mathbf{r})\hat{\Psi}^\dagger(\mathbf{r}')\hat{\Psi}(\mathbf{r}')\hat{\Psi}(\mathbf{r})\rangle \ , \tag{7.7}$$

where we have introduced the factor $(n/2)^2$ for normalisation. Again, for free fermions we expand the field operators in plane waves $\hat{\Psi}(\mathbf{r}) = \frac{1}{\sqrt{V}}\sum_{\mathbf{k}} e^{i\mathbf{kr}}\hat{c}_{\mathbf{k},\sigma}$, $\hat{\Psi}(\mathbf{r})^\dagger = \frac{1}{\sqrt{V}}\sum_{\mathbf{k}} e^{-i\mathbf{kr}}\hat{c}^\dagger_{\mathbf{k},\sigma}$ to obtain [139]

$$\begin{aligned}\left(\frac{n}{2}\right)^2 g^{(2)}(\mathbf{r}-\mathbf{r}') &= \frac{1}{V^2}\sum_{\mathbf{k},\mathbf{k}'}\sum \mathbf{q},\mathbf{q}' e^{-i(\mathbf{k}-\mathbf{k}')\mathbf{r}} e^{-i(\mathbf{q}-\mathbf{q})\mathbf{r}'} \langle \hat{c}^\dagger_{\mathbf{k}}\hat{c}^\dagger_{\mathbf{q}}\hat{c}_{\mathbf{q}'}\hat{c}_{\mathbf{k}'}\rangle \\ &= \left(\frac{n}{2}\right)^2 - \left(\frac{1}{V}\sum_{\mathbf{k}} e^{-i\mathbf{k}(\mathbf{r}'-\mathbf{r}')}\langle \hat{n}_{\mathbf{k}}\rangle\right)^2 \ . \end{aligned} \tag{7.8}$$

In Eq. 7.8 we used the fermionic anticommutation relations. Further, we identify the last term in Eq. 7.8 with the one-particle correlation function [139]

$$\begin{aligned}\frac{n}{2}g^{(1)}(\mathbf{r}-\mathbf{r}') &= \langle \hat{\Psi}^\dagger(\mathbf{r})\hat{\Psi}(\mathbf{r}')\rangle \\ &= \frac{1}{V}\sum_{\mathbf{k},\mathbf{k}'} e^{-i\mathbf{kr}+i\mathbf{k}'\mathbf{r}'} \underbrace{\langle \hat{c}^\dagger_{\mathbf{k}}\hat{c}_{\mathbf{k}'}\rangle}_{=\langle \hat{n}_{\mathbf{k}}\rangle\delta_{\mathbf{k},\mathbf{k}'}} \\ &= \frac{1}{V}\sum_{\mathbf{k}} e^{-i\mathbf{k}(\mathbf{r}-\mathbf{r}')}\langle \hat{n}_{\mathbf{k}}\rangle \ . \end{aligned} \tag{7.9}$$

Thus, we obtain the one-particle correlation function from a Fourier transform of the Fermi-Dirac distribution $\langle \hat{n}_{\mathbf{k}}\rangle = \left(e^{\beta(\epsilon_{\mathbf{k}}-\mu)}+1\right)^{-1}$. Using Eq. 7.9, the expression for the pair distribution function reads

$$g^{(2)}(\mathbf{r},\mathbf{r}') = 1 - \left|g^{(1)}(\mathbf{r}-\mathbf{r}')\right|^2 \ . \tag{7.10}$$

Figure 7.1 shows the pair distribution function of non-interacting fermions on a square lattice for different densities and as a function of the inter particle distance $r = \left|\mathbf{r}-\mathbf{r}'\right|$. While at large distances the particles are uncorrelated, $g^{(2)}(r)$ is suppressed at short distances. This is a direct consequence of the Pauli principle, which leads to a vanishing probability to find two equal fermions at identical positions. Additionally, the larger extent of this *exchange hole* for low fillings shows that the particles are significantly delocalised over the almost empty lattice, while the localisation increases with increasing filling and becomes maximal when the band is completely filled and the gas forms a band insulator. Furthermore, the density-density correlation function is related to the static structure factor via a Fourier transform

$$S(\mathbf{k}) = \int \nu(\mathbf{r})e^{i\mathbf{kr}}\,\mathrm{d}\mathbf{r} \tag{7.11}$$

Using Eq. 7.6 and 7.10 we find

$$S(\mathbf{k}) = 1 + \int n(\mathbf{r})\left(g^{(2)}(\mathbf{r},\mathbf{r}')-1\right)e^{i\mathbf{kr}}\,\mathrm{d}\mathbf{r} \ . \tag{7.12}$$

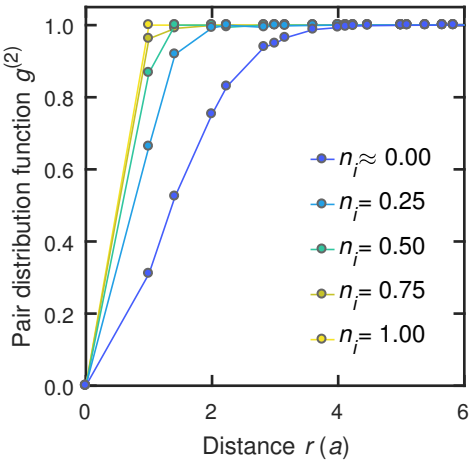

Figure 7.1: Equal spin pair distribution function $g^{(2)}$ (Eq. 7.10) for a Fermi gas on a square lattice for different densities n as a function of the inter particle distance r at a temperature of $k_B T/t = 0.6$.

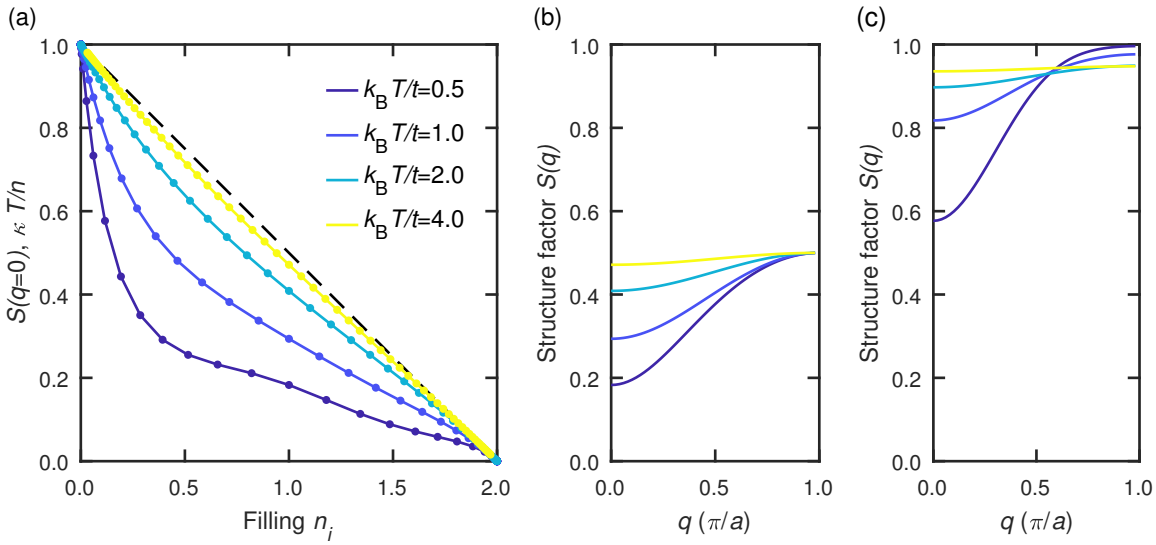

Figure 7.2: Structure factor of the ideal Fermi gas on a square lattice. (a) Structure factor at zero quasi-momentum (solid lines) and rescaled compressibility (solid circles). (b,c) Quasi-momentum resolved structure factor at half-filling $n = 1$ (b) and at quarter filling $n = 0.5$. Colour code in (a) applies also to (b,c).

Figures 7.2(b,c) show the static structure factor of the density as a function of the wave vector for half and quarter filling, respectively. For increasing temperatures, the static structure becomes flat approaching the behaviour of an uncorrelated thermal gas. In the long-wavelength limit, we find

$$\lim_{k\to 0} S(\mathbf{k}) = \frac{\langle \delta N^2 \rangle}{\langle N \rangle} = \frac{k_B T \kappa}{n}, \tag{7.13}$$

which relates the uniform static structure factor $S(k = 0)$ to the isothermal compressibility κ. A comparison of the left-hand and right-hand side of Eq. 7.13 is presented in Figure 7.2(a).

7.3 Measurement

We prepare a spin balanced Fermi gas in the two lowest magnetic hyperfine states ($N_9/N_7 = 1.00(6)$) in a square lattice to emulate the two-dimensional Hubbard model. The ratio between on-site interaction and the tunnelling rate is varied between $1.6 < U/t < 12$. While for $U/t = 1.6$, 8.2, 12.0 the final lattice depth in the experimental stage of the sequence is fixed to $6\,E_\mathrm{R}$, we choose lattice depths of $6.6(1)\,E_\mathrm{R}$ and $5.2(1)\,E_\mathrm{R}$ to realise the intermediate values $U/t = 6.1$ and $U/t = 10.3$, respectively. The lowest temperature achieved is on the order of $k_\mathrm{B}T/t \approx 0.65$. In order to probe the behaviour of non-local correlations at higher temperatures, we either hold the atoms in the lattice for a variable time or apply a periodic modulation of the horizontal lattice beams to heat up the gas (cf. Chapter 3.5.2). Thereafter, we spectroscopically select a single layer in the vertical direction and record the distribution of singly and doubly occupied lattice sites individually (cf. Chapter 4.2.2). The temperature of the prepared distributions is determined from fits to interpolated data from NLCE calculations (cf. 6).

7.4 Suppression of non-local density fluctuations in the repulsive Hubbard model

To begin with, we investigate the uniform static structure factor obtained according to Eq. 7.13, which holds in the thermodynamic limit [140]. Qualitatively, one discriminates three different cases: $S(k = 0) = 1$ is classical shot noise, $S(k = 0) > 1$ is termed bunching and occurs for bosonic particles, and $S(k = 0) < 1$ is anti-bunching, which is expected for a degenerate Fermi gas. Figures 7.3(a-c) show the static structure factor $S(k = 0)$ derived from the measurement of compressibility and density for different temperatures and on-site interaction strength. Generally, we find that for high-filling and low temperature the structure factor is well below 1, which signals non-classical behaviour. For weak interactions, $U/t = 1.6$, this displays anti-bunching due to the Pauli exclusion principle according to which at most one fermion per spin state can occupy each lattice site. For strong interactions, $U/t = 12.0$, the structure factor is even more suppressed by the strong repulsive interaction between atoms. For high temperatures, the structure factor increases due to the thermal contribution.

We now compare the structure factor with the atom number fluctuations $\delta n_i^2/n_i$ on one lattice site. The on-site density fluctuations $\delta n_i^2 = \langle \hat{n}_i^2 \rangle - \langle \hat{n}_i \rangle^2$ directly follow from the measured occupation. Using the fermionic anti-commutation relations as well as $\langle \hat{n}_{i,\uparrow} \rangle = \langle \hat{n}_{i,\downarrow} \rangle$ we find

$$\delta n_i^2 = 2\,\langle \hat{n}_{i\uparrow} \rangle - 4\,\langle \hat{n}_{i\uparrow} \rangle^2 + 2\,\langle \hat{n}_{i\uparrow} \hat{n}_{i\downarrow} \rangle \ . \tag{7.14}$$

This expression provides us with a powerful analysis tool: one can determine the on-site density fluctuations from a measurement of the density distributions of the single- *and* double-occupancy of the lattice sites. Note that, when applying Equation 7.14, we assume that the global density does not vary significantly over the extent of the spatial resolution of our imaging system. Figures 7.3(d-f) present the local density fluctuations for the same data as in Figure 7.3(a-c). For the ideal Fermi gas on a lattice the local fluctuations follow a binomial distribution which is imposed by Pauli's exclusion principle. This implies that generally either zero or one fermion per spin state can occupy each lattice site with the mean given by the particle number per site $n_i = \langle \hat{n}_i \rangle$. Specifically, in the non-interacting ($U = 0$) limit, where $\langle \hat{n}_{i\uparrow} \hat{n}_{i\downarrow} \rangle = \langle \hat{n}_{i\uparrow} \rangle^2$, the on-site fluctuations are given by

$$\delta n_i^2/n_i = 1 - n_i/2\,, \tag{7.15}$$

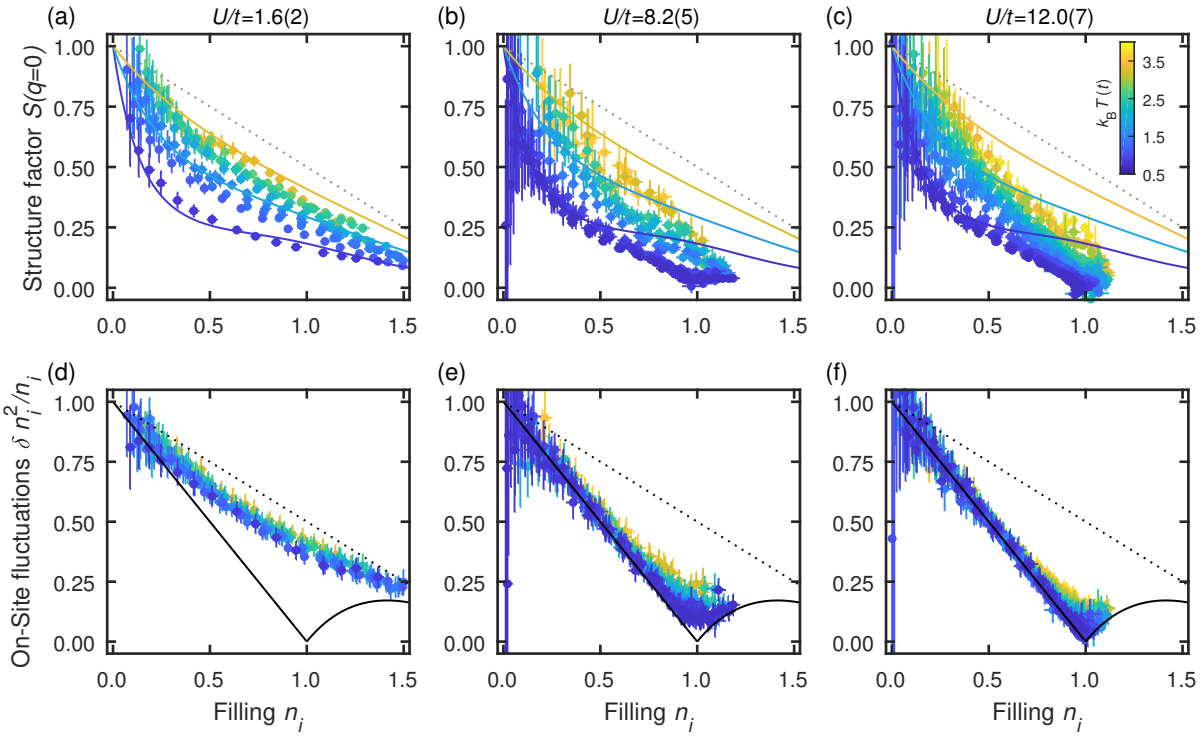

Figure 7.3: Comparison of the thermodynamic and local density fluctuations in the two-dimensional Hubbard model. Left column (a,d): $U/t = 1.6(2)$, middle column (b,e): $U/t = 8.2(5)$, right column (c,f): $U/t = 12.0(7)$. Top row: static structure factor $S(k = 0)$ measuring density fluctuations in thermodynamically large volumes; bottom row: density fluctuations at a single site of the optical lattice. Dashed line: on-site fluctuations in the non-interacting limit. Solid line: on-site fluctuations in the infinite-interactions limit. Temperature is encoded as colour (see legend in (c)).

which is indicated by the dashed line in Figure 7.3. The measured local fluctuations for $U/t = 1.6$ (Fig. 7.3(d)) reproduce the ideal Fermi gas prediction very well, with an additional small suppression of the fluctuations which we attribute to the finite interaction strength. In the limit of infinite repulsive interactions ($U = +\infty$) and $n_i \leq 1$, either zero or one fermion occupy one lattice site and hence

$$\delta n_i^2/n_i = 1 - n_i \,. \tag{7.16}$$

For $n_i > 1$ we find in the same limit

$$\delta n_i^2/n_i = 3 - n_i - 2/n_i \tag{7.17}$$

The on-site fluctuations in the strongly-interacting case are insensitive to temperature unless $k_B T \sim U$ for which thermally induced double-occupancies contribute to the fluctuations. In general, the on-site density fluctuations $\delta n_i^2/n$ for a given filling and temperature are higher than the fluctuations $\delta N^2/N$ of the same data set in the thermodynamic limit. This shows that the thermodynamic fluctuations contain a non-local contribution from density-density correlations on different length scales. In order to understand the difference between local and thermodynamic fluctuations, we transcribe the fluctuation-dissipation

theorem 7.13 to a lattice with discrete sites labelled by the indices i j

$$\kappa = \frac{1}{a^2 k_\mathrm{B} T}\left[\delta n_i^2 + \sum_{j\neq i}\left(\langle \hat{n}_i \hat{n}_j\rangle - \langle \hat{n}_i\rangle \langle \hat{n}_j\rangle\right)\right]. \tag{7.18}$$

Here, we have separated the local fluctuation δn_i^2 from the non-local density correlations. On the microscopic level, the violation of the local fluctuation-dissipation theorem [141, 142] is rooted in the spatial correlations of the density fluctuations and hence is governed by the nature of the underlying quantum state. In a perfectly localised state, such as a band insulator at zero temperature, the off-site correlations are zero since the correlation function factorises $\langle \hat{n}_i \hat{n}_j\rangle = \langle \hat{n}_i\rangle \langle \hat{n}_j\rangle$. In contrast, for a delocalised state at zero temperature, such as a Fermi gas in a partially filled Bloch band, the compressibility cannot be described by local fluctuations alone since the off-site correlations are not negligible. At finite temperature, however, the thermal correlation length limits the range of density correlations and for a classical gas the correlations are restricted to on-site fluctuations. In order to highlight this effect, Figure 7.4 shows the non-local density correlation

$$\delta n_\mathrm{n.l.}^2 = a^2 \kappa k_\mathrm{B} T - \delta n_i^2 \tag{7.19}$$

as a function of temperature and lattice filling. For low filling, $n_i \lesssim 0.4$, the results for all interaction strengths agree very well with the non-interacting Fermi gas in a two-dimensional square lattice with nearest-neighbour tunnelling (solid line). This shows that at low filling the atoms delocalise in the lattice irrespective of the explored interaction strength and that for low temperatures the delocalisation gives rise to non-local density correlations which significantly affect the compressibility. At $n_i \geq 0.5$ we observe the onset of interaction effects in the deviations from the ideal Fermi gas theory. While the weakly-interacting data (blue) remain closer to the ideal Fermi gas prediction, the strongly-interacting data exhibit a suppression of long-range density correlations. Finally, at half-filling, we observe a clear distinction between the two cases. For example, the $U/t = 12$ data show an almost complete suppression of off-site density correlations, while the $U/t = 1.6$ data are still close to the free Fermi gas expectation. The former is a signature for the atoms having formed a localised Mott insulator, the thermodynamics of which is entirely described by local quantities in the density sector. Finally, Figure 7.5 shows the residual non-local density fluctuations $\delta n_\mathrm{n.l.}^2$ as a function of the atom number per site n for the lowest temperatures achieved at each interaction strength. The data highlight that, within the experimental resolution, at low filling the off-site density correlations are essentially independent of interaction strength and equal to the ideal Fermi gas prediction. Upon approaching half-filling, off-site correlations are highly suppressed for the strongly-interacting gas and signal the onset of a Mott insulator with localised spins.

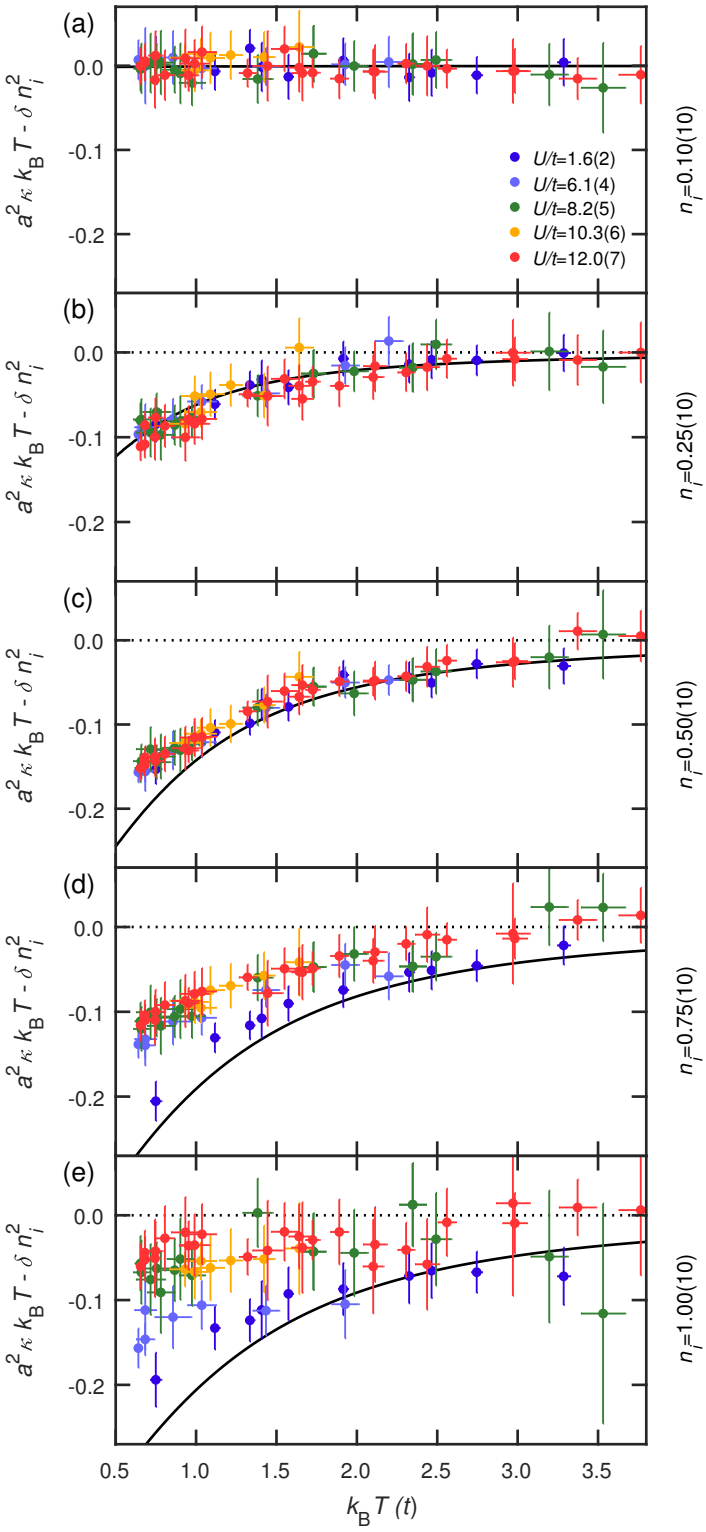

Figure 7.4: Non-local density-density correlations for different lattice site occupations n_i. The solid line is the theoretical expectation of the ideal Fermi gas in a two-dimensional lattice. Colour code: purple: U/t = 1.6(2), light blue: U/t = 6.1(4), green U/t = 8.2(5), yellow: U/t = 10.3(6), red: U/t = 12.0(7).

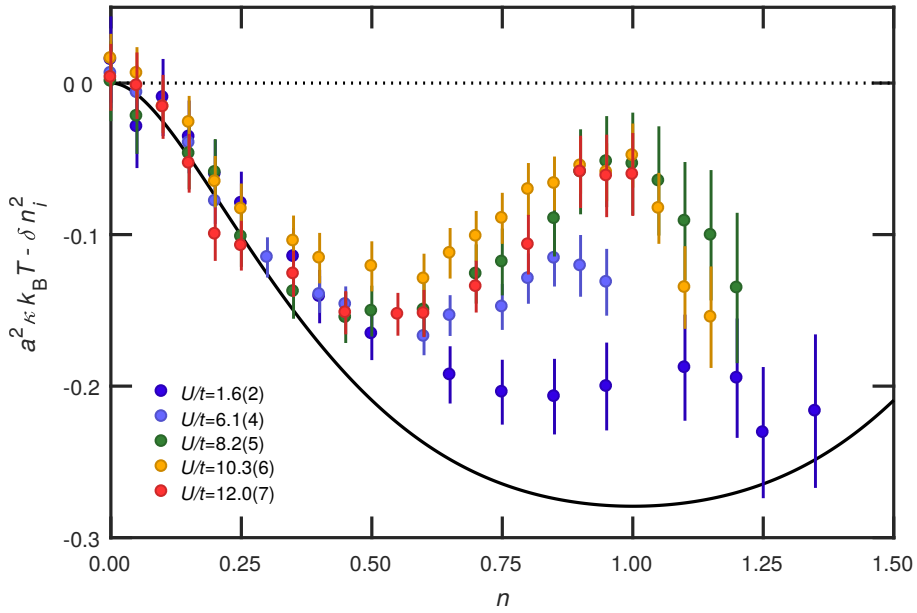

Figure 7.5: Non-local density-density correlations for the lowest temperatures achieved in the experiment. Colour code: purple: $U/t = 1.6(2)$, $k_B T/t = 0.75(3)$, light blue: $U/t = 6.1(4)$, $k_B T/t = 0.64(1)$, green: $U/t = 8.2(5)$, $k_B T/t = 0.65(3)$, yellow: $U/t = 10.3(6)$, $k_B T/t = 0.93(8)$, red: $U/t = 12.0(7)$, $k_B T/t = 0.65(2)$. The solid line shows the prediction of the ideal Fermi gas on a square lattice for $k_B T/t = 0.65$.

CHAPTER 8

Observation of antiferromagnetic spin correlations in the two-dimensional Hubbard model

This chapter presents results published in "Antiferromagnetic correlations in two-dimensional fermionic Mott-Insulating and metallic phases" by J. H. Drewes, L. A. Miller, E. Cocchi, C. F. Chan, N. Wurz, M. Gall, D. Pertot, F. Brennecke and M. Köhl (compare Ref. [143]) and closely follows the description therein.

This chapter presents a study of spin correlations in the 2D Hubbard model. Section 8.1 motivates our work. Section 8.2 provides a summary of the measurement protocol and thermometry. Section 8.3 presents the method used to infer the amount of spin correlations from the experimental data. Finally, Sections 8.4 and 8.5 presents the uniform spin structure factor as a function of interaction, temperature and doping.

8.1 Motivation and previous work

Quantum magnetism arises from repulsive short-range interactions at low temperatures. The occurrence of magnetic long range order however, depends crucially on the interplay of interactions, lattice geometry, dimensionality and doping. Even though the consequences of this interplay are not yet fully understood, quantum magnetism is believed to be connected to a range of complex phenomena in the solid state, most prominently, in the context of high-T_c superconductivity [2, 13]. Ultracold atomic Fermi gases in optical lattices are an ideal platform for studying quantum magnetism in order to reveal the microscopic origin of the magnetic susceptibility in the Hubbard model. Previous experiments have detected evidence for antiferromagnetic (AFM) correlations in measurements averaging over inhomogeneous systems [25, 128]. In parallel with the work presented here, the spin correlation function has been probed with site resolved resolution using quantum gas microscopes [36, 38, 144]. More recently, a system with quasi long-range order could be realised in which the correlation length extended over the whole sample in a system consisting of a small number of lattice sites [39].

Here, we detect the emergence of AFM correlations through the uniform magnetic susceptibility and study its dependence on temperature, interaction strength and filling. To this end, we employ high-resolution absorption imaging (cf. Chapter 5) to record the density distributions of both spin components in a single measurement and determine the spin structure factor as well as the magnetic susceptibility. Since the spin correlations are expected to be strongest at half filling and sensitively depend on the filling, we employ a spatially-resolved detection scheme and, due to the spatially varying trapping potential, determine the spin structure factor as a function of doping. We compare our results

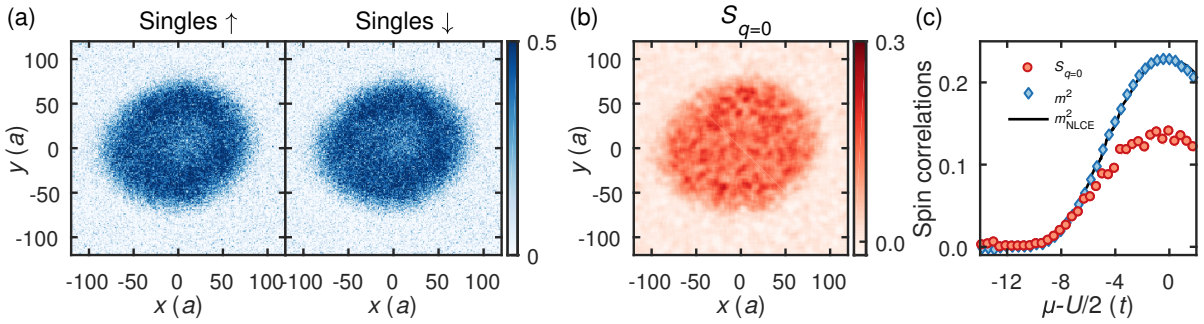

Figure 8.1: Spin-resolved singles density distribution and uniform magnetic structure factor. (a) Average distributions of spin-up and spin-down atoms on singly occupied lattice sites. The data shown are averaged over 36 experimental realisations for an on-site interaction $U/t = 8.2(5)$. (a) Map of the uniform magnetic structure factor $S^{\mathrm{mag}}_{\mathbf{q}=\mathbf{0}}$. (c) Equipotential average of the uniform magnetic structure factor (circles) and the local moment $C_{0,0}$ (diamonds). For the data shown, we extract a temperature $k_{\mathrm{B}}T/t = 0.63^{+0.09}_{-0.02}$ from fits of the averaged spin distributions to NLCE data (solid line).

to state-of-the-art numerical calculations and find agreement where results are available, which is, in particular, at half filling.

8.2 Measurement Scheme

In Chapter 4 we have demonstrated a spin sensitive detection scheme. Here, we apply this technique to access the spin degree of freedom of the two dimensional Hubbard model with repulsive interactions. The experiment starts with the preparation of a cold spin balanced Fermi gas in an optical lattice (cf. Chapter 3). After the experimental stage of the sequence, the lattice depth is increased from $6\,E_{\mathrm{r}}$ to $60\,E_{\mathrm{r}}$. This prevents tunnelling during the detection stage. Then, atoms on doubly occupied sites are selectively removed using spin changing collisions (cf. Chapter 4.3.1). Thereafter, we use dual-frequency high-resolution RF tomography to simultaneously transfer atoms in both spin states of a single vertical layer into two different auxiliary magnetic hyperfine states (cf. Chapter 4.3.2). Finally, two consecutive images are recorded to measure the spatial distribution of atoms in both spin states. Figure 8.1 shows the density profiles $\langle \tilde{s}_{\uparrow}(\mathbf{r})\rangle$ and $\langle \tilde{s}_{\downarrow}(\mathbf{r})\rangle$ for $U/t = 8.2(5)$ and $k_B T/t = 0.63^{+0.09}_{-0.02}$ averaged over a set of 36 experimental realisations. Since we do not access the distribution of doubly occupied sites in the measurement presented in this Chapter, we rely on the singles distribution to determine the temperature. In a variation of the fitting scheme outlined in Chapter 6, we determine the temperature T and the central chemical potential μ_0 from a combined fit of the average singles density distributions of both spin states to NLCE data [74]. For a spin balanced sample, we expect $\langle s_{\uparrow}\rangle = \langle s_{\downarrow}\rangle$. However, since one of the spin states experiences an additional population transfer for protection against off-resonant scattering of imaging light (cf. Chapter 4) we assume independent detection fidelities η_{σ}.

8.3 Correlation analysis

The recorded in-situ images of the spin density $\tilde{s}_{\sigma}(\mathbf{r})$ are convolved with the point spread function $p(\mathbf{r})$ of our imaging system according to $\tilde{s}_{\sigma}(\mathbf{r}) = \sum_i p(\mathbf{r} - \mathbf{r}_i) s_{i,\sigma}$ where $\int p(\mathbf{r}) d^2\mathbf{r} = 1$ and $s_{i,\sigma}$ denotes the probability to find an atom in spin state σ residing on lattice site i. The spatial correlation function of the local magnetisation $\tilde{S}^z(\mathbf{r}) = (\tilde{s}_{\uparrow}(\mathbf{r}) - \tilde{s}_{\downarrow}(\mathbf{r}))/2$ evaluated over the set of images at positions $\mathbf{r}$ and $\mathbf{r} + \mathbf{d}$

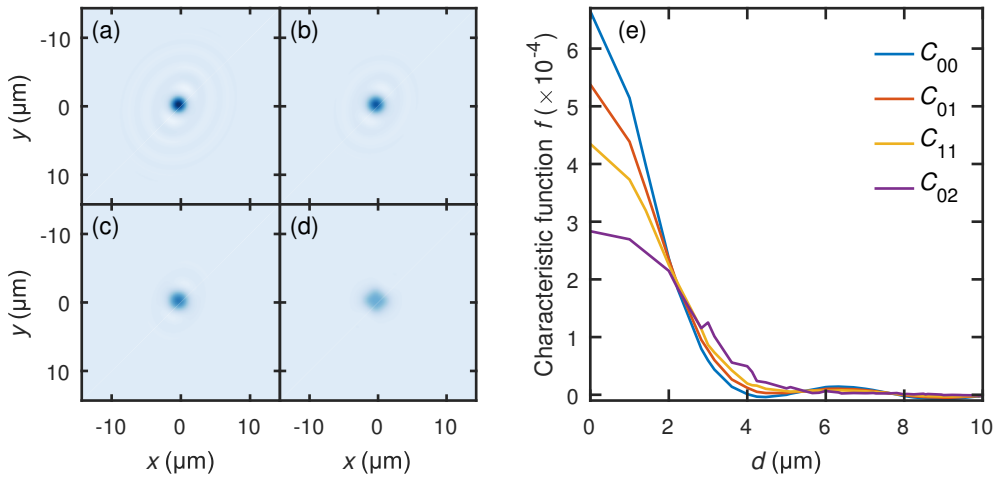

Figure 8.2: Contributions to the correlation function from (a) local moment $C_{0,0}$, (b) nearest-neighbour correlations $C_{0,1}$, (c) diagonal next-nearest neighbour correlations $C_{1,1}$ and (d) straight next-nearest neighbour correlations $C_{0,2}$.

therefore contains contributions from spin correlators $\langle \hat{S}_i^z \hat{S}_j^z \rangle - \langle \hat{S}_i^z \rangle \langle \hat{S}_j^z \rangle$ between several pairs of lattice sites i and j:

$$\begin{aligned} \tilde{C}(\mathbf{r}, \mathbf{d}) &\equiv \langle \tilde{S}^z(\mathbf{r}) \tilde{S}^z(\mathbf{r}+\mathbf{d}) \rangle - \langle \tilde{S}^z(\mathbf{r}) \rangle \langle \tilde{S}^z(\mathbf{r}+\mathbf{d}) \rangle \\ &= \sum_{i,j} p(\mathbf{r}-\mathbf{r}_i) p(\mathbf{r}+\mathbf{d}-\mathbf{r}_j) (\langle \hat{S}_i^z \hat{S}_j^z \rangle - \langle \hat{S}_i^z \rangle \langle \hat{S}_j^z \rangle). \end{aligned} \tag{8.1}$$

To obtain the correlation function $\tilde{C}(\mathbf{r}, \mathbf{d})$, the averages in Eq. 8.1 are evaluated over different experimental realisations. Afterwards, $\tilde{C}(\mathbf{r}, \mathbf{d})$ is averaged over regions $\mathcal{R}_\mu$ of constant chemical potential (binned with a bin size of $\Delta\mu = h \times 100\,\mathrm{Hz}$) to obtain the correlations as a function of distance $\mathbf{d}$ according to

$$\tilde{C}_\mu(\mathbf{d}) \equiv \langle \tilde{C}(\mathbf{r}, \mathbf{d}) \rangle_{\mathbf{r} \in \mathcal{R}_\mu} = \sum_j f(\mathbf{d}, j) C_j \,. \tag{8.2}$$

The last equation expresses that the measured correlation function $\tilde{C}_\mu(\mathbf{d})$ corresponds to the site resolved spin correlation function $C_j = \langle \hat{S}_0^z \hat{S}_j^z \rangle - \langle \hat{S}_0^z \rangle \langle \hat{S}_j^z \rangle$ weighted by the characteristic functions $f(\mathbf{d}, j) = \sum_i p(\mathbf{r}_i) p(\mathbf{d} - \mathbf{r}_{i+j})$ of the imaging system (Figure 8.2). Integrating the correlation function $\tilde{C}_\mu(\mathbf{d})$ over a region whose radius is large compared to the imaging resolution of 1.25 μm (compare chapter 5) as well as the correlation length ξ yields

$$\int d^2\mathbf{d} \tilde{C}_\mu(\mathbf{d}) = \sum_{i,j} p(\mathbf{r}_i) C_j = S^{\mathrm{mag}}_{\mathbf{q}=0} / a^2. \tag{8.3}$$

Here, $S^{\mathrm{mag}}_{q=0} = \sum_j C_j$ denotes the spin structure factor at zero quasi momentum q. To suppress the accumulation of noise in the spatial integration of the correlation function $\tilde{C}_\mu(\mathbf{d})$ we fit the correlation data for each value of the chemical potential with

$$C_{\mathrm{fit}}(|\mathbf{d}|) = \beta \sum_j (-1)^{j_x + j_y} f(|\mathbf{d}|, j_x, j_y) C^{\mathrm{exp}}_{0,0} \exp(-a|j|/\xi) \tag{8.4}$$

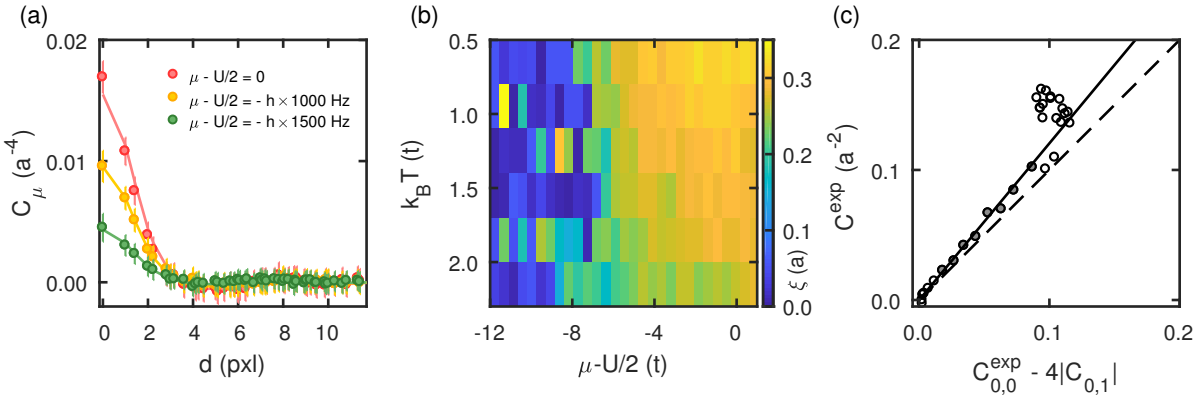

Figure 8.3: (a) Measured spin correlations $\tilde{C}_\mu(|\mathbf{d}|)$ (circles) for $U/t = 8.2$ as a function of distance (in units of the image pixel size pxl = 0.573 μm) for different values of the chemical potential μ together with the fit functions $C_{\mathrm{fit}}(|\mathbf{d}|)$ (solid lines). (b) Extracted correlation length ξ versus chemical potential and temperature for $U/t = 8.2$. For vanishing filling, the extracted value of the correlation length is not physical. (c) Rescaling of integrated correlations. Shown are the integrated correlations C^{exp} (circles) for an exemplary data set ($k_B T/t = 0.63$ and $U/t = 8.2$) versus $|C^{\mathrm{exp}}_{0,0}| - 4|C_{0,1}|$, where $C_{0,1}$ is extracted from NLCE data. We fit a line intercepting zero (solid) to the data in the filling range $0.03 \leq n \leq 0.25$ (filled circles). The fitted slope β is used to rescale the data to fall on the bisecting line (dashed).

assuming an exponential decay of the magnitude of the correlations C_{j_x,j_y} with distance $|j| = \sqrt{j_x^2 + j_y^2}$, see Fig. 8.3(a). The correlation length ξ is a free fit parameter and varies with temperature and chemical potential as shown in Fig. 8.3(b). The local moment $C_{0,0} = \langle(\hat{n}_{i,\uparrow} - \hat{n}_{i,\downarrow})^2\rangle/4$ which enters the fit function is directly extracted from the measured density distributions of singly-occupied sites using the Pauli principle $\langle\hat{n}^2_{i,\sigma}\rangle = \langle\hat{n}_{i,\sigma}\rangle$ and the relation $\langle\hat{n}_{i,\sigma}\rangle = \langle\hat{s}_{i,\sigma}\rangle + \langle\hat{n}_{i,\uparrow}\hat{n}_{i,\downarrow}\rangle$. The characteristic functions $f(\mathbf{d}, j_x, j_y)$ are calculated from the point spread function, which we extract from images of the density distribution following the method described in Section 5.6.2. The additional parameter β is adjusted such that the integrated correlations match in the low-filling regions of the cloud the measured local moment $C^{\mathrm{exp}}_{0,0}$ corrected by a small contribution from nearest-neighbour correlations obtained from NLCE data, see Fig. 8.3(c). Over the range of temperature and interactions investigated, the parameter β varies by 0.03 around a mean value of 1.1. Finally, the uniform spin structure factor is obtained from the spatial integral of the fit function $C_{\mathrm{fit}}(\mathbf{d})$. We note, that the described method to extract the total amount of spin correlations is independent of the experimental imaging resolution as long as averaging over regions of different filling can be neglected and the technical noise does not overwhelm the correlation signal from the atoms.

Influence of a finite detection efficiency

The overall detection fidelity $\eta_\sigma = \eta_{\mathrm{det}}\eta_{\mathrm{MW}}$ is smaller than unity. Here, $\eta_{\mathrm{det}} = 0.85(2)$ is a correction factor to the imaging calibration, which we determine from a histogram over all fitted values of $\eta_\uparrow$. The double-path efficiency of the microwave sweep $\eta_{\mathrm{MW}} = 0.96(2)$ affects the spin-down measurement only and is calibrated independently (cf. Chapter 4.4). In the following, the influence of a limited fidelity on the correlation analysis will be outlined. As an example, we discuss the possibility of random losses of spin-down atoms on any site j during detection and describe these with a binomially distributed random variable ξ_j, i.e. $\langle\xi_j\rangle = 1 - \eta$ and $\langle\xi_j^2\rangle - \langle\xi_j\rangle^2 = (1-\eta)\eta$, where η is the fidelity. Therefore, for the

detected atom number on site j, we find

$$\begin{aligned} \langle \hat{n}_\downarrow^j \rangle_{\text{det}} &= \langle \hat{n}_\downarrow^j - \xi^j \hat{n}_\downarrow^j \rangle \\ &= \eta_\downarrow \langle \hat{n}_\downarrow^j \rangle \ . \end{aligned} \tag{8.5}$$

For the correlator between different spins on sites i,j this implies

$$\begin{aligned} \langle \hat{n}_\uparrow^i \hat{n}_\downarrow^j \rangle_{\text{det}} &= \langle \hat{n}_\uparrow^i (\hat{n}_\downarrow^j - \xi^j \hat{n}_\downarrow^j) \rangle \\ &= \langle \hat{n}_\uparrow^i \hat{n}_\downarrow^j \rangle - \left(1 - \eta_\downarrow\right) \langle \hat{n}_\uparrow^i \hat{n}_\downarrow^j \rangle \\ &= \eta_\downarrow \langle \hat{n}_\uparrow^i \hat{n}_\downarrow^j \rangle \ . \end{aligned} \tag{8.6}$$

And, for correlations between spin-down atoms

$$\begin{aligned} \langle \hat{n}_\downarrow^i \hat{n}_\downarrow^j \rangle_{\text{det}} &= \langle (\hat{n}_\downarrow^i - \xi^i \hat{n}_\downarrow^i)(\hat{n}_\downarrow^j - \xi^j \hat{n}_\downarrow^j) \rangle \\ &= \langle \hat{n}_\downarrow^i \hat{n}_\downarrow^j \rangle + \langle \xi^i \xi^j \rangle \langle \hat{n}_\downarrow^i \hat{n}_\downarrow^j \rangle - 2 \langle \xi \rangle \langle \hat{n}_\downarrow^i \hat{n}_\downarrow^j \rangle \\ &= \eta_\downarrow^2 \langle \hat{n}_\downarrow^i \hat{n}_\downarrow^j \rangle \ , \end{aligned} \tag{8.7}$$

where we have assumed that losses on different sites are independent. For the case of spin-down atoms the arguments are equivalent. Therefore, in the correlation analysis, we take the detection efficiency into account by dividing each recorded density map with the fitted fidelity η_σ.

Background correction

In addition to the atomic correlations, technical noise in the absorption images originating from photon shot noise, camera readout noise and interference fringes enters the correlation analysis. This is accounted for by applying an identical correlation analysis on a set of background images, which were recorded for far off-resonant RF pulses. The corresponding correlations are then subtracted from $\tilde{C}(\mathbf{r}, \mathbf{d})$.

Finally, Figure 8.1(b) shows the spatial distribution of the uniform spin structure factor $S^{\text{mag}}_{\mathbf{q}=0}(\mathbf{r})$ extracted from the same dataset as used to compute the average profiles in Fig. 8.1(a). Figure 8.1(c) presents the corresponding equipotential average taken over regions of constant chemical potential $S_{\mathbf{q}=0}(\mu)$, respectively. In order to infer from our data the presence of spin correlations between different sites, we compare the spin structure factor with the local moment $C_{0,0} = \langle (\hat{S}_i^z)^2 \rangle - \langle \hat{S}_i^z \rangle^2$, which we obtain directly from the singles density distributions according to $C_{0,0} = (\langle \hat{s}_\uparrow \rangle + \langle \hat{s}_\downarrow \rangle)/4$ due to the Pauli principle. The local moment represents the on-site fluctuations of $\hat{S}^z$ and hence the local contribution to the magnetic susceptibility (see Figure 8.1(c)). While for low filling the structure factor closely follows the local moment, a clear mismatch between the structure factor and the local moment is observed around half filling $\mu = U/2$, indicating the emergence of spin correlations.

8.4 Spin correlations at half-filling

We first focus on half filling where for strong interactions the system enters a Mott-insulating state and correlations for a fixed interaction strength and temperature are expected to be strongest. Furthermore, the particle-hole symmetry permits accurate numerical simulations to which we compare our data. Figure 8.4(a) presents the uniform static spin structure factor at half filling $S^{\text{mag}}_{q=0}(\mu = U/2)$ as a function of temperature for weak ($U/t = 1.6$), intermediate ($U/t = 8.2$), and strong ($U/t = 12.0$) interactions.

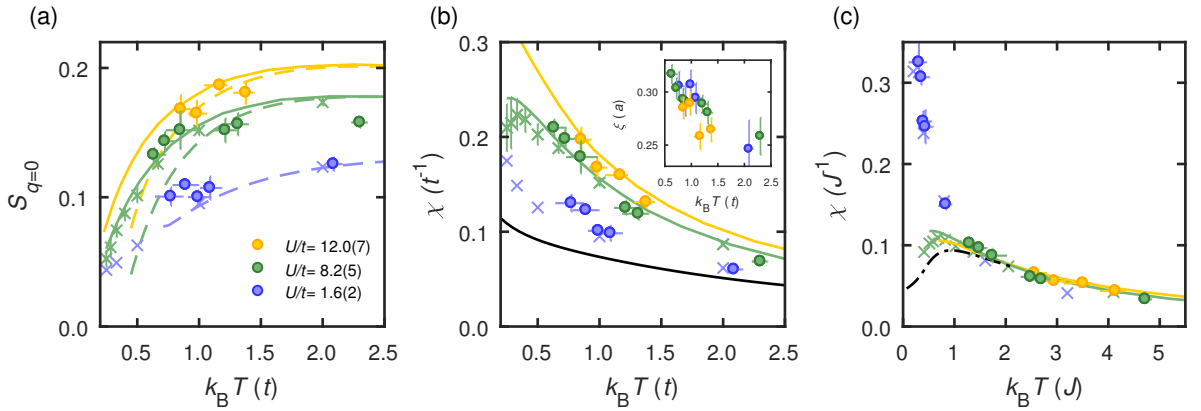

Figure 8.4: Spin correlations at half filling. (a) Measured spin structure factor $S^{\mathrm{mag}}_{\mathbf{q}=0}$ (circles) for different interaction strengths and temperatures. For comparison, data from a numerical linked cluster expansion of the two-dimensional Hubbard model [74] for $S^{\mathrm{mag}}_{\mathbf{q}=0}$ (solid lines) and $|C_{0,0}| - 4|C_{0,1}|$ (dashed lines) are shown for $U/t = 2$ (blue), 8 (green) and 12 (yellow). Crosses show results from quantum Monte-Carlo (QMC) calculations of the two-dimensional Hubbard model [131] of $S_{\mathbf{q}=0}$ for $U/t = 2$ (blue) and 8 (green). (b) Magnetic susceptibility χ extracted from the data shown in (a). Solid lines and crosses show corresponding results from NLCE and QMC. The solid black line shows the magnetic susceptibility χ for vanishing interactions. The inset shows the spin correlation length ξ extracted from fits to the correlation data versus distance. (c) Magnetic susceptibility scaled in units of the superexchange interaction J and comparison to the antiferromagnetic Heisenberg model [145] (dashed-dotted line). Vertical error bars display statistical errors. Horizontal error bars show the propagated systematic uncertainty of the on-site interaction U, which dominates over the statistical error of the temperature.

Within the uncertainties we find good agreement between our experimental data and numerical data from NLCE [74] and quantum Monte-Carlo (QMC) [131] calculations of the two-dimensional Hubbard model at half filling. For a qualitative analysis of beyond-nearest-neighbour AFM correlations at half filling we also plot in Figure 8.4(a) NLCE data for $|C_{0,0}| - 4|C_{0,1}|$. For intermediate and strong interactions at temperatures $k_B T < t$ a comparison with the spin structure factor indicates that contributions from next-nearest-neighbour AFM correlations $C_{1,1}$ become relevant and we observe these to be positive as expected. As is evident from Figure 8.4(a), the spin structure factor can be used as a thermometer in the range $k_B T \lesssim t$ where the density distribution responds only weakly upon further cooling [95] and our data constitute an initial calibration of this technique. At the temperatures realised in this work, the magnitude of the spin correlations are expected to decay exponentially with distance [126] according to

$$|C_{i_x,i_y}| = C_{0,0} \exp\left(-a\sqrt{i_x^2 + i_y^2}/\xi\right) . \tag{8.8}$$

Using our independent knowledge of the local moment and the calibration of the imaging point spread function (compare Chapter 5) we are able to extract the correlation length ξ from fits to the spatial correlations of $\tilde{S}^z(\mathbf{r})$. The resulting correlation length at half filling versus temperature and interaction strength is shown as an inset in Figure 8.4(b). As expected, we observe an increasing correlation length upon lowering the temperature for all interaction strengths realised in the experiment.

Uniform magnetic susceptibility

The magnetic properties of a system are often characterised by the magnetic susceptibility χ, which is defined as the linear response of the total magnetisation $\langle \hat{M}^z \rangle \simeq \langle \hat{M}_0^z \rangle + \chi h$ to a weak external magnetic

field H. Here $\langle \hat{M}_0{}^z \rangle$ is the magnetisation in the absence of an external field. In the spin balanced Hubbard model $\langle \hat{M}_0^z \rangle = 0$. The response of the magnetisation is quantified by the uniform magnetic susceptibility $\chi = \frac{\partial \langle \hat{M}^z \rangle}{\partial H}$. In fact, similar to the relation between density fluctuations and the isothermal compressibility, which is provided by the fluctuation-dissipation theorem, a similar connection exists between fluctuations $\langle \delta \hat{M}^z \rangle$ of the total magnetisation $\hat{M}^z = \sum_i \hat{S}_i^z$ and the magnetic susceptibility. Identifying the fluctuations of the total magnetisation with the uniform spin structure factor $S^{\mathrm{mag}}_{q=0} = \langle \delta \hat{M}^z \rangle / V$ the relation is given by

$$\chi = k_{\mathrm{B}} T S^{\mathrm{mag}}_{q=0} \,. \tag{8.9}$$

At high temperature, the microscopic magnetic moments are randomly oriented due to thermal density fluctuations. Hence, the magnetic susceptibility approaches zero. At low temperature, spin correlations build up, yielding a finite value of χ. Figure 8.4(b) shows the magnetic susceptibility determined from the measured correlations according to Eq. 8.9 together with numerical data. The black solid line is a prediction of the ideal Fermi gas on a lattice, where small antiferromagnetic correlations follow from the Pauli principle. Generally, we observe an increase of χ above the level of the ideal Fermi gas with increasing repulsive interactions. This is caused by the suppression of doubly-occupied sites which otherwise prevent the formation of a local moment. Note, that upon a further reduction of the temperature in future experiments, the peak in the uniform spin susceptibility may act as a sign of antiferromagnetic (quasi) long-range order.

Mapping to the Heisenberg model of localised spins

Figure 8.4(c) illustrates the agreement of the data for intermediate and strong interactions, $U/t > 8$, with the prediction of the antiferromagnetic Heisenberg model (cf. Section 2.4.5) with $J > 0$ (dashed dotted line) [145] when both temperature and magnetic susceptibility are scaled in units of $J = 4t^2/U$. As expected, we observe that for weak interactions, $U/t = 1.6$, the Hubbard model does not map to the Heisenberg model due to large on-site density fluctuations which prevent the formation of strong local moments.

8.5 Spin correlations in the doped Hubbard model

Finally, the spatially varying chemical potential inherently present in our experimental realisation allows us to investigate the reduction of AFM spin correlations upon doping the Mott insulator with holes at constant temperature. The ability to tune doping over an arbitrary range is impossible in the solid state, demonstrating the utility of cold atomic gases for quantum simulation of fundamental physics. Furthermore, numerical simulations of the two-dimensional Hubbard model away from half filling at low temperatures are very challenging due to the fermionic sign problem. While nearest-neighbour correlations have been computed [74], calculations of the magnetic susceptibility, which includes correlations at all length scales, have been published only for very specific parameter sets [146, 147]. Figure 8.5 shows the measured uniform spin structure factor as a function of the filling $n = \langle \hat{n}_{i,\uparrow} + \hat{n}_{i,\downarrow} \rangle$ for different temperatures. We compare the experimental results with the measured local moment and the theoretically expected local moment plus nearest-neighbour contributions $|C_{0,0}| - 4|C_{0,1}|$ (solid line) from NLCE calculations. For the two coldest temperatures, the structure factor at half filling clearly exceeds the sum of local moment (positive contribution) and nearest-neighbour correlations, which contribute with a negative sign in the antiferromagnetic case indicating the presence of next-nearest neighbour correlations, which have the same sign as the local moment. As the chemical potential is reduced and

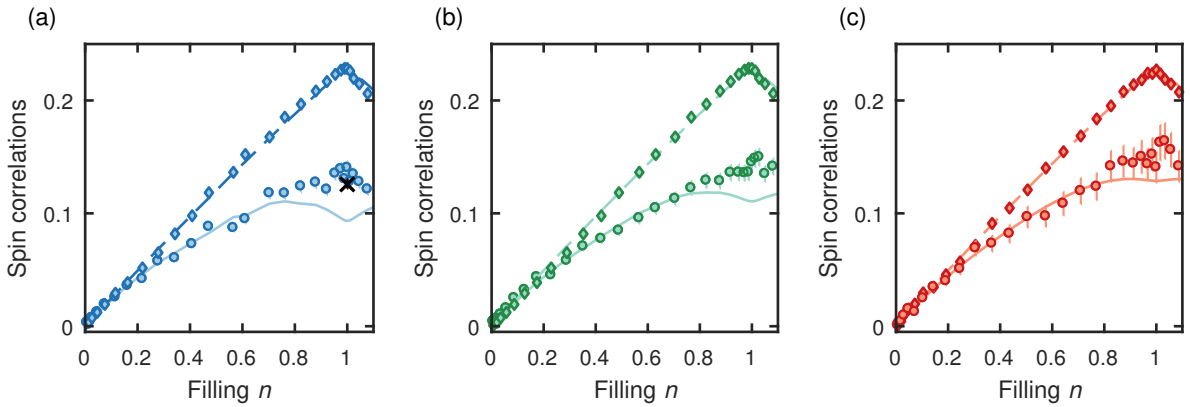

Figure 8.5: Effect of doping a Mott insulator. We compare $S^{\mathrm{mag}}_{\mathbf{q}=0}$ (circles) and local moment (diamonds) versus filling n at $U/t = 8.2(5)$ for temperatures (a) $k_{\mathrm{B}}T/t = 0.63^{+0.09}_{-0.02}$, (b) $0.72^{+0.06}_{-0.07}$ and (c) $0.85^{+0.13}_{-0.12}$. The dashed lines show the theoretical local moment and the solid lines show NLCE calculations of local moment plus nearest-neighbour correlations, $|C_{0,0}| - 4|C_{0,1}|$. For all data a gradual disappearance of spin correlations with increasing doping $0.5 - n$ is observed. The cross in (a) shows $S^{\mathrm{mag}}_{q=0}$ from QMC calculations at half filling for $k_{\mathrm{B}}T/t = 0.67$. Error bars show the standard error of the mean.

thereby the Mott insulator is doped with holes, we find that, at a filling of $n \sim 0.4$, the spin correlations are fully described by nearest-neighbour AFM correlations and, further, at a filling below $n \sim 0.1$ only the local moment persists.

8.6 Conclusion

In the work presented in this chapter, we studied spin correlations in the two-dimensional Hubbard model. To this end we developed a novel spin-resolved detection technique in order to probe the in-situ magnetisation of a gas of fermionic atoms trapped in an optical lattice. The onset of spin correlations manifested in a reduction of the uniform magnetic structure factor, which is expected for the antiferromagnetic case. We then investigated the dependence of the uniform spin structure factor on temperature, interaction strength and doping and inferred the presence of next-nearest neighbour correlations from a comparison of our findings to numerical data. In future experiments, the structure factor may serve as a thermometer, when the density degree of freedom is frozen out.

CHAPTER 9

Discussion and outlook

In the present thesis, I have discussed the experimental realisation of the Hubbard model using ultracold fermionic Potassium-40 trapped in a three-dimensional optical lattice. With strongly anisotropic tunnelling rates along the vertical and horizontal lattice directions, we effectively restrict the dynamics to two-dimensional planes. Thereby, the experiment realises the 2D Hubbard model on a square lattice. The control over all experimental parameters enables a precise quantum simulation of the Hubbard model over a wide range of interaction strengths and temperatures. Furthermore, the spatial variation of the local chemical potential due to the external trapping potential gives access to the equation of state in a single experimental realisation.

In a first set of experiments, we studied the equation of state of the Hubbard model in the density degree of freedom. To this end, we employed a combination of a high resolution imaging system and a spatially selective RF spectroscopy scheme. This approach enabled us to perform occupation resolved measurements of the in-situ density distribution of the many-body system. In the investigated range of temperature and interaction strength, we found excellent agreement with state of the art numerical calculations of the equation of state of the 2D Hubbard model. In the limit of low densities, we compared our data to the theory of a non-interacting Fermi gas on a tight-binding square lattice and found good agreement as well.

In a second set of experiments, we employed our ability to measure the distributions of singly and doubly occupied sites simultaneously to extract the magnitude of non-local correlations. Using the fluctuation dissipation theorem and the on-site density fluctuations, which result from the Pauli principle, we have determined the static structure factor at zero quasi momentum. We found that repulsive interactions lead to an increased suppression of the structure factor below the value that is expected from the Pauli-principle alone. Equivalently, we find a suppression of non-local density fluctuations as compared to the case of the ideal Fermi gas when the filling in the lattice is increased.

Finally, we introduced a novel spin resolved detection technique allowing us to investigate the spin degree of freedom. We applied this technique to study the formation of spin correlations as the system approaches an antiferromagnetically ordered state. Applying the fluctuation–dissipation theorem in the spin sector, we related the measured correlations to the corresponding thermodynamic quantity, the magnetic susceptibility. For low temperatures and strong interactions the magnetic susceptibility agrees well with the prediction of the antiferromagnetic Heisenberg model. Furthermore, using the spatial variation of the trapping potential in our setup allowed us to study magnetic correlations over the full doping range, which is difficult to realise with solid state materials.

Current developments

While writing this thesis, the experimental apparatus has been improved in a number of ways. This progress will be outlined in detail in the doctoral theses of Jeffrey Chan, Marcell Gall and Nicola Wurz. Here, three examples are briefly described:

- The data acquisition rate has been improved by a new scheme to address a single 2D layer. To this end, the existing setup has been upgraded with an additional optical lattice. This superlattice is formed by a red-detuned beam ($\lambda_{\mathrm{SL}} = 1\,064\,\mathrm{nm}$), which is superimposed with the existing vertical lattice using the same optics. This results in a lattice spacing of $\sim 2\,\mu\mathrm{m}$. The control over the optical power in the superlattice allows to remove population on every second plane in the vertical direction. Consequently, the spacing between populated vertical layers is doubled. This allows us to replace the tomography pulse (cf. Chapter 4) with an adiabatic frequency sweep, with a comparably broader and flatter excitation spectrum. Thereby, the tomography becomes more robust against drifts of the magnetic bias field and the data acquisition rate increases by more than a factor of five. At the same time, the contribution to the background signal has been reduced by a factor of almost two, since less planes are off-resonantly imaged.

- The hardware of the microwave addressing scheme has been overhauled in order to eliminate the observed phase noise (cf. Section 4.4) and to increase the fidelity to $f > 0.99$. This improves the reliability of the addressing scheme and ensures that less data has to be excluded from the analysis.

- Recently, we combined our spin-resolved high-resolution imaging technique with a method to imprint periodic spin patterns [148, 149] at arbitrary wavevector using a Ramsey-type sequence in an in-plane magnetic field gradient [118]. In a first application, we combined this technique with the correlation analysis presented in Chapter 8 to extract the magnetic structure factor $S^{\mathrm{mag}}(q, q)$ over the full doping range as a function of the quasi-momentum [150]. At half filling the staggered structure factor $S^{\mathrm{mag}}(\pi, \pi)$ provides an excellent thermometer in the low-temperature regime of the Hubbard model. Furthermore, the method enables us to reconstruct the site resolved correlation function via a Fourier expansion without requiring a site resolved imaging technique [36].

Future directions

During this thesis, the experiment matured into a faithful quantum simulator of the 2D Hubbard model. However, further progress in the field of quantum simulation with cold atoms will depend crucially on improved cooling techniques. Beyond that, it will be interesting to implement quantum many-body Hamiltonians, which go beyond the single band Hubbard model. In fact, this may well turn out to be crucial to understand the microscopic origin of high temperature superconductivity.

Novel cooling schemes

Despite the recent achievements in the quantum simulation of the Hubbard model with ultracold atoms on optical lattices, cold atom experiments still face the requirement of a significant reduction in temperature. Only then, quantum simulators may provide insight into low-energy phases of the Hubbard model, which are not accessible by numerical methods. To reach these goals, we aim to investigate three novel cooling schemes:

- **Arbitrary potentials.** We implemented a digital micro mirror device (DMD), which allows to project arbitrary patterns of light onto the atoms. The lower entropy of band insulating regions

as compared to metallic regions suggests that, with a constant total entropy, lower temperatures could be achieved in a homogeneous band insulating core surrounded by a much larger metallic region acting as a reservoir. With the DMD it is possible to shape the confinement in a controlled way. For our purpose, we need to cancel the harmonic confinement to produce a homogeneous region with a defined chemical potential in the centre of the trap. This region is connected to a larger homogeneous region with at lower chemical potential, where a metal forms. Thereafter, the band insulator in the centre may be adiabatically transferred to a Mott insulator. Initial studies on a system with a small number of lattice sites were carried out [151] but did not lead to a conclusive result yet.

- **Interlayer coupling.** For experiments in the thermodynamic limit, i.e. a larger system size, the approach outlined above might be hampered by the unfavourable scaling of the boundary between insulating and metallic regions and the area of the insulating region. Another possible route towards lower temperature is the (re-)introduction of tunnelling dynamics along the vertical direction together with control over the difference in the chemical potential in neighbouring planes. This can be achieved using a superlattice in the vertical direction. Thereby, the contact region between the system and the reservoir could be largely increased to allow for a more efficient transport of entropy out of the insulating region [152].

- **Splitting a low-entropy band insulator.** As a third option, we currently investigate the possibility to prepare a large low-entropy band-insulator of doubly occupied sites on the attractive side of the Feshbach resonance. We tested an adiabatic splitting scheme employing a ramp of the superlattice to transform the BI into a homogeneous metal at half filling. A subsequent ramp of the magnetic field to the repulsive side of the Feshbach resonance should result in a low-entropy Mott insulator, which could be characterized by an analysis of the spin-correlations.

Extended Hubbard models

The one-band Hubbard model studied in this thesis presents a formidable problem with many unsolved questions both from an experimental and a theoretical point of view. However, the Hubbard model may well turn out to be insufficient to explain the origin of superconductivity and related phenomena in the solid state. Therefore, it will be interesting to experimentally realise situations where extensions to the Hubbard model become important. For example, it is a general result that the single-band Hubbard model with nearest neighbour tunnelling and repulsive on-site interactions favours the formation of an antiferromagnetic ground state. A surprising, yet experimentally unrealistic, exception for bipartite lattices is the case discussed by Nagaoka, where a single hole in a half-filled band at infinite repulsive on-site interaction drives the system into ferromagnetic long range order [153].

However, experimentally more accessible situations with ferromagnetic correlations may arise when corrections to the Hubbard model become relevant, which is in particular at a shallow lattice depth and strong interactions. Here, the finite extent of the Wannier function leads to a contribution of next-nearest neighbour interaction. Indeed, this type of interaction may favour ferromagnetic alignment, since it increases the cost of placing anti-parallel spins on neighbouring lattice sites. The methods presented in Chapter 8 could be readily applied to investigate the existence of ferromagnetism in the Hubbard model. In fact, the uniform magnetic susceptibility is ideally suited to detect ferromagnetism since it diverges at the phase transition and therefore presents a sensitive probe for ferromagnetic order. Low enough temperatures provided, ferromagnetic order would also show in the formation of spin-polarised domains, which would be directly visible with our spin sensitive detection technique (cf. Chapter 4).

Clearly, the prospects of quantum simulation with atoms in optical lattices do not stop here and, due to the efforts being currently undertaken, much can be hoped to be learned about strongly correlated many-body systems in the years to come.

Bibliography

[1] P. W. Anderson, *More Is Different*, Science **177** (1972) 393 (cit. on p. 1).

[2] E. Dagotto, *Correlated electrons in high-temperature superconductors*, Rev. Mod. Phys. **66** (3 1994) 763 (cit. on pp. 1, 2, 101).

[3] I. M. Georgescu, S. Ashhab and F. Nori, *Quantum simulation*, Reviews of Modern Physics **86** (2014) 153, ISSN: 0034-6861 (cit. on p. 1).

[4] N. Ashcroft and N. Mermin, *Solid State Physics*, Cengage Learning, 1976 (cit. on pp. 1, 18).

[5] J. H. de Boer and E. J. W. Verwey, *Semi-conductors with partially and with completely filled 3 d -lattice bands*, Proceedings of the Physical Society **49** (1937) 59 (cit. on p. 2).

[6] N. Mott, *The basis of the Electron Theory of Metals, with Special Referenceto the Transition Metals*, Proceedings of the Physical Society. Section A **62** (1949) 416 (cit. on p. 2).

[7] M. Imada, A. Fujimori and Y. Tokura, *Metal-insulator transitions*, Rev. Mod. Phys. **70** (1998) 1039 (cit. on p. 2).

[8] J. Hubbard, *Electron Correlations in Narrow Energy Bands*, Proceedings of the Royal Society of London A: Mathematical, Physical and Engineering Sciences **276** (1963) 238 (cit. on p. 2).

[9] M. C. Gutzwiller, *Effect of Correlation on the Ferromagnetism of Transition Metals*, Phys. Rev. **134** (4A 1964) A923 (cit. on p. 2).

[10] J. Kanamori, *Electron Correlation and Ferromagnetism of Transition Metals*, Progress of Theoretical Physics **30** (1963) 275 (cit. on p. 2).

[11] A. Auerbach, *Interacting Electrons and Quantum Magnetism*, Springer, New York, 1998 (cit. on pp. 2, 27).

[12] J. G. Bednorz and K. A. Müller, *Possible high-Tc superconductivity in the Ba-La-Cu-O system*, Zeitschrift für Physik B Condensed Matter **64** (1986) 189 (cit. on p. 2).

[13] P. A. Lee, N. Nagaosa and X. G. Wen, *Doping a Mott insulator: Physics of high-temperature superconductivity*, Reviews of Modern Physics **78** (2006) (cit. on pp. 2, 83, 101).

[14] E. Y. Loh et al., *Sign problem in the numerical simulation of many-electron systems*, Phys. Rev. B **41** (13 1990) 9301 (cit. on p. 2).

[15] M. H. Anderson et al., *Observation of Bose-Einstein Condensation in a Dilute Atomic Vapor*, Science **269** (1995) 198 (cit. on pp. 2, 8).

[16] K. B. Davis et al., *Bose-Einstein Condensation in a Gas of Sodium Atoms*, Phys. Rev. Lett. **75** (22 1995) 3969 (cit. on pp. 2, 8, 67).

[17] B. DeMarco and D. S. Jin, *Onset of Fermi Degeneracy in a Trapped Atomic Gas*, Science **285** (1999) 1703 (cit. on pp. 3, 38, 67).

[18] R. Feynman, *Simulating physics with computers*, International journal of theoretical physics **21** (1982) 467 (cit. on p. 3).

[19] T. H. Johnson, S. R. Clark and D. Jacksch, *What is a quantum simulator?*, EPJ Quantum Technology (2014) 1 (cit. on p. 3).

[20] D. Jaksch et al., *Cold Bosonic Atoms in Optical Lattices*, Phys. Rev. Lett. **81** (15 1998) 3108 (cit. on p. 3).

[21] C. Chin et al., *Feshbach resonances in ultracold gases*, Rev. Mod. Phys. **82** (2 2010) 1225 (cit. on pp. 3, 9, 12).

[22] M. Greiner et al., *Quantum phase transition from a superfluid to a Mott insulator in a gas of ultracold atoms*, Nature **415** (2002) (cit. on pp. 3, 67).

[23] R. Jördens et al., *A Mott insulator of fermionic atoms in an optical lattice*, Nature **455** (2008) 204 (cit. on pp. 3, 83, 84).

[24] U. Schneider et al., *Metallic and Insulating Phases of Repulsively Interacting Fermions in a 3D Optical Lattice*, Science **322** (2008) 1520 (cit. on pp. 3, 83, 84).

[25] D. Greif et al., *Short-Range Quantum Magnetism of Ultracold Fermions in an Optical Lattice*, Science **340** (2013) 1307 (cit. on pp. 3, 84, 101).

[26] R. A. Hart et al., *Observation of antiferromagnetic correlations in the Hubbard model with ultracold atoms*, Nature **519** (2014) 1 (cit. on pp. 3, 83).

[27] T.-L. Ho and Q. Zhou, *Obtaining the phase diagram and thermodynamic quantities of bulk systems from the densities of trapped gases*, Nat. Phys. **6** (2010) 131 (cit. on pp. 3, 84).

[28] W. S. Bakr et al., *Probing the Superfluid–to–Mott Insulator Transition at the Single-Atom Level*, Science **329** (2010) 547 (cit. on pp. 3, 84).

[29] N. Gemelke et al., *In situ observation of incompressible Mott-insulating domains in ultracold atomic gases.*, Nature **460** (2009) 995 (cit. on pp. 3, 84).

[30] J. F. Sherson et al., *Single-atom-resolved fluorescence imaging of an atomic Mott insulator.*, Nature **467** (2010) 68 (cit. on pp. 3, 84).

[31] N. Navon et al., *The Equation of State of a Low-Temperature Fermi Gas with Tunable Interactions*, Science **328** (2010) 729 (cit. on pp. 3, 83, 84).

[32] M. J. H. Ku et al., *Revealing the superfluid lambda transition in the universal thermodynamics of a unitary Fermi gas.*, Science (New York, N.Y.) **335** (2012) 563 (cit. on pp. 3, 83).

[33] E. Haller et al., *Single-atom imaging of fermions in a quantum-gas microscope*, Nature Physics **11** (2015) 738 (cit. on pp. 3, 67).

[34] M. F. Parsons et al., *Site-Resolved Imaging of Fermionic* ^{6}Li *in an Optical Lattice*, Phys. Rev. Lett. **114** (21 2015) 213002 (cit. on pp. 3, 67).

[35] L. W. Cheuk et al., *Quantum-Gas Microscope for Fermionic Atoms*, Phys. Rev. Lett. **114** (2015) 193001, ISSN: 0031-9007 (cit. on pp. 3, 67).

[36] M. F. Parsons et al., *Site-resolved measurement of the spin-correlation function in the Fermi-Hubbard model*, Science **353** (2016) 1253, ISSN: 0036-8075 (cit. on pp. 3, 101, 110).

[37] L. W. Cheuk et al., *Observation of spatial charge and spin correlations in the 2D Fermi-Hubbard model*, Science **353** (2016) 1260 (cit. on pp. 3, 67).

[38] M. Boll et al., *Spin- and density-resolved microscopy of antiferromagnetic correlations in Fermi-Hubbard chains*, Science **353** (2016) 1257 (cit. on pp. 3, 101).

[39] A. Mazurenko et al., *A cold-atom Fermi–Hubbard antiferromagnet*, Nature **545** (2017) 462 (cit. on pp. 4, 101).

[40] L. Landau and E. Lifshitz, *Statistical Physics*, 3rd ed., Bd. 5, Elsevier Science, 2013 (cit. on p. 8).

[41] W. Ketterle and M. W. Zwierlein, *Making, probing and understanding ultracold Fermi gases*, (2008) 247 (cit. on pp. 9, 31).

[42] T. Köhler, K. Goral and P. S. Julienne, *Production of cold molecules via magnetically tunable Feshbach resonances*, Reviews of Modern Physics **78** (2006) 1311 (cit. on p. 9).

[43] J. J. Sakkurai, *Modern Quantum Mechanics*, 2nd ed., Addison Wesley, 1994 (cit. on p. 9).

[44] L. D. Landau and E. M. Lifshitz, *Quantum Mechanics: Non-relativistic Theory*, Pergamon Press, 1977 (cit. on p. 10).

[45] K. Huang and C. N. Yang, *Quantum-Mechanical Many-Body Problem with Hard-Sphere Interaction*, Phys. Rev. **105** (3 1957) 767 (cit. on p. 10).

[46] C. J. Foot, *Atomic Physics*, Oxford University Press, 2005 (cit. on pp. 11, 33, 34, 36, 68).

[47] T. G. Tiecke, *Properties of Potassium*, 2010, URL: http://www.tobiastiecke.nl/archive/PotassiumProperties.pdf (visited on 08/02/2018) (cit. on pp. 11, 35).

[48] B. Fröhlich, *A Strongly Interacting Two-Dimensional Fermi Gas*, PhD thesis: University of Cambridge, 2011 (cit. on pp. 12, 31, 33, 34).

[49] A. J. Moerdijk, B. J. Verhaar and A. Axelsson, *Resonances in ultracold collisions of* ^{6}Li, ^{7}Li, *and* ^{23}Na, Phys. Rev. A **51** (6 1995) 4852 (cit. on p. 12).

[50] C. A. Regal, M. Greiner and D. S. Jin, *Lifetime of Molecule-Atom Mixtures near a Feshbach Resonance in* ^{40}K, Phys. Rev. Lett. **92** (8 2004) 083201 (cit. on pp. 12, 13).

[51] C. A. Regal, M. Greiner and D. S. Jin, *Observation of Resonance Condensation of Fermionic Atom Pairs*, Phys. Rev. Lett. **92** (2004) 040403 (cit. on pp. 12, 13).

[52] J. P. Gaebler et al., *Observation of pseudogap behavior in a strongly interacting Fermi gas*, (2010) 1 (cit. on pp. 12, 13).

[53] U. Schneider, *Interacting Fermionic Atoms in Optical Lattices - A Qantum Simulator for Condensed Matter Physics*, PhD thesis: Johannes Guttenberg-Universität Mainz, 2010 (cit. on pp. 12, 13, 86).

[54] J. P. Gaebler et al., *p-Wave Feshbach Molecules*, Phys. Rev. Lett. **98** (20 2007) 200403 (cit. on p. 13).

[55] A. Ludewig, *Feshbach Resonances in* ^{40}K, PhD thesis: Universiteit van Amsterdam, 2012 (cit. on p. 13).

[56] H. Moritz et al., *Confinement Induced Molecules in a 1D Fermi Gas*, Phys. Rev. Lett. **94** (2005) 210401 (cit. on p. 14).

[57] M. Feld et al., *Observation of a pairing pseudogap in a two-dimensional Fermi gas*, Nature **480** (2011) 75 (cit. on pp. 14, 46).

[58] T. Uehlinger et al., *Artificial graphene with tunable interactions*, Phys. Rev. Lett. **90** (2013) 11 (cit. on p. 14).

[59] R. Grimm, M. Weidemüller and Y. B. Ovchinnikov, *Optical Dipole Traps for Neutral Atoms*, Advances In Atomic, Molecular, and Optical Physics **42** (2000) 95, ed. by B. Bederson and H. Walther (cit. on pp. 14, 15).

[60] F. Gerbier et al., *Probing Number Squeezing of Ultracold Atoms across the Superfluid-Mott Insulator Transition*, Phys. Rev. Lett. **96** (2006) 090401 (cit. on p. 14).

[61] C. J. Pethick and H. Smith, *Bose-Eintein Condensation in Dilute Gases*, Cambridge University Press, 2002 (cit. on p. 15).

[62] D. Steck, *Quantum and Atom Optics*, Open Publication License, 2015 (cit. on pp. 15, 49, 53, 54, 68).

[63] C. Kittel, *Introduction to Solid State Physics*, Wiley, 2004 (cit. on p. 18).

[64] G. H. Wannier, *The Structure of Electronic Excitation Levels in Insulating Crystals*, Phys. Rev. **52** (3 1937) 191 (cit. on p. 19).

[65] D. Jaksch and P. Zoller, *The cold atom Hubbard toolbox*, Annals of Physics **315** (2005) 52 (cit. on p. 20).

[66] S. Giorgini, L. P. Pitaevskii and S. Stringari, *Theory of ultracold atomic Fermi gases*, Reviews of Modern Physics **80** (2008) 1215 (cit. on p. 21).

[67] R. Walters et al., *Ab initio derivation of Hubbard models for cold atoms in optical lattices*, Phys. Rev. A **87** (4 2013) 043613 (cit. on p. 22).

[68] R. Walters et al., *Wannier states for optical lattices*, 2013, URL: `https://ccpforge.cse.rl.ac.uk/gf/project/mlgws/` (visited on 08/02/2018) (cit. on p. 22).

[69] D. Mitra et al., *Quantum gas microscopy of an attractive Fermi-Hubbard system*, Nature Physics **14** (2017) 173 (cit. on p. 22).

[70] T. Busch et al., *Two Cold Atoms in a Harmonic Trap*, Foundations of Physics **28** (1998) 549 (cit. on p. 23).

[71] Z. Idziaszek and T. Calarco, *Two atoms in an anisotropic harmonic trap*, Phys. Rev. A **71** (5 2005) 050701 (cit. on p. 23).

[72] Z. Idziaszek and T. Calarco,
Analytical solutions for the dynamics of two trapped interacting ultracold atoms,
Physical Review A - Atomic, Molecular, and Optical Physics **74** (2006) 1 (cit. on p. 23).

[73] P. I. Schneider, S. Grishkevich and A. Saenz, *Ab initio determination of Bose-Hubbard parameters for two ultracold atoms in an optical lattice using a three-well potential*,
Phys. Rev. A **80** (2009) 1 (cit. on p. 23).

[74] E. Khatami and M. Rigol,
Thermodynamics of strongly interacting fermions in two-dimensional optical lattices,
Phys. Rev. A **84** (2011) 053611 (cit. on pp. 23, 83, 86–89, 102, 106, 107).

[75] E. Khatami and M. Rigol,
Effect of particle statistics in strongly correlated two-dimensional Hubbard models,
Phys. Rev. A **86** (2 2012) 023633 (cit. on p. 23).

[76] B. Tang, E. Khatami and M. Rigol, *A short introduction to numerical linked-cluster expansions*,
Computer Physics Communications **184** (2013) 557 (cit. on p. 23).

[77] R. Scalettar, *Quantum Materials: Experiments and Theory*, ed. by E. Pavarini et al., vol. 6,
Modeling and Simulation, Forschungszentrum Jülich, 2016, chap. 4 420 p. (Cit. on pp. 23, 25).

[78] J. E. Hirsch, *Two-dimensional Hubbard model: Numerical simulation study*,
Phys. Rev. B **31** (1985) 4403 (cit. on p. 25).

[79] S. Murmann et al.,
Two Fermions in a Double Well: Exploring a Fundamental Building Block of the Hubbard Model,
Phys. Rev. Lett. **114** (8 2015) 080402 (cit. on p. 27).

[80] A. H. MacDonald, S. M. Girvin and D. Yoshioka, $\frac{t}{U}$ *expansion for the Hubbard model*,
Phys. Rev. B **37** (16 1988) 9753,
URL: https://link.aps.org/doi/10.1103/PhysRevB.37.9753 (cit. on p. 29).

[81] P. W. Anderson, *New Approach to the Theory of Superexchange Interactions*,
Phys. Rev. **115** (1 1959) 2 (cit. on p. 29).

[82] N. D. Mermin and H. Wagner, *Absence of Ferromagnetism or Antiferromagnetism in One- or Two-Dimensional Isotropic Heisenberg Models*, Phys. Rev. Lett. **17** (22 1966) 1133
(cit. on p. 29).

[83] M. Feld, *Low Temperature Phases of Interacting Fermions in Two Dimensions*,
PhD thesis: University of Cambridge, 2011 (cit. on pp. 31, 34).

[84] E. Vogt, *Collective Modes and Polarons in two-dimensional Fermi Gases*,
PhD thesis: University of Cambridge, 2013 (cit. on p. 31).

[85] L. Miller, *Ultracold Fermions in Two-Dimensional Optical Lattices: Quantum Simulation of the Hubbard Model*, PhD thesis: University of Cambridge, 2016 (cit. on pp. 32, 39, 83).

[86] D. E. Pritchard, *Cooling Neutral Atoms in a Magnetic Trap for Precision Spectroscopy*,
Phys. Rev. Lett. **51** (15 1983) 1336 (cit. on pp. 32, 34).

[87] C. S. Adams et al., *Evaporative Cooling in a Crossed Dipole Trap*,
Phys. Rev. Lett. **74** (18 1995) 3577 (cit. on p. 32).

[88] E. L. Raab et al., *Trapping of Neutral Sodium Atoms with Radiation Pressure*,
Phys. Rev. Lett. **59** (23 1987) 2631 (cit. on p. 33).

[89] H. J. Metcalf and P. van der Straten, *Laser Cooling and Trapping*, Springer, 1999 (cit. on p. 33).

[90] S. Chu et al.,
Three-dimensional viscous confinement and cooling of atoms by resonance radiation pressure,
Phys. Rev. Lett. **55** (1 1985) 48 (cit. on p. 33).

[91] R. V. Pound, *Electronic Frequency Stabilization of Microwave Oscillators*,
Review of Scientific Instruments **17** (1946) 490 (cit. on p. 34).

[92] U. Schünemann et al., *Simple scheme for tunable frequency offset locking of two lasers*,
Review of Scientific Instruments **70** (1999) 242 (cit. on p. 34).

[93] T. Weber et al., *Bose-Einstein Condensation of Cesium*, Science (2002) (cit. on p. 38).

[94] T. Esslinger, *Fermi-Hubbard Physics with Atoms in an Optical Lattice*,
Annual Review of Condensed Matter Physics **1** (2010) 129 (cit. on pp. 38, 83).

[95] E. Cocchi et al., *Equation of State of the Two-Dimensional Hubbard Model*,
Physical Review Letters **116** (2016) 175301 (cit. on pp. 39, 41, 83, 106).

[96] E. Cocchi,
Analogue Quantum Simulation of the Two-Dimensional Hubbard Model with Ultracold Fermions,
PhD thesis: University of Cambridge, 2016 (cit. on pp. 40, 83).

[97] S. Friebel et al., CO_2*-laser optical lattice with cold rubidium atoms*,
Phys. Rev. A **57** (1 1998) R20 (cit. on p. 42).

[98] M. Greiner et al., *Exploring Phase Coherence in a 2D Lattice of Bose-Einstein Condensates*,
Physical Review Letters **87** (2001) 160405, ISSN: 0031-9007 (cit. on p. 42).

[99] A. Kastberg et al., *Adiabatic Cooling of Cesium to 700 nK in an Optical Lattice*,
Phys. Rev. Lett. **74** (9 1995) 1542 (cit. on p. 42).

[100] T. Rom et al.,
Free fermion antibunching in a degenerate atomic Fermi gas released from an optical lattice.,
Nature **444** (2006) 733 (cit. on pp. 43, 77).

[101] M. Garwood and L. DelaBarre,
The Return of the Frequency Sweep: Designing Adiabatic Pulses for Contemporary NMR,
Journal of Magnetic Resonance **153** (2001) 155 (cit. on p. 60).

[102] X. Lacour et al., *Uniform analytic description of dephasing effects in two-state transitions*,
Phys. Rev. A **75** (2007) 033417 (cit. on p. 66).

[103] T. Noel et al., *Adiabatic passage in the presence of noise*, Phys. Rev. A **85** (2012) 023401
(cit. on p. 66).

[104] S. Nascimbène et al., *Exploring the thermodynamics of a universal Fermi gas*,
Nature **463** (2010) 1057 (cit. on p. 67).

[105] I. Boettcher et al.,
Equation of State of Ultracold Fermions in the 2D BEC-BCS Crossover Region,
Phys. Rev. Lett. **116** (2016) 045303 (cit. on p. 67).

[106] A. Omran et al.,
Microscopic Observation of Pauli Blocking in Degenerate Fermionic Lattice Gases,
Phys. Rev. Lett. **115** (26 2015) 263001 (cit. on pp. 67, 92).

[107] D. Greif et al., *Site-resolved imaging of a fermionic Mott insulator*, Science **351** (2016) 953 (cit. on pp. 67, 84).

[108] G. Reinaudi et al., *Strong saturation absorption imaging of dense clouds of ultracold atoms.*, Optics letters **32** (2007) 3143 (cit. on pp. 68, 72).

[109] J. C. Mullikin et al., "Methods for CCD camera characterization", *Image Acquisition and Scientific Imaging Systems*, ed. by H. C. Titus and A. Waks, vol. 2173, International Society for Optics and Photonics, SPIE, 1994 73 (cit. on p. 72).

[110] K. Sperlich and H. Stolz, *Quantum efficiency measurements of (EM)CCD cameras: high spectral resolution and temperature dependence*, Measurement Science and Technology **25** (2014) 15502 (cit. on p. 72).

[111] M. Pappa et al., *Ultra-sensitive atom imaging for matter-wave optics*, New Journal of Physics **13** (2011) 115012 (cit. on p. 72).

[112] C. F. Ockeloen et al., *Detection of small atom numbers through image processing*, Phys. Rev. A **82** (2010) (cit. on p. 73).

[113] C. Lauriane, *Coherence and superfluidity of Bose gases in reduced dimensions: from harmonic traps to uniform fluids*, PhD thesis: Ecole Normale Supérieure, 2014 (cit. on p. 74).

[114] S. Fölling et al., *Spatial quantum noise interferometry in expanding ultracold atom clouds*, Nature **434** (2005) 481 (cit. on p. 77).

[115] N. Wiener, *Generalized harmonic analysis*, Acta Math. **55** (1930) 117 (cit. on p. 77).

[116] E. Altman, E. Demler and M. Lukin, *Probing many-body states of ultracold atoms via noise correlations*, Phys. Rev. A **70** (2004) 013603 (cit. on p. 79).

[117] G. M. Bruun et al., *Antiferromagnetic noise correlations in optical lattices*, Physical Review A - Atomic, Molecular, and Optical Physics **80** (2009) 1 (cit. on p. 79).

[118] N. Wurz, *Imprinting Spin Spirals into an Ultracold Fermi Gas*, 2016 (cit. on pp. 79, 110).

[119] C.-L. Hung et al., *Extracting density–density correlations from in situ images of atomic quantum gases*, New Journal of Physics **13** (2011) 075019 (cit. on p. 79).

[120] C.-L. Hung, *In situ probing of two-dimensional quantum gases*, Thesis (2011) 1 (cit. on p. 80).

[121] W. Zwerger, *The BCS-BEC Crossover and the Unitary Fermi Gas*, Springer, 2012 (cit. on p. 83).

[122] M. Köhl et al., *Fermionic Atoms in a Three Dimensional Optical Lattice: Observing Fermi Surfaces, Dynamics, and Interactions*, Phys. Rev. Lett. **94** (2005) 080403 (cit. on p. 83).

[123] S. Taie et al., *An SU(6) Mott insulator of an atomic Fermi gas realized by large-spin Pomeranchuk cooling*, Nature Physics **8** (2012) 825 (cit. on pp. 83, 84).

[124] P. M. Duarte et al., *Compressibility of a Fermionic Mott Insulator of Ultracold Atoms*, Phys. Rev. Lett. **114** (7 2015) 070403 (cit. on pp. 83, 84).

[125] A. Georges et al., *Dynamical mean-field theory of strongly correlated fermion systems and the limit of infinite dimensions*, Rev. Mod. Phys. **68** (1 1996) 13 (cit. on p. 83).

[126] J. P. F. LeBlanc and E. Gull, *Equation of state of the fermionic two-dimensional Hubbard model*, Phys. Rev. B **88** (15 2013) 155108 (cit. on pp. 83, 86–89, 106).

[127] R. Jördens et al., *Quantitative Determination of Temperature in the Approach to Magnetic Order of Ultracold Fermions in an Optical Lattice*, Phys. Rev. Lett. **104** (2010) 180401 (cit. on p. 84).

[128] R. A. Hart et al., *Observation of antiferromagnetic correlations in the Hubbard model with ultracold atoms*, Nature **519** (2015) 211 (cit. on pp. 84, 101).

[129] C. Hofrichter et al., *Direct Probing of the Mott Crossover in the* SU(N) *Fermi-Hubbard Model*, Phys. Rev. X **6** (2 2016) 021030 (cit. on p. 84).

[130] K. Van Houcke et al., *Feynman diagrams versus Fermi-gas Feynman emulator*, Nature Physics **8** (2012) 366 (cit. on p. 84).

[131] T. Paiva et al., *Fermions in 2D Optical Lattices: Temperature and Entropy Scales for Observing Antiferromagnetism and Superfluidity*, Physical Review Letters **104** (2010) 066406 (cit. on pp. 88, 89, 106).

[132] J. H. Drewes et al., *Thermodynamics versus Local Density Fluctuations in the Metal–Mott-Insulator Crossover*, Phys. Rev. Lett. **117** (13 2016) 135301 (cit. on p. 91).

[133] R. Kubo, *The fluctuation-dissipation theorem*, Reports on Progress in Physics **29** (1966) 306 (cit. on p. 91).

[134] K. Huang, *Statistical Mechanics*, 2nd ed., Wiley, New York, 1987 (cit. on p. 92).

[135] Q. Zhou and T. L. Ho, *Universal thermometry for quantum simulation*, Physical Review Letters **106** (2011) 1 (cit. on p. 92).

[136] T. Müller et al., *Local Observation of Antibunching in a Trapped Fermi Gas*, Phys. Rev. Lett. **105** (2010) 040401 (cit. on p. 92).

[137] C. Sanner et al., *Suppression of Density Fluctuations in a Quantum Degenerate Fermi Gas*, Phys. Rev. Lett. **105** (4 2010) 040402 (cit. on p. 92).

[138] C. Sanner et al., *Speckle imaging of spin fluctuations in a strongly interacting fermi gas*, Physical Review Letters **106** (2011) 1 (cit. on p. 92).

[139] F. Schwabl, *Quantenmechanik für Fortgeschrittene (QM II) (Springer Lehrbuch)*, Springer-Verlag Berlin Heidelberg, 2000 (cit. on p. 93).

[140] M. Klawunn et al., *Local atom-number fluctuations in quantum gases at finite temperature*, Phys. Rev. A **84** (2011) 1 (cit. on p. 95).

[141] E. Duchon, Y. Kato and N. Trivedi, *Diagnostic for phases and quantum critical regions using deviations from the local fluctuation-dissipation theorem*, Phys. Rev. A **86** (6 2012) 063608 (cit. on p. 97).

[142] S. Fang et al., *Quantum criticality from in situ density imaging*, Phys. Rev. A **83** (2011) 1 (cit. on p. 97).

[143] J. H. Drewes et al., *Antiferromagnetic Correlations in Two-Dimensional Fermionic Mott-Insulating and Metallic Phases*, Phys. Rev. Lett. **118** (17 2017) 170401 (cit. on p. 101).

[144] L. W. Cheuk et al., *Observation of 2D fermionic Mott insulators of K40 with single-site resolution*, Phys. Rev. Lett. **116** (23 2016) 235301 (cit. on p. 101).

[145] A. W. Sandvik, *Computational Studies of Quantum Spin Systems*, AIP Conference Proceedings **1297** (2010) 135 (cit. on pp. 106, 107).

[146] A. Moreo, *Magnetic susceptibility of the two-dimensional Hubbard model*, Phys. Rev. B **48** (5 1993) 3380 (cit. on p. 107).

[147] J. Bonca and P. Prelovsek, *Thermodynamics of the planar Hubbard model*, Phys. Rev. B **67** (8 2003) 085103 (cit. on p. 107).

[148] M. Koschorreck et al., *Universal spin dynamics in two-dimensional Fermi gases*, Nature Physics **9** (2013) 405 (cit. on p. 110).

[149] S. Hild et al., *Far-from-Equilibrium Spin Transport in Heisenberg Quantum Magnets*, Phys. Rev. Lett. **113** (14 2014) 147205 (cit. on p. 110).

[150] N. Wurz et al., *Coherent manipulation of spin correlations in the Hubbard model*, Phys. Rev. A **97** (5 2018) 051602 (cit. on p. 110).

[151] C. S. Chiu et al., *Quantum statee engineering of a Hubbard system with ultracold fermions*, (2017), arXIv: 1712.07114 (cit. on p. 111).

[152] A. Kantian, S. Langer and A. J. Daley, *Dynamical disentangling and cooling of atoms in bilayer optical lattices*, Phys. Rev. Lett. **120** (2016) 60401 (cit. on p. 111).

[153] Y. Nagaoka, *Ferromagnetism in a Narrow, Almost Half-Filled s Band*, Phys. Rev. **147** (1 1966) 392 (cit. on p. 111).